
Synthesis and Functionalization of Molecular Vanadium Oxides

Dissertation zur Erlangung des Grades „Doktor der
Naturwissenschaften“ im Promotionsfach Chemie am
Fachbereich Chemie, Pharmazie, Geographie und
Geowissenschaften der Johannes Gutenberg-Universität Mainz

M. Sc. Moritz Remmers

geboren in Aschaffenburg

Mainz, 2025

CC-BY-4.0

„Neugier steht immer an erster Stelle eines Problems, das gelöst werden will.“

– Galileo Galilei

Zusammenfassung

Polyoxovanadate haben aufgrund ihrer vielseitigen Eigenschaften großes Interesse geweckt. Die durch die Möglichkeit der Funktionalisierung mit 3d-Übergangsmetallen und organischen Gruppen einstellbaren Redox-Eigenschaften führten zu Anwendungen in der Katalyse, der supramolekularen Chemie, der Biologie und der Energiespeicherung. Insbesondere die Verwendung von Vanadaten in Redox-Flow-Batterien gehört zu den wichtigsten Forschungsthemen, wobei der Schwerpunkt auf der Maximierung der Ladungsdichte durch Erhöhung der Elektronenanzahl pro aktiver Einheit, der Löslichkeit und der Stabilität der aktiven Spezies während des Ladens und Entladens liegt. Diese Arbeit konzentrierte sich auf die Entwicklung neuartiger, hoch redoxaktiver und hochlöslicher Materialien sowie deren Funktionalisierung und Lösungsverhalten.

Im ersten Projekt wurde die von Streb et al. entwickelte Platzhalterstrategie verwendet, um das Polyoxovanadat-Anion $\{V_{12}\}_{\text{tube}}$ an beiden Bindungspositionen mit Magnesium zu funktionalisieren. Wir zeigen, wie der Ersatz des Platzhalterkations Dimethylammonium (DMA) durch ein kompetitives Bindungsgleichgewicht zwischen Heterometall und Platzhalter kontrolliert wird und gemäß Le Chatelier durch Zugabe von DMA zu den Edukten verschoben werden kann. Die monofunktionalisierte Spezies wurde in Lösung durch ^{51}V -NMR und ESI-MS charakterisiert, und Titrationsstudien ergaben ein Verhältnis von 1:1 von Magnesium zu Cluster im vollständig oxidierten Zustand. Zur Reduktion des Clusters wurde sichtbares Licht eingesetzt, und die Zunahme der negativen Ladung in Verbindung mit den strukturellen Veränderungen des gemischten Clusters führte zur Bildung von zweifach mit Magnesium funktionalisiertem $\{V_{12}\}_{\text{tube}}$. Die Struktur wurde vollständig charakterisiert, und die Reduktion wurde durch die zunehmende IVCT-Bande des um ein Elektron reduzierten, gemischt valenten Clusters verfolgt.

Im zweiten Projekt wird ein synthetischer Ansatz vorgestellt, bei dem das Redox-Selbstgleichgewicht eines gemischten Clustersystems mit $\{MV_{13}\}$ mit $M = [VO]^{2+}$ oder Mg^{2+} erreicht wurde. Die Eintopf-Synthese ermöglichte die Bildung einer 1:1-Mischung aus zwei isostrukturellen Clustern, die im elektrochemischen Potentialbereich von Acetonitril bis zu 16 Elektronen reversibel speichern können. Die Aktivierungsenergie für die Zersetzung des $(nBu_4N)_4\{V_{10}\}_{red}$ Vorläufers durch Magnesiumchlorid als Lewis-Säure wurde durch temperaturabhängige UV-Vis-Spektroskopie bestimmt, die eine Kinetik erster Ordnung anzeigte, die zur gleichzeitigen Bildung beider strukturell verwandter Cluster führte. Die Kombination von zwei oder mehr Spezies für elektrochemische Anwendungen wurde bisher nicht untersucht, was höchstwahrscheinlich auf Nebenreaktionen inkompatibler Cluster zurückzuführen ist. Das Material wurde vollständig charakterisiert, und die Bulk-Elektrolyse in Kombination mit EPR und Einkristall-Röntgenbeugung ergab drei Elektronen auf dem $\{MgV_{13}\}$ - und fünf Elektronen auf dem $\{V_{14}\}$ -Cluster.

Die Anwendung in einem nichtwässrigen, symmetrischen Redox-Flow-Batterie-Aufbau wurde in einem dritten Projekt getestet. Für erste mechanistische Einblicke wurde der Diffusionskoeffizient mittels Square-Wave-Voltammetrie bei variabler Frequenz und Linear-Sweep-Voltammetrie an einer rotierenden Scheibenelektrode bestimmt. Der Crossover für die Celgard-2400 Membran wurde in einem Flow-Aufbau getestet, und es wurden vergleichbare Permeabilitätswerte zu Literaturwerten erhalten. Die Verbindung zeigte eine ausgezeichnete Batteriestabilität über 20 Zyklen mit vernachlässigbarer Kapazitätsabnahme und einer Coulomb-Effizienz von bis zu 99 %, kombiniert mit guter Spannungseffizienz und einer Energieeffizienz von etwa 67 %. Die Berechnung zeigt, dass 99 % der theoretischen Kapazität erreicht werden. Zukünftige Arbeiten werden die Optimierung der Batterieparameter, spektroelektrochemische Untersuchungen und OCP-Tracking im Anolyt und Katholyt sowie die Modifikation der aktiven Spezies über eine Salzmetathese-Route umfassen, bei der nBu_4N^+ durch Alkylammonium-Kationen mit längeren Alkylketten ersetzt wird, um die Löslichkeit zu verbessern.

In einem vierten Projekt wurde das Lösungsverhalten von $\{\text{MnV}\}^{3-}$ in Abhängigkeit vom Oxidationszustand untersucht. Der Cluster ist eine Modellverbindung für die photokatalytische und elektrokatalytische Wasseroxidation, stabil in reinem Acetonitril. Der Einfluss des Mischlösungsmittelsystems aus Acetonitril und Wasser auf die Zersetzung und Katalyse ist wichtig für das grundlegende Verständnis der zugrunde liegenden Reaktionsmechanismen. Die Berechnungen zeigen eine Präferenz von Wasser, eine Lösemittelhülle um $\{\text{MnV}\}^{3-}$ auszubilden. Für die ein- oder zweifach oxidierten Spezies $\{\text{MnV}\}^{2-}$ bzw. $\{\text{MnV}\}^{1-}$ kann dies nicht beobachtet werden. Die Solvatisierung führt zu spektralen Veränderungen im UV-Vis-Spektrum aufgrund von d-d-Übergängen der Mn-Zentren. Die Veränderungen traten bei der einfach oxidierten Spezies bereits bis zu einem Wassergehalt von 2 Vol-% auf, während der ursprüngliche Cluster erst bis zu 4 Vol-% Veränderungen zeigt. Dies wurde weiterhin durch Flüssig-FTIR belegt, das Veränderungen in den V=O-Schwingungen mit der Zugabe von Wasser zeigte. Zusätzliche Effekte wie Ligandenaustausch und Agglomeration wurden als Ergebnis der unterschiedlichen Solvatisierung diskutiert. Das grundlegende Verständnis der Solvatisierungseffekte wird in Zukunft helfen, das katalytische Verhalten von Polyoxovanadat-Clustern in Acetonitril-Wasser-Gemischen zu verstehen.

Abstract

Polyoxovanadates have gained widespread interest due to their highly versatile properties. The tunable redox properties due to the possibility of functionalization with 3d transition metals and organic groups led to applications in catalysis, supramolecular chemistry, biology and energy storage. Especially the use of vanadates in redox flow batteries is among the most important research topics focusing on maximizing the charge density by increasing the number of electrons per active unit, the solubility and the stability of the active species during cycling. This work focused on the development of novel highly redox active and highly soluble materials as well as their functionalization and solution behavior.

In the first project the placeholder strategy developed by Streb et al. was used to functionalize $\{V_{12}\}_{\text{tube}}$ with magnesium at both binding positions. We demonstrate how the replacement of the placeholder cation dimethylammonium (DMA) was controlled by a competitive binding equilibrium between heterometal and placeholder and can be shifted to the reactants according to Le Chatelier by adding an excess of DMA. The monofunctionalized species was characterized in solution by ^{51}V NMR and ESI-MS, and titration studies revealed the 1:1 ratio of magnesium per cluster in the fully oxidized state. Visible light irradiation was used to reduce the cluster and the increase of the negative charge combined with the structural changes of the mixed cluster led to the formation of di-magnesium-functionalized $\{V_{12}\}_{\text{tube}}$. The structure was fully characterized, and the reduction was followed by the increasing IVCT band of the one-electron reduced, mixed-valent cluster.

In the second project a synthetic approach is presented, where the redox self-equilibration of a mixed cluster system containing $\{MV_{13}\}$ with $M = [\text{VO}]^{2+}$ or Mg^{2+} was achieved. The one-pot synthesis allowed for the formation of a 1:1 mixture of two compatible clusters, which can store up to 16 electrons on the electrochemical potential range accessible in acetonitrile. The activation energy for the decomposition of $(\text{nBu}_4\text{N})_4\{V_{10}\}_{\text{red}}$ precursor by magnesium chloride as a Lewis acid was determined by temperature-dependent UV-Vis spectroscopy which indicated first-order kinetics leading to simultaneous formation of both structurally related clusters. The combination of two or more species for electrochemical applications so far has not been studied,

most likely due to side reactions of incompatible clusters. The material was fully characterized and bulk electrolysis combined with EPR and single-crystal X-ray diffraction revealed three electrons on the $\{\text{MgV}_{13}\}$ cluster and five electrons on the $\{\text{V}_{14}\}$ cluster.

The application in a non-aqueous, symmetric redox-flow battery setup was tested in a third project. For initial mechanistic insights, the diffusion coefficient was determined using square-wave voltammetry at variable frequency and linear-sweep voltammetry at a rotating disc electrode. The crossover through the separating membrane was tested in a flow setup and comparable permeability to the literature values was obtained. The compound revealed excellent battery cycling stability after 20 cycles with negligible capacity fading and a coulombic efficiency of up to 99% combined with good voltage efficiency and energy efficiency of about 67%. The calculation reveals that 99% of the theoretical capacity is achieved. Future work will include the optimization of the battery parameters, spectroelectrochemical investigations and OCP tracking in the anolyte and catholyte as well as modification of the active species via a salt metathesis route where $n\text{Bu}_4\text{N}^+$ is replaced by alkylammonium cations with longer alkyl chains to improve solubility.

In a fourth project the solution behavior of $\{\text{MnV}\}^{3-}$ depending on the oxidation state, was investigated. The cluster is a model compound for photocatalytic and electrocatalytic water oxidation, stable in pure acetonitrile. The influence of the mixed solvent system of acetonitrile and water on decomposition and catalysis is important for the fundamental understanding of the underlying mechanisms. The calculations show a preference of water to form a solvation shell around $\{\text{MnV}\}^{3-}$. This cannot be observed for the one-electron or two-electron oxidized species $\{\text{MnV}\}^{2-}$ and $\{\text{MnV}\}^{1-}$. The solvation leads to spectral changes in the UV-Vis spectrum due to d-d transitions of the Mn centers. The changes occurred at up to 2 vol% water for the one-electron oxidized species compared to the original cluster which shows changes up to 4 vol%. This was further evidenced by liquid FTIR which was used to show changes in the $\text{V}=\text{O}$ vibrations with the addition of water. Additional effects like ligand exchange and agglomeration were discussed as a result of the different solvation. The fundamental understanding of the solvation effects will help to understand the catalytic behavior of polyoxovanadate clusters in acetonitrile-water mixtures in the future.

Contents

Zusammenfassung	i
Abstract.....	iv
Abbreviations	ix
Notation	x
Compounds	x
1. Introduction	1
1.1. Polyoxometalates	2
1.2. Isopolyoxometalates	4
1.3. Heteropolyoxometalates	4
1.4. Synthesis via Self-Assembly	5
1.5. Aqueous Chemistry of Vanadates	7
1.6. From aqueous to non-aqueous conditions	8
1.7. The Role of Templates	10
1.7.1. Internal Templates	11
1.7.2. External Templates	15
1.8. Seeded Growth Mechanisms in Organic Solvents	19
1.9. Controlled Functionalization via Lacunary Positions	22
1.10. Placeholder Strategy	24
1.11. Hybrid Supramolecular Organic-Inorganic Materials	26
1.12. Energy storage	29
1.12.1. Redox Flow Batteries	29
1.12.2. Electrode Materials	31
1.12.3. Ionic liquids	33
2. Objectives	35
3. Results and Discussion	37
3.1. New synthetic strategies for cluster functionalization using light	37

3.1.1. Introduction	37
3.1.2. Results.....	39
3.1.3. Discussion	47
3.1.4. Methods	48
3.2. Supplementary Information	50
3.2.1. Instrumentation.....	50
3.2.2. Experimental Section and Characterization	53
3.2.3. Mechanistic studies	62
3.2.4. Theoretical calculations	69
3.3. Synthesis of electrochemically promising novel materials.....	72
3.3.1. Introduction.....	72
3.3.2. Results and Discussion	74
3.3.3. Conclusion.....	81
3.4. Supporting Information	82
3.4.1. Instrumentation.....	82
3.4.2. Experimental data.....	85
3.5. Implementation into Redox-Flow Batteries.....	108
3.5.1. Introduction.....	108
3.5.2. Results and Discussion	111
3.5.3. Conclusion.....	117
3.6. Supporting Information	118
3.6.1. Instrumentation.....	118
3.6.2. Experimental data.....	119
3.7. The Influence of Mixed Solvent Systems	128
3.7.1. Introduction.....	128
3.7.2. Results and Discussion	131
3.7.3. Conclusion.....	137

3.8. Supporting Information:	138
3.8.1. Instrumentation	138
3.8.2. Experimental data	140
3.8.3. Molecular Dynamics Simulations	156
4. Summary and Perspective	159
References.....	164
5. Figures	179
6. Tables	194
Scientific Contributions	196
Curriculum Vitae	197
Danksagung.....	Fehler! Textmarke nicht definiert.
Eigenständigkeitserklärung.....	199

Abbreviations

Table 1: List of abbreviations.

Dichloromethane	DCM
Density Functional Theory	DFT
Dimethylammonium	DMA
N,N-dimethylformamide	DMF
Dimethyl sulfoxide	DMSO
Deoxyribonucleic Acid	DNA
Diffusion Ordered Spectroscopy	DOSY
Electron Paramagnetic Resonance	EPR
Electrospray Ionization Mass Spectrometry	ESI-MS
Fourier Transform Infrared Spectroscopy	FTIR
Gemini Surfactant	gem
Inductively Coupled Plasma Optical Emission Spectroscopy	ICP-OES
Intervalence Charge Transfer	IVCT
Light Emitting Diode	LED
Ligand to Metal Charge Transfer	LMCT
Acetonitrile	MeCN
Molecular Dynamics	MD
Tetraalkylammonium Cation	nEt ₄ N ⁺ , nBu ₄ N ⁺
N-Methylpyrrolidone	NMP
Nuclear Magnetic Resonance	NMR
Open Circuit Potential	OCP
Proton-Coupled Electron Transfer	PCET
Palladium(0) bis(1,5-cyclooctadiene)	PdCOD
Polyoxometalate	POM
Radial Distribution Function	RDF
Thermogravimetric Analysis	TGA
Total Correlation Spectroscopy	TOCSY
Tris(hydroxymethyl)aminomethane	Tris
Ultraviolet-Visible Spectroscopy	UV-Vis
X-ray Diffraction	XRD

Notation

For simplification curly brackets enclosing the number and type of the addenda-atoms are used aside the standard square brackets to abbreviate the metal oxo clusters. The unique structural description written in subscript is included in the case of same number of addenda atoms. In case of varying templates, the abbreviation is extended by the formula of the template. e.g. $((n\text{Bu})_4\text{N})_5[\text{V}_{12}\text{O}_{32}(\text{Cl})] = \{\text{V}_{12}\}_{\text{bowl}}@\text{Cl}$

Polyhedral cluster building blocks are written in square brackets e.g. $[\text{MO}_x]$ (M= addenda atom; x = coordination number) to provide structural information only. The fragment charge is therefore not included. Metal-oxygen bonds are simplified as M=O for double bonds and M-O for single bonds.

Compounds

The following abbreviations were used in addition to the standard notation:

Table 2: List of compounds.

$[\text{V}_2\text{O}_7]^{4-}$	$\{\text{V}_2\}$
$[\text{V}_4\text{O}_{16}]^{4-}$	$\{\text{V}_4\}$
$[\text{V}_5\text{O}_{18}]^{4-}$	$\{\text{V}_5\}$
$[\text{V}_{10}\text{O}_{28}]^{6-}$	$\{\text{V}_{10}\}_{\text{ox}}$
$[\text{V}_{10}\text{O}_{26}]^{4-}$	$\{\text{V}_{10}\}_{\text{red}}$
$[\text{V}_{12}\text{O}_{32}]^{4-}$	$\{\text{V}_{12}\}_{\text{bowl}}$
$(\text{M})_2[\text{V}_{12}\text{O}_{32}\text{Cl}]^{3-}$ (M = DMA or heterometal site)	$\{\text{V}_{12}\}_{\text{tube}}$
$[\text{HV}_{12}\text{O}_{32}\text{Cl}]^{4-}$	$\{\text{V}_{12}\}_{\text{protonated}}$
$(n\text{Bu}_4\text{N})_4[(\text{MgCl})_2\text{V}_{12}\text{O}_{32}\text{Cl}]$	$\{\text{Mg}_2\text{V}_{12}\}$
$(n\text{Bu}_4\text{N})_4(\text{DMA})[(\text{MgCl})\text{V}_{12}\text{O}_{32}\text{Cl}]$	$\{\text{MgV}_{12}\}$
$(n\text{Bu}_4\text{N})_4(\text{DMA})[(\text{CaCl})\text{V}_{12}\text{O}_{32}\text{Cl}]$	$\{\text{CaV}_{12}\}$
$(n\text{Bu}_4\text{N})_8[(\text{MgOH})\text{V}_{13}\text{O}_{33}\text{Cl}][\text{V}_{14}\text{O}_{34}\text{Cl}]$	$\{\text{MV}_{13}\}$
$[(\text{Mn}_4\text{O}_4)(\text{V}_4\text{O}_{13})(\text{OAc})_3]^{3-}$	$\{\text{MnV}\}^{3-}$
$[(\text{Mn}_4\text{O}_4)(\text{V}_4\text{O}_{13})(\text{OAc})_3]^{2-}$	$\{\text{MnV}\}^{2-}$
$[(\text{Mn}_4\text{O}_4)(\text{V}_4\text{O}_{13})(\text{OAc})_3]^{-}$	$\{\text{MnV}\}^{1-}$

1. Introduction

In response to the growing impact of climate change, there is an urgent need for renewable energy sources, efficient energy storage systems, catalysts for energy efficient chemical synthesis, and technologies capable of capturing greenhouse gases or preventing their release. A crucial step towards addressing these challenges is the development of innovative materials. Such examples include CO₂ adsorbents like ionic liquids or metal organic frameworks, compounds capable of photochemical catalytic water splitting to use hydrogen as energy source and advanced battery materials, each contributing to the reduction of CO₂ emissions and to enhanced overall energy efficiency in modern society.^[1-3]

The main challenge is to develop robust and reusable materials with enhanced properties suitable for practical applications which can meet the requirements to be ecofriendly.^[4] To achieve this, it is essential to gain a comprehensive understanding of how structural properties of a material determine its functionality. One effective approach to understanding chemical behavior in reactions involves considering the following five fundamental concepts.^[5]

1. matter transformation
2. energy transfer and transformation
3. activation
4. stabilization
5. equilibration

These concepts are perfectly applicable for the field of polyoxometalates, where a lot of innovation comes from already existing structures modified by organic or inorganic functionalities.

The transformation of matter begins with the self-assembly of precursor species that originate from solid-state metal oxides, providing a foundation for further functionalization and chemical reactivity.^[6] Energy transfer processes, including electrochemical reactivity and light absorption, can be precisely tuned to improve the overall efficiency and responsiveness of the system, while thermodynamic activation parameters offer valuable insights to predict and control reaction pathways.^[7]

Stabilization of binding sites by hydrogen bonding or electrostatic interactions provides a means to achieve selective functionalization of molecular structures.^[8] Moreover, chemical equilibria can be purposefully shifted in accordance with Le Chatelier's principle to drive reactions toward the formation of desired products.^[9]

Nevertheless, the mechanisms underlying the self-assembly process towards specific cluster structures remain largely unknown, and there is a need for new strategies in both cluster synthesis and functionalization, as well as for the investigation and understanding of more complex systems.^[10]

This work focuses on both fundamental understanding and applications to make the development of new polyoxometalate based materials more predictable.

1.1. Polyoxometalates

Polyoxometalates are molecularly well-defined metal oxo clusters first discovered by Berzelius in 1826, who reported a precipitate after the addition of phosphoric acid to a molybdate solution.^[11] The structure was later solved by J. F. Keggin using powder x-ray diffraction in 1933 and is known since then as the Keggin anion with the formula $[\text{PM}_{12}\text{O}_{40}]^{3-}$ ($M = \text{W}, \text{Mo}$).^[12,13] Five symmetrical isomers of the Keggin structure, obtained by the 60° rotation of one, two, three or four of the $[\text{M}_3\text{O}_{13}]$ triads, were found and referred to as α - ϵ structure as defined by Baker and Figgis.^[10,14–16] In the fully oxidized state the alpha and beta isomer (Figure 1) are the most stable since the rotation of two, three or four triads leads to the formation of repulsive interaction between the positively charged metal ions and thereby a structural destabilization. These stability trends are supported by density functional theory (DFT) calculations, which are frequently applied to rationalize energetic differences, and with the advent of modern analytical methods such as single crystal X-ray diffraction, mass spectrometry, NMR and electrochemistry, the structural characterization of polyoxometalates in both solid state and solution has become increasingly accessible.^[17,18]

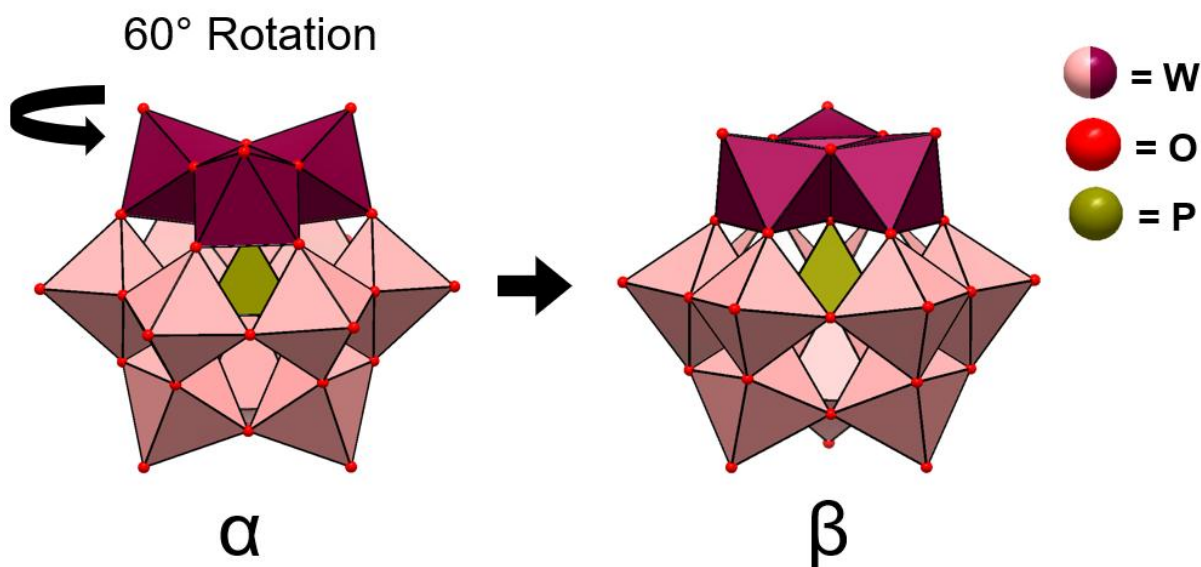


Figure 1: Difference between α - and β - isomer of the Keggin structure. The β -isomer is obtained by the 60° rotation of one $[M_3O_{13}]$ triad highlighted by a darker color.^[16,17]

The capability of the early high valent transition metals e.g. Mo, W, Nb, Ta and V to form M=O multiple bonds results in a tendency to form precise molecular clusters rather than polymeric metal oxide networks. This unique property is caused by a reduced electron density at the terminal oxygen site, causing an immense structural variety ranging from small cluster units to large assemblies with up to 368 metal centers for the largest observed polyoxometalate known as 'blue lemon', thereby reaching the size of a protein.^[19–21]

Vanadates differ from other polyoxometalates because the coordination sphere of 3d metals is not restricted to octahedral $[MO_6]$ units but may also include square pyramidal $[MO_5]$ and tetrahedral $[MO_4]$ geometries. The different coordination environments enable a greater potential for structural diversity, but this is often accompanied by limited stability. A representative example, in contrast to the molybdate and tungstate analogues described above, is the α -Keggin vanadate structure $[PV_{12}O_{40}]^{15-}$, which is unstable due to its higher intrinsic cluster charge. It can only be stabilized in the presence of two $[VO]^{3+}$ capping groups within the cluster shell, together with five additional protons, which lower the overall charge from 15⁻ to 4⁻ to form $[H_5PV_{14}O_{42}]^{4-}$.^[10,22] The instability is further evidenced by the observation of the all-vanadium Keggin anion $[H_{12}V_{13}O_{40}]^{3-}$ as a transient intermediate formed upon acidification of an aqueous vanadate solution, exhibiting a half-life of only 80 minutes at 298 K.^[23,24]

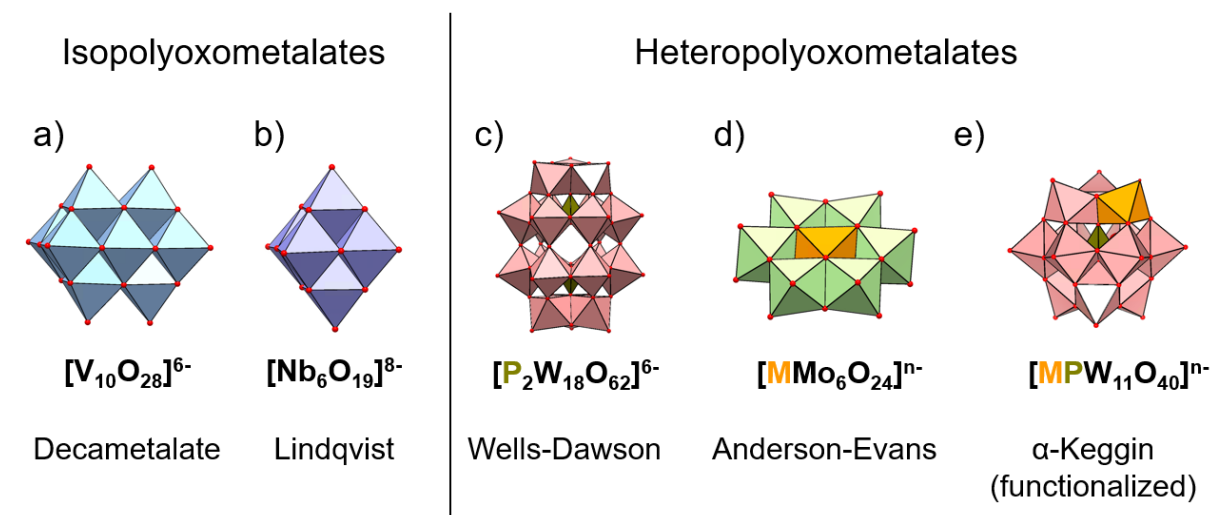
Polyoxometalates can be subdivided into two classes based on the composition: iso- and heteropolyoxometalates.^[6,25,26]

1.2. Isopolyoxometalates

The metal sites of the cluster shell are referred to as addenda atoms. If all metal sites are of the same type, the cluster is described as an isopolyoxometalate with the general formula $[M_xO_y]^{m-}$. Their higher charge often results in increased surface basicity and reduced stability compared to heteropolyanions, so protonation of the cluster shell is required to stabilize the structures. Isopolyoxometalates are frequently used as precursor materials, and their fragmentation provides a straightforward strategy for forming new structures.^[6,26] Well known isopolyanion motifs include the decametallate $[M_{10}O_{28}]^{n-}$ and the Lindqvist structure $[M_6O_{19}]^{n-}$, two examples of which are shown in Figure 2a and 2b.

1.3. Heteropolyoxometalates

Once a cluster contains one or more heterometals, it is classified as a heteropolyoxometalate. The general formula can be written as $[X_zM_xO_y]^{n-}$ with $z \leq x$. Functional metal sites are most commonly p- or d-block elements, which may be located at the center of the cluster as a template, as in the Wells–Dawson structure Figure 2c or the Anderson–Evans structure Figure 2d, but can also replace addenda atoms, as in the mono-functionalized α -Keggin structure Figure 2e.^[25] Heteroatoms can not only stabilize a given structure in their role as templates but also tune its electrochemical, magnetic, and catalytic properties.^[27–30] Controlled functionalization of polyoxometalates is therefore a key step toward their application.



Color code (addenda atom polyhedra):

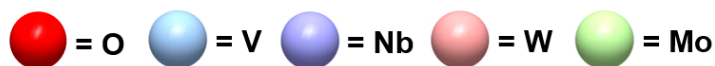


Figure 2: Examples for iso- and heteropolyoxometalates are given. Isopolyoxometalates include decavanadate a) and the hexaniobate Lindqvist structure b) and heteropolyoxometalates include the Wells-Dawson tungstate c), the Andersson-Evans molybdate d) or the mono-functionalized α -Keggin tungstate e). The given general color code for the coordination polyhedra is used in this work to distinguish the different addenda atoms. Heteroatom color scheme: P = olive; metal site (M) = orange.

1.4. Synthesis via Self-Assembly

The underlying mechanism for the formation of an initial polyoxometalate cluster is self-assembly. Self-assembly is a process often occurring in nature, which is driven by interactions such as non-directional electrostatic attraction and van der Waals forces or directional coordinative bonds or hydrogen bonds. Examples include the formation of double-stranded DNA and the folding of proteins into secondary and tertiary structures. Building on a fundamental understanding of these mechanisms, researchers are developing multi-stimuli-responsive materials for advanced biological applications.^[31]

For polyoxometalates it is coordinative metal–oxygen bonds driving the self-assembly process, which can be exploited to design materials for specific application. Although the bottom-up assembly of specific polyoxometalate clusters is less understood than e.g. the directional assembly of DNA structures the first steps can be explained by a simple condensation reaction. Typically, protonation of terminal $M=O$ bonds leads to elongated and destabilized $M-O$ bonds, initiating the cluster formation. Further protonation can generate labile water ligands, which subsequently enable condensation reactions (Figure 3a). Two metal centers can be connected via corner-sharing, edge-sharing or, more rarely, face-sharing modes (Figure 3b-d).^[10,32]

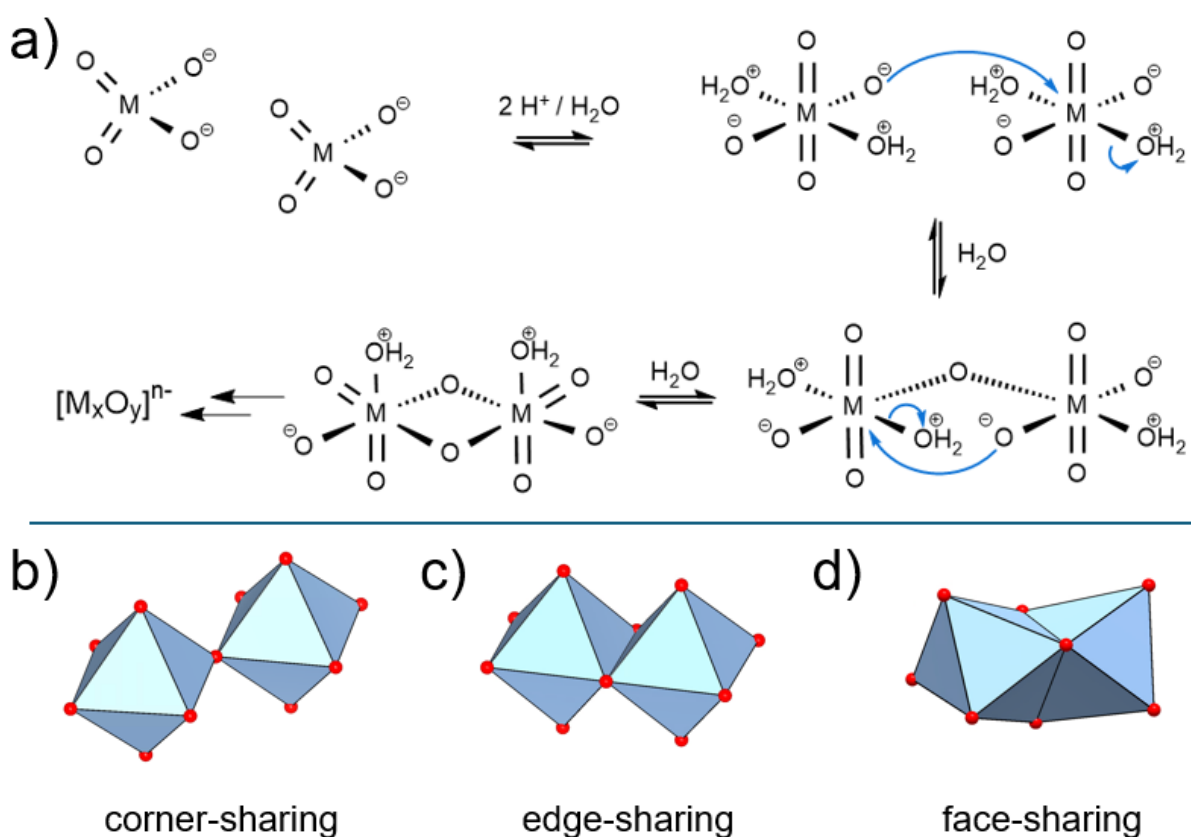


Figure 3: a) Condensation reaction of the initial reaction steps during the self-assembly of polyoxometalates. The connection of two octahedral coordinated addenda atoms can be b) corner sharing, c) edge sharing or rarely d) face sharing.^[10,32]

It is well known that the self-assembly process is pH dependent and templates as well as solvents and other influences can impact the resulting structure.

Owing to the thermodynamic stability of decavanadate, the synthesis of more complex structures in aqueous media is challenging. In aqueous systems, octahedral and tetrahedral coordination geometries are predominant, whereas in organic media square pyramidal coordination is also common. Adjustment of the vanadium to oxygen ratio through water elimination induced by acid addition enables the conversion of tetrahedral precursors into square pyramidal species, thereby facilitating the assembly of advanced cluster architectures.^[26,35]

1.6. From aqueous to non-aqueous conditions

To enhance the solubility of polyoxovanadates in organic solvents such as acetonitrile, DMF, and DMSO, bulky alkylammonium cations, known for their phase-transfer properties, are introduced. This modification enables water-free synthesis strategies, which open a variety of novel reaction pathways.^[26,36]

To obtain tetraalkylammonium polyoxometalates, one approach involves dissolving solid-state vanadium pentoxide using $n\text{Bu}_4\text{NOH}$. At a pH of around 10, the predominant species is $\{\text{V}_4\}$, which can be isolated by carefully adjusting the pH followed by evaporation of water. A protonated and a non-protonated structure have been reported.^[37,38] However, this method is both time- and energy-intensive. A second, often more practical approach requires the product to be insoluble in water and involves exchanging the counter cation via salt metathesis (Figure 5), which, in the case of decavanadate at pH 2.5 - 5.8, yields water-insoluble tetraalkylammonium salts.^[34,39]

salt metathesis reaction:



Figure 5: General formula of a salt metathesis reaction with the example of the conversion of sodium decavanadate to the insoluble tetrabutylammonium decavanadate in water.

A common crystallization strategy for polyoxometalates, applicable also in organic solvents, involves the introduction of a smaller tetraalkylammonium ion, which reduces solubility and thereby promotes crystallization.^[40]

The length of the alkyl chains not only influences the solubility of decavanadate but also affects the stabilization of different protonation states. For example, with the smaller tetramethylammonium cation ($n\text{Me}_4\text{N}^+$) compared to tetrabutylammonium cations ($n\text{Bu}_4\text{N}^+$), only the $\text{H}_2\text{-}\{\text{V}_{10}\}_{\text{ox}}$ dimer is known, whereas with $n\text{Bu}_4\text{N}^+$ both dimeric $\text{H}_3\text{-}\{\text{V}_{10}\}_{\text{ox}}$ and polymeric $\text{H}_4\text{-}\{\text{V}_{10}\}_{\text{ox}}$ compounds have been isolated. In solution, the cluster can be protonated with up to six protons, depending on the pH, whereas in the solid state the tetraalkylammonium counterions partially replace these protons. Longer alkyl chains promote a higher degree of protonation in the crystal structure due to their larger size and the resulting smaller Madelung energy. Increased protonation reduces the Connolly surface area of the aggregates, which compensates for the smaller Madelung energy and decreases the number of counterions required. In contrast, smaller alkyl chains can pack more densely in the crystal lattice, thereby stabilizing less protonated structures.^[41]

The choice of counterion in organic media, such as tetraethylammonium ($n\text{Et}_4\text{N}^+$) instead of $n\text{Bu}_4\text{N}^+$, can have a substantial impact on the reaction outcome. A representative example is provided by the study of Hayashi et al., which demonstrated how the hydrophobic “lid effect” of $n\text{Et}_4\text{N}^+$ alters the positioning of a guest molecule within a cluster cavity compared to the less compact packing of $n\text{Bu}_4\text{N}^+$ at the opening of $\{\text{V}_{12}\}_{\text{bowl}}$ discussed later in this work.^[36]

During self-assembly, such effects can alter the reaction pathway and hinder product formation.

A key advantage of organic solvents is their ability to stabilize smaller vanadyl fragments, which can promote the stepwise assembly of larger clusters. Streb et al. provided experimental evidence for this by crystallizing such a fragment from DMSO, thereby illustrating how solvent coordination can suppress direct condensation into decavanadate and instead enable access to a broader variety of polyoxovanadate architectures.^[42]

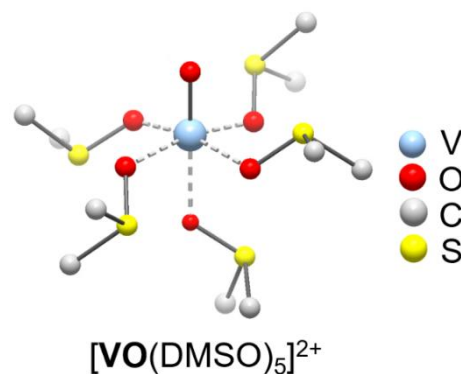


Figure 6: DMSO stabilizes small vanadyl fragments as building blocks for more complex structures.^[42]

The outcome of polyoxometalate synthesis depends on the careful adjustment of several reaction parameters, such as pH, solvent composition, precursors, reducing agents, and templates. Fine-tuning these variables, alongside temperature and reaction time, is essential for guiding the self-assembly process toward the desired product.^[43]

1.7. The Role of Templates

The formation of clusters via self-assembly can be directed by both internal and external templates. In solution, interactions between the accessible basal face of the square pyramidal coordination sphere of the addenda atoms and anionic or even neutral small molecules can result in the encapsulation of an internal template, whereas external stabilization is often achieved through hydrogen bonding to template molecules or coordination to heterometals, mainly via bridging oxygen positions.^[44,45]

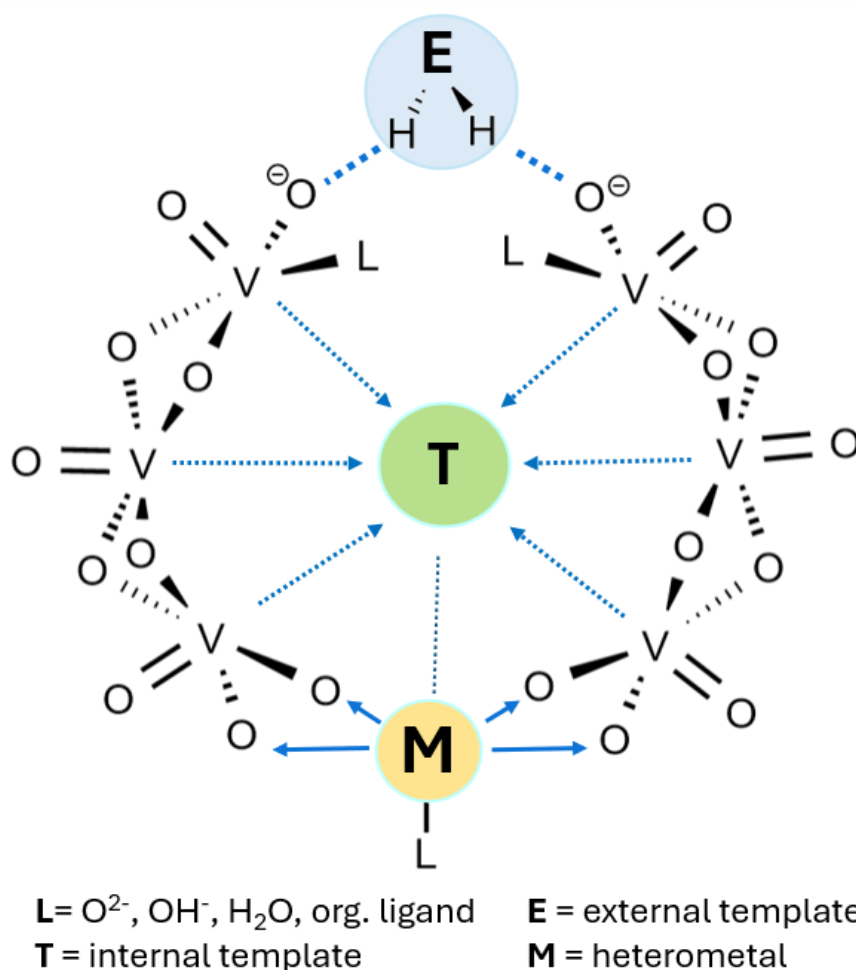


Figure 7: Schematic influences of internal and external templates as well as heterometals on the formation of polyoxometalate clusters.^[44]

1.7.1. Internal Templates

Internal templates are located at the cluster center and can become encapsulated within the cluster shell during self-assembly. Examples include neutral templates like solvent molecules e.g. acetonitrile or anionic templates like halides. While their stabilizing effect in the final structure may appear minimal, such templates can still play a crucial role during self-assembly by guiding the formation pathway.^[8]

Neutral Templates

Although neutral templates are relatively rarely observed, one notable example is the previously mentioned $\{V_{12}\}_{\text{bowl}}$, which can be stabilized by solvent molecules such as acetonitrile and benzonitrile, as first reported by Klemperer et al., or by other neutral molecules like nitromethane Figure 8 a-c.^[46,47] Due to the large open site with a diameter of 4.4 Å, the guest exchange is readily possible and is additionally facilitated by weak interactions of the functional groups with the basal face of the coordination polyhedra. Hayashi et al. succeeded in isolating the template free structure (Figure 8 d) in which one terminal oxygen position is flipped inward, replacing the solvent molecule. DCM was used as a volatile template to prevent decomposition during the required heating of the solid material for its removal. By gradually adding defined amounts of guest molecules their binding affinity can be determined using ^{51}V -NMR. The affinity constants strongly depend on the functional group and shape of the guest molecule that can sterically prevent incorporation, although the cluster can adapt its geometry to a certain extent. ^[40,47,48]

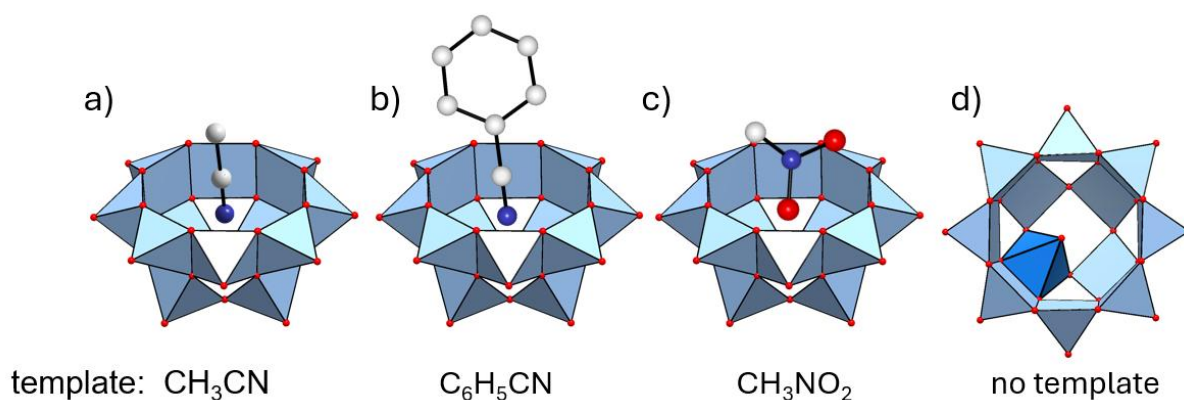


Figure 8: $\{V_{12}\}_{\text{bowl}}$ stabilized by a) acetonitrile, b) benzonitrile and c) nitromethane as internal neutral templates and d) the top view of the cluster without template and a flipped V=O unit highlighted in dark blue.

Since the binding affinity for bromides is very high it can be used to direct a bromination reaction. Therefore, the neutral bromine molecule was introduced as a possible template and single crystals containing elemental bromine were found. Since the cluster acts as an electron acceptor the bromine is polarized to enable the formation of Br^+ as electrophilic reagent which can cleave C-H bonds to brominate alkanes. Compared to elemental bromine, the reaction with pentane showed a higher selectivity towards 3-bromopentane among the mono-bromopentane species and yielded a preferred threo isomer of 2,3-dibromopentane.^[49]

Very rarely, neutral templates are encapsulated into spherical clusters. This was achieved recently by Hayashi et al. starting from the mixed-valent $(\text{nBu}_4\text{N})_4\{\text{V}_{10}\}_{\text{red}}$. Applying the concepts explained earlier, the addition of an acid was used to convert the partial tetrahedral coordination environment of the precursor to a square pyramidal coordination in the final product. Here, p-toluene sulfonic acid was used to avoid any small anionic templates or water. It was assumed that reductive conditions were required to form a closed cluster shell. Partial reduction of the vanadium centers from the oxidation state +5 to +4 by the bulky reductant dimethyl phenyl silane was used to obtain the mixed valent product. The amount was adjusted to achieve a V(IV):V(V) ratio of 1:3 from the precursor ratio of 1:4. Single crystals were isolated for the acetonitrile- and nitromethane-encapsulated structures (Figure 9a,b), and the removal of acetonitrile by heating resulted in a structure with a flipped V=O unit (Figure 9c) comparable to $\{\text{V}_{12}\}_{\text{bowl}}$ described before. Since the pores of the cluster are much smaller than those of the $\{\text{V}_{12}\}_{\text{bowl}}$, this finding suggests a mechanism in which one bridging oxygen is transferred to the inside of the cluster shell by a trigonal-bipyramidal pseudo-rotation and the simultaneous formation of a tetrahedrally coordinated unit, opening a pore large enough for the acetonitrile guest molecule to be released. The external terminal oxygen of the trigonal bipyramidal unit finally reforms the cluster shell and fills the pore.^[50]

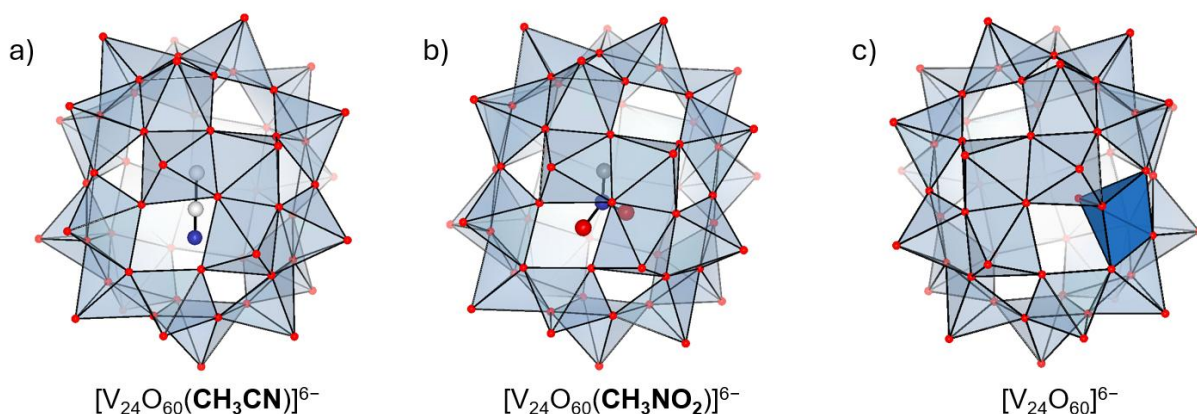


Figure 9: $\{V_{24}\}$ encapsulates the neutral internal template molecules a) acetonitrile and b) nitromethane and c) without template and a flipped V=O unit highlighted in dark blue.

It was shown that the presence of anionic templates can interfere with the reaction due to their stronger interaction with the open face of square pyramidal vanadium polyhedra during the self-assembly. Upon addition of nitrate, the only product observed in this reaction was the smaller $[V_{18}O_{44}(\text{NO}_3)]^{5-}$.^[50]

Anionic Templates

Anionic templates can strongly drive the self-assembly towards specific structures. Aside from neutral templates, they can be further divided into two classes depending on their strong or weak interactions with the cluster shell of the final structure.^[10]

There are many examples of spherical clusters with anionic templates that interact only very little with the surrounding cluster shell, similar to the neutral templates. Although the total negative charge of the oxo anions leads to a formal repulsion of anionic guests, the template is trapped inside the closed cluster shell and weak attractions to the cationic metal centers balance these interactions. As a result of the pseudo mechanical encapsulation, the distance of the template to the cluster shell is larger than a typical V-Cl coordination bond length.^[10,51] The $\{V_{12}\}_{\text{tube}}$ stabilized by two dimethylammonium cations, reported by Streb et al. is a good example, and DFT calculations show that the removal of the chloride template is essentially thermoneutral.^[8]

Although the stabilization effect of the template on the final structure and electrochemical properties is minimal, the photochemical properties can be influenced by the heavy-atom effect, and it was shown that the larger bromide can improve the photoactivity of the cluster. The use of fluoride and iodide for the same cluster was not possible due to their too small or too large size.^[30,52] Larger templates, like perchlorate, azide, or iodide can be incorporated into clusters with higher nuclearity (Figure 10a-c), which adapt to the shape of the guest molecule.^[53,54]

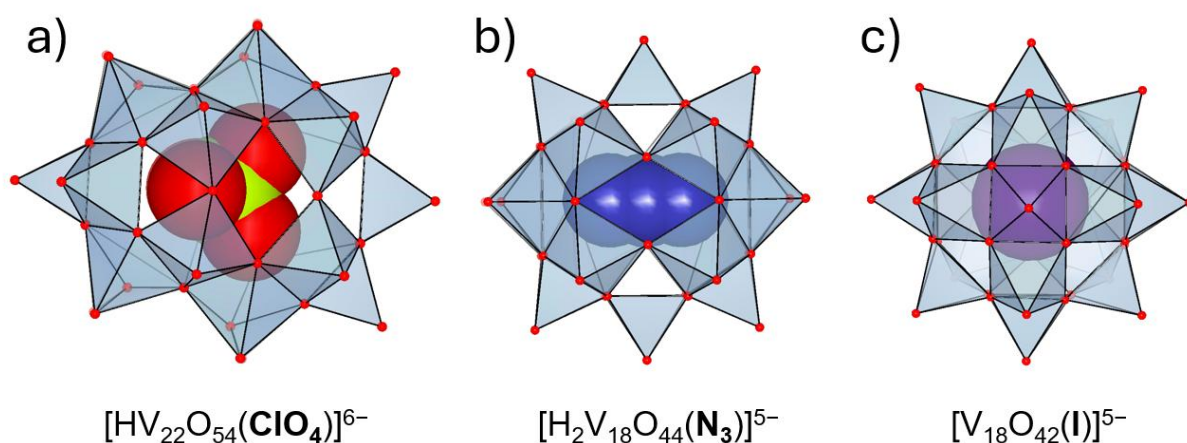


Figure 10: The size of the template defines the cluster shape, demonstrated by the example of a) perchlorate, b) azide and c) iodide as internal weak interacting anionic template.

The best example of strongly interacting anionic templates is the Keggin structure, where for example a phosphate or silicate forms coordinative bonds with the cluster shell. The bond length between the cluster shell and the oxygen-containing template is comparable to that of the bridging oxoanions and the stabilization of the structure is much more significant than for weak interacting templates.^[10]

1.7.2. External Templates

External templates can influence the self-assembly process of polyoxovanadate clusters through hydrogen bonding, electrostatic interactions, and spatial confinement, primarily involving bridging oxygen atoms.

Hydrogen Bonds

The $\{V_{12}\}_{\text{bowl}}$ is a representative example in which the interaction between internal and external templates and the cluster shell affects the resulting structure. Streb et al. showed that cyclen interacts with the open face of the cluster as an external template (Figure 11a). Its presence, along with its protonation state, was found to influence the distance between the internal and external templates as well as the position inside the cavity compared to a reference structure without an external template.^[55,56]

Hydrogen bonding can be strong enough to induce a structural transformation of the cluster, converting it from a bowl-type to a tube-type geometry. In such cases, the internal template plays a decisive role in determining the final cluster architecture, similar to the closed-shell structures discussed in the previous chapter on weakly interacting anionic templates. While the internal template defines the shape and size of the cluster, hydrogen bonding from the external template helps stabilize the vanadate shell (Figure 11b,c). For example, the introduction of hydrogen-bond-donors such as NH_4^+ can induce the formation of tube-type tetradecavanadates when NO_3^- , N_3^- , or OCN^- are present as internal templates, whereas Cl^- and Br^- lead to the formation of $\{V_{12}\}_{\text{tube}}$.^[57,58]

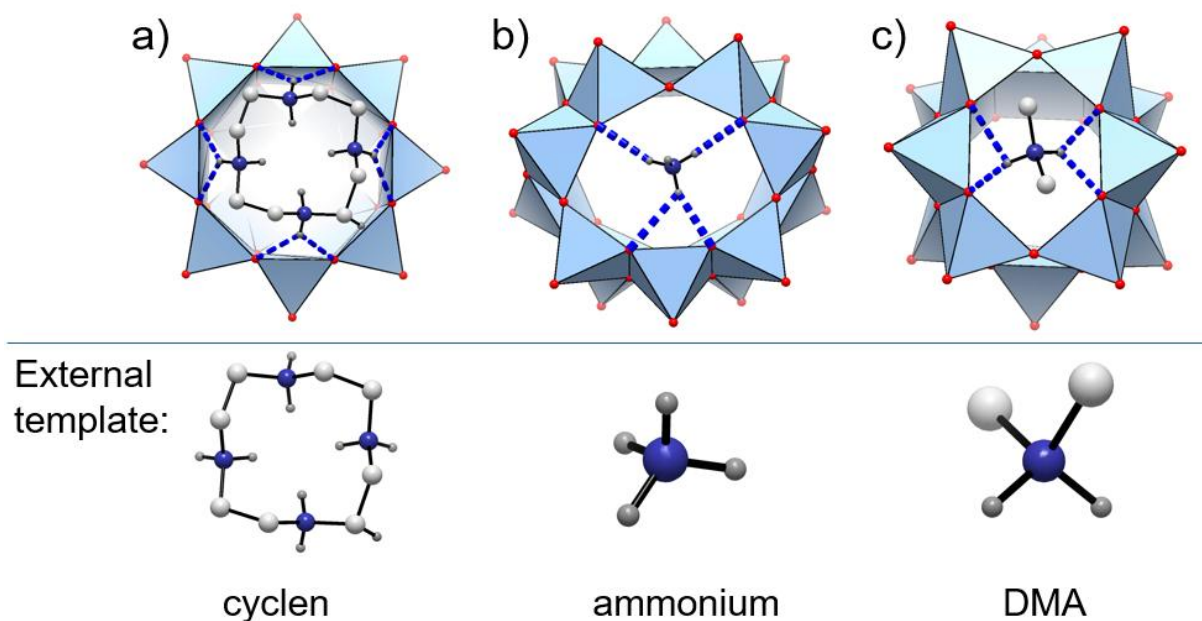


Figure 11: External templates stabilize polyoxovanadate structures by hydrogen bonding. Examples include a) cyclen at the top of $\{V_{12}\}_{\text{bowl}}$, b) ammonium at the top of tube-type tetradecavanadate and c) dimethylammonium (DMA) at the top of $\{V_{12}\}_{\text{tube}}$. Possible hydrogen bonds are marked in blue. The internal template was omitted for clarity.

Molecular Cages

The self-assembly can be directed within confined spaces through the introduction of molecular cages.^[59] Molecular cages are three-dimensional, highly symmetrical coordination complexes formed by self-assembly, which can be designed through an appropriate choice of ligand and metal center to form large polygonal or polyhedral geometries.^[60] The cavities of these structures can trap smaller molecules and have been used for molecular recognition, gas storage, separation, sensing, catalysis, and drug delivery.^[61] Another noteworthy application is the use of the well-defined, porous sponge-like single crystals, to adsorb a wide range of organic molecules for crystal structure analysis, providing information on stereocenters.^[62]

The defined shape of the cavities can be designed to match the cluster, and it was shown by Parac-Vogt et al. that in the presence of $Pt_6L_4(NO_3)_{12}$ ^[59,62,63] which perfectly matches the shape of the Lindqvist structure the self-assembly and stabilization of otherwise labile clusters are possible. The aqueous synthesis of $[M_6O_{19}]^{2-}$ was conducted via acidification of molybdate or tungstate precursors that are small enough to enter the cage forming $[M_6O_{19}]Pt_6L_4(NO_3)_{10}$. The robust structure was able to stabilize the clusters and enable efficient catalysis for green and selective sulfoxidation reactions in water.^[63]

Since cage structures are adjustable in size and shape, they offer great potential for further cavity-directed POM synthesis as well as to enhance selectivity during catalysis.

Templating Effect of Heterometals

One of the first examples of a heterometal as template is probably the mixed-valent $\{V_{10}\}_{red}$ cluster Figure 12a. Although it only contains vanadium centers, the two vanadyl cations located on the top and the bottom of the cluster are distinguishable by the oxidation state +4, which stabilizes the eight-membered ring of the vanadate in oxidation state +5. This becomes much clearer when considering that the vanadyl cations can easily be replaced by copper forming a heteropolyoxovanadate. As we have seen in Chapter 11 under aqueous basic conditions small cyclic vanadates up to five centers are present in equilibrium. Depending on the cation further ring sizes are stabilized and like macrocyclic organic molecules it can depend on the ion radius and the number of metal centers acting as a template. Examples include $[PdV_6O_{18}]^{4-}$, $[Cu_2V_8O_{24}]^{4-}$ and $[Ni_4V_{10}O_{30}(OH)_2(H_2O)_6]^{4-}$ shown in Figure 12b-d. [26,64]

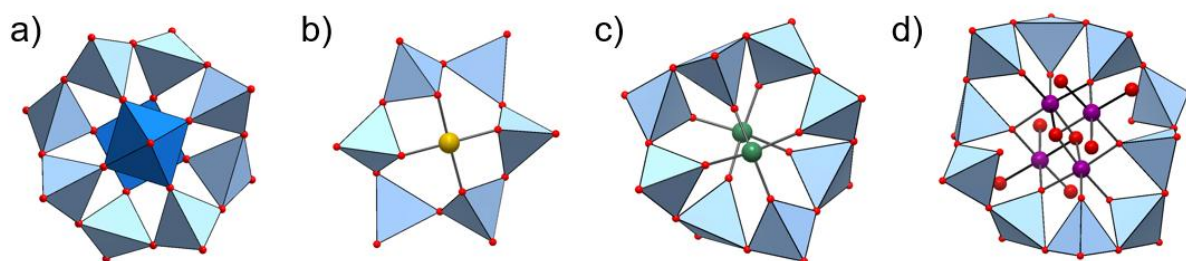


Figure 12: Heterometals stabilize different ring sizes of polyoxovanadates. Examples are a) $\{V_{10}\}_{red}$, b) $[PdV_6O_{18}]^{4-}$, c) $[Cu_2V_8O_{24}]^{4-}$ and d) $[Ni_4V_{10}O_{30}(OH)_2(H_2O)_6]^{4-}$. Color scheme of the heterometals: Pd = dark yellow; Cu = green; Ni = purple. The vanadium positions of oxidation state +4 are marked in dark blue.

Like external templates heterometals can replace addenda atoms during self-assembly. Such functionalization is commonly used to tune the electrochemical and catalytic behavior of polyoxometalates. [29,30,65] Due to synthetic challenges functionalized vanadates have received little attention so far and their synthesis has often relied on design, empirical knowledge, and serendipity. [8] A good example is the titanium-functionalized Lindqvist vanadate investigated by Matson et al. which is obtained under reductive solvothermal conditions. It was found that the choice of the solvent as well as the choice of the precursor material can determine if a product is

formed or no yield is obtained.^[29] Additionally the ratio of titanium to vanadate precursor can yield mono- and difunctionalized structures (Figure 13a,b) specifically in the cis configuration of the two titanium atoms.^[66] The fundamental studies on these functionalized vanadium Lindqvist structures reveal the potential of heterometal-functionalized systems. However, such specific reaction conditions are difficult to transfer to other cluster systems and generally applicable synthesis strategies are still urgently required.^[8]

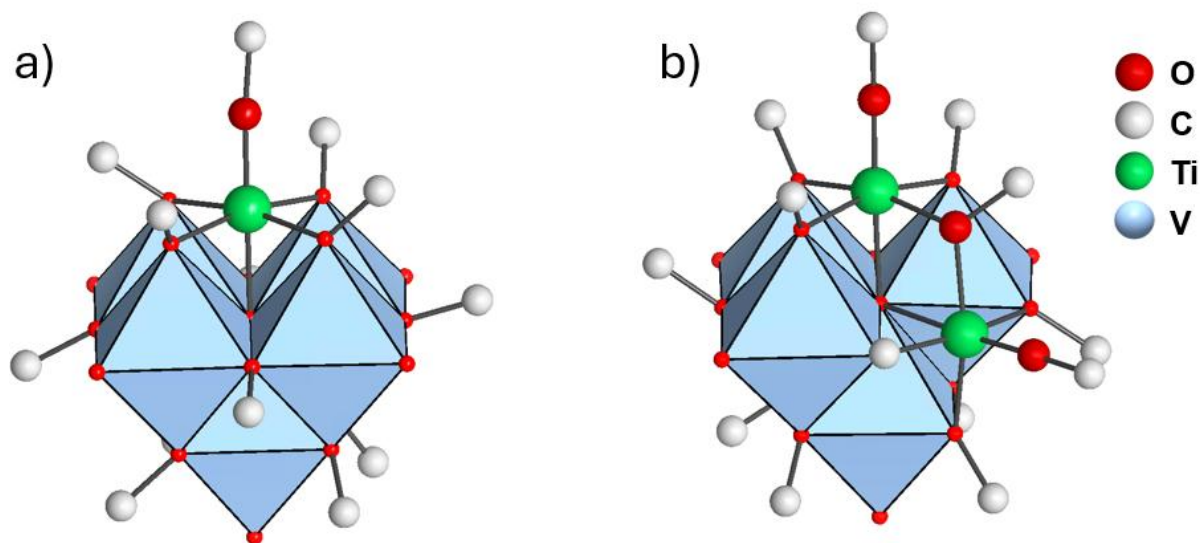


Figure 13: Methoxylated hexavanadate Lindqvist structure functionalized by a) one and b) two titanium centers with the very specific conditions for the respective hydrothermal reaction.

Table 3: Reaction conditions for the synthesis of methoxylated hexavanadate Lindqvist structures a) with one and b) with two titanium centers.^[66]

	Compound a)	Compound b)
Temperature	100 °C	125 °C
Reaction time	24 h	64 h
Reductant	MeOH, (NBu ₄)BH ₄	MeOH, no reductant
Ratio V:Ti	5:1	4:2

To gain control of the otherwise difficult-to-predict self-assembly mechanism, a stepwise reaction design can be beneficial.

1.8. Seeded Growth Mechanisms in Organic Solvents

In organic media the absence of water leads different reaction mechanisms compared to aqueous hydrolysis. As described earlier smaller vanadyl cations can be stabilized by organic solvent molecules. While the fragmentation of precursors with purely corner sharing building blocks may be complete, the full fragmentation of larger precursors is likely hindered, and a seeded growth can be assumed to direct the reaction pathway.^[67] This means that the choice of the precursor can be crucial to obtain the desired product in a good yield.

When using $\{V_4\}$ in combination with a variety of reagents in a one-pot reaction like for the synthesis of $\{V_{12}\}_{\text{tube}}$ reported by Streb et al., monomeric vanadium species can form, which can reassemble uncontrollably. Following the theory that the correct oxygen-to-vanadium ratio is required. The addition of acids may enhance the product formation, and it was shown that a Lewis acid like indium chloride or aluminum chloride is required to observe any product. Since the intermediate species are unknown and all reagents are introduced simultaneously the formation of stable side products is likely to occur and the yield may be lowered (Figure 14).^[8]

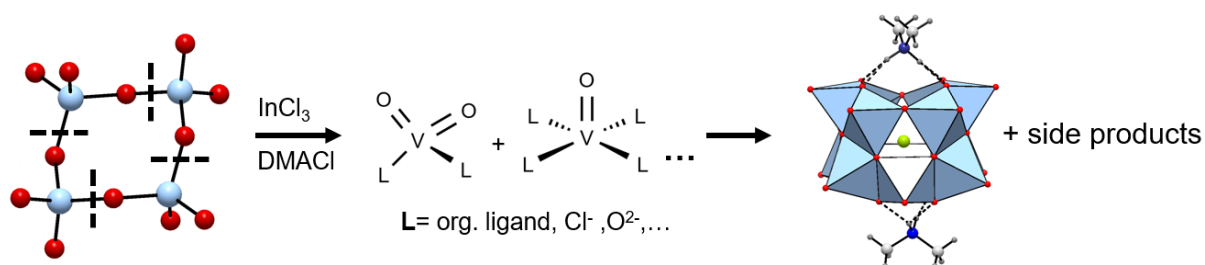


Figure 14: Synthesis of $\{V_{12}\}_{\text{tube}}$ by complete fragmentation of $\{V_4\}$ in presence of indium chloride and dimethylamine hydrochloride.

An improved strategy is to use separate reaction steps, a more condensed precursor, and to introduce the reagents one by one. To gain control the first step could be an acid base reaction, where the oxygen-to-vanadium ratio is adjusted appropriately to form a square pyramidal coordination sphere. It was shown by Hayashi et al. that decavanadate can act as a “seed” for the formation of $\{V_{12}\}_{\text{bowl}}$ in acetonitrile, which is an isomer of $\{V_{12}\}_{\text{tube}}$. By deprotonation and heating the reaction is enhanced and the great thermodynamic stability due to the templating nitrile group of the solvent and the absence of water present pushes the equilibrium chemoselectively towards the product. Essentially quantitative yields can be expected (Figure 15).^[68]

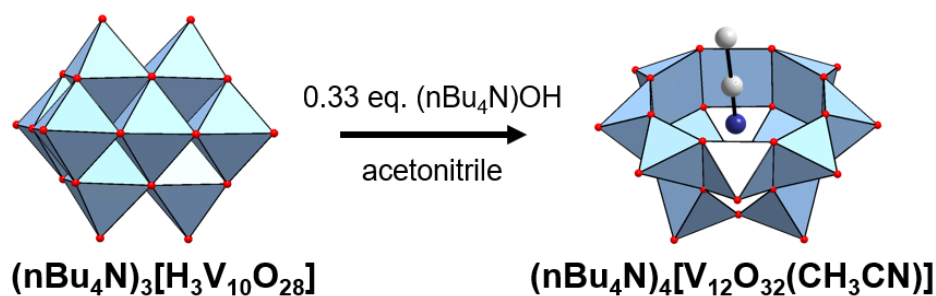


Figure 15: Chemoselective reaction of decavanadate to $\{\text{V}_{12}\}_{\text{bowl}}@ \text{MeCN}$.

It was explained previously that due to the large opening of the cluster the template exchange at $\{\text{V}_{12}\}_{\text{bowl}}$ is possible. Hayashi et al. introduced halides by substituting nitromethane and the template exchange rate and the position in the cluster were found to be dependent on the atomic radius.^[69] The compounds were isolated and single crystals were measured. Although the reaction was conducted in nitromethane due to its low affinity to the cluster, preliminary experiments of our group suggest that in combination with external templates the exchange of the internal template can be facilitated, and the reaction can be conducted in acetonitrile despite the strong affinity of the nitrile group.

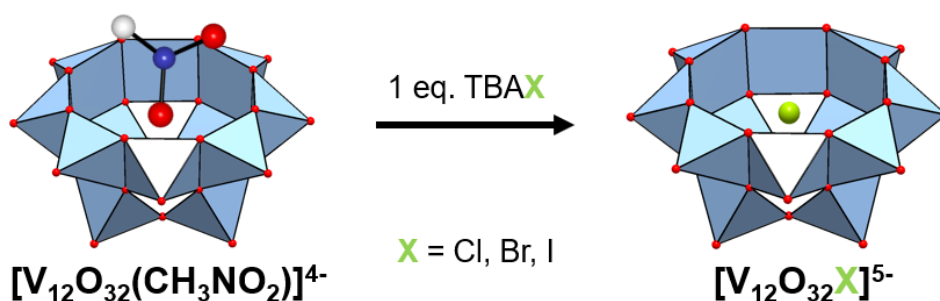


Figure 16: Exchange of the nitromethane template by halides at $\{\text{V}_{12}\}_{\text{bowl}}$.

Three related dodecavanadates are known and it was shown by Hayashi et al. that the protonation of $\{\text{V}_{12}\}_{\text{bowl}}@ \text{Cl}$ by trifluoro acetic acid proceeds to completion. The removal of the proton was achieved by the addition of ethylene diamine, proving the reversibility of the reaction. Notably, $\{\text{V}_{12}\}_{\text{tube}}$ was observed as intermediate species and the deprotonation by diethylamine in presence of diethylamino hydrochloride yielded up to 87% of this product. It is likely that the isomeric clusters are not fragmented completely according to the seeded growth mechanism.

Preliminary experiments of our group suggest that the reaction towards $\{V_{12}\}_{\text{tube}}$ is possible in acetonitrile with a good yield starting from $\{V_{12}\}_{\text{bowl}}@Cl$, which completes the connection between all three clusters (Figure 17).^[57]

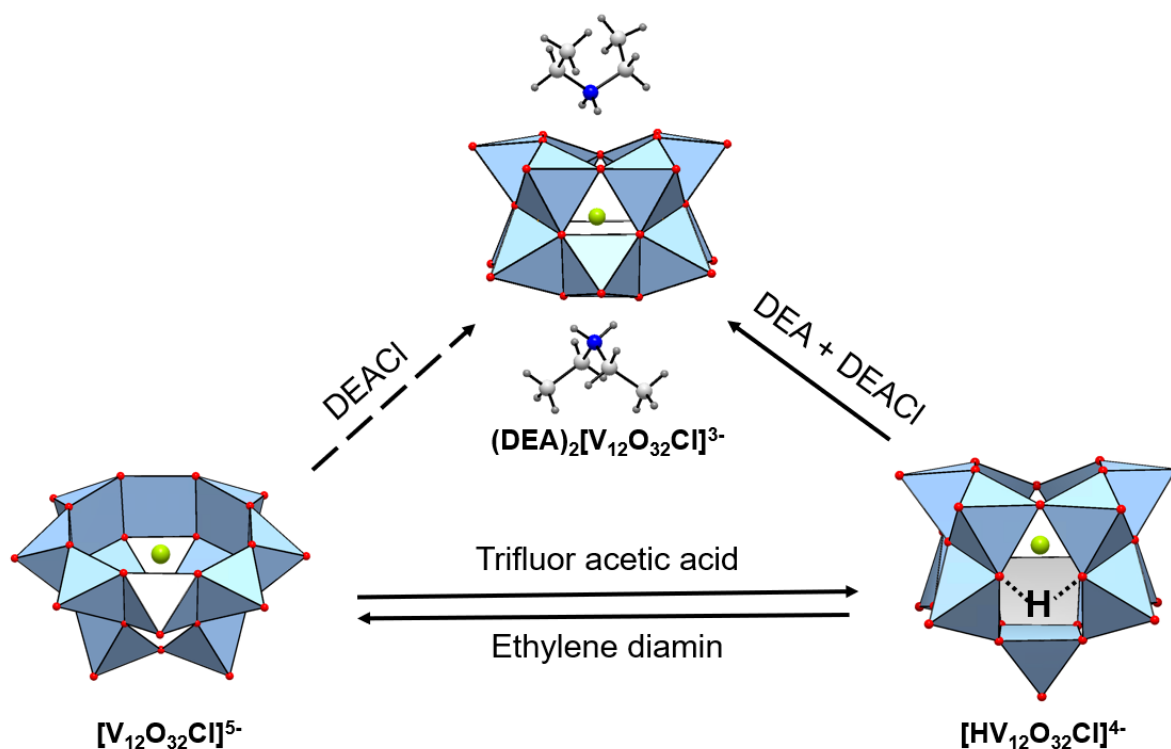


Figure 17: Conversion reactions between $\{V_{12}\}_{\text{bowl}}@Cl$, $\{V_{12}\}_{\text{protonated}}$ and $\{V_{12}\}_{\text{tube}}$.

Next to the careful choice of the precursor, the introduction of capping groups can help to gain control on the self-assembly mechanism. Christou and co-workers were able to conduct a stepwise cluster growth by the addition of defined amounts of silver acetate as oxidant to vanadyl chloride in acetonitrile. It was observed that the acetate capping group can block the cluster growth and for the addition of two equivalents of silver acetate a cluster of the composition $[V_5O_9Cl(OAc)_4]^{2-}$ was observed. By the addition of three equivalents of silver acetate the chloride template is precipitated and a cluster with higher nuclearity and a formula of $[V_9O_{19}(OAc)_5]^{3-}$ can be isolated. Using 4 equivalents the cluster shell is closed and even without the chloride template the compound $[V_{15}O_{36}]^{5-}$ was crystallized. In addition, the cluster conversion of $[V_9O_{19}(OAc)_5]^{3-}$ to $[V_{15}O_{36}]^{5-}$ by the addition of one equivalent of silver acetate was observed and although the mechanism of the first steps to $[V_5O_9Cl(OAc)_4]^{2-}$ is not fully understood this reaction again shows how related structures can convert by seeded growth.^[70]

A stepwise growth was also achieved by Hayashi et al. by reductive coupling of (n-Bu₄N)VO₃ using organometallic palladium PdCOD as a coupling agent. The thermal decomposition of the palladium supported $[(\eta^3\text{-C}_4\text{H}_7)\text{Pd}]_2\text{V}_4\text{O}_{12}]^{2-}$ leads to the formation of the mixed valent $\{\text{V}_{10}\}_{\text{red}}$. By the addition of PdCOD to $\{\text{V}_{10}\}_{\text{red}}$ the same structure of $[\text{V}_{15}\text{O}_{36}\text{Cl}]^{4-}$ was observed as in the previous example but the chloride template was maintained.^[71]

Another important factor is the specific reaction conditions like temperature or even light exposure. Streb et al. was able to show the reactivity link between $\{\text{V}_4\}$, $\{\text{V}_5\}$ and the mixed-valent $\{\text{V}_{10}\}_{\text{red}}$. In that case the formation of $\{\text{V}_5\}$ from $\{\text{V}_4\}$ can be triggered by heat and is a temperature dependent reversible process. In a following reaction step the light driven reduction of $\{\text{V}_5\}$ led to the formation of the mixed valent $\{\text{V}_{10}\}_{\text{red}}$, which was also a reversible process and $\{\text{V}_5\}$ was obtained after aerobic oxidation.^[7]

This shows how the choice of reaction conditions combined with the right choice of precursor and reagents can offer valuable insights towards the cluster specific assembly mechanisms and provides a toolbox to selectively synthesize certain structures.

1.9. Controlled Functionalization via Lacunary Positions

Heterometals can be introduced into polyoxometalate structures by substituting addenda atoms within the cluster shell as described previously. To gain better control over this functionalization step, a common strategy involves the isolation of lacunary structures in which one or more addenda atoms have been selectively removed in a preliminary reaction step. These lacunary derivatives are typically obtained from well-known archetypal structures, such as the Keggin structure. This approach offers a valuable alternative to direct one-pot synthesis of functionalized POMs, which are often limited to specific structural types. By separating the self-assembly of the cluster from its functionalization, greater precision and tunability in the final product can be achieved.^[32]

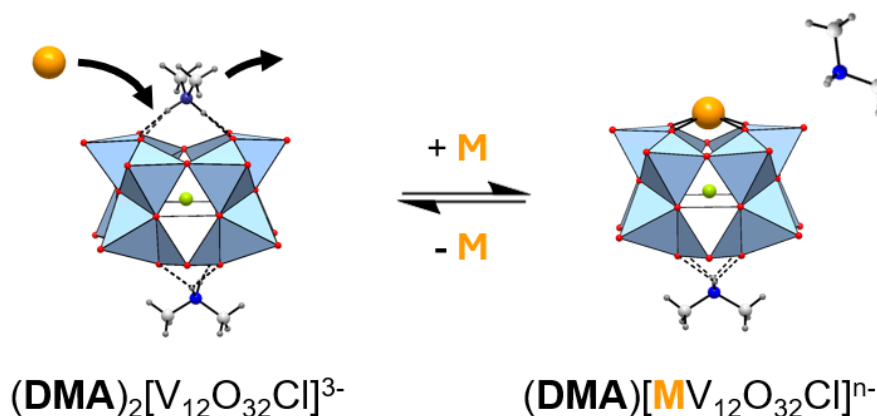


Figure 20: Replacement of a first placeholder cation DMA by a reactive metal center at the fully oxidized state in an equilibrium.

Interestingly the replacement of only one placeholder cation was observed for the fully oxidized cluster, likely due to the overall geometrical change of the structure by a shortening of the bond lengths and angles after functionalization.^[8]

The introduction of a second heterometal was achieved by the reduction of the cluster, increasing the overall negative cluster charge and thereby the affinity to the positively charged heterometal by a reducing agent like N_2H_4 .^[28]

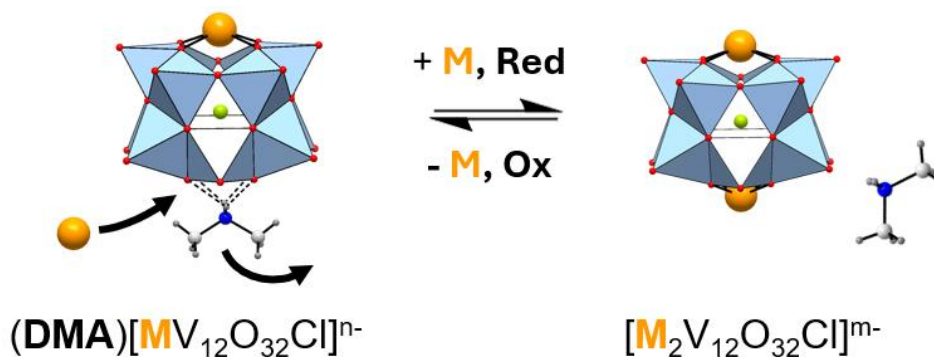


Figure 21: Replacement of the second placeholder cation DMA by a reactive metal center. Due to a lower overall cluster charge after the binding of the first metal center a reduction of one V^{V} to V^{IV} is often required to stabilize the di-functionalized structure.

Many examples of functionalized $\{\text{V}_{12}\}_{\text{tube}}$ have been reported and their catalytic and electrochemical behavior as well as their supramolecular aggregation was investigated.^[74–76] Since the strategy offered control of stepwise functionalization the introduction of two different heterometals to investigate synergistic effects will be a future challenge and lead to promising first results by our group.

1.11. Hybrid Supramolecular Organic-Inorganic Materials

For the design of more sophisticated structures the introduction of organic functional groups is a well-established method. Triols are among the most common covalent linkers, which have been investigated for tungstates, vanadates and molybdates shown for the example of Tris-NH₃ bound to a vanadium functionalized Wells-Dawson, vanadium Lindqvist and the copper centered Anderson-Evans molybdate (Figure 22a-c).^[77-79]

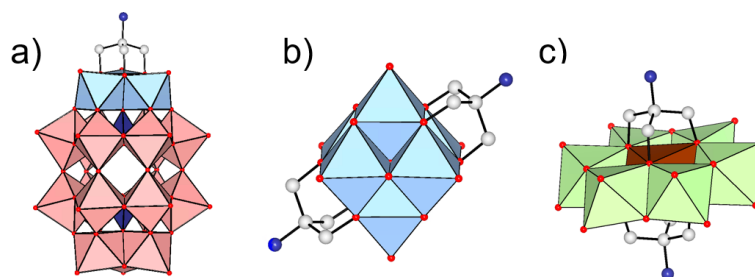


Figure 22: Schematic of a possible Tris-NH₃ functionalization of vanadium functionalized Wells-Dawson tungstate a), hexavanadate Lindqvist b) and Andersson-Evans structure c) (heterometal Cu = brown).

Typically, the functionalization proceeds via refluxing the triol in presence of the POM under inert atmosphere. To demonstrate the versatility of this reaction Parac-Vogt et al. designed POM-POM hybrid materials by using bridging dipentaerythritol to link all three cluster types shown in Figure 22 to yield mixed cluster trimers (Figure 23).^[80]

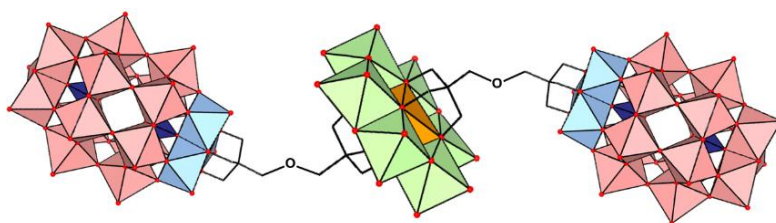


Figure 23: POM-POM hybrid material covalently connected via triol linkers. (heterometal Cr = orange)

For vanadates alkoxides are the most important covalent organic functionalization as a platform for versatile design strategies. Due to its symmetry, tris derivatives match perfectly the three oxygen positions of three corner-sharing vanadium centers with octahedral coordination sphere. To further extend the toolbox of organic functionalization Parac-Vogt et al. were able to develop a tris linker enabling a post-functionalization strategy which is otherwise not accessible due to the reductive potential of vanadium in the oxidation state (V). It was shown that upon a nucleophilic

substitution valeric acid, phenylacetic acid, adamantane carboxylic acid, and biotin can bind to the cluster and single crystals of the valeric acid functionalized POM were obtained.^[81] Even more impressive examples of this post-functionalization strategy were shown by the coupling of pillar[5]arenes to the cluster (Figure 24). The introduction of additional linker molecules enabled the assembly of catalytically active supramolecular structures which show different morphologies depending on the solvent polarity.^[82]

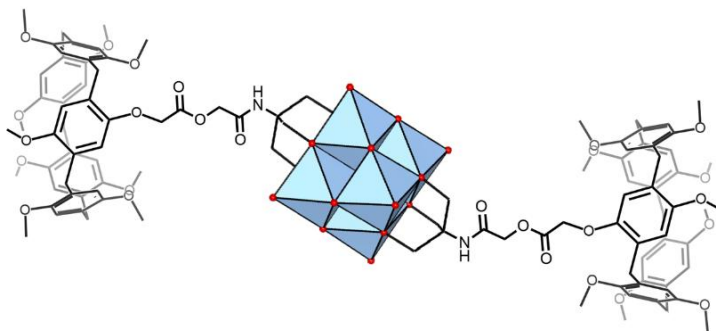


Figure 24: Vanadium Lindqvist structure functionalized by triol linkers. The pillar[5]arene derivate was introduced by a post-functionalization strategy.

The linkage of polyoxometalates can also be promoted by heterometals additional to organic linker molecules. The connection of clusters with more than one functional site can then lead to the formation of polymeric species. Depending on the geometry 1D chains or multidimensional networks can form, which often show enhanced properties compared to the monomeric clusters. For a deeper understanding of the mechanisms behind polymeric polyoxometalate hybrids a controlled growth of low dimensional model systems is necessary. A first step towards the comprehensive understanding of polyoxometalate polymers was the solvent-controlled growth of 1D strontium vanadate polymeric chains reported by Streb et al. The monomeric cluster was crystallized in presence of bulky DMSO. By changing the solvent to less steric DMF or NMP it was possible to induce a ligand exchange initiating the chain growth and several oligomeric species were observed by ESI-MS.^[74]

Similar linear chains were observed for the calcium containing analogue crystallized from DMF. The introduction of redox inactive metal functionalization enhances the electrochemical activity and explicitly the deposition on surfaces to study their redox behavior and catalytic activity is one of the future challenges.^[75]

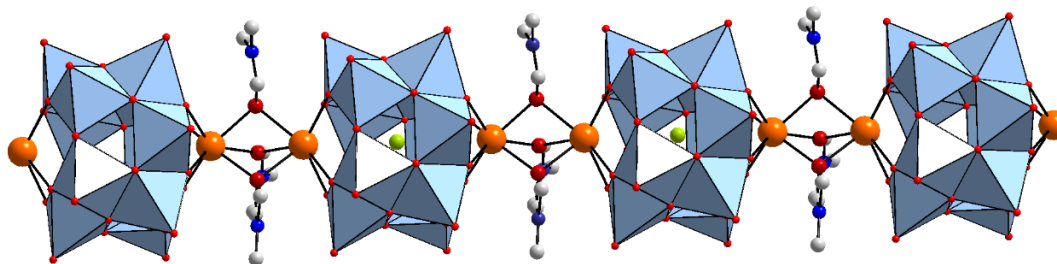


Figure 25: Calcium di-functionalized $\{V_{12}\}_{\text{tube}}$. Three DMF molecules bridge the gap between two heterometal positions to form one-dimensional polymeric structures. Color scheme: Ca = dark orange; C = light grey; N = blue

Polyoxometalate polymeric structures typically possess well defined porosity, good accessibility of active sites and improved stability which allows for reusability for numerous cycles during catalysis.^[83] Additionally, the synergistic effects of different metal sites in close proximity can improve their catalytic activity drastically. To give one example NENU-MV-5 is a metal organic framework composed of $\{V_{10}\}_{\text{red}}$, Cu1 and 1,1'-(1,4-butanediyl)bis(imidazole) obtained under mild hydrothermal conditions. It was used to catalytically degrade 1-Phenyl-2-phenoxyethanol, which is a model system for lignin, to more valuable products. It was shown that the catalytic activity was stable above 96% and the combination of vanadium centers and Cu1 under aerobic conditions in methanol was effective for C-C bond cleavage even without co-catalyst.^[84]

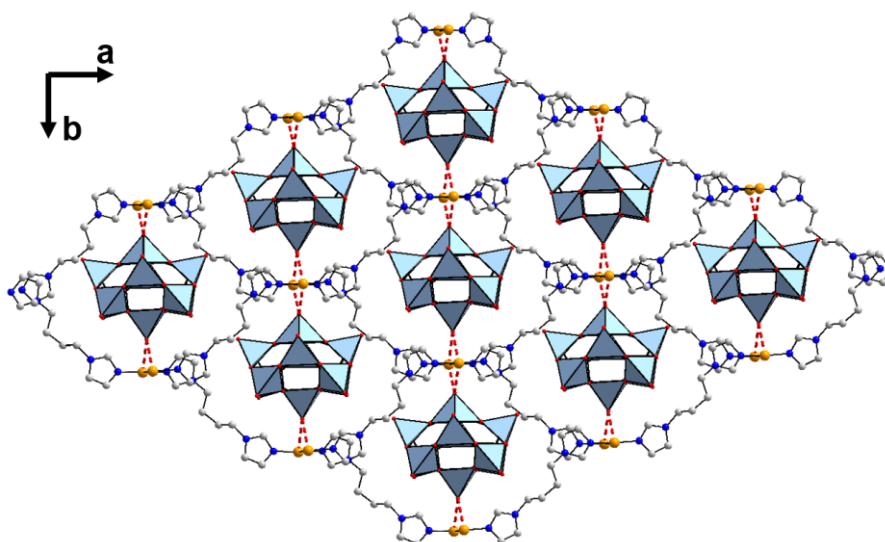


Figure 26: Two-dimensional metal organic framework of 1,1'-(1,4-butanediyl)bis(imidazole) and copper coordinating the mixed valent decavanadate $\{V_{10}\}_{\text{red}}$. Color scheme: Cu = orange; C = light grey; N = blue

1.12. Energy storage

Next to the already mentioned supramolecular chemistry and catalytic activity, polyoxometalates are used in a variety of other applications. Due to the rich redox activity, energy storage is among the most important. Since polyoxometalates are defined at a molecular level with customizable structures and possess multi-electron redox properties, strong stability, high solubility and tunable redox potential, they are ideal candidates for electrode materials, ionic liquids as electrolyte or stabilization agents for electrodes and redox flow batteries.^[1,85]

1.12.1. Redox Flow Batteries

The general setup of a redox flow battery consists of two electrolyte reservoirs, one for the anolyte and one for the catholyte. The electrical energy is stored chemically and set free by pumping the anolyte through the porous electrodes of redox flow battery system where the active species will release the electrons. The anolyte and catholyte are separated by an ion selective membrane for the exchange of a charge carrier. The design can be subdivided by the solvent into aqueous and non-aqueous and by the composition of the anolyte and catholyte into symmetric and asymmetric setups.^[86]

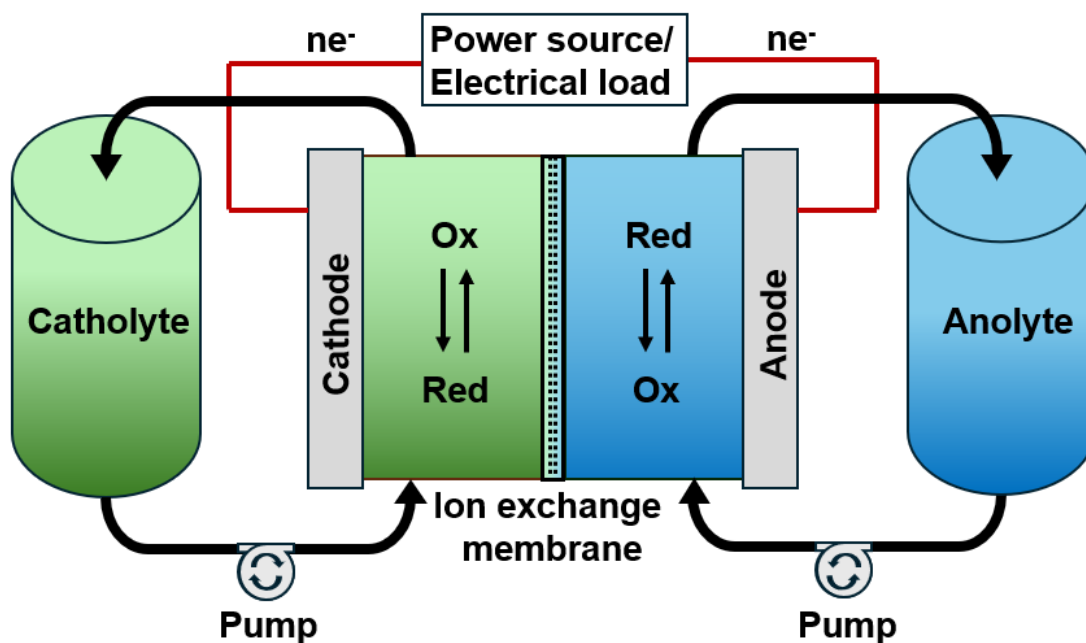


Figure 27: Schematic setup of a redox flow battery.

For vanadates often symmetric redox-flow batteries are applied as the crossover of the active species is less critical. Additionally, to improve the volumetric energy density E_u , it is beneficial to use non-aqueous conditions as the potential window to operate the battery due to the solvent decomposition is increased.^[87] The number of electrons transferred within this range n in combination with the concentration of the active species C_{active} are the factors which offer most potential for improvement.^[88] This is expressed in equation (1) which summarizes these parameters including the average cell voltage V_{cell} and Faraday's constant F . The lower molecular weight of polyoxovanadates is beneficial for achieving higher specific energy densities and lower energy losses through electrolyte pumping.^[1]

$$E_u = \frac{1}{2} n V_{\text{cell}} C_{\text{active}} F \quad (1)$$

A good example is the already mentioned Lindqvist vanadate. The electrochemical profile can be fine-tuned by the introduction of heterometals as mentioned before, to improve the potential range for transferred electrons. To address the challenge of cluster solubility Matson et al. investigated tris functionalized di-Ti doped Lindqvist structures revealed a solubility of up to 0.66 M by modification of the organic moiety. This leads to a 14-fold higher theoretical energy density compared to the previously reported homoleptic cluster which was only soluble at a concentration of 0.044 M. Up to this point, the only strategy to enhance solubility has mainly been the variation of the alkoxy chain length.^[88–90]

1.12.2. Electrode Materials

Polyoxometalates are promising candidates for electrode materials due to their fast ion conductivity and reversible redox processes. Especially decavanadate was a good prototype example for the design of electrodes for lithium and sodium ion batteries synthesized at high yield from aqueous solution. Since the crystal structure often contains water like for $\text{Na}_6\text{-}\{\text{V}_{10}\}_{\text{ox}} \cdot 16 \text{H}_2\text{O}$ an intermediate heating step is required to enable the operation under non-aqueous conditions. However, heating at 200 - 600 °C often results in decomposition to solid state vanadium oxides.^[91]

Nevertheless, due to its layered structure vanadium oxide still is an interesting material for lithium or sodium ion battery electrodes. To enhance the material Newton et al. was able to control the microstructure of the crystalline orthorhombic vanadium oxide by the counterion of the decavanadate precursor. By using nBu_4N^+ the cluster orientation in the precursor crystal structure is random, whereas by the surfactant 1,3-bis[(3-octadecyl-1)-imidazolio)methyl]benzene (gem) the structure is well ordered. After pyrolysis the random orientation in the presence of nBu_4N^+ resulted in smaller rounded crystallites whereas the ordered structures produced highly crystalline micro structured vanadium oxide. The lithium-ion intercalation was tested and the difference in morphology results in higher initial capacity and superior capacity retention for the ordered structure and faster lithium insertion kinetics for the smaller rounded crystallites due to higher surface area.^[92]

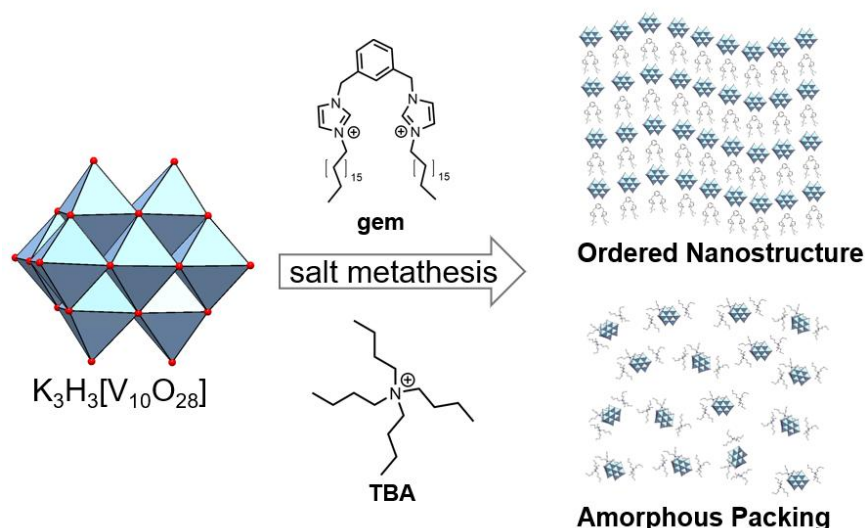


Figure 28: The salt metathesis of decavanadate leads to ordered nanostructures for gem and to amorphous packing for $n\text{Bu}_4\text{N}^+$ as counter ion after precipitation.^[92]

The thermal decomposition can be prevented by a careful choice of the counterion. The stabilization of molecular decavanadate during the removal of water at elevated temperatures up to 220 °C was achieved by Anjass et al. by using guanidinium as counterion. The mass loss at even higher temperatures than the $n\text{Bu}_4\text{N}^+$ implies a stronger interaction to the decavanadate. The formation of a hydrogen bonding network leads to improved cycling stability compared to the water free $n\text{Bu}_4\text{N}^+$ containing decavanadate.^[91]

These examples demonstrate how the choice of the counter-cation can drastically change the material properties to improve their performance. Aside from the thermal decomposition and crystal structure other physical properties like the melting point or the solubility can be influenced. In the previous examples of reference material typically tetrabutylammonium cations are used. By increasing the length of the alkyl chains of the tetraalkyl ammonium cations e.g. to tetraoctyl ammonium, the interactions to the polyoxometalate are decreased and the melting point is lowered to obtain ionic liquids.^[93,94]

1.12.3. Ionic liquids

Ionic liquids are defined as salts with a melting point below 100 °C. This property is specifically advantageous for the preparation of coatings which can be used as anti-corrosion, anti-bacterial surface modifications, in dye-sensitized solar cells and to improve electrode surfaces.^[21,95–98] Further applications include water purification systems and the extraction of metals from aqueous solution.^[94]

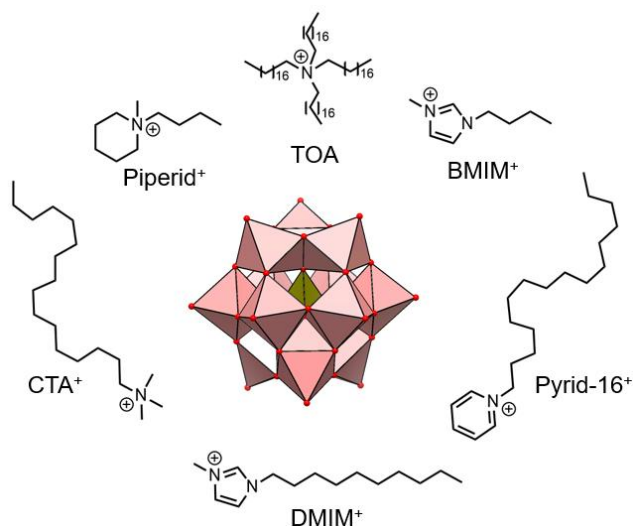


Figure 29: Possible counter ions forming ionic liquids in combination with the α -Keggin tungstate.^[98]

A good example for their application is the use as electrolyte additive in lithium-ion batteries to prevent dendrite formation. The combination of the anionic polyoxometalate capable of binding cations like Li^+ at different surface sites with the large organic cation like hexadecyl trimethyl ammonium or 1-butyl-3-methylimidazolium helps to form a solid/electrolyte and cathode/electrolyte interphase. The positively charged cations can have a repulsive effect on the Li^+ cations and are mainly adsorbed at exposed parts of the electrodes. The negatively charged POM on the other hand can co-assemble with the lithium at the surface and delocalize the electrons to homogenize the lithium deposition. The formation of interlayers is crucial to improve cyclability, since the formation of dendrites could otherwise pierce the separator and could result in an internal short-circuit.^[98]

For battery applications the non-flammability and low volatility additionally are a major improvement.^[21] The higher solubility and low melting point of ionic liquids can potentially be beneficial for redox-flow batteries, where the low solubility of the active species and the use of large amounts of volatile organic solvents are a major drawback so far.^[1]

The given examples highlight how polyoxometalates can be used for a great variety of applications the development of controlled functionalization methods, cluster synthesis and modification of well-known structures. Polyoxovanadates are specifically interesting for their structural flexibility and lower molecular weight compared to molybdates or tungstates regarding energy storage as well as their photochemical and catalytic properties. Despite their high potential, the complex reaction mechanisms and lower stability of vanadates have discouraged many researchers from studying them in depth.

The aim of this work is to gain insight into the mechanisms of polyoxovanadate functionalization, their behavior in solution, as well as the development of novel, highly redox-active materials for battery applications, thereby establishing a foundation for advanced modifications toward future applications.

2. Objectives

Polyoxometalates are highly versatile regarding their use, ranging from catalysis, molecular magnetism, energy storage to biological applications. Their development started from the discovery of the molecular precise kegging structure and was further advanced by the introduction of heterometals via lacunary positions and the step-by-step synthesis to control the final cluster structure. Furthermore, the role of external and internal templates was shown to direct and stabilize distinct cluster sizes and shapes and the introduction of organic molecules enables the supramolecular assembly of large multidimensional structures. Since due to their complexity vanadates are often less researched than tungstates and molybdates, the aim of this work is to use these synthetic strategies to design novel and highly functional polyoxovanadate materials.

Three major objectives were addressed in this work:

A new synthetic strategy for cluster functionalization using light

Since the functionalization of polyoxometalates is a powerful method to precisely tune their electrochemical and catalytic behavior the controlled post-functionalization via lacunary positions is important. The placeholder method developed by Streb et al. is the first example of the controlled functionalization of $\{V_{12}\}_{\text{tube}}$.^[8] It was shown that mono- and di-functionalized species can co-exist in solution and the isolation of one or the other was possible by the chemical reduction of the cluster.^[28] In this work, the goal was to develop a robust and broad-scope synthetic concept to gain further control over the reduction step using light as an eco-friendly alternative to chemical reducing agents like hydrazine hydrate. The use of light as a reaction parameter to shift the coupled equilibria between mono- and di-magnesium functionalized $\{V_{12}\}_{\text{tube}}$ was explored, and mechanistic studies including various NMR techniques, UV-Vis and further spectroscopic methods were conducted to provide a valuable foundation for transferring the concept to the functionalization with other reactive metal centers.

Synthesis of electrochemically promising novel materials and implementation into redox-flow batteries

Since redox-flow batteries are among the most important applications for polyoxovanadates, the development of stable and soluble materials with rich electrochemical behavior is important. To achieve an increased capacity, most studies have focused on increasing the concentration of the electrochemically active species by improving their solubility. In contrast, our goal was to enhance the number of redox events within a defined potential window, thereby increasing the number of transferred electrons per active species. Therefore, a redox self-equilibration strategy was developed and mechanistic studies on the reaction of $(n\text{Bu}_4\text{N})_4\{\text{V}_{10}\}_{\text{red}}$ induced by magnesium chloride as a Lewis acid were conducted to gain a deeper understanding of the system. To build a foundation for the application in batteries the material was fully characterized, including composition, number of electrons and redox behavior. To test the applicability of the concept, the material was tested in a redox-flow battery setup. To maximize the capacity, solubility tests and optimization of the battery parameters were conducted. In addition, in-operando tests were performed to test the stability of the material and to determine the state of charge. Charge and discharge capacity as well as further mechanistic studies were conducted to validate the concept of enhanced capacity by the increased number of transferred electrons.

The influence of mixed solvent systems on molecular polyoxovanadates

The stability of polyoxovanadates and their functionalization, as well as their catalytic activity, can be highly solvent-dependent. As the interaction of water with the cluster shell is of major interest, theoretical MD simulations of $(n\text{Bu}_4\text{N})_3\{\text{MnV}\}$ were conducted to investigate the formation of a solvation shell at the different oxidation states involved in the catalytic process. To validate the results, a water titration study in the stability range of 0-5 vol% water in acetonitrile was conducted. Mechanistic insights were gained by multiple spectroscopic techniques including NMR, UV-Vis, and liquid FTIR, as well as electrochemical methods at different oxidation states of the cluster. The solvation induced spectral changes and behavior in solution is investigated to provide a basis for the application and design of polyoxovanadate catalysts in the future.

3. Results and Discussion

3.1. New synthetic strategies for cluster functionalization using light

Preliminary Note: This Chapter is based on the published journal article: S. Repp, M. Remmers, A.S.J. Rein, D. Sorsche, D. Gao, M. Anjass, M. Mondeshki, L. M. Carrella, E. Rentschler and C. Streb, Coupled reaction equilibria enable the light-driven formation of metal-functionalized molecular vanadium oxides. *Nat Commun* **14**, 5563 (2023). <https://doi.org/10.1038/s41467-023-41257-y> These authors contributed equally: Stefan Repp, Moritz Remmers, Alexandra S. J. Rein

3.1.1. Introduction

Molecular metal oxides, so-called polyoxometalates (POMs)^[99,100], are an emerging class of inorganic materials. Their well-defined molecular structure and tuneable properties and reactivity have made POMs ideal analogues for the corresponding solid-state metal oxides^[101–104]. This has led to applications in areas including energy conversion and storage^[1,105], molecular magnetism^[106,107], and catalysis^[108,109]. Typically, POM reactivity can be tuned by functionalization with functional metal centers:^[8,110] In molecular magnetism, the incorporation of lanthanides in POMs is a widely used principle^[111], while energy conversion and storage schemes often use transition metal functionalized POMs^[112], In catalysis, the introduction of Lewis-acidic sites in POMs is a well-known concept^[113].

Thus, robust and broad-scope synthetic concepts for the metal-functionalization of POMs are critical for the targeted development of new functional compounds. For polyoxotungstates (and, to a lesser degree, for polyoxomolybdates), controlled metal-functionalization is possible using so-called lacunary cluster derivatives where one or several of the original metal ions (W or Mo) have been hydrolytically removed from the cluster shell^[110]. Selective binding of suitable metal ions at the resulting vacancy then leads to the targeted metal-functionalized species^[110,114]. This approach has led to ground-breaking molecular components, e.g., for catalysis^[108, 112,115] molecular electronics^[111,116,117] and medicine^[118,119]. In contrast, in polyoxovanadate (POV)

chemistry, controlled and predictable metal-functionalization approaches are still in their infancy^[1, 10, 26,27, 67,120], and the field is currently dominated by a combination of empirical knowledge and serendipity^[1, 10, 26,121]. Thus, the development of controlled approaches for the predetermined and selective metal-functionalization of POMs is critical to enable knowledge-based materials design.

Early studies by Streb and co-workers have used a placeholder strategy for the predictable metal-functionalization of POVs. This approach uses the dodecanuclear species $\{(\text{NMe}_2\text{H}_2)_2[\text{V}_{12}\text{O}_{32}\text{Cl}]\}^{3-}$, (= $(\text{DMA})_2\{\text{V}_{12}\}$, DMA = dimethyl ammonium), where two vacant metal coordination sites are blocked by hydrogen-bonded DMA cations. In-situ exchange of these cations with a variety of metals is possible, leading to the mono- or (more rarely) di-metal-functionalized species ($\{\text{MV}_{12}\}$ and $\{\text{M}_2\text{V}_{12}\}$, respectively), and applications ranging from (light-driven) catalysis^[65,76] to energy storage^[75,122]. Note that for most of the di-metal-functionalized $\{\text{V}_{12}\}$ species were only accessible as mixed $\text{V}^{IV/V}$ oxidation state clusters^[28, 30,74,75]. Recently, a similar synthetic approach to metal-functionalized molybdates has been pioneered by Yamaguchi, Suzuki and co-workers. They used pyridine moieties to coordinatively stabilize and functionalize lacunary polyoxomolybdates which are otherwise difficult to access^[114,123].

Most often, temperature, solvent, solution acidity and type of metal salt are the key synthetic parameters varied to facilitate metal-functionalization of POVs^[26]. In contrast, the use of light, i.e. photons with energies in the visible spectral range has rarely been discussed as a systematic control parameter to trigger POM and POV functionalization. This is surprising, as the (visible) light photoactivity of POMs is well-documented, and the light-induced excitation of $\text{O} \rightarrow \text{M}$ ligand-to-metal charge-transfer transitions is an easy tool to selectively access reduced POM species^[1,124–127]. The concept has been pioneered by Yamase and co-workers who demonstrated that previously unknown mixed-valent POMs and POVs can be accessed photochemically in the presence of suitable electron donors, e.g., organic amines^[125,128,129]. POV chemistry is particularly sensitive to photoinduced reactions triggered by visible light, as POVs typically show higher visible light absorption compared with tungstates and molybdates^[124]. This approach has recently been explored by Liu and co-workers who demonstrated the visible-light-assisted synthesis of mixed-valent POVs^[130]. Here, we demonstrate how light-dependent, coupled reaction equilibria can be used to selectively target the partial reduction and metal-functionalization of $\{\text{V}_{12}\}$, leading to a

di-magnesium functionalized species, $\{\text{Mg}_2\text{V}_{12}\}$, as an intriguing model compound for future studies, e.g., in electrochemical energy storage^[1,75].

3.1.2. Results

Synthesis and characterization

The starting point was our study into the design of magnesium(II)-functionalized $\{\text{V}_{12}\}$ as molecular models for Mg ion batteries, where solid-state magnesium vanadates are under investigation as active electrode materials^[131]. Initial experiments to functionalize $\{\text{V}_{12}\}$ with Mg^{2+} were performed by reacting Mg^{2+} with $(\text{DMA})_2\{\text{V}_{12}\}$ in acetonitrile under the standard placeholder-functionalization conditions described above^[8,28]. Despite the extensive variation of the reaction and isolation conditions, reproducible formation of Mg-functionalized $\{\text{V}_{12}\}$ was not possible. Systematic study of the key reaction parameters showed that visible light irradiation and oxygen-free conditions were required to access the target compound, $(\text{nBu}_4\text{N})_4[(\text{MgCl})_2\text{V}_{12}\text{O}_{32}\text{Cl}]$ ($=\{\text{Mg}_2\text{V}_{12}\}$, **1**). Diffusion crystallization using diethyl ether as diffusion solvent gave green single crystals of $\{\text{Mg}_2\text{V}_{12}\}$ in yields of 64% (based on $\{\text{V}_{12}\}$, see Methods and Supplementary Section 3.2.2). When the reaction was performed in the dark under otherwise identical conditions, only the starting material $\{\text{V}_{12}\}$ was recovered as yellow crystals. Crystallographic analysis by single-crystal X-ray diffraction shows that $\{\text{Mg}_2\text{V}_{12}\}$ crystallizes in the monoclinic space group $\text{P}2_1/\text{c}$ with cell axes $a = 24.3414(9)$ Å, $b = 16.7474(7)$ Å, $c = 24.4623(9)$ Å and cell angles $\beta = 94.6107(17)^\circ$, $\alpha = \gamma = 90^\circ$ (for crystallographic details see Methods and Supplementary Section 3.2.2). Note that this crystal lattice is virtually identical to the previously reported di-functionalized species $\{\text{Mn}_2\text{V}_{12}\}$ $(\text{nBu}_4\text{N})_4[(\text{MnCl})_2\text{V}_{12}\text{O}_{32}\text{Cl}]$ ^[28]. For full characterization of $\{\text{Mg}_2\text{V}_{12}\}$ see Supplementary Section 3.2.2. The metal oxo framework of $\{\text{Mg}_2\text{V}_{12}\}$ is isostructural to the di-metal-functionalized $\{\text{V}_{12}\}$ species reported earlier (i.e., $\{\text{Mn}_2\text{V}_{12}\}$ ^[28], $\{\text{Ca}_2\text{V}_{12}\}$ ^[75], $\{\text{K}_2\text{V}_{12}\}$ ^[122], $\{\text{Sr}_2\text{V}_{12}\}$ ^[74], $\{\text{Ce}_2\text{V}_{12}\}$ ^[76]), the two square pyramidal Mg^{2+} ions reside in the metal binding sites on top and bottom of the cluster and feature a terminal chloride ligand (Figure 30a, b).

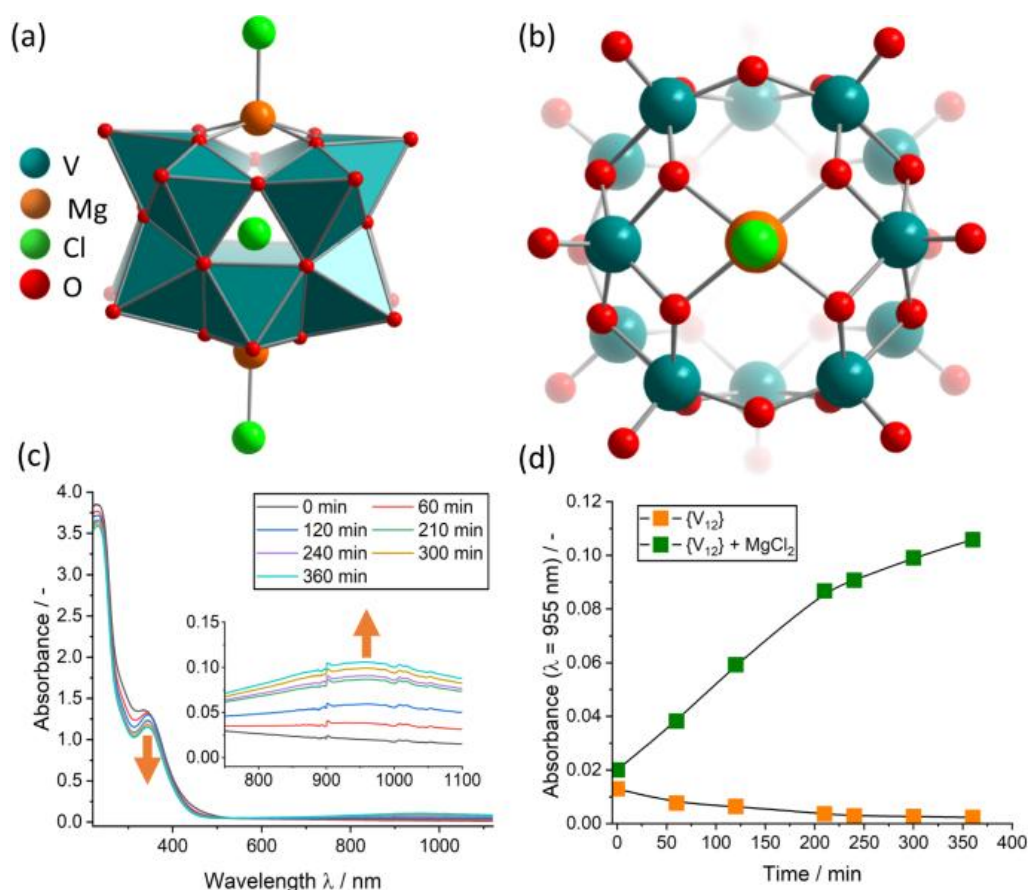


Figure 30: Structural and spectroscopic information on the formation of {Mg₂V₁₂}: (a) side view of {Mg₂V₁₂}; (b) top view of the Mg binding site in {Mg₂V₁₂}; (c) time-lapse UV-Vis/NIR spectroscopy of the {Mg₂V₁₂} reaction mixture containing {V₁₂} and MgCl₂ in acetonitrile. (d) time-dependent reduction of {V₁₂} in the presence (green squares) and absence (orange squares) of Mg²⁺. Conditions: irradiation with a broadband high-power LED light source ($P_{\text{optical}} \sim 5 \text{ W}$), $[\{V_{12}\}] = 0.05 \text{ mM}$, $[Mg^{2+}] = 0.21 \text{ mM}$.

UV-Vis/NIR spectroscopy of {Mg₂V₁₂} confirms the mixed valent (V^{IV/V}) character of the species, as indicated by the characteristic, broad intervalence charge-transfer (IVCT) band between ~600–1200 nm^[28]. Further support of the mixed-valent nature of {Mg₂V₁₂} is given by continuous wave electron paramagnetic resonance (EPR) spectroscopy which unambiguously shows the presence of one V^{IV} species with $S = \frac{1}{2}$ (Supplementary Figure 36), while a pure V^V cluster would be EPR silent. Furthermore, EPR-based spin counting is in good agreement with one V^{IV} center per {Mg₂V₁₂}.

Photochemical studies

Irradiation of a reaction mixture containing $\{V_{12}\}$ and Mg^{2+} in MeCN with a broadband LED light source resulted in the emergence of the IVCT transitions characteristic for the formation of mixed-valence $VI^{VI/IV}$ species (vide supra). Thus, the change of the UV-Vis/NIR signals over time can be used to monitor the rate of $\{Mg_2V_{12}\}$ formation, see Figure 30c, d. This provides the ideal conditions to explore the fundamentals of the light-induced formation mechanism of metal-functionalized vanadates: to this end, we compared the photoreduction of $\{V_{12}\}$ in the presence and absence of Mg^{2+} (Figure 30d). Strikingly, $\{V_{12}\}$ reduction is only observed in the presence of Mg^{2+} , while in the absence of Mg^{2+} , no formation of V^{IV} centers and no IVCT signal is detected. We hypothesized that this finding indicates that Mg^{2+} interacts with $\{V_{12}\}$ in the reaction solution to give a photoactive reactive intermediate. Based on our understanding of the system, we suggested that this intermediate could be the mono-functionalized species $\{MgV_{12}\}$ ($= \{(DMA)[(MgCl)V^V_{12}O_{32}Cl]\}^{3-}$). The formation of an intermediate species is indicated by UV-Vis/NIR spectroscopy, which shows distinct spectral changes in the region between 300 nm to 500 nm upon addition of Mg^{2+} to the $\{V_{12}\}$ reaction solution (Figure 31a). Also, ^{51}V NMR spectroscopy shows that immediately after addition of Mg^{2+} to an acetonitrile solution of $\{V_{12}\}$, a four-signal spectrum is observed which is characteristic for the mono-metal-functionalized $\{MV_{12}\}$ species (Figure 31b).

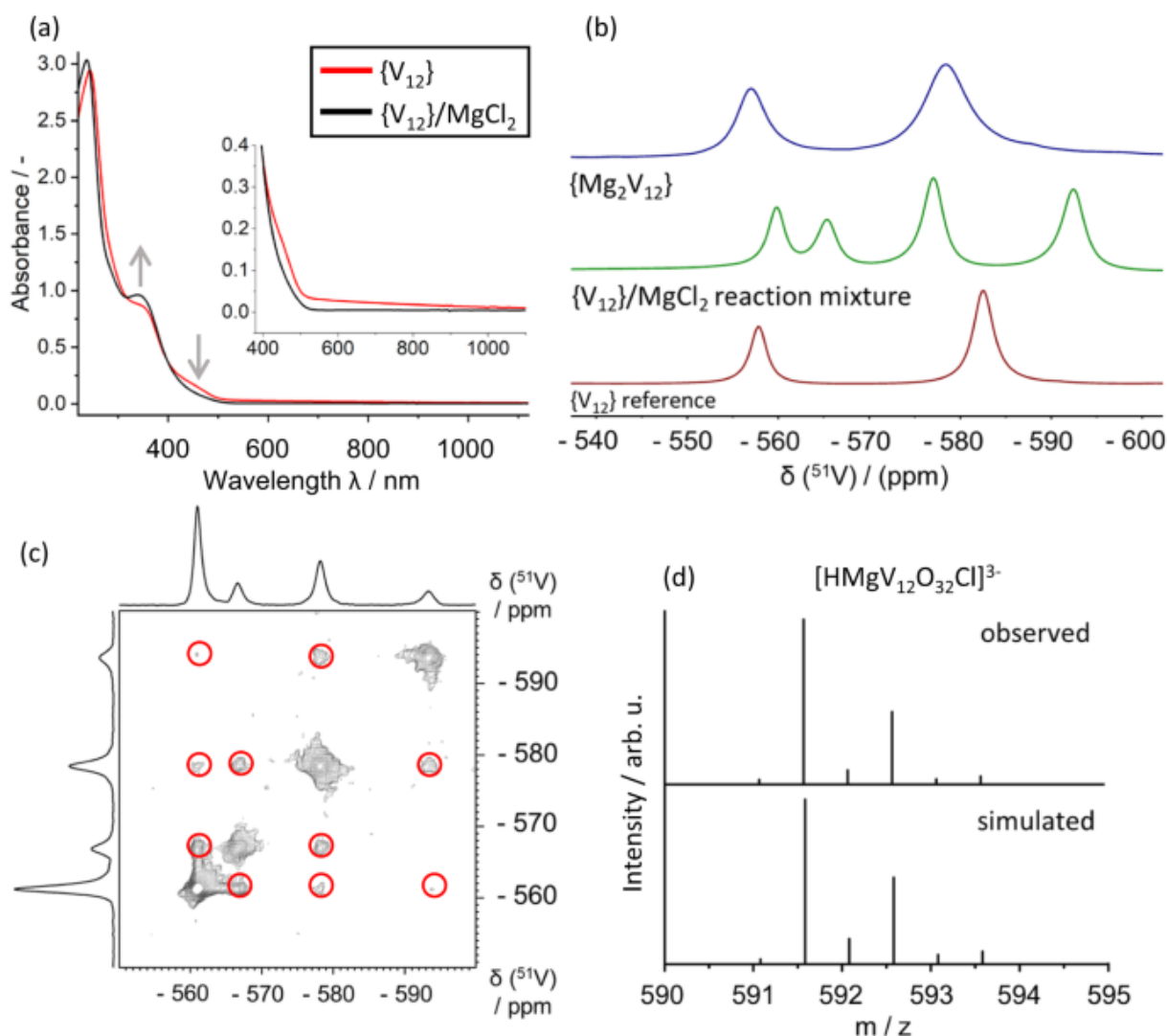


Figure 31: Experimental verification for the in-situ formation of the photoactive $\{\text{MgV}_{12}\}$ intermediate under reaction conditions. (a) UV-Vis/NIR spectral changes observed upon reaction of $\{\text{V}_{12}\}$ (0.05 mM) with Mg^{2+} (0.21 mM) in acetonitrile, resulting in the formation of the visible-light photoactive $\{\text{MgV}_{12}\}$. (b) ^{51}V -NMR spectroscopic observation of the characteristic four-line pattern of mono-functionalized $\{\text{MgV}_{12}\}$ formed by reaction of $\{\text{V}_{12}\}$ (10 mM) with Mg^{2+} (42 mM) in acetonitrile. ^{51}V -NMR spectra of $\{\text{V}_{12}\}$ (in acetonitrile) and $\{\text{Mg}_2\text{V}_{12}\}$ (in dimethyl sulfoxide) are shown for comparison. (c) ^{51}V TOCSY-NMR spectrum indicating that all four signals belong to one ^{51}V spin system i.e., one $\{\text{MgV}_{12}\}$ cluster. Non-diagonal signals are marked with red circles. Conditions: $[\{\text{V}_{12}\}] = 5.0$ mM, $[\text{Mg}^{2+}] = 21.1$ mM, solvent: acetonitrile. (d) Negative ion-mode high-resolution ESI mass spectrum showing the observed and simulated isotopic pattern for $[\text{HMgV}_{12}\text{O}_{32}\text{Cl}]^{2-}$ ($= \text{H}\{\text{MgV}_{12}\}$), $[\{\text{V}_{12}\}] = 0.05$ mM, $[\text{Mg}^{2+}] = 0.21$ mM, solvent: acetonitrile.

Note that a virtually identical four-line signal pattern has been reported for the mono- Zn^{2+} -functionalized species $\{\text{ZnV}_{12}\}$ ($= \{(\text{DMA})[(\text{ZnCl})\text{V}_{12}\text{O}_{32}\text{Cl}]\}^{3-}$)^[8]. In addition, ^{51}V -NMR total correlation spectroscopy (TOCSY) of the reaction solution showed, that the four ^{51}V -NMR signals assigned to $\{\text{MgV}_{12}\}$ belong to one molecular species (Figure 31c).

Mechanistic analyses

Further evidence for the formation of $\{\text{MgV}_{12}\}$ is revealed by characteristic changes in the respective ^1H and ^1H DOSY spectra (Supplementary Section 3.2.3). Upon addition of Mg^{2+} to a $\{\text{V}_{12}\}$ solution in acetonitrile, DMA cations are released from their original, $\{\text{V}_{12}\}$ -bound positions into solution, resulting in a dynamic equilibrium between cluster-bound and “free” DMA cations. This results in a characteristic low-field shift of the N-H proton resonances from $\delta \sim 6.3$ ppm to $\delta \sim 7.0$ ppm (Supplementary Figure 45 and Figure 46). ^1H -DOSY-NMR spectra were collected to further study the release of DMA cations upon Mg^{2+} addition to $\{\text{V}_{12}\}$ solutions in acetonitrile. Specifically, we studied the characteristic changes of the respective diffusion coefficients D based on analysis of the DMA- ^1H resonances (methyl groups, δ ca. 2.6 ppm; ammonium groups, δ ca. 6.3 – 8.6 ppm, (Supplementary Figure 47)^[132]. These analyses show the expected trend, i.e., the diffusion coefficients decrease with increasing size of the species studied in the order “free” DMA $< \{\text{MgV}_{12}\} < \{\text{V}_{12}\}$.

Further, high-resolution electrospray ionization mass spectrometry (HR-ESI-MS) allowed us to identify a series of signals corresponding to the mono-Mg-functionalized species, e.g., $[\text{HMgV}_{12}\text{O}_{32}\text{Cl}]^{2-}$ (observed: 591.590 m/z, calculated: 591.852 m/z, see Figure 31d, and Supplementary Section 3.2.2 for further peak assignments). Note that the characteristic four-line ^{51}V -NMR signal pattern assigned to $\{\text{MgV}_{12}\}$ was observed even under the dilute concentration conditions of the HR-ESI-MS experiments ($[\text{Mg}^{2+}] = 0.21$ mM, $[\{\text{V}_{12}\}] = 0.05$ mM, see Supplementary Figure 48).

Next, we explored the Mg^{2+} functionalization further by performing a ^{51}V -NMR spectroscopy titration, where increasing amounts of Mg^{2+} were added to $\{\text{V}_{12}\}$ solutions in acetonitrile. To assess the formation of $\{\text{MgV}_{12}\}$, the characteristic ^{51}V -NMR signals were integrated, and the integral areas were plotted as a function of the Mg^{2+} equivalents added. As shown in Figure 32, integration of the three non-overlapping signals unambiguously indicates, that changes of the integrated area are only observed up to 1.0 equivalents Mg^{2+} . Higher equivalents do not change the spectra observed. This strongly suggest the presence of a 1:1 molar species, which is in line with the formation of $\{\text{MgV}_{12}\}$. These observations are supported by an identical ^1H -NMR titration study which shows that upon Mg^{2+} binding to $\{\text{V}_{12}\}$, release of DMA cations (indicated by characteristic shifts of the DMA proton signals) is observed, see Supplementary Figure 46.

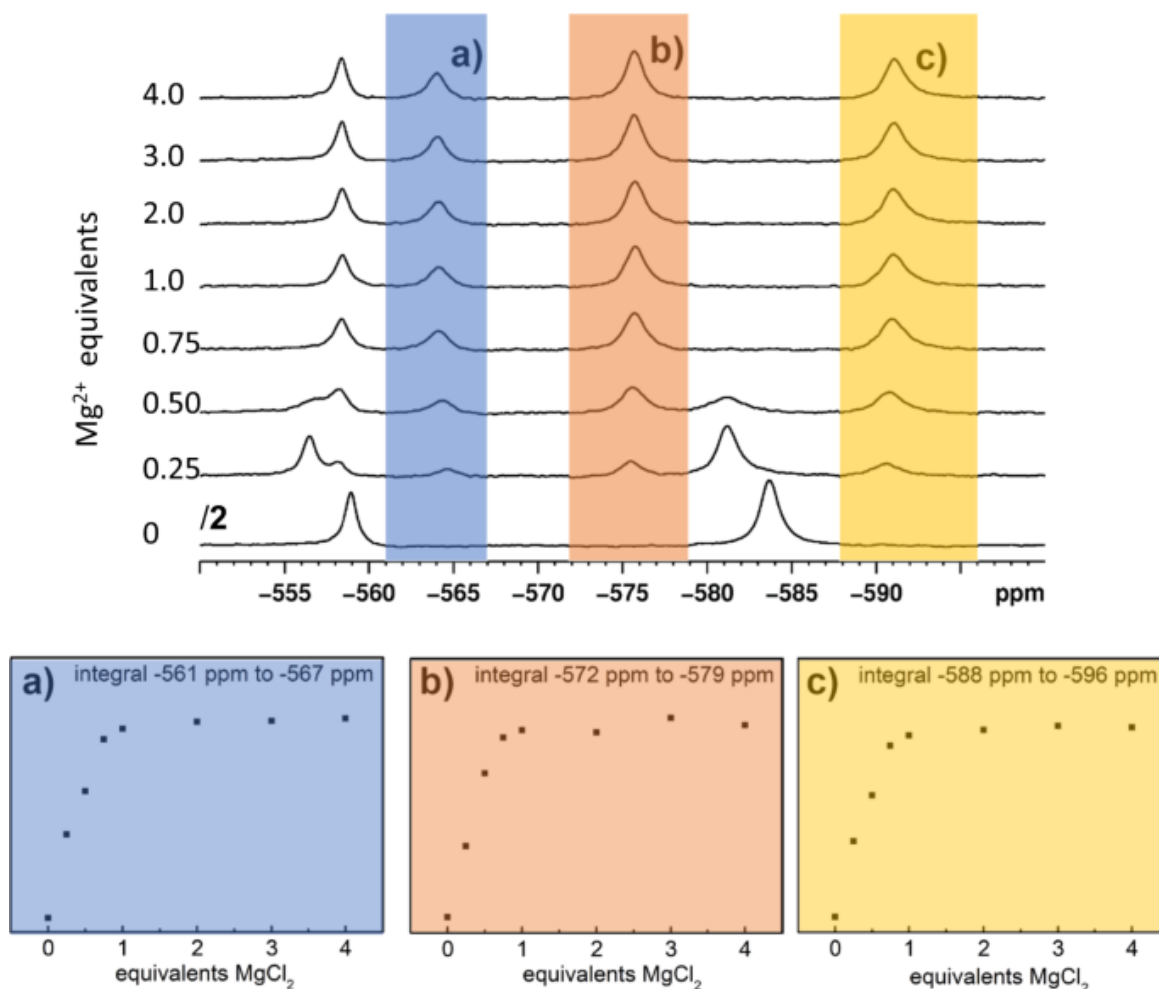


Figure 32: In-situ ^{51}V -NMR spectroscopic titration to assess the $\{\text{MgV}_{12}\}$ formation. Top: stacked ^{51}V -NMR spectra of acetoneitrile solutions containing $\{\text{V}_{12}\}$ and varying Mg^{2+} molar equivalents (between 0 eq. to 4 eq. relative to $\{\text{V}_{12}\}$). Bottom: the area integrals of the three characteristic $\{\text{MgV}_{12}\}$ signals marked a), b), c) are shown. In each instance, integral changes are only observed up to 1.0 Mg^{2+} equivalents, indicating that a 1:1 species, i.e., $\{\text{MgV}_{12}\}$ is formed. Conditions: $[\{\text{V}_{12}\}] = 5.0 \text{ mM}$, $[\text{Mg}^{2+}] = 0 - 21.1 \text{ mM}$, solvent = acetoneitrile.

The different photoactivities of $\{\text{V}_{12}\}$ and $\{\text{MgV}_{12}\}$ were probed experimentally by wavelength-selective irradiation: when the standard $\{\text{V}_{12}\}/\text{Mg}^{2+}$ reaction mixture in acetoneitrile was irradiated with a monochromatic 405 nm LED light source, the characteristic $\{\text{MgV}_{12}\}$ reduction and formation of the characteristic IVCT band was observed. In contrast, when the same experiment was performed for a pure $\{\text{V}_{12}\}$ solution (in acetoneitrile, without added Mg^{2+}), no vanadate reduction was observed. Also, irradiation of the standard $\{\text{V}_{12}\}/\text{Mg}^{2+}$ reaction mixture using a monochromatic 470 nm LED light source also did not lead to reduction of the vanadate cluster, see Supplementary Figure 51.

Further insights into the electronic structure of $\{\text{MgV}_{12}\}$ and $\{\text{Mg}_2\text{V}_{12}\}$ were obtained by theoretical computations using density functional theory (DFT) using the B3LYP functional^[133,134] combined with the def2-SVP basis set^[135]. Analysis of the HOMO-

LUMO levels of $\{\text{MgV}_{12}\}$ and analysis of the calculated UV-Vis/NIR spectrum show an intense ligand-to-metal-charge-transfer (LMCT) transition at the UV-to-Vis border, which we attribute to the experimentally observed Vis photoactivity of $\{\text{MgV}_{12}\}$. For $\{\text{Mg}_2\text{V}_{12}\}$, similar LMCT transitions are observed, and in addition, the broad characteristic IVCT transition in the Vis-NIR range are reproduced by the calculations. For details, see Supplementary Section 3.2.4.

Based on Le Chatelier's principle, we hypothesized that addition of DMA to the reaction solution should shift the equilibrium to the reagent side (see Figure 32a), thus preventing the formation of the photoactive $\{\text{MgV}_{12}\}$. This behaviour is indeed observed: when an excess of DMA is added to the standard $\{\text{V}_{12}\}$ reaction solution and the sample is irradiated, no reduction is observed by UV-Vis/NIR spectroscopy (Supplementary Figure 52). This suggests that the reactive intermediate which enables photoreduction is not present under these conditions and lends further support to $\{\text{MgV}_{12}\}$ being the photoactive intermediate. Also, when the $\{\text{V}_{12}\}$ photoreduction is performed in the presence of Mg^{2+} and air, virtually no vanadate reduction is observed (as indicated by the absence of IVCT bands in the UV-Vis/NIR spectrum, see Supplementary Figure 53). This provides further support that a light-induced electron transfer to the photoexcited $\{\text{MgV}_{12}\}$ is a key process in the formation of $\{\text{Mg}_2\text{V}_{12}\}$ and suggests that interference between the photoexcited $\{\text{MgV}_{12}\}$ and O_2 (e.g., by triplet quenching^[52]) could prevent formation of the reduced vanadate species^[136].

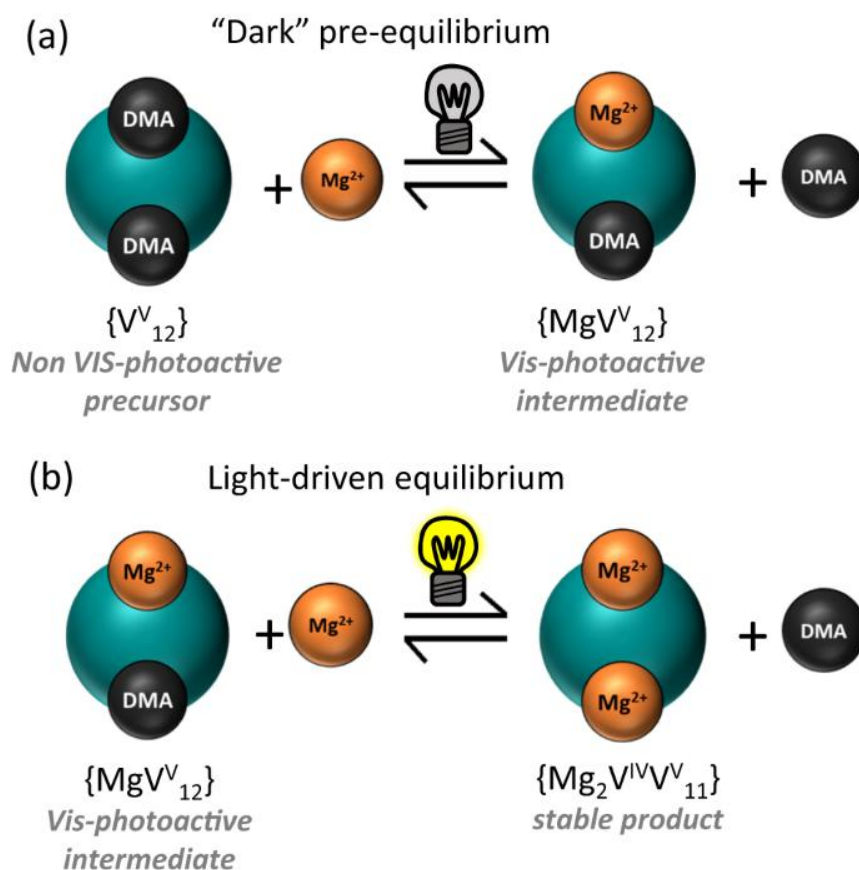


Figure 33: Proposed coupled solution-phase equilibria during $\{Mg_2V_{12}\}$ formation: (a) the light-independent pre-equilibrium forming the photoactive intermediate $\{MgV_{12}\}$ and (b) light-driven formation of the di-Mg-functionalized $\{Mg_2V_{12}\}$.

In sum, these data suggest that reaction of $\{V_{12}\}$ and Mg^{2+} results in formation of the mono-functionalized $\{MgV_{12}\}$ as photoactive, reactive intermediate, which can then be converted to the di-functionalized $\{Mg_2V_{12}\}$ upon irradiation with visible light. To gain insights into the sacrificial electron donor, we used cyclic voltammetry to compare the redox potentials of the possible donors (DMA, nBu_4N^+ , MeCN). Based on this data, DMA is the most likely sacrificial electron donor, as it is significantly easier to oxidize ($E_{ox} = 0.7 \text{ V vs } Fc^+/Fc$) compared with the other possible electron donors, i.e., nBu_4N^+ and MeCN ($E_{ox} > 1.6 \text{ V vs } Fc^+/Fc$), see Supplementary Figure 54. Based on these considerations, the following coupled reaction equilibria are proposed, see Figure 33. Finally, to probe whether the observed light-induced reactivity is unique to Mg^{2+} or can be extended to other metal functionalizations, we performed the $\{V_{12}\}$ metal functionalization experiments using Ca^{2+} instead of Mg^{2+} (experimental details see Supplementary Section 3.2.3). Reaction of $CaCl_2 \cdot 2H_2O$ (21.1 mM) with $\{V_{12}\}$ (5.0 mM) in acetonitrile led to the observation of the characteristic four-line ^{51}V -NMR signal pattern assigned to $\{CaV_{12}\}$ (Supplementary Figure 55). Visible light-irradiation of the

$\{V_{12}\} / Ca^{2+}$ reaction solution resulted in the formation of the characteristic IVCT bands between ~600 and 1200 nm which is indicative of the formation of the reduced, di-metal-substituted vanadate species (see Supplementary Figure 56). These findings suggest that the light-induced metal functionalization reported here is not unique to Mg^{2+} and can be transferred to other metal cation species, and possibly also to other vanadate cluster architectures.

3.1.3. Discussion

We report the first example of a light-dependent, coupled set of solution-phase equilibria, enabling the controlled metal-functionalization of molecular vanadium oxides. Light-independent reaction of $\{V_{12}\}$ with Mg^{2+} results in a dynamic pre-equilibrium, where one DMA placeholder cation on $\{V_{12}\}$ is replaced with one Mg^{2+} ion, resulting in formation of the Vis-photoactive intermediate $\{MgV_{12}\}$. The formation of a 1:1 species was verified by ^{51}V -NMR / 1H -NMR spectroscopy as well as HR-ESI-MS studies. Competitive binding studies using DMA and Mg^{2+} show, that this pre-equilibrium is sensitive to the Mg^{2+} / DMA molar ratio, essentially allowing an on/off switching of the metal functionalization.

Visible light-irradiation of $\{MgV_{12}\}$ solutions results in the one-electron photoreduction of the cluster, release of the second DMA placeholder cation, and binding of a second Mg^{2+} metal center, yielding $\{Mg_2V_{12}\}$. The increased visible-light photoactivity is in line with recent literature reports which show that metal-incorporation in POMs leads to a lowering of the HOMO-LUMO gap and thus, increased photactivity.^[137] The photoredox processes at $\{MgV_{12}\}$ only occur in the absence of water and oxygen, indicating possible interference of these species with the light-induced electron transfer to the cluster. Electrochemical studies suggest that DMA is the most likely electron donor based on analysis of the redox potentials of the reagents used. Mechanistic experimental and theoretical studies show the light-dependent nature of the assembly process and emphasize how supramolecular reaction control can be used to trigger or inhibit photoactivity. Finally, initial experiments show that a similar route can be followed to enable $\{V_{12}\}$ functionalization with Ca^{2+} using light-induced cluster assembly. Thus, the principles outlined in this report open new paths for designing multi-stimuli-responsive molecular materials.

3.1.4. Methods

Synthesis of **1**. $(n\text{Bu}_4\text{N})_4[(\text{MgCl})_2\text{V}^{\text{IV}}\text{V}^{\text{V}}\text{V}_{11}\text{O}_{32}\text{Cl}]] \times \text{CH}_3\text{CN} (= (n\text{Bu}_4\text{N})_4\{\text{Mg}_2\text{V}_{12}\})$

The synthesis of **1** was performed in a glovebox under argon atmosphere: in a 25 mL round-bottom flask 0.200 g (0.100 mmol) $(n\text{Bu}_4\text{N})_3(\text{NMe}_2\text{H}_2)_2[\text{V}_{12}\text{O}_{32}\text{Cl}]] \times \text{CH}_3\text{CN}$, 0.056 g (0.200 mmol) $n\text{Bu}_4\text{NCl}$ and 0.0400 g (0.420 mmol) anhydrous MgCl_2 were dissolved in 12 mL water-free, deaerated acetonitrile and stirred at room temperature. After four hours of stirring, the yellow solution was filtered through a glass Pasteur pipette filled with glass wool. Diffusion crystallization with diethyl ether was setup and the samples were exposed to light via the glovebox fluorescent lamps or a broadband LED light source (see Supplementary Figure 34 for emission spectrum of the light source). After two days, dark green crystals of **1** were obtained, filtered, washed twice with acetone and diethyl ether and dried vacuum. Yield: 0.146 g (0.0634 mmol, 63.8% based on V). Characteristic IR bands (in cm^{-1}): 3336; 2961 (C-H stretching, alkane); 2934 (C-H stretching, alkane); 2874 (C-H stretching, alkane); 1659; 1641; 1613; 1482; 1461; 1381; 1422; 1345; 1278; 1251; 1163; 1151; 1107; 1067; 995 (symmetric V = O, terminals Oxygen); 890; 875 (anti-symmetric stretching VO unit); 817; 752 (V-O-V, symmetric); 661 ($\text{V}_3\text{-O}_{\mu 3}$, asymmetric); 593; 412. UV-Vis/NIR spectroscopic maxima ($\{\{\text{Mg}_2\text{V}_{12}\} = 56 \mu\text{M}$ in DMF): $\epsilon_{338} = 11,875 \text{ M}^{-1} \text{ cm}^{-1}$; $\epsilon_{991} = 1,400 \text{ M}^{-1} \text{ cm}^{-1}$. $^1\text{H-NMR}$ (400 MHz, DMSO-d_6): δ (ppm) = 3.44 (s, H_2O); 3.18 (m, 2 H, $n\text{Bu}_4\text{N}^+$); 2.45 (s, unassigned); 2.07 (s, acetonitrile); 1.56 (m, 2 H, $n\text{Bu}_4\text{N}^+$); 1.30 (s, 2 H, $n\text{Bu}_4\text{N}^+$); 0.92 (t, 3 H, $n\text{Bu}_4\text{N}^+$). $^{51}\text{V-NMR}$ (105 MHz, DMSO-d_6): δ (ppm) = - 557.0 (s, 4 V); -578.3 (s, 8 V).

Crystallographic data for 1.

(nBu₄N)₄[Mg₂Cl₃V₁₂O₃₂] x CH₃CN, (M = 2289.15 g/mol): monoclinic, space group P2/c, a = 24.3414(9) Å, b = 16.7474(7) Å, c = 24.4623(9) Å, β = 94.6107(17), V = 9939.9(7) Å³, Z = 4, T = 150 K, ρ_{calc} = 1.530 g/cm³, μ(MoKα) = 1.238 mm⁻¹, 332994 reflections measured, 22031 unique (R_{int} = 0.0771, R_{sigma} = 0.0266), R₁ = 0.0518 (I ≥ 2σ(I)), wR₂ = 0.1449 (all data). CCDC 2240239 contains the supplementary crystallographic data for this paper. These data can be obtained free of charge from The Cambridge Crystallographic Data Centre via www.ccdc.cam.ac.uk/structures.

Solution-phase NMR spectroscopic analyses.

Mechanistic reactivity studies using ¹H- and ⁵¹V-NMR spectroscopy were carried by dissolving the compound under study in the respective solvent. The reactions were performed under the given conditions as stated above and in the Supplementary Information. All solutions were prepared in an argon-filled glovebox unless stated otherwise.

Data availability

The datasets generated during and/or analyzed during the current study are available in the zenodo.org repository and can be retrieved using the following link: <https://doi.org/10.5281/zenodo.8316822>. The crystallographic data reported for 1 (CCDC no 2240239) can be obtained free of charge from The Cambridge Crystallographic Data Centre via www.ccdc.cam.ac.uk/structures.

3.2. Supplementary Information

3.2.1. Instrumentation

Single-crystal X-Ray diffraction (scXRD) was performed on a Bruker D8 Quest single-crystal diffractometer with a PHOTON II detector using Mo-K α radiation (wavelength $\lambda = 0.71073 \text{ \AA}$).

Attenuated total reflectance-Fourier-transform infrared spectroscopy (ATR-FT-IR) was performed on a Bruker Alpha II equipped with an ATR Platinum Diamond unit. The data were recorded with 24 scans at a resolution of 4 cm^{-1} .

UV-Vis/NIR spectroscopy was performed on a V-670 JASCO UV-VIS/NIR Spectrometer. Quartz glass cuvettes ($d = 10.0 \text{ mm}$) were used for all measurements.

NMR spectroscopy: NMR spectra were recorded on a Bruker AVANCE DRX 400 MHz spectrometer (Bruker Biospin GmbH, Rheinstetten, Germany) equipped with 5 mm inverse probe head operating at 400.13 MHz ^1H frequency and 105.51 MHz ^{51}V frequency at ambient temperature. Stimulated echo sequence with bipolar gradient pulses and a longitudinal eddy current delay was used for the ^1H diffusion ordered spectroscopy (DOSY) experiments. The gradient strength was linearly incremented in 16 steps from 2 % to 95 % of the maximum gradient strength. The diffusion time and the gradient pulse length for all samples were 100 ms and 2.8 ms with 2 s recycle delay, respectively. After Fourier transformation and baseline correction, the diffusion dimension of the 2D DOSY spectra was processed using the Topspin 1.3 software package (2007, patchlevel 8, Bruker Biospin GmbH, Rheinstetten, Germany). The diffusion analysis was performed using the Topspin T1/T2 relaxation package.

The ^{51}V Total COrrrelation SpectroscopY (TOCSY) experiment was performed using the mlevph pulse sequence with a MLEV-17 spin-lock pulse of 18 ms duration recording 512 data points in the direct dimension with 512 increments, 32 transients and a recycle delay of 0.1 s. Sweep widths of 50 ppm and an offset of -574 ppm were used in both dimensions. Zero filling to 1024 data points and broadening of 60 Hz was applied before Fourier transformation. The ^1H chemical shift values (δ) are given in part per million (ppm) using residual solvent protons ($\delta\text{H} = 1.94 \text{ ppm}$ for CD_3CN , $\delta\text{H} = 2.50 \text{ ppm}$ for $(\text{CD}_3)_2\text{SO}$). ^{51}V -NMR spectra were referenced to external $\text{VOCl}_3 + 5\% \text{ C}_6\text{D}_6$ at 0 ppm.

High resolution electrospray ionization mass spectrometry (ESI-MS) was carried out in on an Agilent 6545 QTOF-HRAM-MS system in negative ion mode at a drying gas temperature of $T = 180\text{ }^{\circ}\text{C}$.

Thermogravimetric analysis (TGA) was carried out on a NETZSCH TG 209F1 analyzer at a heating rate of 5.0 K min^{-1} in a range between 30 and $700\text{ }^{\circ}\text{C}$ under air in an Al_2O_3 crucible.

Electron paramagnetic resonance (EPR) spectroscopy was performed on a X-band Bruker Magnettech ESR5000 spectrometer at room temperature on a microcrystalline sample of $\{\text{Mg}_2\text{V}_{12}\}$. The solid sample was filled in a glass EPR-tube (diameter 3 mm), the measurement range was 225 to 450 mT with a modulation of 1 mT , a microwave power of 25 mW and a sweep time of 120 s . The SpinCount software option was used to calculate the spin quantity in the sample.

Irradiation setup: a 20 W broadband LED light source from REV Ritter GmbH, model number: ESFL-6620-ST was used. The following parameters are provided by the manufacturer: nominal power: 20 W ; number of LEDs: 28 ; luminous flux 1700 lm ; luminous efficacy 85 lm/W . The following parameters were measured by a cosine corrector: 2D radiometry corrected power: 4.98 W ; optical power: 4.97 W ; photon flux: 0.223 mmol/s . For wavelength-selective irradiations, 405 nm LEDs (Edison, 3.2 V , 500 mA) or 470 nm LEDs (Quadrios, 3.0 V , 20 mA) were used.

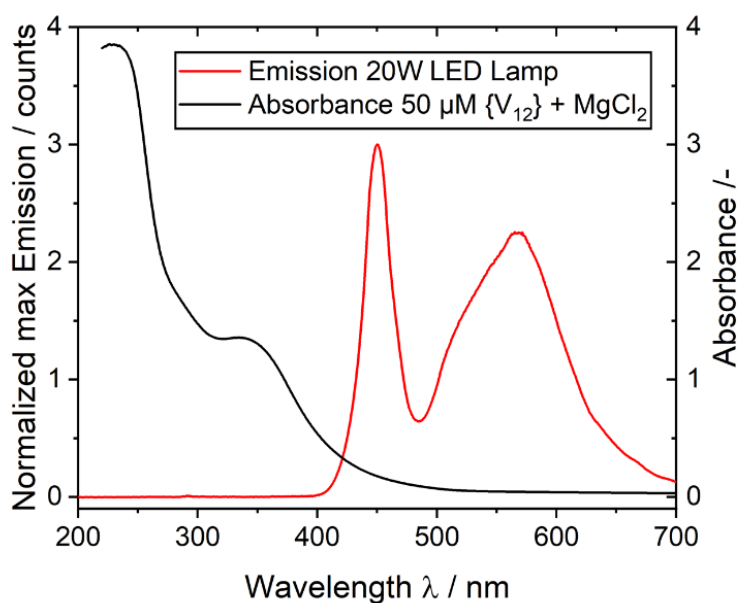


Figure 34: Normalized emission spectrum of the 20 W LED light source, and comparison with the absorbance of the standard $\{\text{V}_{12}\} / \text{MgCl}_2 / \text{MeCN}$ reaction solution.

Solution electrochemistry: DC cyclic voltammetry (CV) experiments were performed on a Pine Research WaveDriver 200 electrochemical workstation equipped with a standard three-electrode arrangement: working electrode: glassy carbon electrode (d = 3.0 mm), quasi reference electrode: Ag wire (in a glass frit containing electrolyte solution), counter electrode: Pt wire. All potentials are quoted relative to the ferrocene/ferrocenium internal standard. All experiments were performed in anhydrous MeCN using nBu₄NPF₆ (0.1 M) as supporting electrolyte. The solutions were purged with desired gas (Ar or O₂) for at least 25 min and kept under a slight positive Ar or O₂ pressure while performing the experiments.

Bond Valence Sum Calculation was performed using the program Visualization for Electronic and Structural Analysis (VESTA),^[138] as outlined in reference ^[139] using the published parameters from the file `bvparm2016.cif` (<https://www.iucr.org/resources/data/datasets/bond-valence-parameters>)

Theoretical calculations: Geometry optimizations of the clusters were carried out using density functional theory calculations with the B3LYP^[133,134] functional combined with the def2-SVP basis set.^[135] Solvation effects were considered using the SMD implicit solvation model (acetonitrile).^[140] UV-Vis absorption spectra were computed at all stable local minima using the B3LYP functional and def2-SVP basis set. Implicit solvation was implemented using C-PCM (acetonitrile).^[141] All calculations were performed using the Gaussian 16 package.^[142]

3.2.2. Experimental section and characterization

All chemicals were purchased from Sigma Aldrich, VWR or Alfa Aesar and were of reagent grade. The chemicals were used without further purification unless stated otherwise. All experiments were performed under inert conditions in the glovebox. All solvents in the glovebox were oxygen and water free. $(n\text{Bu}_4\text{N})_3(\text{NMe}_2\text{H}_2)_2[\text{V}_{12}\text{O}_{32}\text{Cl}] \times \text{CH}_3\text{CN}$ (= **V₁₂**) was synthesized as described in reference.^[8]

Synthesis of Compound 1: $(n\text{Bu}_4\text{N})_4[(\text{MgCl})_2\text{V}^{\text{IV}}\text{V}^{\text{V}}_{11}\text{O}_{32}\text{Cl}] \cdot \text{CH}_3\text{CN}$ (= $(n\text{Bu}_4\text{N})_4\{\text{Mg}_2\text{V}_{12}\}$)

The synthesis of **1** was performed in a glovebox under argon atmosphere: in a 25 mL round-bottom flask 0.200 g (0.100 mmol) $(n\text{Bu}_4\text{N})_3(\text{NMe}_2\text{H}_2)_2[\text{V}_{12}\text{O}_{32}\text{Cl}] \times \text{CH}_3\text{CN}$, 0.056 g (0.200 mmol) $n\text{Bu}_4\text{NCl}$ and 0.0400 g (0.420 mmol) anhydrous MgCl_2 were dissolved in 12 mL water-free, deaerated acetonitrile and stirred at room temperature. After four hours of stirring, the yellow solution was filtered through a glass Pasteur pipette filled with glass wool. Diffusion crystallization with diethyl ether was setup and the samples were exposed to light, either via the glovebox fluorescent lamp or the broadband visible light source described in Supplementary Figure 1. After two days, dark green crystals of **1** were obtained, filtered, washed twice with acetone and diethyl ether and dried under vacuum. Molecular weight: 2289.15 g/mol, yield: 0.146 g (0.064 mmol, 63.8% based on V).

UV-Vis/NIR spectroscopy

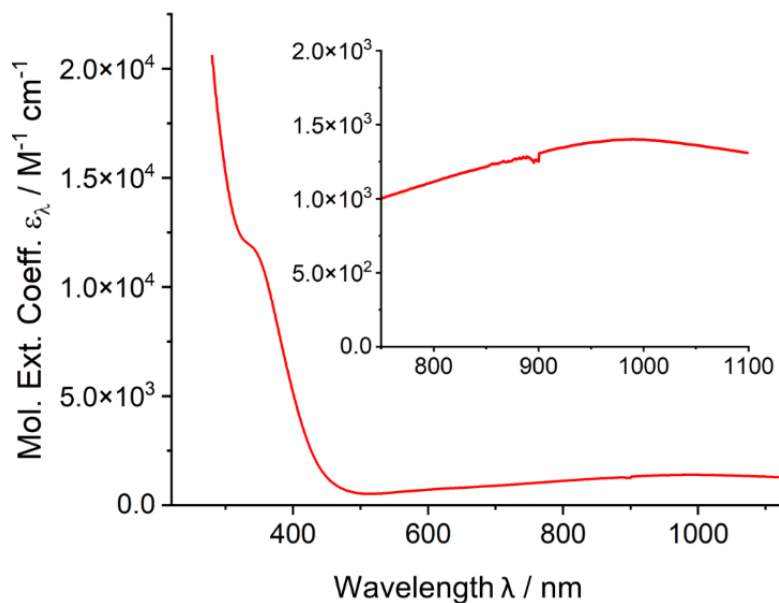


Figure 35: UV-Vis/NIR spectrum of a DMF solution of **1** (56 μM): ϵ_{338} : 11,875 $\text{M}^{-1} \text{cm}^{-1}$; ϵ_{991} : 1,400 $\text{M}^{-1} \text{cm}^{-1}$. Inset: magnified view of the region between 750 nm and 1100 nm, showing the characteristic IVCT transition indicative of the presence of a mixed-valent VIV/V species.

EPR spectroscopy

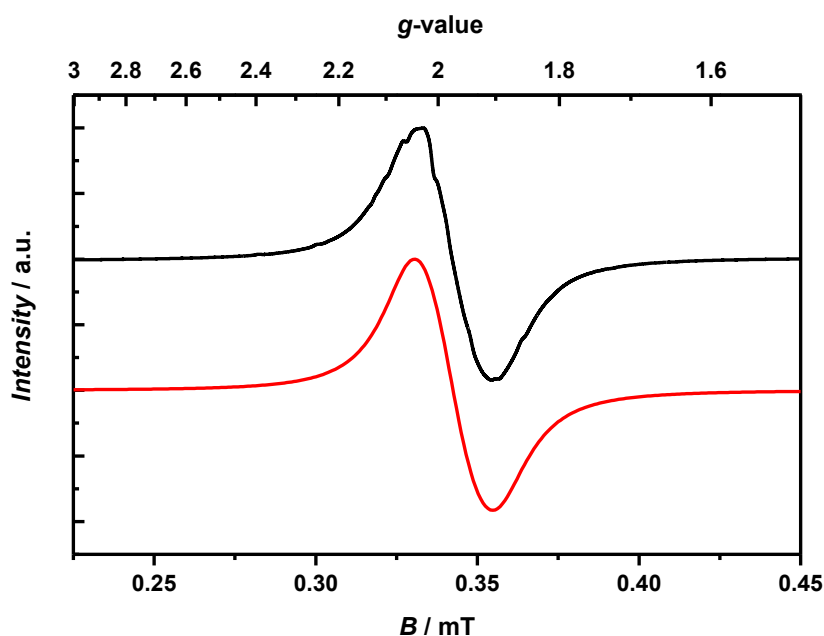


Figure 36: Black: Solid state CW-EPR spectrum of **1** between 225 mT to 450 mT with a modulation of 1mT, a microwave power of 25 mW and a sweep time of 120 s. Red: simulation with $S = \frac{1}{2}$, $g_1 = 1.904(1)$, $g_2 = 1.979(1)$, $g_3 = 2.049(1)$ and isotropic line width = 0.696(5) GHz.

¹H-NMR spectroscopy

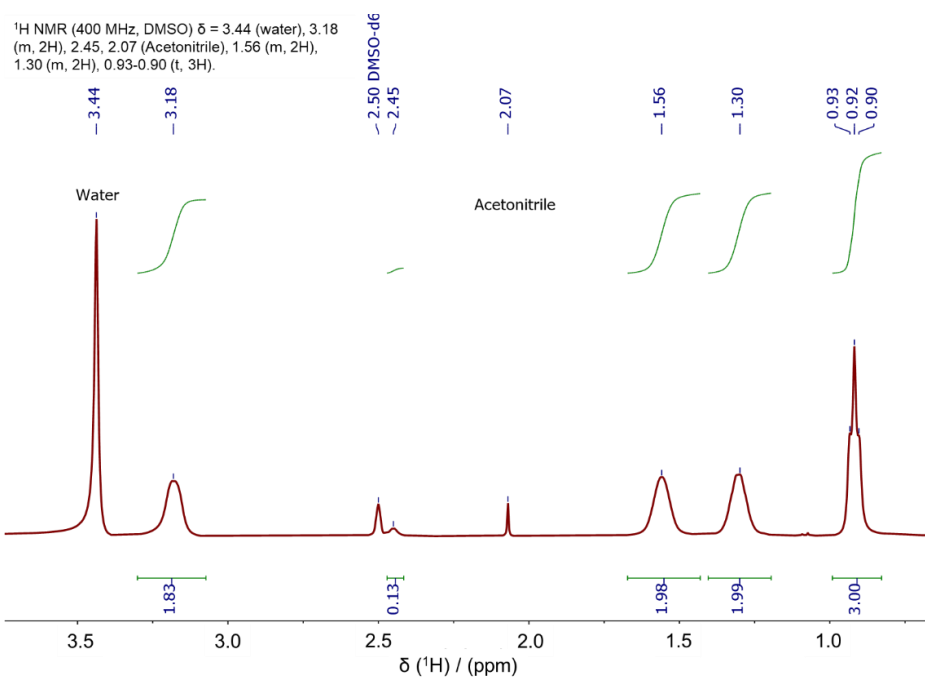


Figure 37: ¹H-NMR spectrum of 1. Conditions: solvent: DMSO-d₆, 400 MHz, 64 scans. Signal assignments: δ (ppm) = 3.44 (s, H₂O); 3.18 (m, 2 H, nBu₄N⁺); 2.45 (impurity); 2.07 (s, acetonitrile); 1.56 (m, 2 H, nBu₄N⁺); 1.30 (s, 2 H, nBu₄N⁺); 0.92 (t, 3 H, nBu₄N⁺)

⁵¹V-NMR spectroscopy

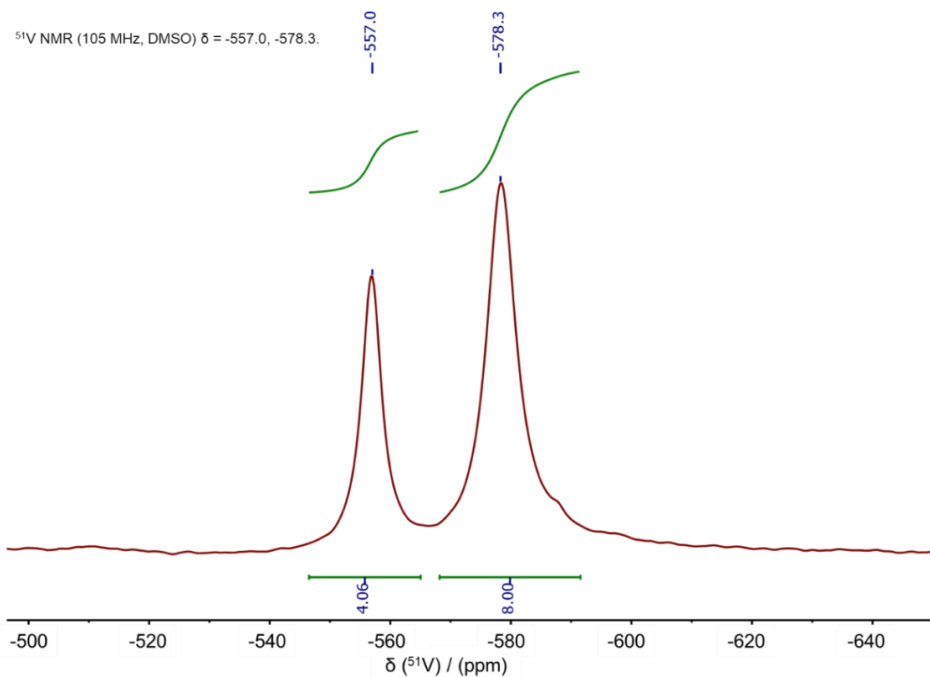


Figure 38: ⁵¹V-NMR spectrum of 1. Conditions: [1] ca. 7.5 mM in DMSO-d₆, 10,000 scans; 105 MHz, δ (ppm) = -557.0 (s, 4V); -578.3 (s, 8V).

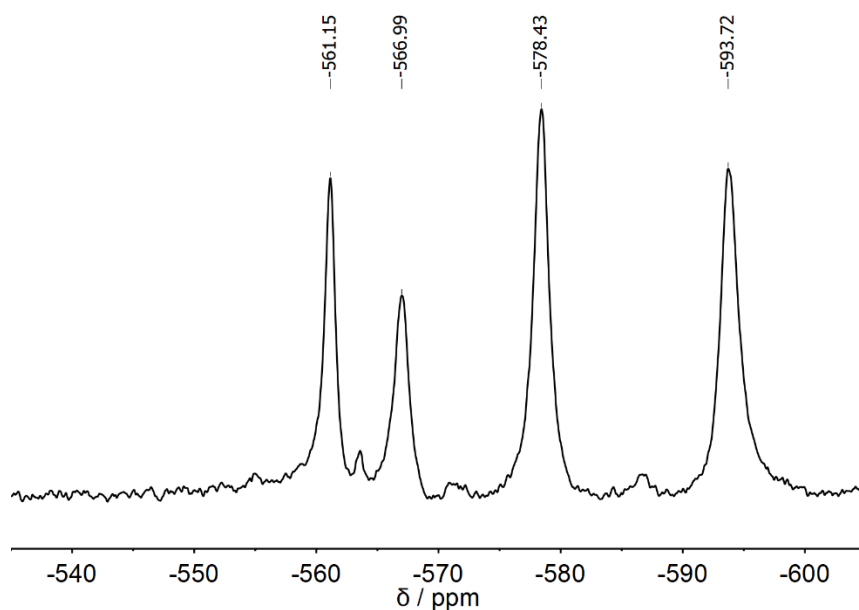


Figure 39: ^{51}V NMR spectrum of 1, $\{\text{Mg}_2\text{V}_{12}\}$ in MeCN, indicating that upon dissolving $\{\text{Mg}_2\text{V}_{12}\}$ in MeCN, one Mg^{2+} is released and $\{\text{MgV}_{12}\}$ is re-formed. Conditions: [1] ca. 5.0 mM in MeCN.

ATR-IR-spectroscopy

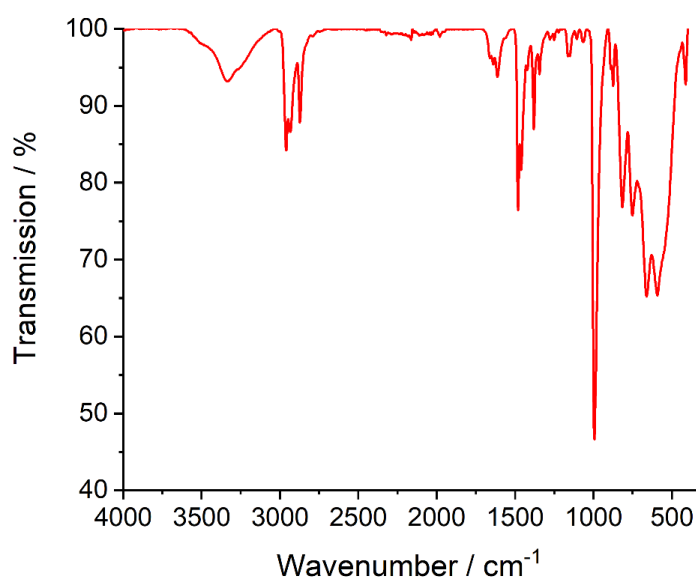


Figure 40: ATR-FT-IR spectrum of compound 1. Characteristic IR bands (in cm^{-1}): 3336; 2961 (C-H stretching, alkane); 2934 (C-H stretching, alkane); 2874 (C-H stretching, alkane); 1659; 1641; 1613; 1482; 1461; 1381; 1422; 1345; 1278; 1251; 1163; 1151; 1107; 1067; 995 (symmetric V=O, terminals Oxygen); 890; 875 (anti-symmetric stretching V-O); 817; 752 (V-O-V, symmetric); 661 ($\text{V}_3\text{-O}_\mu 3$, asymmetric); 593; 412.

Thermogravimetric analysis

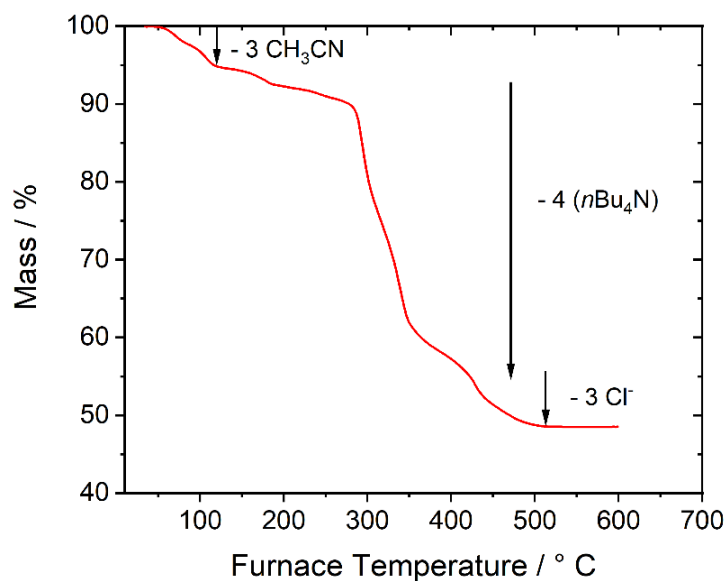


Figure 41: Thermogravimetric analysis (under air) of compound 1. A weight loss of 5.01 wt.-% between 30 °C and 116 °C is shown, which corresponds to the loss of three acetonitrile (calc.: 5.21 wt.-%). A further weight loss of 41.97 wt.-% between 116 °C and 434 °C, corresponds to the loss of four tetra-n-butylammonium cations (calc.: 41.04 wt.-%). The loss of 4.47 wt.-% above 436 °C can be assigned to the loss of the three chlorides (calc.: 4.50 %).

High-resolution ESI mass spectrometry

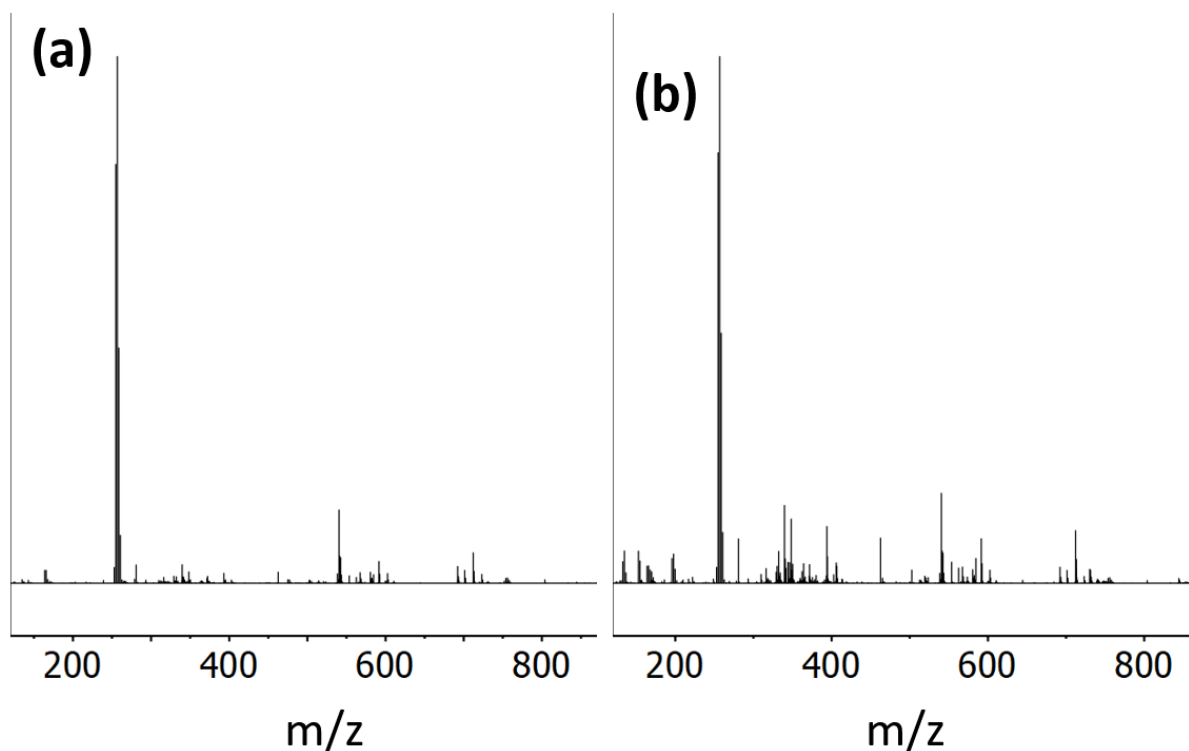


Figure 42: High-resolution negative-ion mode ESI mass spectra of (a) the reference sample, $\{V_{12}\}$ (0.05 mM) dissolved in MeCN; (b) the reaction solution containing $\{V_{12}\}$ (0.05 mM) and $MgCl_2$ (0.21 mM) dissolved in MeCN. Detailed peak assignment, see below.

Table 4: ESI-MS peak assignments for {V₁₂} and the reaction mixture, {V₁₂}+MgCl₂

ESI-MS of reaction mixture ({V₁₂} + MgCl₂ in MeCN)		
observed m/z	calculated m/z	peak assignment
280.785	280.801	[V ₆ O ₁₆] ²⁻
339.746	339.754	[V ₇ O ₁₈ Cl] ²⁻
371.727	371.735	[V ₈ O ₂₁] ²⁻
394.073	394.052	[MgV₁₂O₃₂Cl]³⁻
462.653	462.670	[V ₅ O ₁₃] ⁻
591.590	591.582	[HMgV₁₂O₃₂Cl]²⁻
701.208	701.236	(ⁿ Bu ₄ N)[V ₁₂ O ₃₂ Cl] ²⁻
ESI-MS of reference sample ({V₁₂} in MeCN)		
280.785	280.801	[V ₆ O ₁₆] ²⁻
339.746	339.754	[V ₇ O ₁₈ Cl] ²⁻
371.727	371.735	[V ₈ O ₂₁] ²⁻
462.653	462.670	[V ₅ O ₁₃] ⁻
580.563	580.597	H₃[V₁₂O₃₂Cl]²⁻
701.208	701.236	(ⁿBu₄N)[V₁₂O₃₂Cl]²⁻

Note that the vanadate fragments observed are most likely artefacts due to the ionization / gas phase transfer process and have been observed for the native {V₁₂}^[8] as well as other related POM species previously.^[143]

Crystallographic Details

Suitable single crystals were mounted onto a microloop using Fomblin oil. X-ray diffraction intensity data were measured at 150 K on a Bruker D8 QUEST diffractometer ($\lambda(\text{MoK}\alpha) = 0.71073 \text{ \AA}$) equipped with a graphite monochromator. Structure solution was carried out using SHELX-2013^[144] package through OLEX2.^[145] Corrections for incident and diffracted beam absorption effects were applied using empirical methods.^[146] Structures were solved by a combination of direct methods and difference Fourier syntheses and refined against F2 by the full matrix least-squares technique. Non-hydrogen atoms were refined anisotropically. Hydrogen atoms were added to carbon atoms using a riding model. The metal oxo framework was refined fully anisotropically. The $n\text{Bu}_4\text{N}^+$ counter cations were severely disordered, and restraints (SIMU and DELU) were applied. CCDC 2240239 contains the supplementary crystallographic data for this paper. These data can be obtained free of charge from The Cambridge Crystallographic Data Centre via www.ccdc.cam.ac.uk/structures.

Table 5: Crystallographic Parameters for 1

CCDC Number	2240239
Empirical formula	$(n\text{Bu}_4\text{N})_4[\text{Mg}_2\text{Cl}_3\text{V}_{12}\text{O}_{32}] \cdot \text{CH}_3\text{CN}$
Formula weight	2289.15
Temperature/K	150.0
Crystal system	monoclinic
Space group	P2 ₁ /c
a/Å	24.3414(9)
b/Å	16.7474(7)
c/Å	24.4623(9)
$\alpha/^\circ$	90
$\beta/^\circ$	94.6107(17)
$\gamma/^\circ$	90
Volume/Å ³	9939.9(7)
Z	4
$\rho_{\text{calc}}/\text{g/cm}^3$	1.530
μ/mm^{-1}	1.238
F(000)	4740.0
Radiation	MoK α ($\lambda = 0.71073$)
2 θ range for data collection/ $^\circ$	3.616 to 54.374
Index ranges	$-31 \leq h \leq 31, -21 \leq k \leq 21, -31 \leq l \leq 31$
Reflections collected	332994
Independent reflections	22031 [$R_{\text{int}} = 0.0771, R_{\text{sigma}} = 0.0266$]
Data/restraints/parameters	22031/1591/1098
Goodness-of-fit on F^2	1.104
Final R indexes [$ I > 2\sigma(I)$]	$R_1 = 0.0518, wR_2 = 0.1345$
Final R indexes [all data]	$R_1 = 0.0650, wR_2 = 0.1449$
Largest diff. peak/hole / $e \text{ \AA}^{-3}$	1.58/-0.88

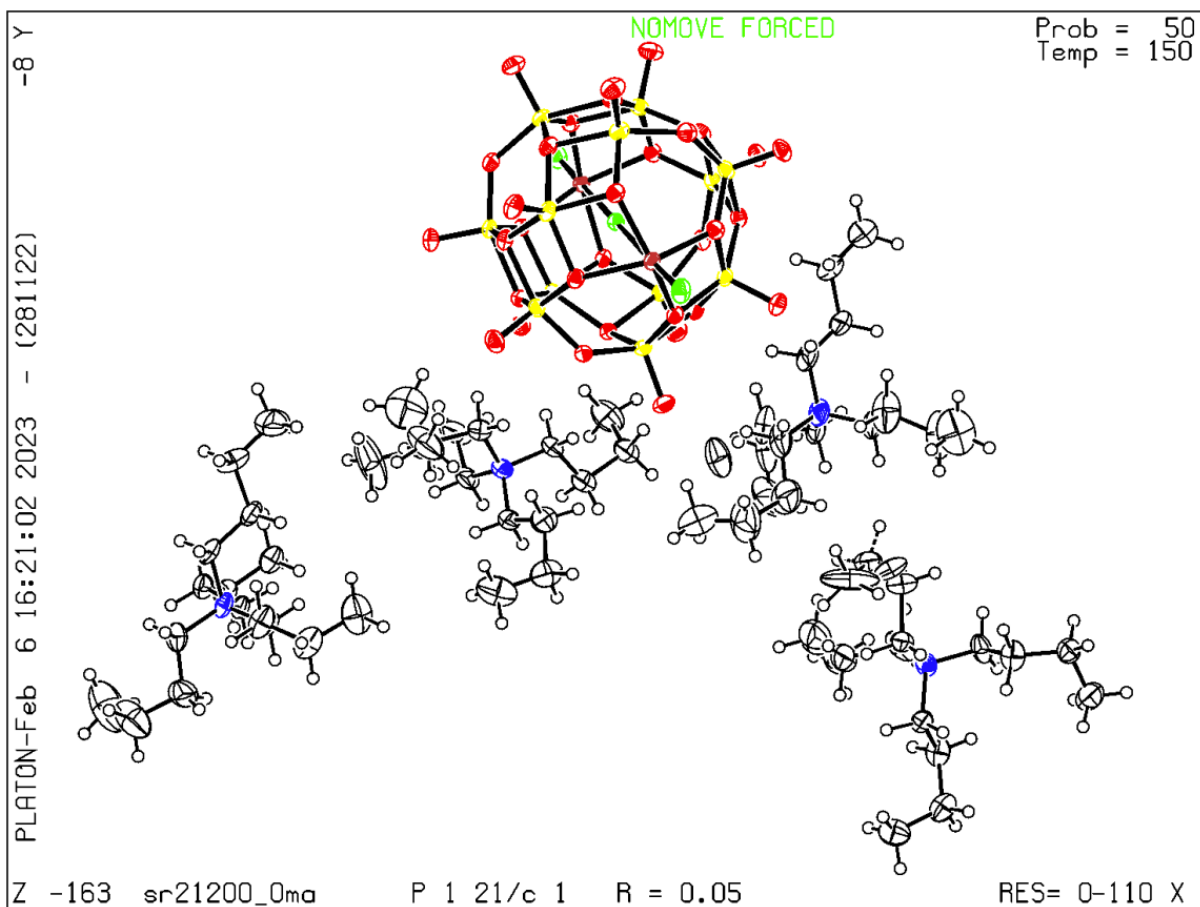


Figure 43: ORTEP illustration of the single-crystal XRD structure of $\{Mg_2V_{12}\}$. Probability ellipsoids drawn at 50 % probability.

Bond Valence Sum (BVS) Calculations

BVS calculations were carried out on the single-crystal XRD structure of 1 using the following equations.

$$S_{ij} = \exp\left(\frac{R_0 - R_{ij}}{B}\right) \quad (2)$$

$$V_i = \sum_j S_{ij} \quad (3)$$

$$G_{ii} = \sqrt{\frac{1}{N} \sum_{i=1}^N (V_i - V_i^0)^2} \quad (4)$$

S_{ij} = bond valence; R_0 = bond valence constant parameter; B = bond valence constant parameter; i = atom; j = neighboring atoms; V_i = formal oxidation state of the atom i ; G_{ii} = global instability index; N = Number of atoms; V_i^0 = Oxidation state of the formal ionic charge.

R_0 (V(V) to O(-II)) = 1.803 Å with $B = 0.37$ were used. $V_i^0 = 5$ was used as formal ionic charge.

The data show that the single reduced V(IV) center is not localized on a specific vanadium ion at $T = 150$ K (i.e., the collection temperature for the single-crystal XRD data which is the basis for the BVS analysis).

Table 6: Bond Valence Sum calculation summary for the vanadium atoms of 1.

Vanadium	V_i	G_{ii}	Vanadium	V_i	G_{ii}
V1	5.041	0.04095	V7	4.791	0.2089
V2	5.100	0.1002	V8	5.029	0.02889
V3	4.986	0.0141	V9	4.885	0.1151
V4	5.060	0.06001	V10	5.110	0.1099
V5	5.051	0.05133	V11	4.922	0.07843
V6	5.073	0.07322	V12	5.061	0.06094

3.2.3. Mechanistic studies

NMR spectroscopy

^1H - and ^{51}V -NMR spectra of a solution of 10.0 mg (5.0 μmol) $\{\text{V}_{12}\}$ in acetonitrile- d_3 (500 μL) were recorded. The same experiments were performed for the identical solution also containing 2.0 mg (21.0 μmol) MgCl_2 . The solution was investigated after storage in the dark and after irradiation (vide infra). All experiments were prepared in a glovebox under argon atmosphere and compared with a $\{\text{V}_{12}\}$ and $\{\text{Mg}_2\text{V}_{12}\}$ references (recorded under ambient conditions). The NMR spectra are shown below.

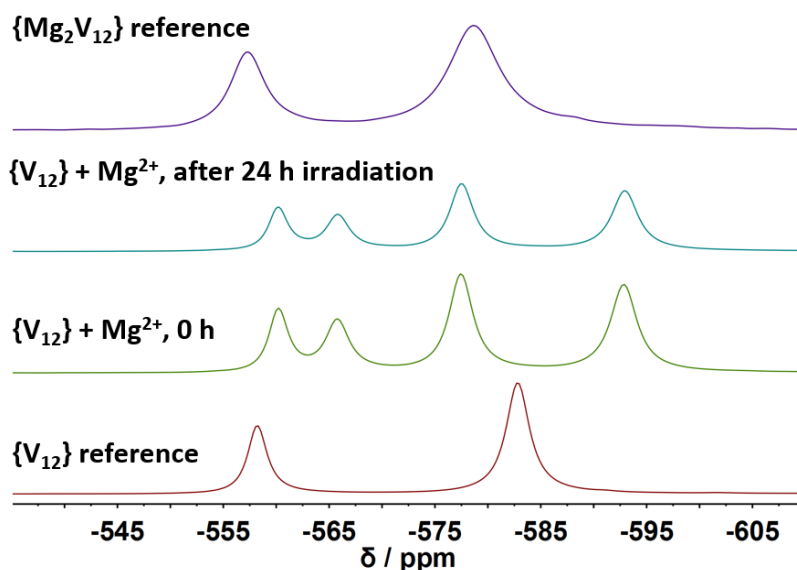


Figure 44: ^{51}V -NMR spectra of $\{\text{V}_{12}\}$ in acetonitrile upon addition of MgCl_2 before and after irradiation for 24 h, in comparison with ^{51}V -NMR spectra of the $\{\text{V}_{12}\}$ (in acetonitrile) and $\{\text{Mg}_2\text{V}_{12}\}$ (in DMSO) reference compounds. Conditions: $[\text{Mg}^{2+}]$ ca. 42 mM, $[\{\text{V}_{12}\}]$ ca. 10 mM.

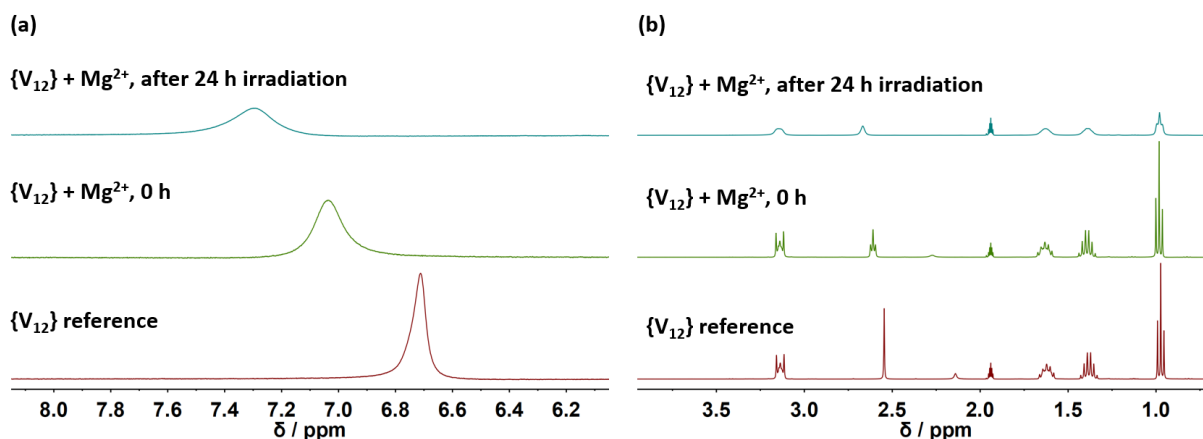


Figure 45: ^1H -NMR spectra ((a) 6 - 8 ppm region, (b) 1 - 3.5 ppm region) of pure $\{\text{V}_{12}\}$ (red) as well as a mixture of $\{\text{V}_{12}\}$ (10 mM) and MgCl_2 (42 mM) in CD_3CN immediately after preparation (green), and after 24 h irradiation using a 20 W broadband LED light source (blue). The characteristic low-field shift of the DMA N-H protons upon MgCl_2 addition shown in (a) indicate the release of one DMA upon formation of $\{\text{MgV}_{12}\}$ and release of another DMA cation upon light-induced formation of $\{\text{Mg}_2\text{V}_{12}\}$, see main manuscript, Fig. 4 for a schematic illustration of the processes.

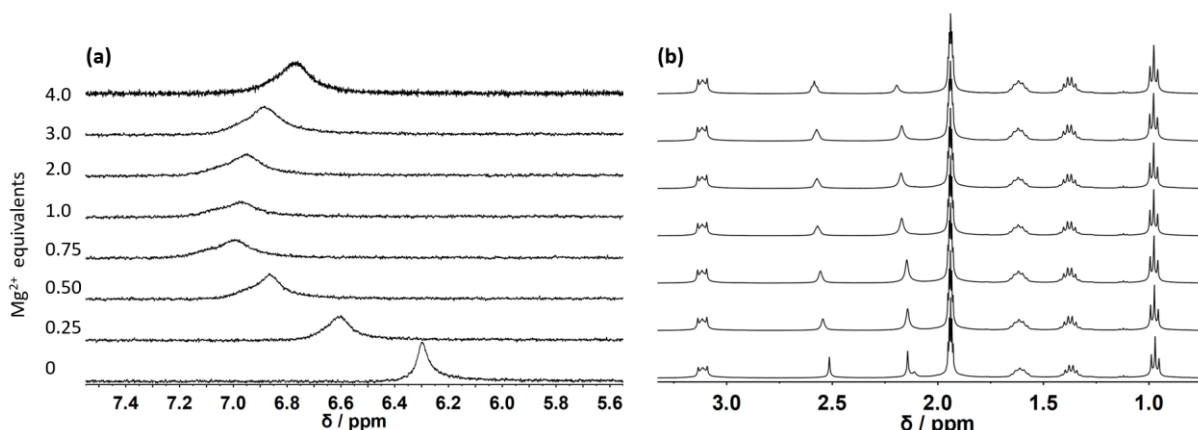


Figure 46: Stacked ^1H -NMR spectra ((a) 5.6 – 7.5 ppm region, (b) 0.9 – 3.3 ppm region) of acetonitrile solutions containing $\{\text{V}_{12}\}$ and varying Mg^{2+} molar equivalents (between 0 eq. to 4 eq. relative to $\{\text{V}_{12}\}$). Upon Mg^{2+} addition, characteristic low-field shifts of the N-H protons of the DMA cations are observed ($\delta \sim 6.3$ ppm to $\delta \sim 7.0$ ppm), indicating a dynamic equilibrium between cluster-bound and “free” DMA. Conditions: $[\{\text{V}_{12}\}] = 5.0$ mM, $[\text{Mg}^{2+}] = 0 - 21.1$ mM, solvent = acetonitrile.

Table 7: Summary of the observed ^1H and ^{51}V NMR signals.

Sample:	^1H -NMR chemical shift / ppm	^{51}V -NMR chemical shift / ppm
$\{\text{V}_{12}\}$ (oxygen-free, CD_3CN)	6.71 (s, 1H), 3.16 – 3.12 (m, 8H), 2.55 (s, 5H), 2.14 (water), 1.66 – 1.58 (m, 8H), 1.43 – 1.34 (m, 8H), 0.99 – 0.96 (t, 12H).	-557.7 (s, 4V), -582.4 (s, 8V).
$\{\text{V}_{12}\} + \text{MgCl}_2$ (oxygen-free, dark conditions, CD_3CN)	7.04 (s, 2H), 3.16 – 3.12 (m, 8H), 2.62 – 2.60 (t, 5H), 2.27 (s, 1H), 1.67 – 1.59 (m, 8H), 1.44 – 1.35 (m, 8H), 1.00 – 0.96 (t, 12H).	-364.4, -559.8 (s, 2V), -565.3 (s, 2V), -577.0 (s, 4V), -592.3 (s, 4V).
$\{\text{V}_{12}\} + \text{MgCl}_2$ After visible light irradiation for 24 h (oxygen-free, CD_3CN)	7.29 (s, 2H), 3.15 (m, 8H), 2.67 (s, 5H), 1.63 (m, 8H), 1.40 – 1.38 (m, 8H), 1.00 – 0.96 (t, 12H).	-364.6, -559.8 (s, 2V), -565.4 (s, 2V), -577.1 (s, 4V), -592.4 (s, 4V).
$\{\text{Mg}_2\text{V}_{12}\}$ reference (ambient, DMSO-d_6)	3.44 (s, H_2O); 3.18 (m, 2 H); 2.45 (n/a); 2.07 (s, acetonitrile); 1.56 (m, 2H); 1.30 (s, 2H); 0.92 (t, 3H)	-557.3, -578.8, -949.8

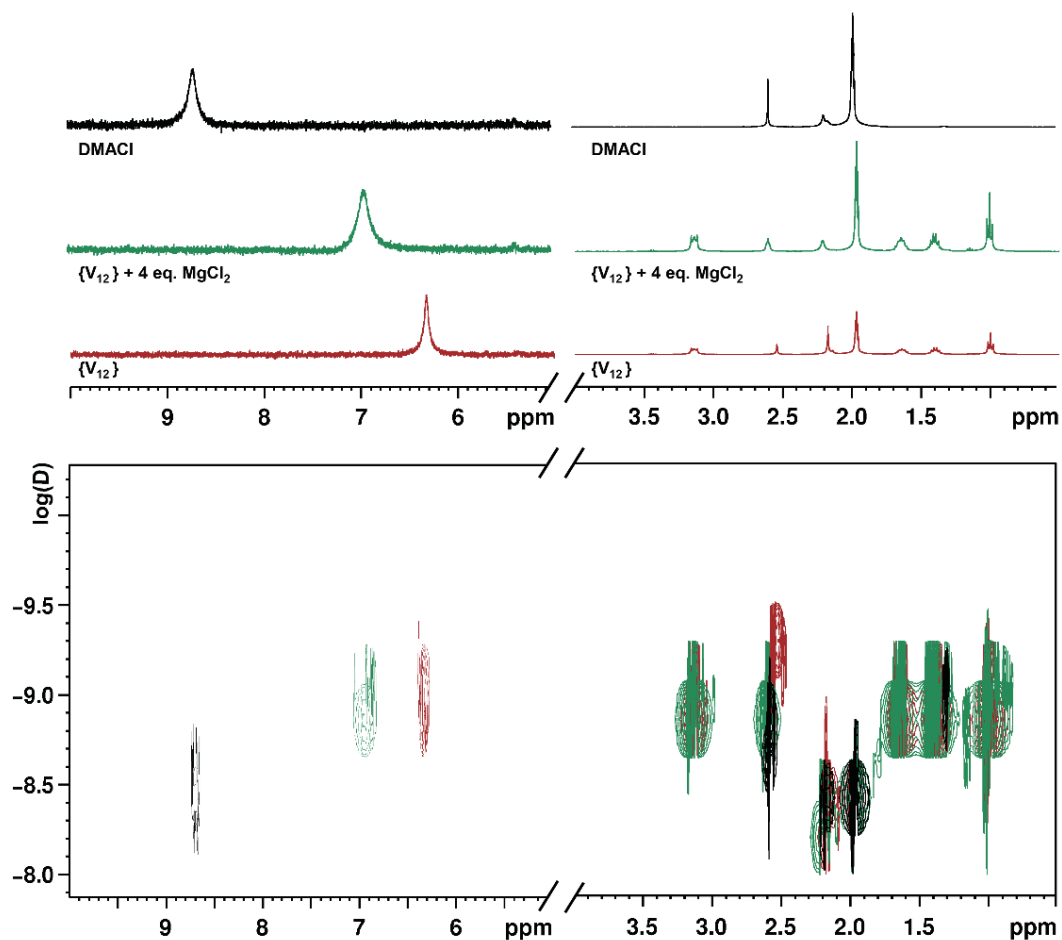


Figure 47: $^1\text{H-NMR}$ spectra of $\{\text{V}_{12}\}$ (red), the $\{\text{V}_{12}\}/\text{Mg}^{2+}$ reaction mixture (green) and pure DMA (black) in CD_3CN . The ammonium resonance for the $\{\text{V}_{12}\}/\text{Mg}^{2+}$ mixture is located between the resonances of the “free” and the cluster-bound DMA, suggesting a Mg^{2+} -concentration-dependent dynamic equilibrium in solution. The DMA ^1H methyl resonance is virtually unaffected in all measurements shown, as the chemical environment for the methyl groups does not significantly change, independent on whether the species is cluster-bound or “free” in solution. Bottom: $^1\text{H-DOSY-NMR}$ spectra of $\{\text{V}_{12}\}$ (red), the $\{\text{V}_{12}\}/\text{Mg}^{2+}$ reaction mixture (green) and pure DMA (black) overlaid. The data show that the diffusion coefficients decrease in the order “free” DMA $<$ $\{\text{MgV}_{12}\}$ $<$ $\{\text{V}_{12}\}$. This is expected, as the $\{\text{MgV}_{12}\}$ reaction solution contains a mixture of cluster-bound and “free” DMA (released during Mg^{2+} binding), so that an averaged signal of the two DMA species is observed. Conditions: solvent: CD_3CN , $[\text{Mg}^{2+}] = 21 \text{ mM}$, $[\{\text{V}_{12}\}] = 5.0 \text{ mM}$, $[\text{DMA}] = 10 \text{ mM}$.

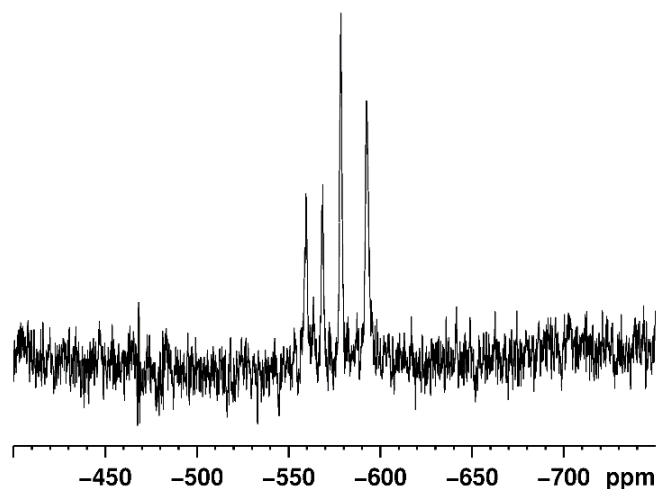


Figure 48: $^{51}\text{V-NMR}$ spectrum of $\{\text{V}_{12}\}$ upon addition of MgCl_2 at HR-ESI-MS concentrations. Conditions: solvent: CH_3CN , $[\text{Mg}^{2+}] = 0.21 \text{ mM}$, $[\{\text{V}_{12}\}] = 0.05 \text{ mM}$.

UV-Vis/NIR spectroscopy

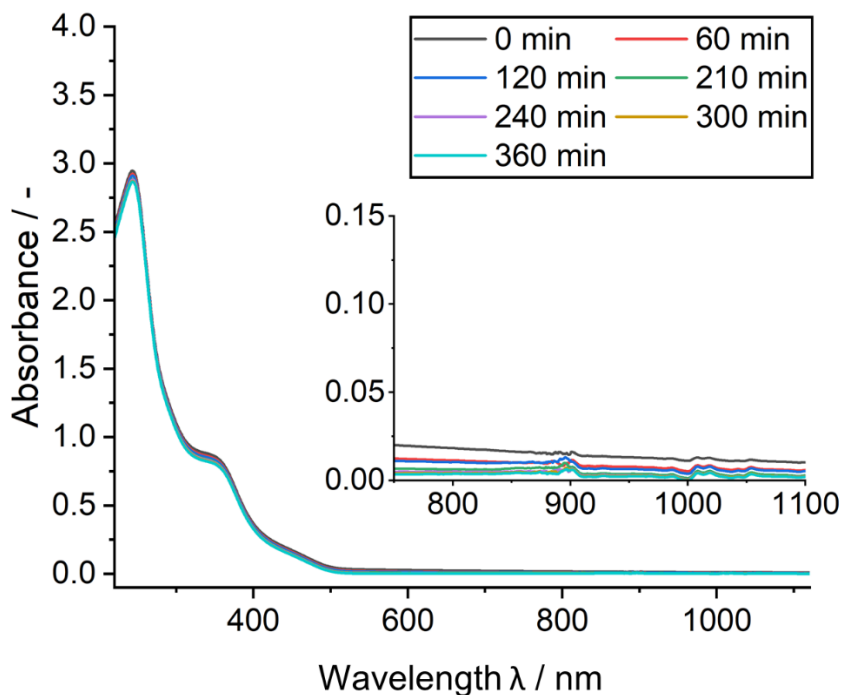


Figure 49: Time-lapse UV-Vis spectra of $\{V_{12}\}$ when irradiated with a broadband high-power LED light source ($P_{\text{nominal}} = 20$ W). Conditions: solvent: acetonitrile, $[\{V_{12}\}] = 50 \mu\text{M}$, Ar atmosphere. Note that no reduction (indicated by the characteristic IVCT transitions between 600 nm – 1100 nm) of $\{V_{12}\}$ is observed.

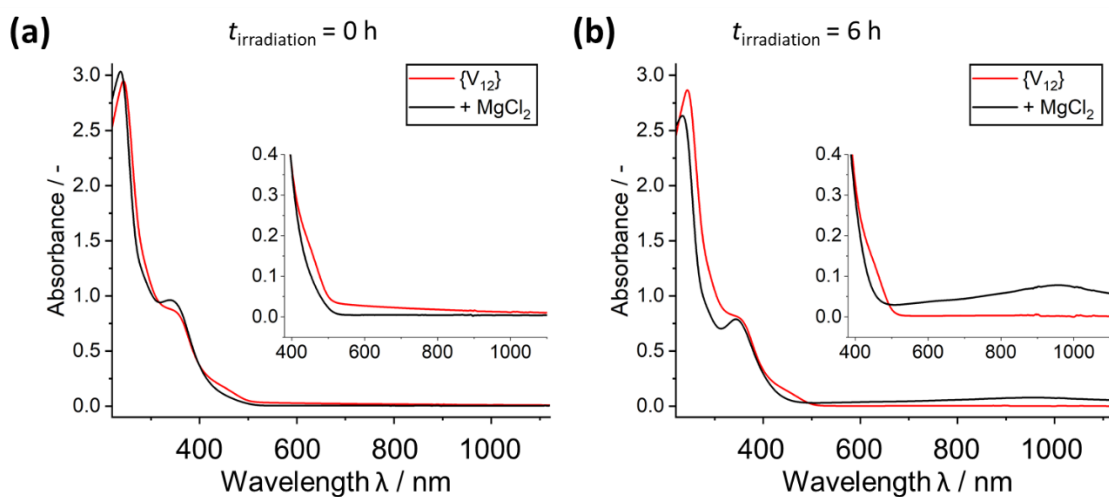


Figure 50: UV-Vis/NIR spectra of $\{V_{12}\}$ in the absence (black) and presence (red) of Mg^{2+} . (a) showing the reaction mixture before irradiation, indicating the in-situ formation of $\{\text{Mg}V_{12}\}$ (characteristic changes between 300 nm to 500 nm). (b) after 6 h irradiation, showing the formation of the 1-electron-reduced $\{\text{Mg}2V_{12}\}$ (by the characteristic IVCT transitions between 700 nm – 1100 nm). Conditions: solvent: acetonitrile, $[\{V_{12}\}] = 50 \mu\text{M}$, $[\text{MgCl}_2] = 211 \mu\text{M}$, Ar atmosphere.

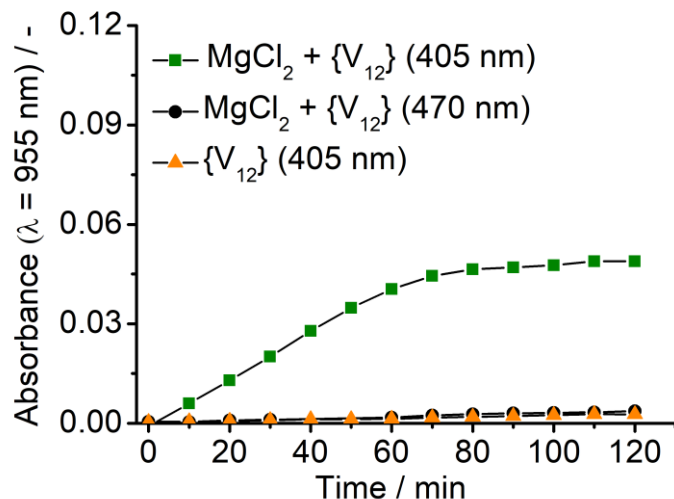


Figure 51: UV-Vis spectroscopic analysis of changes of the IVCT absorption band (detected at $\lambda = 955$ nm) when the $\text{Mg}^{2+} / \{\text{V}_{12}\}$ reaction mixture or the $\{\text{V}_{12}\}$ reference is irradiated with monochromatic LEDs (405 nm or 470 nm). Conditions: solvent: acetonitrile, $[\{\text{V}_{12}\}] = 0.05$ mM, $[\text{Mg}] = 0.21$ mM.

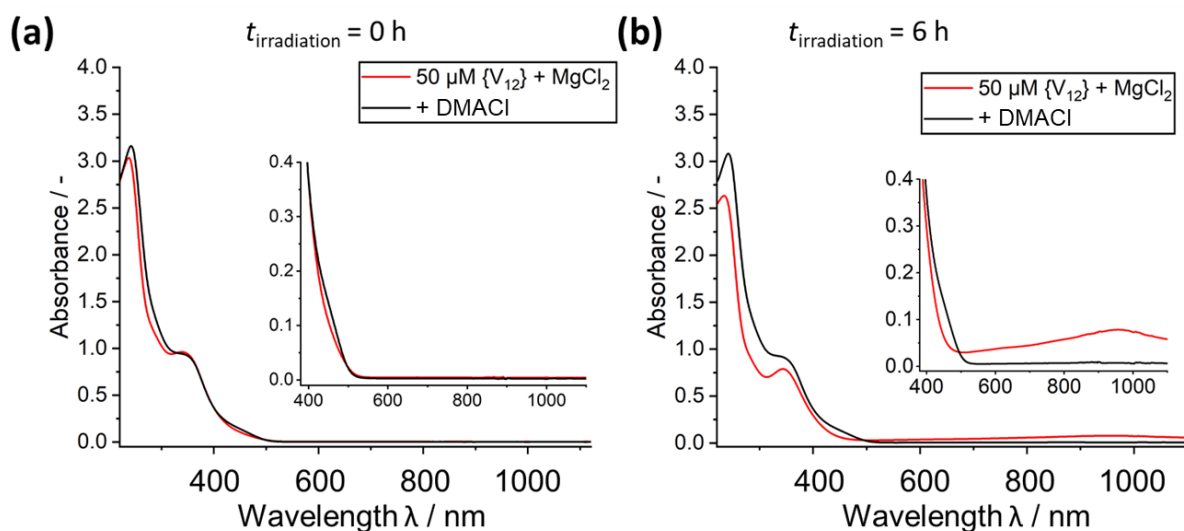


Figure 52: UV-Vis/NIR spectra of the $\{\text{V}_{12}\} + \text{MgCl}_2$ reaction mixture in the presence and absence of DMACl. (a) before irradiation; (b) after 6 h irradiation with a broadband high-power LED light source ($P_{\text{nominal}} = 20$ W). In the presence of DMACl, no reduced vanadate species are formed (indicated by the absence of the characteristic IVCT band). We propose that this indicates the presence of an excess of DMA cations affects the $\{\text{V}_{12}\} / \{\text{MgV}_{12}\}$ equilibrium, prevents the formation of the photoactive $\{\text{MgV}_{12}\}$ and can therefore be used as a supramolecular control parameter to trigger or prevent vanadate photoreduction. Conditions: solvent: acetonitrile, $[\{\text{V}_{12}\}] = 50 \mu\text{M}$, $[\text{MgCl}_2] = 211 \mu\text{M}$, Ar atmosphere.

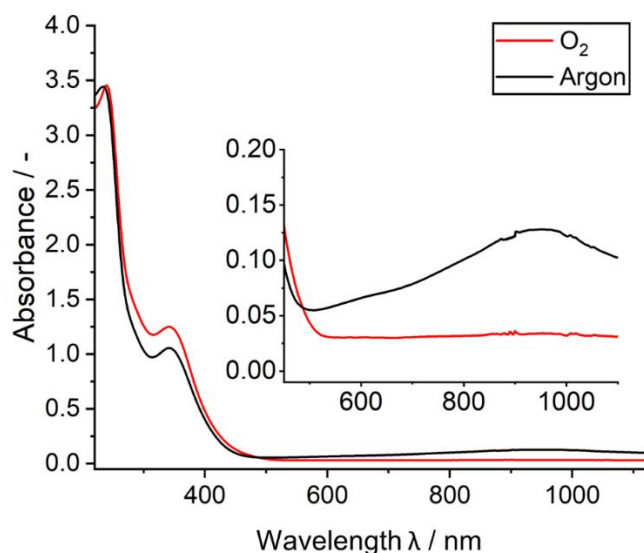


Figure 53: UV-Vis spectrum comparison of $\{V_{12}\} + MgCl_2$ when irradiated with a broadband high-power LED light source ($P_{nominal} = 20\text{ W}$) after 6 hours. Conditions: solvent: acetonitrile, $[\{V_{12}\}] = 50\ \mu\text{M}$, $[MgCl_2] = 211\ \mu\text{M}$.

Electrochemistry

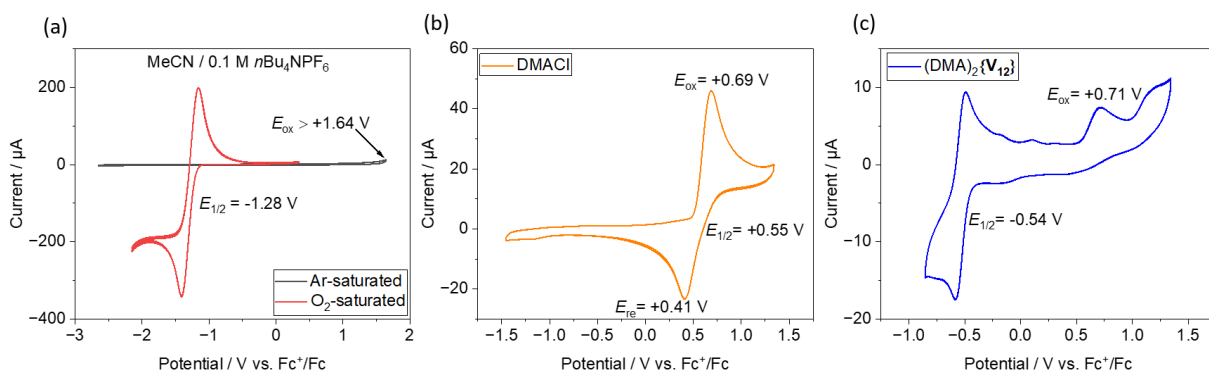


Figure 54: Cyclic voltammetry analysis. (a) CV analysis of the electrolyte when purged with Ar or O_2 . (b) CV analysis of DMACI (Ar atmosphere). (c) CV analysis of $(DMA)_2\{V_{12}\}$ (Ar atmosphere). Conditions: solvent: anhydrous MeCN containing $0.1\text{ M } nBu_4NPF_6$; $[DMACI] = 2\text{ mM}$, $[(DMA)_2\{V_{12}\}] = 1\text{ mM}$; samples referenced against Fc^+/Fc as internal standard. Scan rate: 100 mV/s .

Mg²⁺ replacement with Ca²⁺

To understand whether the observed reactivity between Mg²⁺ and {V₁₂} is unique for Mg²⁺ or can be transferred to other metal cations, identical experiments for metal-functionalization of {V₁₂} were performed using CaCl₂ x 2 H₂O instead of MgCl₂. The samples were then irradiated, and the reactions were followed by ⁵¹V-NMR and UV-Vis/NIR spectroscopy. In sum, ⁵¹V-NMR spectrum show the characteristic four-line signal pattern indicating formation of {CaV₁₂} upon Ca²⁺ addition to {V₁₂}. Irradiation of the reaction solution containing this species with visible light results in the formation of the IVCT band (between ~600-1100 nm) as observed also for the formation of {Mg₂V₁₂}, see details in main manuscript. The experimental data are shown below.

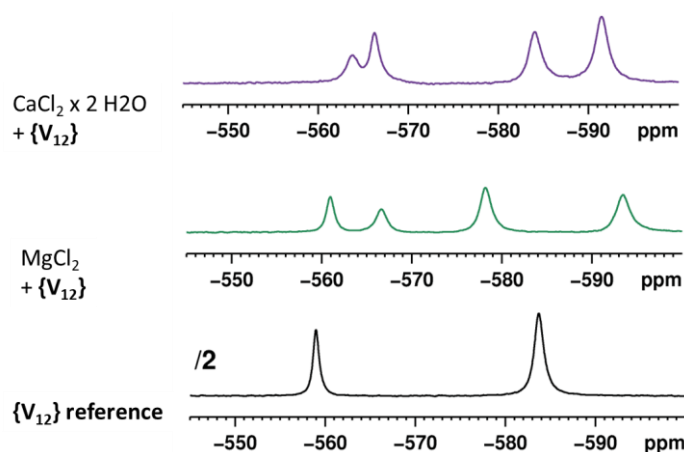


Figure 55: ⁵¹V-NMR spectra of {V₁₂} upon addition of MgCl₂ and upon addition of CaCl₂ x 2 H₂O under otherwise identical reaction conditions. In both cases, the characteristic four-line signal indicating the formation of the mono-metal-functionalized species (i.e., {MgV₁₂} or {CaV₁₂}) is observed. Conditions: [Mg²⁺] ca. 21 mM, [Ca²⁺] ca. 21 mM, [{V₁₂}] ca. 5.0 mM, solvent: CH₃CN.

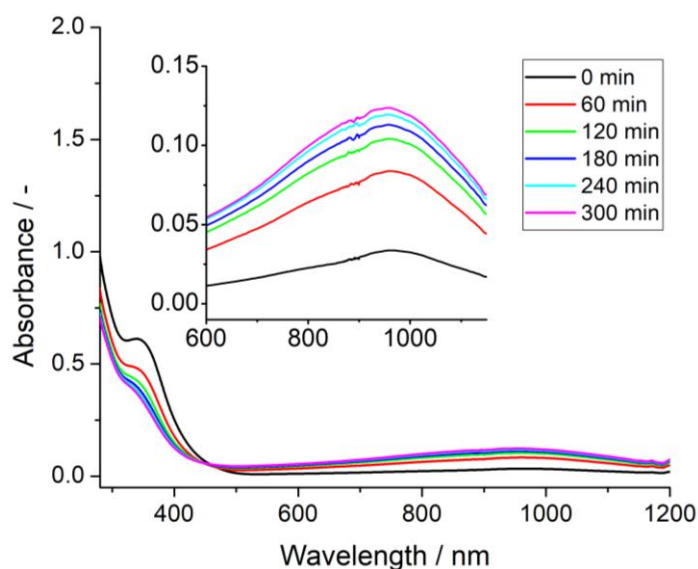


Figure 56: UV-Vis/NIR spectra showing the formation of the characteristic IVCT band indicative of formation of a reduced vanadate cluster upon irradiation of a DMF solution containing Ca²⁺ and {V₁₂}. Conditions: [Ca²⁺] ca. 0.21 mM, [{V₁₂}] ca. 0.05 mM, solvent: DMF.

3.2.4. Theoretical calculations

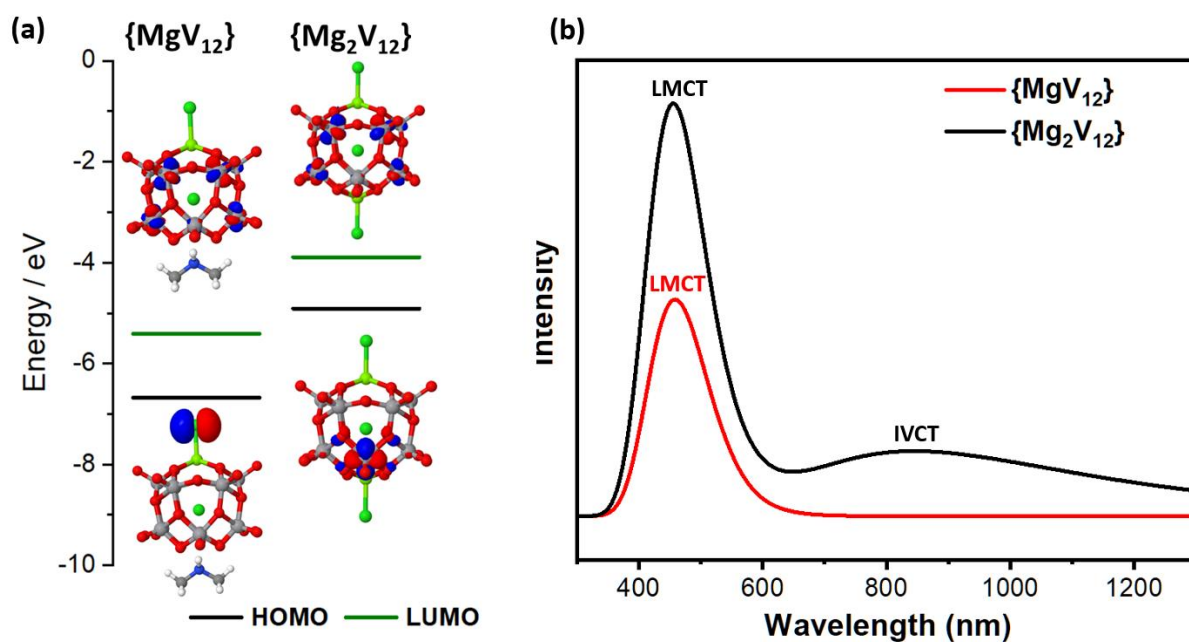


Figure 57: Left: Calculated HOMO-LUMO levels of $\{\text{MgV}_{12}\}$ and $\{\text{Mg}_2\text{V}_{12}\}$. Right: Calculated UV-Vis/NIR spectra for $\{\text{MgV}_{12}\}$ and $\{\text{Mg}_2\text{V}_{12}\}$.

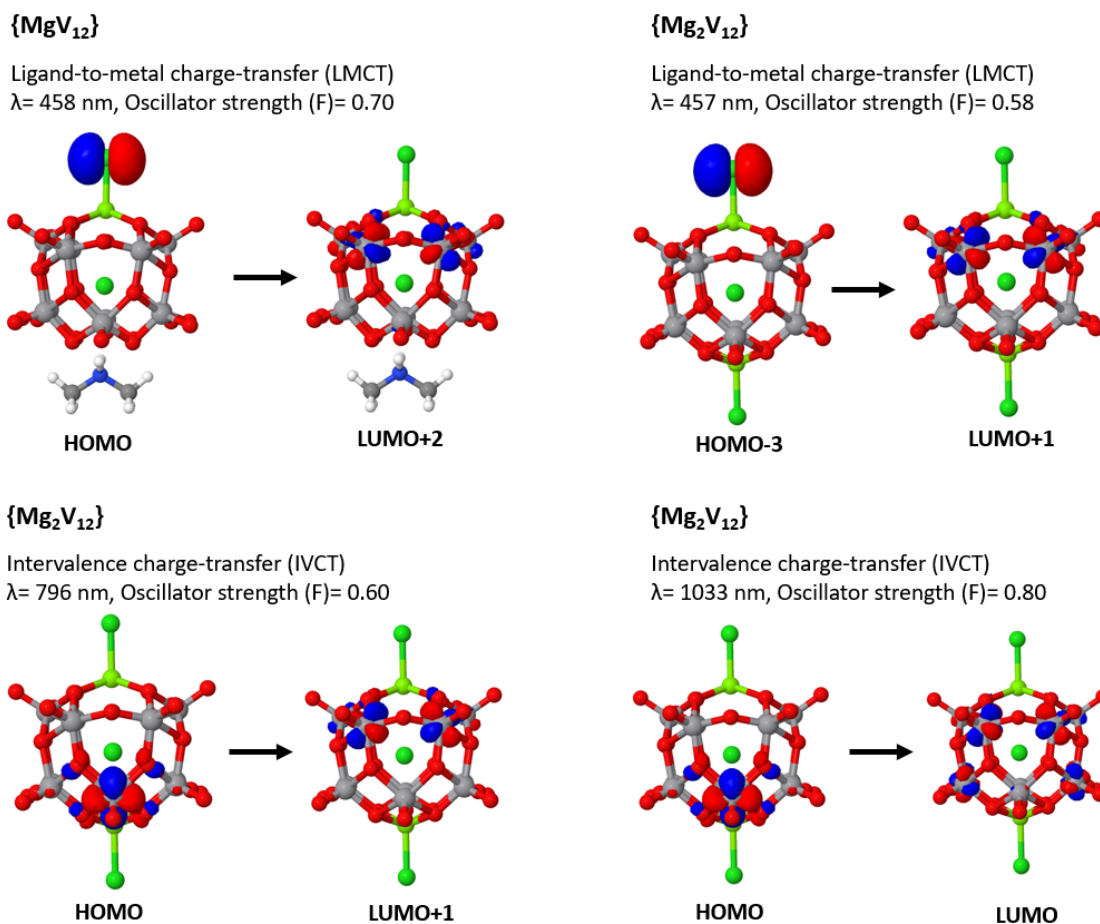


Figure 58: Top: orbital illustrations for the calculated high oscillator-strength LMCT transitions in $\{\text{MgV}_{12}\}$ and $\{\text{Mg}_2\text{V}_{12}\}$. Bottom: orbital illustrations for the calculated high oscillator-strength IVCT transitions in $\{\text{Mg}_2\text{V}_{12}\}$.

Acknowledgements

Financial support by the Deutsche Forschungsgemeinschaft DFG, project no 390874152 (S.R., C.S.), 389183496 (C.S.), 404530119 (C.S.), 510966757 (D.G.) and the ERC Consolidator Grant “SupraVox”, rant no: 101002212 (C.S.) is gratefully acknowledged. C.S. gratefully acknowledges the Gutenberg Research College Mainz and the Top-Level Research Area SusInnoScience for financial support. M.Sc. D. Kowalcyk and Prof. D. Ziegenbalg (Ulm University) are acknowledged for characterization of the emission features of the LED light source. Prof. Sven Rau (Ulm), M.Sc. Ludwig Schwiedrzik (Vienna University) and M.Sc. David Hernández-Castillo are gratefully acknowledged for constructive comments and discussions.

Competing Interests

The authors declare no competing interests.

Author Contributions

S. Repp	Concept, synthesis, characterization, crystallography, spectroscopy and data analysis
M. Remmers	Synthesis and characterization
A. S. J. Rein	Synthesis and characterization
D. Sorsche	Concept, synthesis and characterization
M. Mondeshki	NMR spectroscopy
D. Gao	Electrochemical experiments
M. Anjass	Computational analysis
L.M. Carrella	EPR spectroscopy
E. Rentschler	EPR spectroscopy results discussion
C. Streb	Concept, results discussion

All authors co-wrote the manuscript.

Modifications for the Dissertation

This chapter is based on an article published under the Creative Commons Attribution 4.0 International License (CC BY 4.0). Minor modifications were made for integration into the dissertation. Specifically, the abstract was removed, and the numbering of figures and references was adjusted accordingly. No other changes were made.

3.3. Synthesis of electrochemically promising novel materials

Preliminary Note: This Chapter is based on the published journal article: M. Remmers, B. Mashtakov, S. Repp, A. S. J. Rein, K. Wang, M. Anjass, Z. Chen, L. M. Carrella, E. Rentschler, C. Streb, *Angew. Chem. Int. Ed.* 2025, 64, e202418864. <https://doi.org/10.1002/anie.202418864> These authors contributed equally: Moritz Remmers, Boris Mashtakov

3.3.1. Introduction

Molecular metal oxides, so-called polyoxometalates (POM) are unique functional molecules which have attracted immense interest due to their tunable structure and reactivity.^[99] POMs have been used in diverse areas of science and technology, ranging from biomedicine and therapeutics^[118,119,147] to molecular electronics,^[107,148] supramolecular assemblies^[149,150] and catalysis.^[113]

One key function of POMs is their ability to reversibly store and release multiple electrons, making them ideal molecular components for energy conversion and storage technologies.^[1,151] In general, each electron added to a POM cluster shifts the reduction potential to more negative values.^[152] The electrochemical potential difference between two reversible one-electron transitions in POMs is commonly in the range of ~0.4 V to 0.6 V (see SI, Section 3.4.2 Electrochemical reference studies). In addition, the maximum overall number of electrons which can be stored per cluster unit is controlled by the cluster type (i.e. the number and type of metal centers present), as well as the electrochemical stabilities of the cluster, the solvent and the supporting electrolyte. For most applications in energy storage (batteries, redox-flow batteries, solar energy storage, etc.), increasing the number of electrons stored is a major development driver.^[153,154]

Inspired by these challenges, ground-breaking works have focused on how to maximize electron storage in POMs. Irle, Yoshikawa, Awaga and co-workers showed that POM integration into lithium ion battery electrodes allows reversible storage of up to 24 electrons on the Keggin polyoxotungstate $[\text{PMo}_{12}\text{O}_{40}]^{n-}$ ($n=3-27$).^[155,156] Pioneering work on the solution redox chemistry of POMs by Symes, Poblet, Nyman and Cronin showed that super-reduced Dawson polyoxotungstates $[\text{P}_2\text{W}_{18}\text{O}_{62}]^{n-}$ ($n=6-$

24) can reversibly store up to 18 electrons per cluster in aqueous media in the presence of charge-balancing Li^+ or H^+ counterions. The system was further developed for electrochemical on-demand hydrogen generation.^[157,158]

Polyoxovanadates (POVs) have recently become a focal point for multi-electron storage due to their unique structural and electronic versatility^[10, 46,159–161] combined with exceptional redox properties.^[1, 67,162] In a series of outstanding reports, Matson and co-workers showed that derivatives of alkoxide-functionalized Lindqvist POVs $[\text{V}_6\text{O}_7(\text{OR})_{12}]$ (R=Me, Et) can undergo multiple (proton-coupled) electron transfers, enabling energy storage in non-aqueous POV-based redox-flow batteries.^[88,163,164] Also, some of us recently showed how metal-functionalization in dodecavanadate derivatives can be used to tune the number and position of redox-transitions.^[30, 73,75] While these studies were primarily focused on energy technologies, it is worth noting that mixed-valent POVs have also received widespread interest from the molecular magnetism and spintronics communities as potential components for data storage systems. When considering the use of POMs in multi-electron storage and transport, one common theme is that these studies typically employ only one POM cluster species at a time. In contrast, the combined use of two or more species to maximize electron storage capacity has not been explored to date. This might be due to challenges related to incompatibilities between species including inter-cluster redox-reactions, divergent chemical stability or solubility ranges.

Here, we propose a concept to overcome these challenges by developing designer electron storage materials where two individual POV clusters are synthesized and selectively crystallized from one common reaction solution. Importantly, cluster formation and redox equilibration are achieved within the reaction solution, thereby ensuring that no chemical incompatibilities arise for the two targeted cluster species. This approach results in a 1 : 1 mixture of two POVs with the formal assembly shown in Figure 59, where the combination of individual redox-processes at both clusters results in up to fourteen redox-transitions in the potential range between -2.15 V to $+1.35$ V (vs Fc^+/Fc). Mechanistic studies rationalize cluster formation, cluster stability and charge-storage mechanism. These insights shed light on how physical and electronic structure interact to give rise to technologically important redox properties.

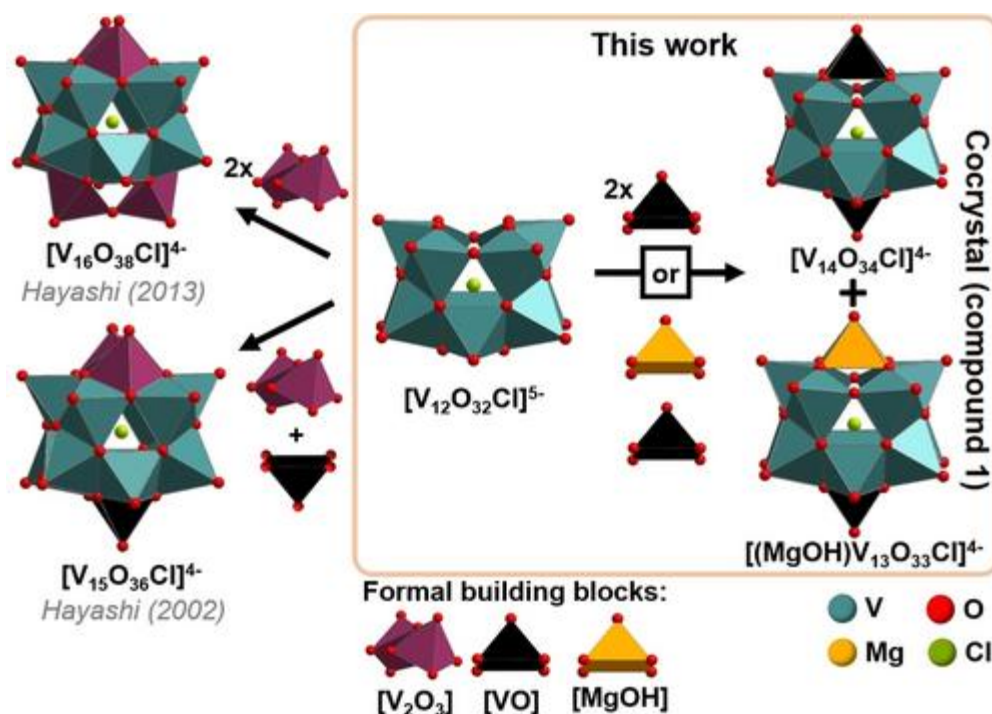


Figure 59: Formal assembly Scheme and structure comparison of the mixed-cluster cocrystal **1**, compared with structurally related literature-known single-cluster species $(nBu_4)_4[V_{16}O_{38}Cl]$ and $(nBu_4)_4[V_{15}O_{36}Cl]$.^[71,72] Note that synthetically, **1** is obtained using $[V_{10}O_{26}]^{4-}$ as vanadate precursor.

3.3.2. Results and Discussion

To develop the mixed-cluster system, we built on previous studies by some of us, where we explored the mono- or di-metal-functionalization of the dodecavanadate cluster $(NMe_2H_2)_2[V_{12}O_{32}Cl]^{3-}$ ($=\{V_{12}\}$).^[8,9, 28, 75,165] Here, we demonstrate how under non-aqueous synthesis conditions, simultaneous formation and redox equilibration of two closely related $\{V_{12}\}$ derivatives was achieved, This gave access to mixed co-crystals showing reversible multi-electron uptake and release.

The title compound **1** was synthesized by reaction of the mixed-valent precursor $(nBu_4N)_4[V^{IV}_2V^V_8O_{26}]$ ($= (nBu_4N)_4\{V_{10}\}_{red}$)^[166,167] with the magnesium and chloride source $MgCl_2$ (anhydrous) in acetonitrile at 75 °C. Diffusion of diethyl ether into the green reaction solution gave deep green crystals of **1** suitable for single-crystal X-ray diffraction (yield: 70 % based on V). The composition and purity of the compound were confirmed by ATR-IR- UV-Vis/NIR and EPR spectroscopies, high-resolution electrospray ionization mass spectrometry (ESI-MS), thermogravimetric analysis (TGA) and single-crystal X-ray diffraction, for details see Supporting Information.

Single-crystal X-ray diffraction analysis showed that **1** crystallizes in the monoclinic space group C_2 with cell axes $a=23.189(4)$ Å, $b=23.197(4)$ Å, $c=17.660(3)$ Å and angles $\alpha=\gamma=90^\circ$, $\beta=90.089(6)$, crystallographic details see SI Section 3.4.2 Crystallographic Information.

Structural analysis of the crystallographic data reveal that **1** is composed of a 1 : 1 mixture of two $\{V_{12}\}$ derivatives, that is the mixed magnesium and vanadium/functionalized species $[(MgOH)V_{13}O_{33}Cl]^{4-}$ ($=\{MgV_{13}\}$) and the di-vanadium-functionalized species $[V_{14}O_{34}Cl]^{4-}$ ($=\{V_{14}\}$). Note that to the best of our knowledge, both clusters, $\{MgV_{13}\}$ and $\{V_{14}\}$ have not been reported previously. For charge-balance, each unit cell contains two cluster units and eight nBu_4N^+ cations. The amount of nBu_4N^+ cations in the bulk was verified by CHN elemental analysis and TGA (see SI, Section 3.4.2). The $\{V_{14}\} : \{MgV_{13}\}$ molar ratio in the bulk of **1** was analyzed by inductively coupled plasma optical emission spectroscopy (ICP-OES), which gave a Mg : V atomic ratio of 1.17 : 27 (calculated: 1.0 : 27.0 for a 1 : 1 molar ratio of $\{MgV_{13}\}$ and $\{V_{14}\}$). The presence of the Mg–OH group in **1** was substantiated by ATR-IR spectroscopy, where a weak, characteristic signal was detected at 3460 cm^{-1} (Figure 60a).^[168] The presence of both cluster species, $\{MgV_{13}\}$ and $\{V_{14}\}$, was also observed by negative-ion mode high-resolution electrospray ionization mass spectrometry (ESI-MS), see Figure 60c, d. For example, the $\{MgV_{13}\}$ -related species $(nBu_4N)[HMgV_{12}O_{32}Cl]^-$ was observed at 1667.69 m/z (calcd: 1667.73 m/z), while the $\{V_{14}\}$ species $(nBu_4N)[V_{14}O_{34}Cl]^{2-}$ was observed at 767.15 m/z (calcd: 767.17 m/z)

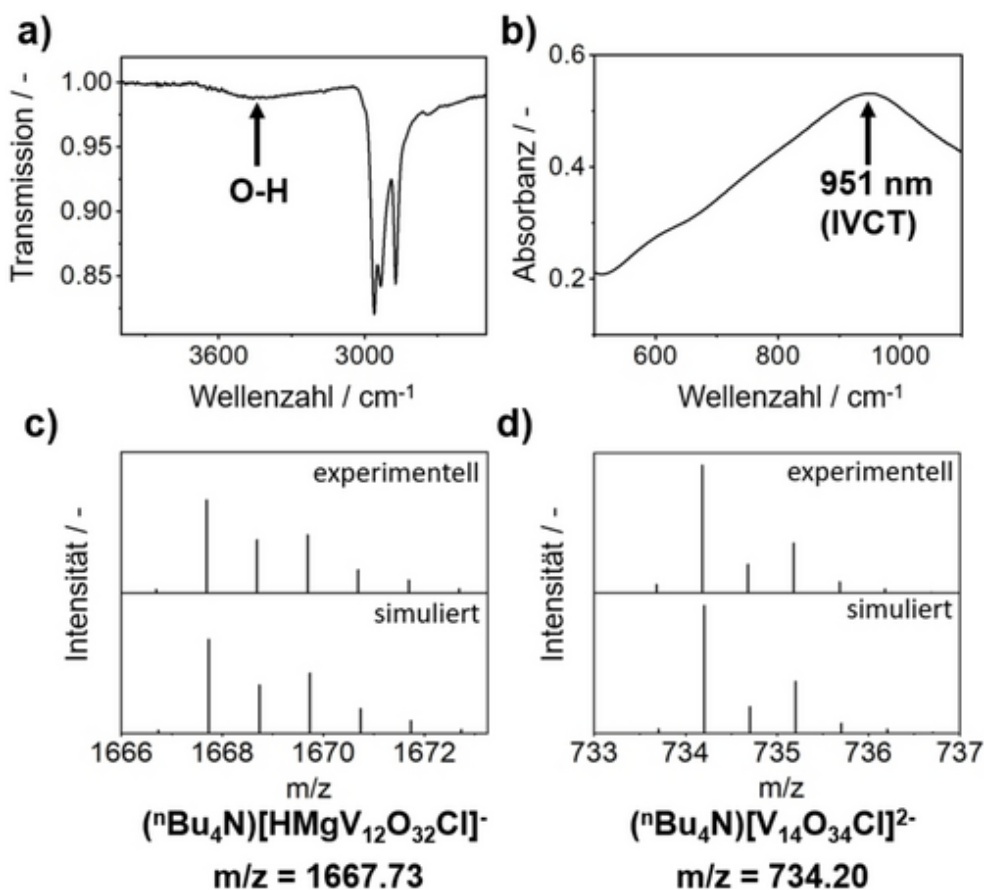


Figure 60: Characterization of **1**. a) ATR-IR spectroscopy showing the presence of O–H vibrations; b) UV-Vis/NIR spectroscopy showing characteristic V(IV/V) intervalence charge-transfer (IVCT) transitions; c), d) simulated and observed isotopic patterns from high resolution ESI-MS analyses, indicating the presence of {MgV₁₃} and {V₁₄}.

In sum, these analyses suggest that **1** can be given as $(n\text{Bu}_4\text{N})_8[(\text{MgOH})\text{V}_{13}\text{O}_{33}\text{Cl}][\text{V}_{14}\text{O}_{34}\text{Cl}] = (n\text{Bu}_4\text{N})_8\{\text{MgV}_{13}\}\{\text{V}_{14}\}$.

Based on this initial analysis it can be proposed that each cluster features a fourfold negative charge. This would result in three V^{IV} centers for {MgV₁₃}, and five V^{IV} centers for {V₁₄}, for details on the charge calculations see SI, Section 3.4.2. Since most mixed-valent POMs feature antiferromagnetic coupling,^[148, 160, 169–171] it can be put forward that both, {MgV₁₃} and {V₁₄} feature one unpaired electron. Thus, the presence of unpaired electrons in **1** was probed by EPR spectroscopy (Figure 61). As a reference compound for spin counting, we utilized the mixed-valent precursor $(n\text{Bu}_4\text{N})_4\{\text{V}_{10}\}_{\text{red}}$ ^[166, 167] which features two isolated V^{IV} centers. Note that only the EPR spectrum of the reference compound shows hyperfine coupling, as electron delocalization in **1** results in a non-observable hyperfine coupling.^[172] A comparison of the spin count of both compounds at the same concentration and same sample volume, gave 1.87 unpaired electrons per formula unit of **1**. This is in line with our previous oxidation state and charge assignments which suggested that both {MgV₁₃} and {V₁₄} feature one unpaired

electron each. In addition, UV-Vis/NIR spectroscopy of **1** in MeCN also supported the presence of reduced V^{IV} centers as indicated by characteristic intervalence charge transfer (IVCT) transitions in the ~ 500 nm – 1400 nm spectral region (Figure 60b).

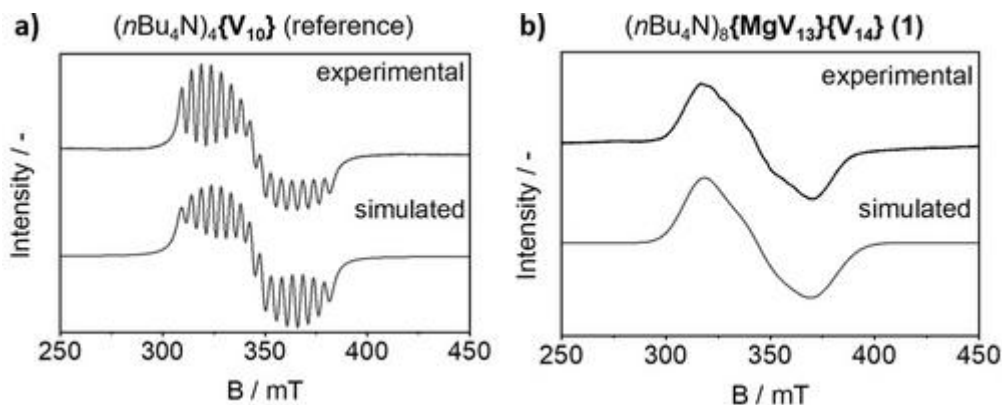


Figure 61: Simulated and experimental EPR spectra ($T=40^\circ\text{C}$) of: a) the reference compound $(n\text{Bu}_4\text{N})_4[\text{V}^{IV}_2\text{V}^V_8\text{O}_{24}]^{16-}$ (3 mM in MeCN); b) compound **1** (3 mM in MeCN). Comparison of the spin counts gave a value of 1.87 unpaired electrons for **1**.

We were interested in the Mg^{2+} -induced conversion of the mixed-valent $\{\text{V}_{10}\}_{\text{red}}$ precursor into compound **1**. Note that in the absence of MgCl_2 , no conversion of $\{\text{V}_{10}\}_{\text{red}}$ into **1** occurs. We used UV-Vis/NIR spectroscopy to follow the changes of the characteristic signals of $\{\text{V}_{10}\}_{\text{red}}$ (at $\lambda=500$ nm) and **1** (at $\lambda=1000$ nm), see Figure 62a. We hypothesized that the reaction might be initiated by reaction of Mg^{2+} with $\{\text{V}_{10}\}_{\text{red}}$, possibly by a Lewis-acid mechanism. Thus, we investigated the impact of $\{\text{V}_{10}\}_{\text{red}}/\text{Mg}^{2+}$ molar ratios on the conversion rate by a series of $[\text{Mg}^{2+}]$ -dependent analyses. As shown in Figure 62, between 0–1 molar equivalents of Mg^{2+} (relative to $\{\text{V}_{10}\}_{\text{red}}$), increasing Mg^{2+} concentrations result in equilibria with decreasing $\{\text{V}_{10}\}_{\text{red}}$ concentration (Figure 62b) and increasing concentrations of **1** (Figure 62c). When more than ~ 1 equivalent of Mg^{2+} is added to the reaction solution, the characteristic UV-Vis/NIR spectral signatures of $\{\text{V}_{10}\}_{\text{red}}$ are lost, and no further changes of the characteristic signatures of **1** are observed. These data suggest that the $\{\text{V}_{10}\}_{\text{red}}$ conversion to **1** is driven by the presence of Mg^{2+} . Previous studies have reported similar observations, where Lewis-acidic metals, such as Mg^{2+} ,^[9] Ca^{2+} ,^[30,75] Co^{2+} , Ti^{4+} or Cu^{2+} ^[173] have triggered conversion processes in polyoxovanadates, particularly in organic solvents.

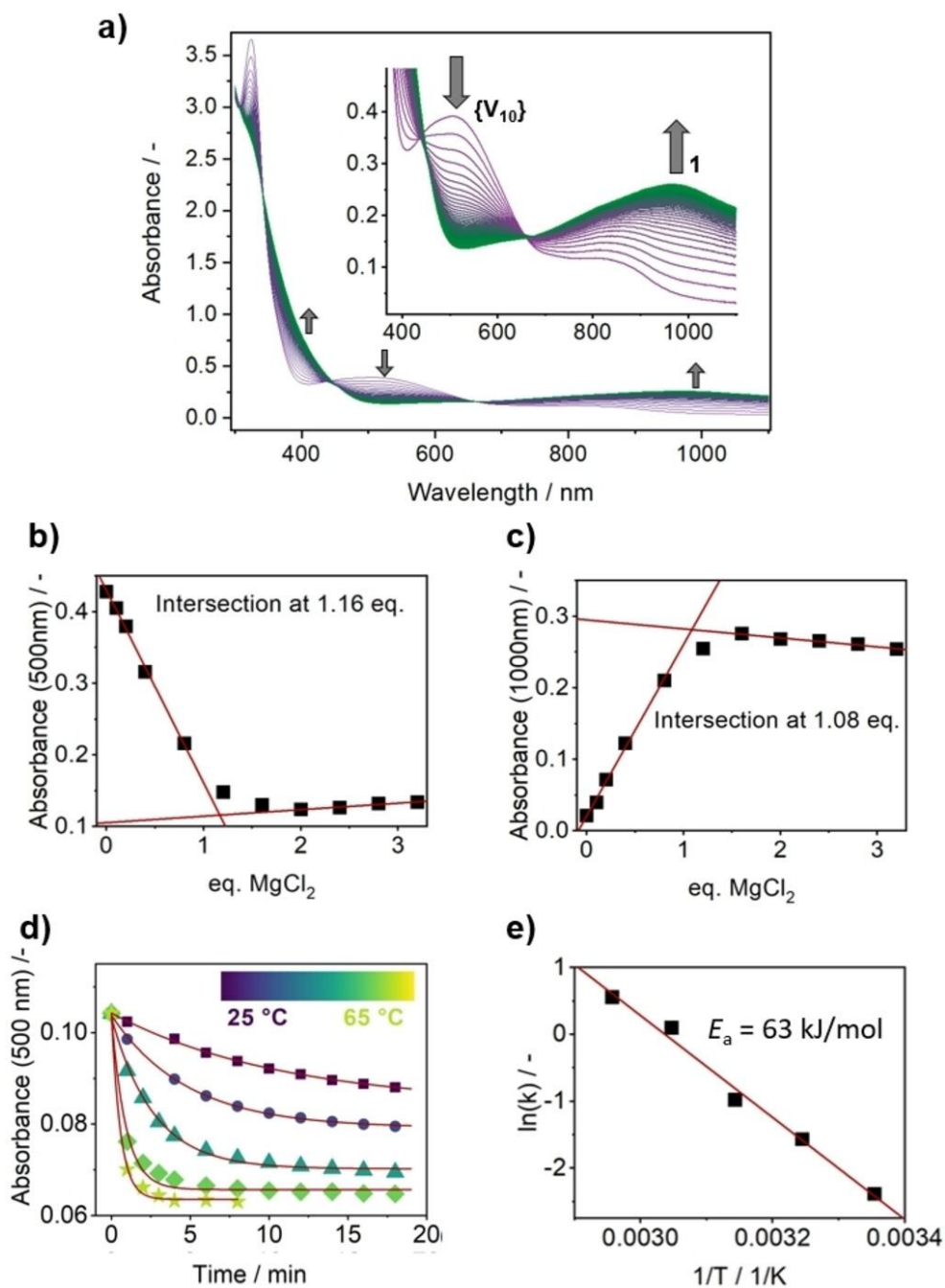


Figure 62: a) Time-lapse UV-Vis/NIR spectroscopy of the conversion of $\{V_{10}\}_{red}$ to **1** at time intervals of 1 min. Three isosbestic points at $\lambda_1=665$ nm, $\lambda_2=446$ nm and $\lambda_3=340$ nm indicate a direct conversion process. Conditions: $T=35$ °C, cuvette path length 10.0 mm, $[\{V_{10}\}_{red}] : [MgCl_2 \text{ (anhydrous)}]=1 : 1.2$, $[\{V_{10}\}_{red}]=230$ μ M). b) Decrease of $\{V_{10}\}_{red}$ concentration as a function of $[Mg^{2+}]$ concentration, monitored by following the characteristic $\{V_{10}\}_{red}$ absorbance at $\lambda=500$ nm; samples were equilibrated for 1 h before measurement; c) Increase of the concentration of **1** as a function of Mg^{2+} concentration, monitored by following the characteristic absorbance of **1** at $\lambda=1000$ nm; samples were equilibrated for 1 h before measurement. d) Kinetic traces and mono-exponential fits of the $\{V_{10}\}_{red}$ - to-**1** conversion (monitored by following the decrease of $\{V_{10}\}_{red}$ concentration at $\lambda=500$ nm) at temperatures between 25 °C to 65 °C. Conditions: $\Delta T=10$ °C, cuvette path length 2.0 mm, $[\{V_{10}\}_{red}] : [MgCl_2 \text{ (anhydrous)}]=1 : 2.2$, $[\{V_{10}\}_{red}]=500$ μ M. e) Arrhenius plot based on the kinetic traces shown in e).

Thus, we determined the apparent conversion rate constant k at temperatures between 25 °C – 65 °C to provide initial thermochemical data for the $\{V_{10}\}_{\text{red}}$ -to-**1** conversion. As illustrated in Figure 62d, this allowed an Arrhenius-type plot showing linear behavior, which gave an activation energy for the conversion of 63 kJ/mol.

Next, we explored the electrochemistry of **1**, as we hypothesized that the presence of both, $\{MgV_{13}\}$ and $\{V_{14}\}$ clusters in **1** could result in enhanced redox-reactivity and electron storage capacity. To prevent any effects of surface oxidation of the crystalline sample (which was suggested by microscopic analysis of the native crystals after storage in air), we purified **1** by re-crystallization from acetonitrile under inert atmosphere and water-free conditions in an Ar-filled glovebox (see SI, Section 3.4.2 Synthesis). These samples were used for all electrochemical and EPR studies. Electrochemistry was performed in inert Ar atmosphere in a glovebox (for details see SI, Section 3.4.2 Electrochemistry and Bulk Electrolysis).

Initial electrochemical analyses of **1** (0.5 mM) were performed by cyclic voltammetry (CV) and square-wave voltammetry (SWV) in anhydrous, degassed acetonitrile solution containing nBu_4NPF_6 (0.1 M) as supporting electrolyte (Figure 63). All electrochemical data were recorded using a silver/silver nitrate reference electrode, and the potentials were then referenced against an internal ferrocene/ferrocenium (Fc^+/Fc) redox couple. In the potential range between -2.15 V and +1.35 V, **1** showed up fourteen redox transitions (see green labels in Figure 63). Integration of the complex SWV data results in the tentative assignment that twelve processes (processes 1, 2, 5–14) are 1-electron transfers, while two processes (processes 3, 4) are 2-electron transfers (see SI, Section 3.4.2 Bulk Electrolysis). In sum, this suggests uptake/release of 16 electrons by **1** in the given potential range. Note that initial density functional theory (DFT) computations for the first reduction of $\{V_{14}\}$ and $\{MgV_{13}\}$ gave theoretical redox potentials which are in close agreement ($\Delta E < 5$ mV) with the experimentally observed data (i.e., redox-transitions 8 and 9). For details see SI, Section 3.4.2 Computational Section.

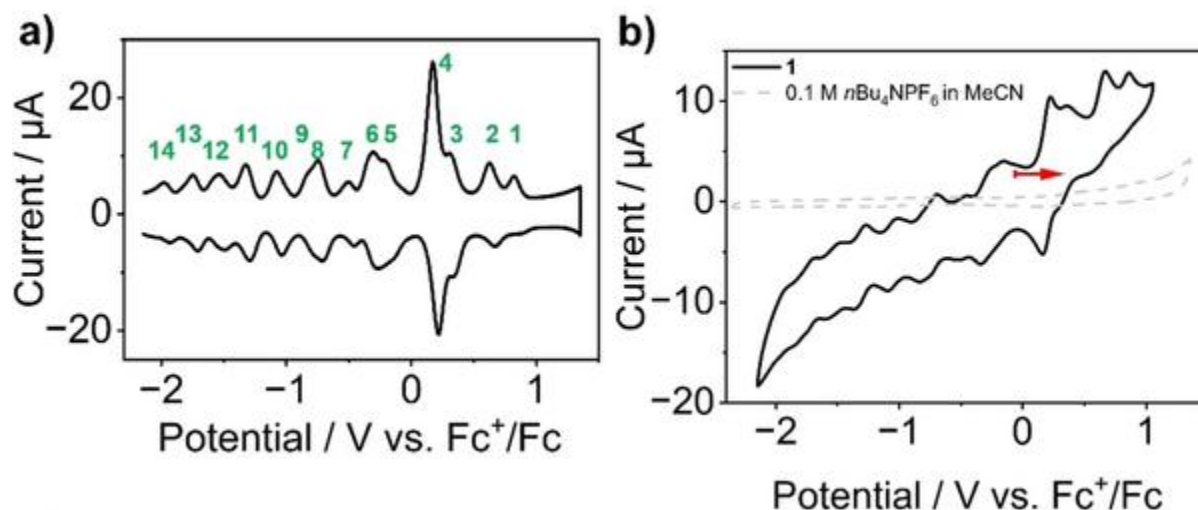


Figure 63: a) Square-wave voltammogram and b) cyclic voltammogram of **1**, showing 14 pseudo-reversible redox transitions in the scan range between -2.15 V to $+1.35$ V vs Fc^+/Fc , open circuit potential and scan direction are indicated by the red arrow. Conditions: anhydrous, deoxygenated acetonitrile containing nBu_4NPF_6 (0.1 M) as supporting electrolyte. Scan rate 50 $mV\ s^{-1}$, [**1**]: 0.5 mM, Ar atmosphere.

To verify these findings and assess the bulk redox activity of **1**, we performed bulk electrolysis (BE) under the conditions used for CV and SWV. Under reductive BE conditions ($E_{red} = -1.45$ V), the data show that 7.86 ± 0.82 electrons can be taken up per formula unit of **1** (i.e., per one $\{MgV_{13}\}$ and one $\{V_{14}\}$ cluster) when starting from the native compound. Note that no significant changes of the SWV data are observed upon bulk reduction, indicating that the structural integrity of the clusters are retained (SI, Section 3.4.2 Bulk Electrolysis). Also, an increase of the characteristic IVCT transitions in the VIS-NIR range are in line with the increasing number of V^{IV} centers. Under oxidative conditions ($E_{ox} = +1.22$ V), BE resulted in the release of 8.66 ± 0.86 electrons per formula unit of **1**. This is in line with a four-electron oxidation of the $\{MgV_{13}\}$ and $\{V_{14}\}$ species, respectively, resulting in the complete removal of all V^{IV} centers. This is supported by UV-Vis/NIR spectroscopy of the oxidized sample of **1**, where a complete loss of the IVCT transitions in the VIS-NIR range (characteristic of delocalized V^{IV} centers) was observed (SI, Section 3.4.2). Note that for the fully oxidized sample, the SWV signatures became somewhat less well defined compared to the native sample. However, upon re-reduction of the sample at the open-circuit potential OCP ($E_{OCP} = -0.06$ V vs. Fc^+/Fc), the original SWV signals of **1** were recovered (SI, Section 3.4.2, Figure 79), suggesting that the structural integrity in this sample is retained or regenerated upon re-reduction. In sum BE analyses indicate that reversible uptake and release of up to 16 electrons per formula unit of **1** is possible in the potential range between -1.08 V to 1.07 V vs. Fc/Fc^+ (for details see SI, Section 3.4.2 Bulk

Electrolysis). This is in line with the data observed from integration of the SWV data, where 16 electron transfers were estimated (Figure 63 and SI, Section 3.4.2). Note that the physical mixing of two chemically or structurally related polyoxovanadates leads to complex mixtures where redox reactions between the clusters can occur, which can lead to (partial) degradation or cluster rearrangements. Thus, redox equilibration during synthesis is an effective path to avoid this detrimental reaction (see SI, Figure Figure 80).

3.3.3. Conclusion

In sum, we have shown that redox-equilibration of structurally related but chemically different polyoxovanadate clusters is a new and viable synthetic route to access electroactive compounds with remarkable reversible redox-reactivity. Specifically, self-assembly and co-crystallization of two vanadium oxide clusters, $\{\text{MgV}_{13}\}$ and $\{\text{V}_{14}\}$ results in an unusual system where the redox-events of the two species facilitate closely aligned redox-transitions, so that up to 16 electrons can be stored in a potential range of ~ 3.5 V. In future, this new materials design approach will be used to develop high-performance electrolytes for non-aqueous redox-flow batteries.

3.4. Supporting Information

3.4.1. Instrumentation

Single-crystal X-ray diffraction (sc-XRD) was measured on a Bruker APEX-II CCD Single-crystal X-ray diffractometer equipped with a graphite monochromator using Mo K α radiation (wavelength $\lambda(\text{Mo K}\alpha) = 0.71073 \text{ \AA}$)

Thermogravimetric analysis: (TGA) was performed on METTLER TOLEDO TGA 2 STARe system under air flow with a flow rate of 60 mL min⁻¹. A polycrystalline aluminium oxide crucible (PCA) was used. Samples were analyzed in a temperature range of 303.15–1173.15 K. A heating rate of 10 K min⁻¹ was applied.

Attenuated total reflectance-Fourier-transformed infrared spectroscopy (ATR-FT-IR) were performed using a Bruker Alpha II equipped with an ATR Platinum Diamond unit. The data were recorded with 24 scans at a resolution of 4 cm⁻¹. All spectra were background-corrected within the Bruker OPUS 8.1 program suite.

¹H nuclear magnetic resonance (¹H-NMR) spectroscopy was recorded on a Bruker AVANCE Neo 400 MHz spectrometer at ambient temperature. ¹H-NMR spectra were measured at 400 MHz. Chemical shifts value (δ) for are given in part per million (ppm) using residual solvent protons ($\delta_{\text{H}} = 1.94 \text{ ppm}$ for CD₃CN).

Electron paramagnetic resonance (EPR) spectroscopy was performed on a X-band Bruker Magnettech ESR5000 spectrometer at 40 °C temperature on 5 mM acetonitrile solution of **1**. The sample was filled in a glass EPR-tube (diameter 3 mm), the measurement range was 250 to 450 mT with a modulation of 1mT, a microwave power of 100 mW and a sweep time of 120s. The SpinCount software option was used to calculate the spin quantity in the sample.

Electrochemical investigations

All experiments were carried out inside an argon-filled glovebox (MBraun LABmaster130/M200B eco) in water-free, degassed acetonitrile at room temperature, using 0.1 M $n\text{Bu}_4\text{NPF}_6$ as supporting electrolyte.

a) Voltammetry

Cyclic voltammetry and square-wave voltammetry were performed on a CH Instruments 760E potentiostat in three-electrode configuration: a glassy carbon with $d = 3.0$ mm was used as working electrode, a silver wire in acetonitrile containing 0.1 M $n\text{Bu}_4\text{NPF}_6$ and 10 mM AgNO_3 was used as reference electrode and a platinum wire was used as counter electrode. All electrodes were cleaned with acetone and acetonitrile each time before use and the working electrode was additionally polished with $0.05 \mu\text{m Al}_2\text{O}_3$ before each measurement. The recorded potentials were then referenced against the internal standard ferrocene/ferrocenium Fc^+/Fc , unless stated otherwise.

b) Bulk Electrolysis

Chronoamperometry was performed on a CH Instruments 760E potentiostat in three-electrode configuration: platinum wires were used as working and counter electrode, a silver wire in acetonitrile containing 0.1 M $n\text{Bu}_4\text{NPF}_6$ and 10 mM AgNO_3 was used as a reference electrode. All electrodes were cleaned with acetone and acetonitrile before each experiment. During the experiment the working electrode was kept at the defined potential while the solution was stirred vigorously. The electrolysis was stopped once the current dropped below 0.5 % of the initial current.

UV-Vis/NIR spectroscopy was performed on a Cary 3500 UV-Vis/NIR spectrophotometer equipped with a Xenon flash lamp (250 Hz). Measurements were performed in quartz glass cuvettes ($d = 10.0$ mm).

High resolution electrospray ionization mass spectrometry (ESI-MS) was carried out on an Agilent 6545 QTOF-HRAM-MS system in negative ion mode at a drying gas temperature of $T = 180\text{ }^{\circ}\text{C}$.

CHN Elemental Analysis was carried out by the central analytical service of the Department of Chemistry at Johannes Gutenberg University Mainz using an Elementar Vario EL Cube.

Inductively coupled plasma optical emission spectroscopy (ICP-OES) was performed on Agilent 5800 VDV ICP-OES (optical emission spectrometer) with the automatic sampler SPS 4. The bulk samples were diluted with 5% aqueous nitric acid.

Chemicals: All chemical reagents were obtained commercially and used as received unless stated otherwise. $(\text{nBu}_4\text{N})_4[\text{V}^{\text{IV}}_2\text{V}^{\text{V}}_8\text{O}_{24}]$ ($(\text{nBu}_4\text{N})_4\{\text{V}_{10}\}_{\text{red}}$) was prepared according to the literature.^[167]

3.4.2. Experimental data

Synthesis of $(n\text{Bu}_4\text{N})_8[\text{V}_{14}\text{O}_{34}\text{Cl}][(\text{MgOH})\text{V}_{13}\text{O}_{33}\text{Cl}]$ (Compound 1)

1.003 g $(n\text{Bu}_4\text{N})_4\{\text{V}_{10}\}_{\text{red}}$ (0.473 mmol, 1 eq.) and 0.101 g MgCl_2 (1.061 mmol, 2.2 eq.) was dissolved in 25 mL acetonitrile. The solution was stirred for 4 h at 75 °C. During this period, the mixture turned dark green, indicating formation of mixed/valent $\text{V}^{\text{IV/V}}$ species. The solution was filtered and set up for diffusion crystallization using diethyl ether as diffusion solvent. After a few days, black cubic single crystals were obtained. The crystals were recovered by filtration, washed twice with water, ethyl acetate and ether. Upon drying, a grey powder was obtained.

Yield: 530 mg (0.234 mmol, 69 % based on V)

MW: 4499.31g/mol

FT-IR (cm^{-1}): 2960.45, 2933.71, 2871.99, 1481.40, 1460.12, 1379.97, 1150.82, 985.35, 876.58, 818.80, 733.83, 672.65, 602.97, 422.83

Elemental Analysis for $\text{C}_{128}\text{H}_{289}\text{N}_8\text{V}_{27}\text{O}_{68}\text{Cl}_2\text{Mg}$ in wt. % (calcd.): C 34.16 (33.97), H 6.43 (6.37), N 2.49 (2.48)

ICP-OES analysis revealed a V : Mg atomic ratio of 27 : 1.17, confirming the expected stoichiometry.

$^1\text{H-NMR}$ (400 MHz, MeCN-d_3): δ 3.20 (8H, $n\text{Bu}_4\text{N}^+$), 1.96 (MeCN-d_3), 1.65 (8H, $n\text{Bu}_4\text{N}^+$), 1.42 (8H, $n\text{Bu}_4\text{N}^+$), 1.00 (12H, $n\text{Bu}_4\text{N}^+$)

A purified sample of **1** for electrochemistry and EPR analyses was prepared under inert atmosphere in the glove box (to prevent traces of surface-oxidation of the crystals of **1** by air). A sample of **1** was dissolved in water-free, de-aerated acetonitrile. Diffusion of diethyl ether into the solution (in the glove box) gave pure crystals of **1** (verified by single-crystal XRD unit cell checks).

¹H-NMR Spectroscopy

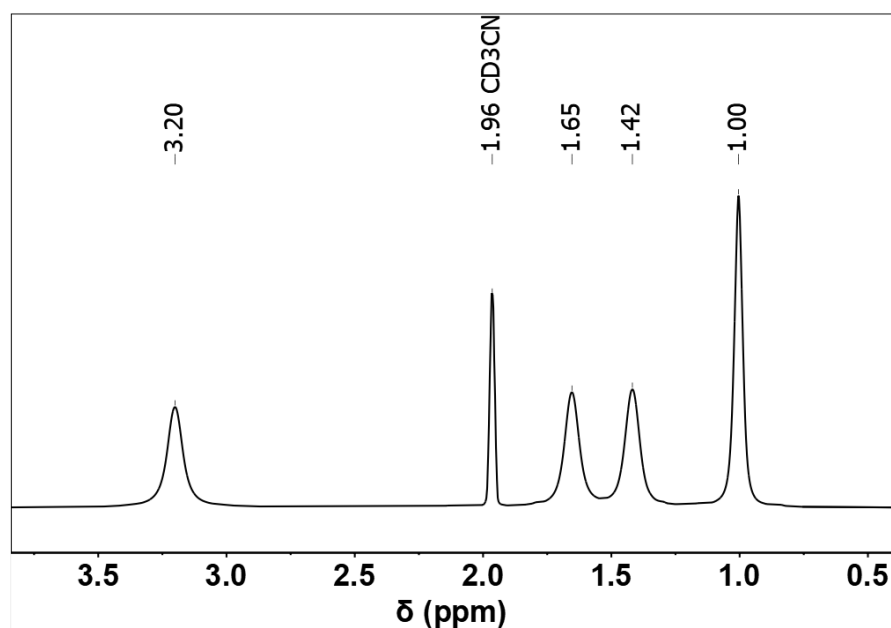


Figure 64: ¹H-NMR of compound 1 in deuterated acetonitrile.

EPR Spectroscopy

The Easyspin 6.0.2. software suite (<https://easyspin.org/>) was used to simulate isotropic and fast-motional cw EPR spectra of radicals in solution via the implemented garlic algorithm.^[174]

Experimental parameters:

Microwave frequency 9.4463 GHz; microwave power 100 mW; 100kHz modulation amplitude 1 mT.

Simulation parameters for the EPR spectrum of {V₁₀}_{red}:

Exchange interactions between two ($n = 2$) ⁵¹V nuclei ($I = 7/2$; 99.2 % abundance), two hyperfine coupling constants A and two localized electrons indicated by a narrow line width, result in an $(2n)I+1$ hyperfine coupling pattern.^[175] An axial system with two g -values (g_{\parallel} in the direction of the z axis and g_{\perp} in the xy plane) were chosen based on the cluster symmetry.^[176] Optimum fits were obtained using Lorentzian line shapes with a line width of $34.33 \times 10^{-4} \text{ cm}^{-1}$, 103 MHz or 3.83 mT.

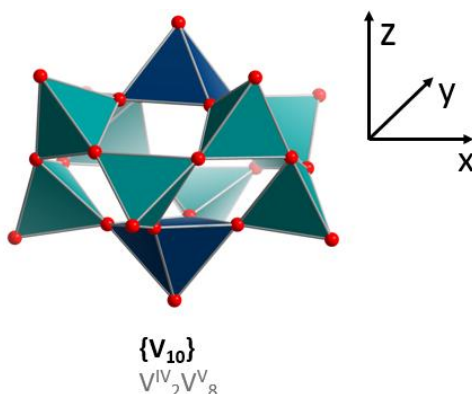


Figure 65: Structure of the $\{V_{10}\}_{\text{red}}$ cluster indicating an axial symmetry of the system.^[167]

Table 8: EPR simulation parameters for $\{V_{10}\}_{\text{red}}$.

g_{\perp}	g_{\parallel}	A_{\perp}	A_{\parallel}
1.962	1.950	$47.948 \times 10^{-4} \text{ cm}^{-1}$ 144 MHz	$42.429 \times 10^{-4} \text{ cm}^{-1}$ 127 MHz

Simulation parameters for the EPR spectrum of compound 1:

For a 1:1 mixture of $\{\text{MgV}_{13}\}$ (3 V^{IV} centers) and $\{V_{14}\}$ (5 V^{IV} centers) with strong antiferromagnetic coupling and an odd number of electrons for both clusters, a total spin count of $2 \times S = \frac{1}{2}$ (caused by two unpaired electrons) is expected, which is identical to the well-known $\{V_{10}\}_{\text{red}}$ reference compound. This was simulated by the combination of two spin systems, both with a weight of 0.5 and $S = \frac{1}{2}$. Due to the interaction of the unpaired electron with the ^{51}V nucleus ($I = 7/2$; 99.2 % abundance), a hyperfine structure could be expected. However, for **1** no hyperfine structure is observed, indicative of the delocalization of the unpaired electrons over a number of structurally similar V sites. For both spin systems optimum fits were obtained with a gaussian line shape and the following line width lw , isotropic hyperfine interaction A and isotropic g -factor g , see Table S2.

Table 9: EPR simulation parameters for compound 1.

Spin system 1			Spin system 2		
g_{iso}	lw	A_{iso}	g_{iso}	lw	A_{iso}
2.025	$174.666 \times 10^{-4} \text{ cm}^{-1}$ 524 MHz 18.485 mT	$36.44 \times 10^{-4} \text{ cm}^{-1}$ 109 MHz	1.890	$188.333 \times 10^{-4} \text{ cm}^{-1}$ 565 MHz 21.343 mT	$30.83 \times 10^{-4} \text{ cm}^{-1}$ 92 MHz

Thermogravimetric Analysis

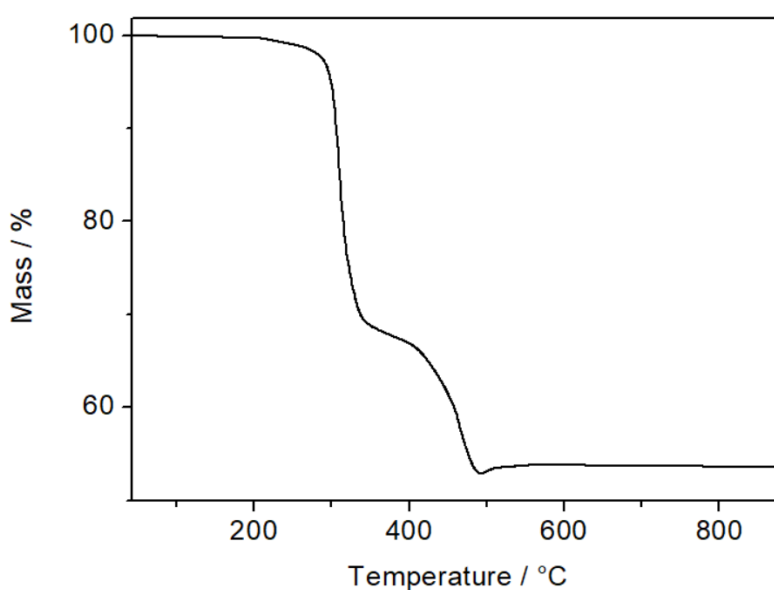


Figure 66: TGA measurement of compound 1. The observed weight loss of 45 % between 200 °C and 600 °C indicates the presence of 8 nBu₄N⁺ cations in 1 (calcd.: 43 %).

Cluster Charge Calculations

Based on the EPR results an odd number of V^{IV} centers for each cluster was indicated. The overall amount of eight tetra-n-butylammonium cations to balance the charge results in only three different reasonable electron distributions on the two clusters {V₁₄} and {MgV₁₃}. Based on the crystallographic analysis (four nBu₄N⁺ cations are in close proximity of each cluster), a cluster charge of 4- is proposed.

Table 10: Possible distributions of electrons on {V₁₄}.

Possible Formula for {V ₁₄ }	(nBu ₄ N) ₂ [V ₁₄ O ₃₄ Cl]	(nBu ₄ N) ₄ [V ₁₄ O ₃₄ Cl]	(nBu ₄ N) ₆ [V ₁₄ O ₃₄ Cl]
Number of V ^V Centers	11	9	7
Number of V ^{IV} centers	3	5	7
Total Cluster Charge	2-	4-	6-

Table 11: Possible distributions of electrons on {MgV₁₃}.

Theoretically Calculated Formula of {MgV ₁₃ }	(nBu ₄ N) ₂ [(MgOH)V ₁₃ O ₃₃ Cl]	(nBu ₄ N) ₄ [(MgOH)V ₁₃ O ₃₃ Cl]	(nBu ₄ N) ₆ [(MgOH)V ₁₃ O ₃₃ Cl]
Number of V ^V centers	12	10	8
Number of V ^{IV} centers	1	3	5
Total Cluster Charge	2-	4-	6-

ESI Mass Spectrometry

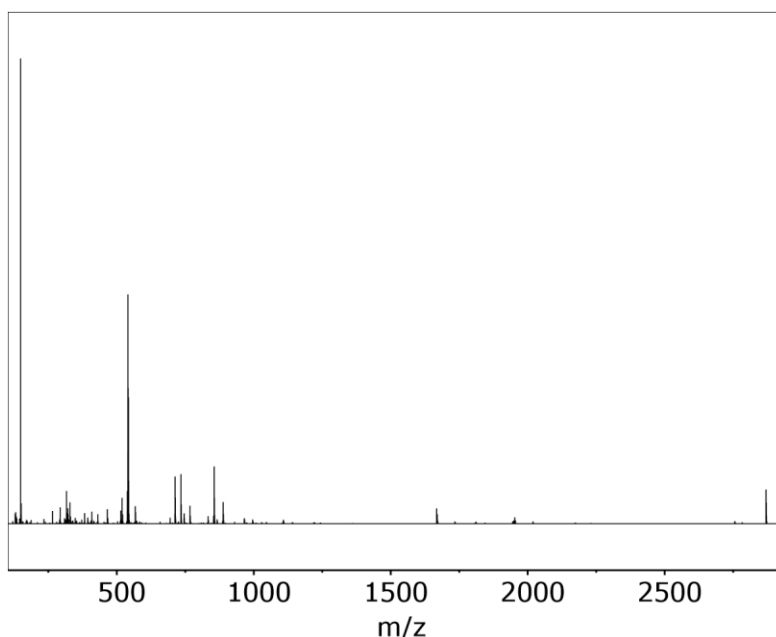


Figure 67: High-resolution negative-ion mode ESI mass spectrum of **1** (0.05mM) in MeCN.

Table 12: Detailed peak assignment of the high-resolution negative-ion mode ESI mass spectrum of **1**.

calculated m/z	observed m/z	peak assignment
694.702	694.717	$(^n\text{Bu}_4\text{N})_3 [\text{H}_2\text{V}_7\text{O}_{19}]^{2-}$
712.667	712.705	$(^n\text{Bu}_4\text{N})_3 [\text{V}_7\text{O}_{17}\text{Cl}_2]^{2-}$
734.203	734.181	$(^n\text{Bu}_4\text{N})[\text{HV}_{13}\text{O}_{33}\text{Cl}]^{2-}$
745.691	745.671	$(^n\text{Bu}_4\text{N})[\text{MgV}_{13}\text{O}_{33}\text{Cl}]^{2-}$
753.186	753.158	$\{(^n\text{Bu}_4\text{N})[\text{MgV}_{13}\text{O}_{34}\text{Cl}]-\text{H}\}^{2-}$
767.170	767.147	$(^n\text{Bu}_4\text{N})[\text{V}_{14}\text{O}_{34}\text{Cl}]^{2-}$
833.363	833.348	$(^n\text{Bu}_4\text{N})_2[\text{MgV}_{12}\text{O}_{32}\text{Cl}]^{2-}$
855.346	855.324	$(^n\text{Bu}_4\text{N})_2[\text{HV}_{13}\text{O}_{33}\text{Cl}]^{2-}$
874.328	874.301	$\{(^n\text{Bu}_4\text{N})_2[\text{MgV}_{13}\text{O}_{34}\text{Cl}]-\text{H}\}^{2-}$
888.289	888.313	$(^n\text{Bu}_4\text{N})_2[\text{V}_{14}\text{O}_{34}\text{Cl}]^{2-}$
1667.734	1667.691	$(^n\text{Bu}_4\text{N})_2[\text{HMgV}_{12}\text{O}_{32}\text{Cl}]^-$
1733.668	1733.623	$(^n\text{Bu}_4\text{N})_2[\text{MgV}_{13}\text{O}_{34}\text{Cl}]^-$

Note that the vanadate fragments observed are most likely artefacts formed during the ionization / gas phase transfer process and have been observed for the native $\{\text{V}_{12}\}$ as well as other related POM species previously.

UV-Vis/NIR Spectroscopy

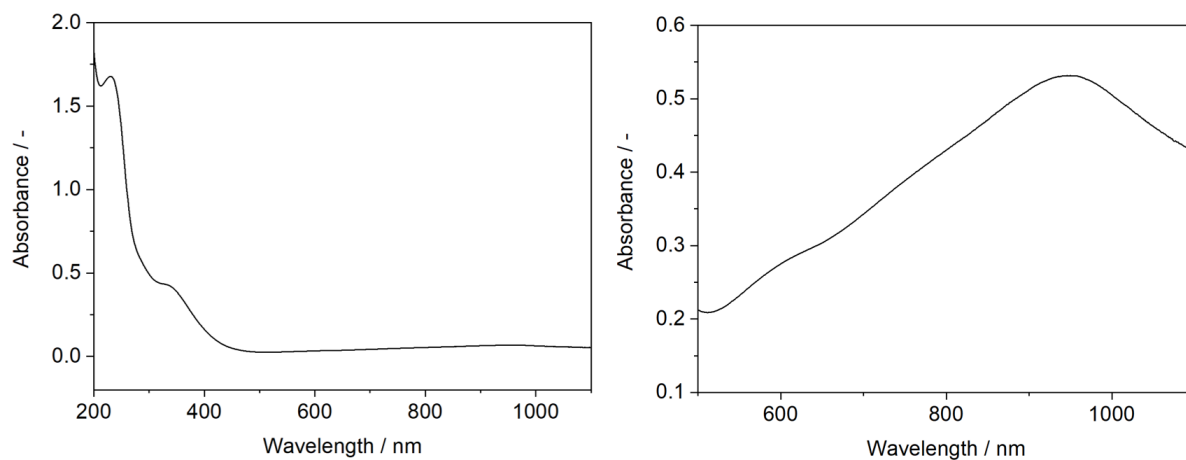


Figure 68: UV-Vis/NIR spectra of **1** in MeCN. left: $[1] = 15.625 \mu\text{mol/L}$; right: $[1] = 125 \mu\text{mol/L}$.

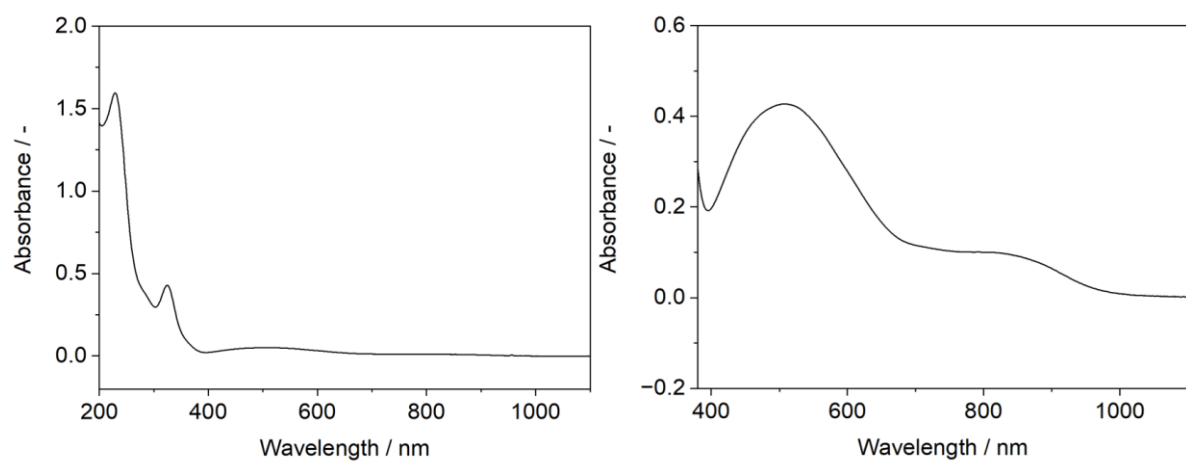


Figure 69: UV-Vis/NIR spectra of $\{V_{10}\}_{\text{red}}$ in MeCN. left: $[\{V_{10}\}_{\text{red}}] = 31.25 \mu\text{mol/L}$; right: $[\{V_{10}\}_{\text{red}}] = 250 \mu\text{mol/L}$.

Temperature dependent UV-Vis/NIR Spectroscopy

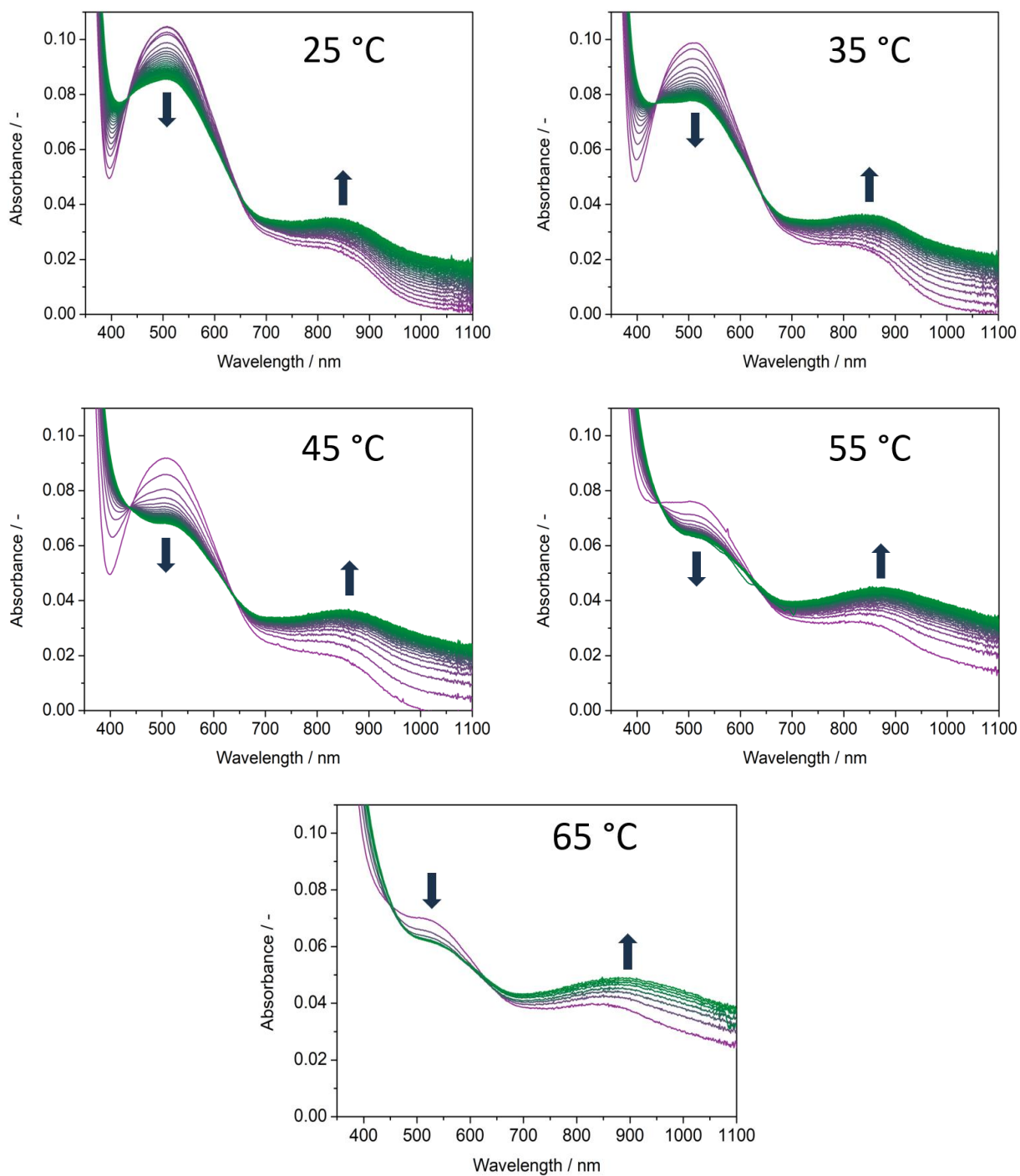


Figure 70: Temperature dependent UV-Vis/NIR Spectra were measured with a time increment of 60 s, cuvette path length of 2.0 mm, $[\{V_{10}\}_{red}] : [MgCl_2 \text{ (anhydrous)}] = 1 : 2.2$ and $[\{V_{10}\}_{red}] = 500 \mu\text{M}$.

Determination of the Molar Activation Energy

Temperature dependent UV-Vis/NIR experiments were evaluated using the Arrhenius Equation.^[177]

Arrhenius equation:

Rate constant = k

Absolute Temperature = T

Pre-exponential factor = k_0

Molar activation energy = E_a

Universal gas constant = R

$$k = k_0 e^{-\frac{E_a}{RT}} \quad (5)$$

Exponential decay fit function for a reaction of first order assuming the decomposition of $\{V_{10}\}_{red}$ in presence of Mg^{2+} as the rate determining step:

$$y = y_0 + k_0 e^{-kt} \quad (6)$$

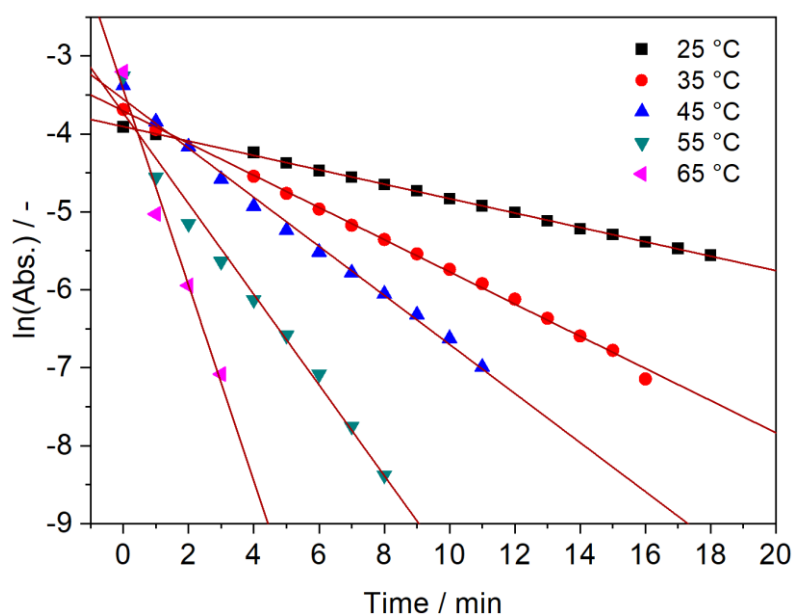


Figure 71: Linear change of $\ln(\text{Abs. } (\lambda = 500 \text{ nm}))$ vs time confirms the first order kinetics.

Table 13: The fit parameters of the mono-exponential fit Figure 62d were used for the Arrhenius Plot Figure 62c.

Temperature dependent Exponential Decay Fit Parameters						
Temperature / °C	y_0	Δy_0	k_0	Δk_0	k	Δk
25	0.08419	3.10467E-4	0.02007	2.75406E-4	0.09191	0.00304
35	0.07918	1.31221E-4	0.02458	2.08578E-4	0.20856	0.00438
45	0.07022	2.12505E-4	0.03309	5.84747E-4	0.37575	0.01379
55	0.06567	2.83053E-4	0.0381	0.00115	1.10502	0.08029
65	0.06353	2.94462E-4	0.04062	7.84384E-4	1.74749	0.10992

Table 14: The fit parameters of the Arrhenius Plot were used to calculate the activation energy.

Linear Fit Parameters of the Arrhenius Plot and Calculated Molar Activation Energy					
$-\frac{E_a}{R} / 1/K$	$\Delta -\frac{E_a}{R} / 1/K$	$\ln(A) / -$	$\Delta \ln(A) / -$	$E_a / kJ/mol$	$\Delta E_a / kJ/mol$
-7620.4453	-467.37833	23.1448	1.47342	63.356	3.886

Mg²⁺ Concentration-dependent UV-Vis/NIR

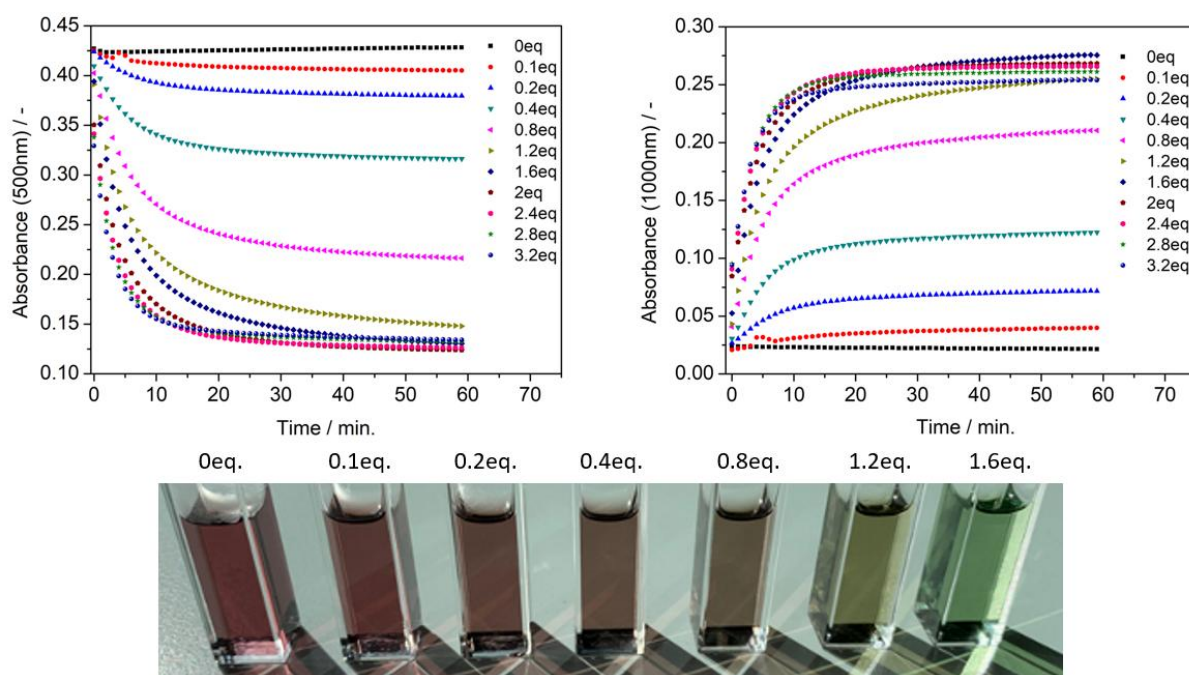


Figure 72: UV-Vis/NIR of $\{V_{10}\}_{red}$ was measured during the equilibration time of 1h with a time interval of 1 min at $[\{V_{10}\}_{red}] = 230 \mu M$, a temperature of 35 °C and a cuvette pathlength of 10 mm pathlength.

ATR-FT-IR spectroscopy

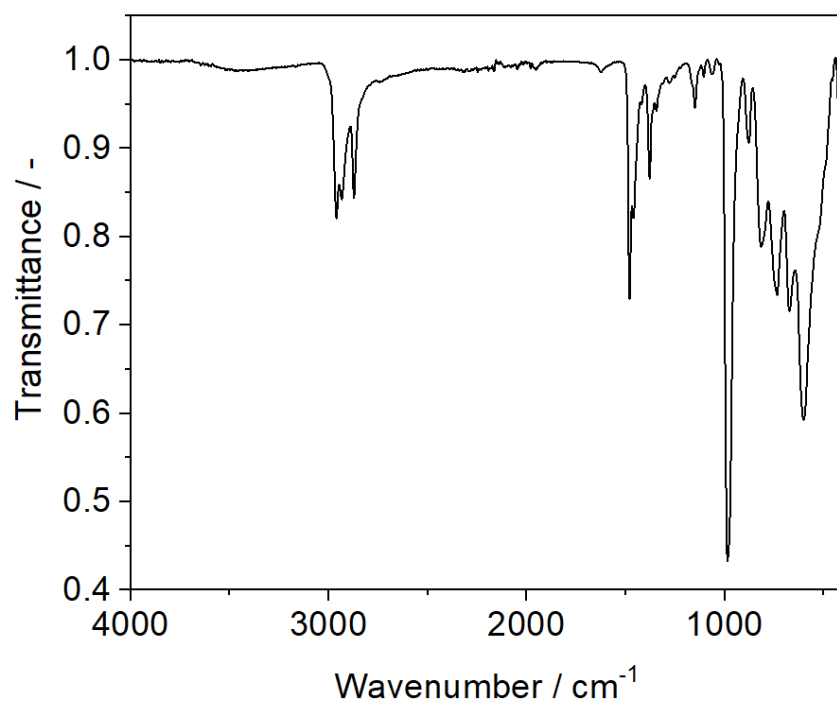


Figure 73: ATR-FT-IR spectrum of compound 1.

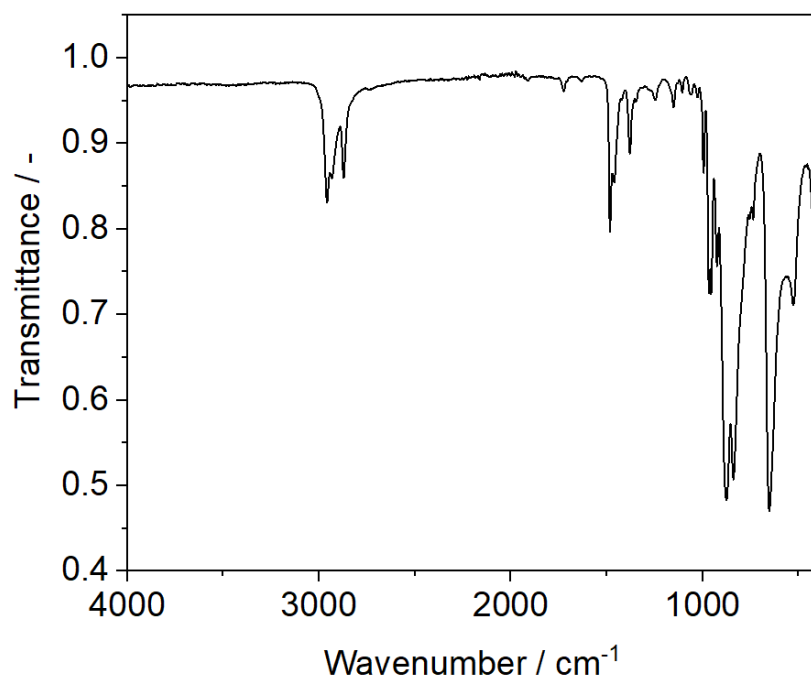


Figure 74: ATR-FT-IR spectrum of {V₁₀}_{red}.

Electrochemistry

Electrochemical intervals in one-component POMs

Table 15: Summary of electrochemical intervals between individual redox events in selected classical single-cluster polyoxometalates.

Entry	Abbreviation of POM	Average $\Delta E_{1/2}$ [V]	Reference
1	α -[PW ₁₂ O ₄₀] ³⁻	0.55	T. Ueda et.al [178]
2	H ₃ [PMo ₁₂ O ₄₀]	0.30	M. A. Barteau et.al [179]
3	α -[W ₁₈ O ₅₄ (SO ₃) ₂] ⁵⁻	0.45	L. Cronin et.al [180]
4	[Ca ₂ V ₁₂ O ₃₂ Cl(DMF) ₃] ²⁻	0.41	C. Streb et.al [75]
5	[V ₆ O ₇ (OEt) ₁₂]	0.56	E. Matson et.al [88]
6	(NEt ₄) ₅ [V ₁₈ O ₄₂ (I)]	0.37	K.Y. Monakhov et.al [181]
7	(nBu ₄ N) ₈ [(MgOH)V ₁₃ O ₃₃ Cl][V ₁₄ O ₃₄ Cl] (compound 1)	0.22	This work

Voltammetry

CV and SWV of **1** show fourteen quasi-reversible redox transitions in the potential range from -2.15 V to + 1.35 V (0.1 M nBu₄PF₆ in MeCN): $E_{1/2}$ (vs. Fc/Fc⁺) = - 1.98 V; - 1.76 V; - 1.55 V; - 1.33 V; - 1.08 V; - 0.83 V; - 0.74 V; - 0.51 V; - 0.30 V; - 0.20 V; + 0.18 V; + 0.32 V; + 0.62 V; + 0.82 V.

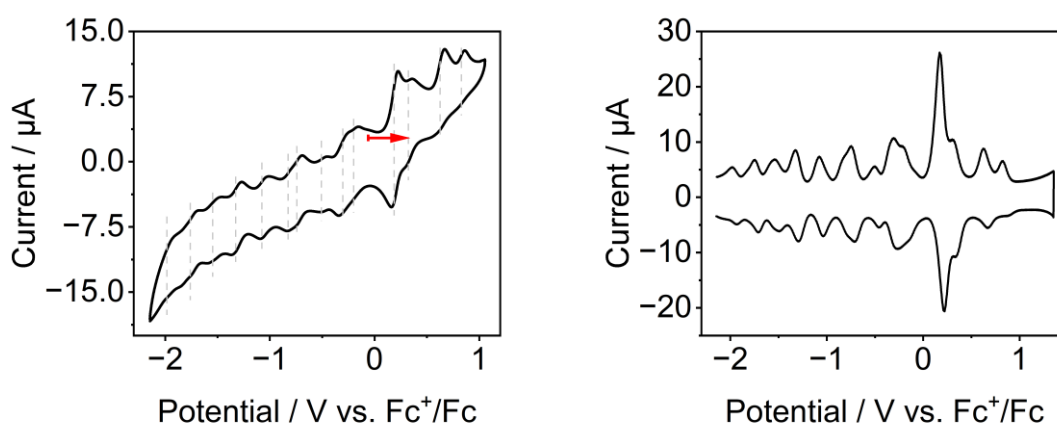


Figure 75: Cyclic voltammogram (left) and square-wave voltammogram (right) of **1**. Conditions: anhydrous, deoxygenated acetonitrile containing nBu₄NPF₆ (0.1 M) as supporting electrolyte (scan rate 0.05 V s⁻¹), [**1**]: 0.5 mM.

Bulk Electrolysis

Bulk Reduction (BR) of **1**

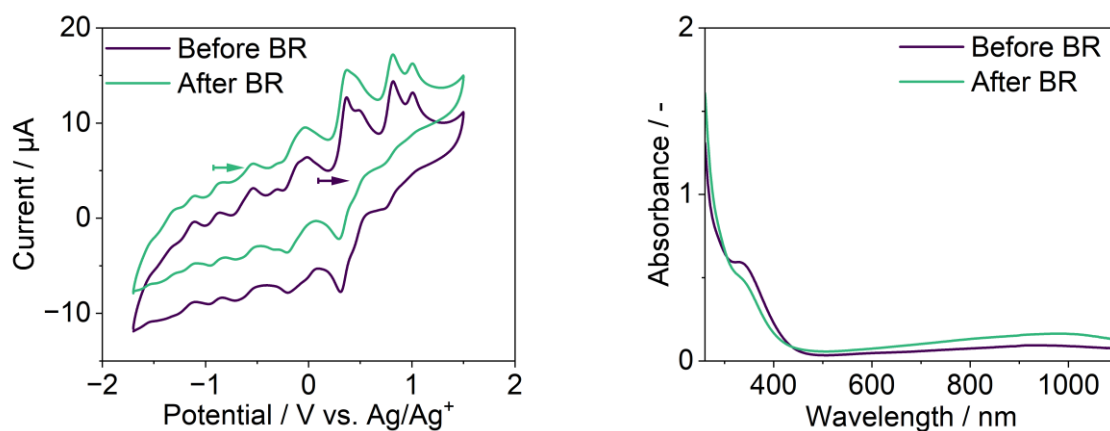


Figure 76: Left: Comparison of CVs of **1** before (dark blue) and after (turquoise) bulk reduction (BR) ($E = -1.45$ V). Open circuit potentials and scan directions are indicated by arrows. Right: UV-Vis/NIR absorption spectra of **1** before (dark blue) and after (turquoise) bulk reduction.

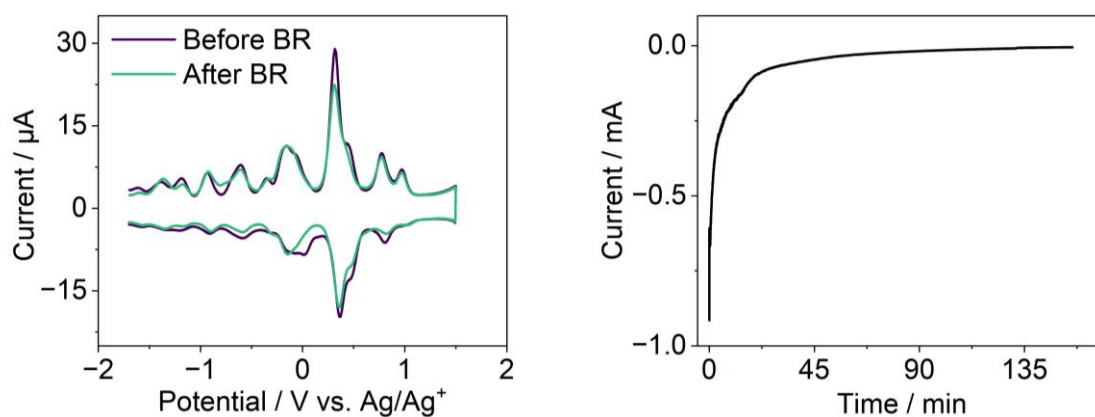


Figure 77: Left: Square wave voltammogram of **1** before (dark blue) and after (turquoise) bulk reduction ($E = -1.45$ V). Right: Chronoamperogram of bulk electrolysis ($E = -1.45$ V).

Bulk Oxidation (BOx) of 1

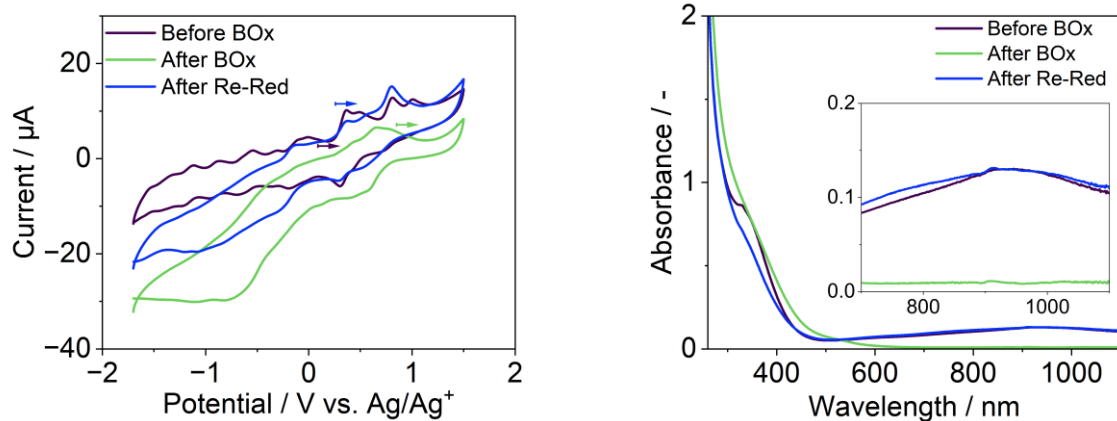


Figure 78: Left: Comparison of CVs of 1 before (dark blue) and after (green) bulk oxidation (BOx) ($E = + 1.22 \text{ V}$) and after re-reduction (Re-Red) (blue) ($E = + 0.09 \text{ V}$). Open circuit potentials and scan directions are indicated by arrows. Right: UV-Vis/NIR absorption spectra of 1 before (dark blue) and after (green) bulk oxidation

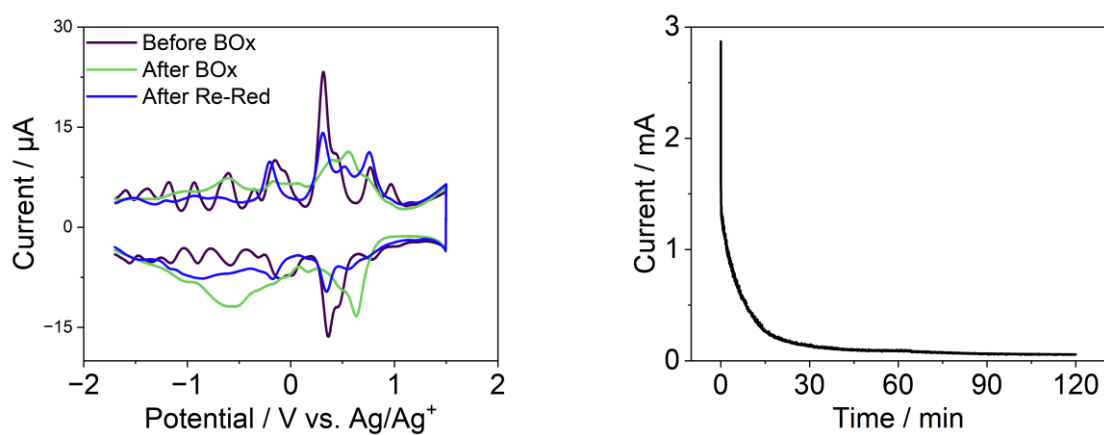


Figure 79: Left: Square-wave voltammogram of 1 before (dark blue) and after (green) bulk electrolysis ($E = + 1.22 \text{ V}$) and after re-reduction (Re-Red) (blue) ($E = + 0.09 \text{ V}$). Right: Chronoamperogram of bulk electrolysis ($E = + 1.22 \text{ V}$).

Table 16: Summary of bulk electrolyses with calculated average number of transferred electrons per cluster.

Entry	Type of Electrolysis	Average # of transferred e ⁻ / cluster	Average # of transferred e ⁻ / formula unit of 1 (containing one {MgV ₁₃ } and one {V ₁₄ } cluster)
1	Bulk Reduction (E = - 1.45 V)	3.93 ± 0.42	7.86 ± 0.84
2	Bulk Oxidation (E = +1.22 V)	4.33 ± 0.43 ^[a]	8.66 ± 0.86 ^[a]

^[a] the slightly increased number of electrons transferred during bulk oxidation is currently assigned to undesired oxidative side reactions.

Integration of square-wave voltammetry data

To gain initial insights into the number of electrons transferred during the redox transitions in compound 1, the oxidative branch of the square-wave voltammogram (Figure S11) was integrated. In Figure S16, colored potential ranges indicate each integration region. The integrals cover all 14 observed redox transitions.

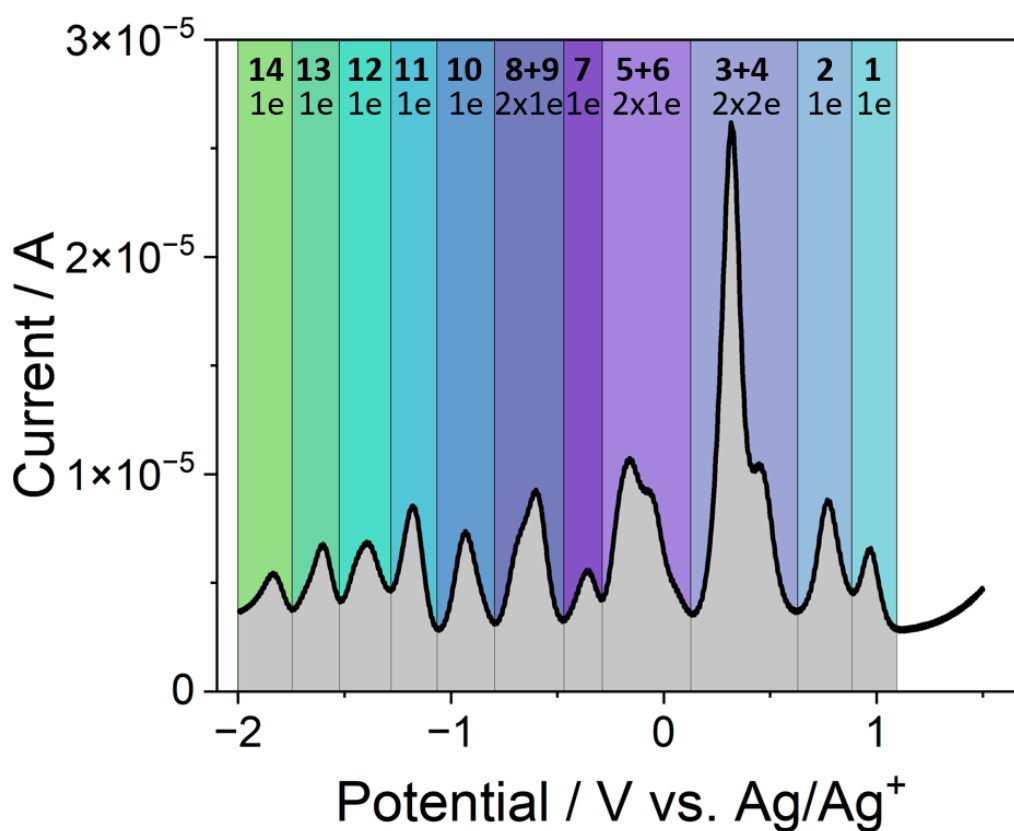


Figure 80: Upper segment of square-wave voltammogram of 1 showing the integration limits indicated by differently colored regions. The integrals were used to estimate the numbers of electrons transferred for each process, see below.

To estimate the number of electrons transferred in each observed redox transition, we first determined an average integral area assigned for an expected 1-electron transfer. This mean integral area A_{mean} was obtained as average of well-separated signals 1,2,7, 10, 11, 12, 13.

This analysis gave $A_{\text{mean}} [\text{A}\cdot\text{V}] = 1.20 \times 10^{-6} \pm 0.23 \times 10^{-6}$

This value was used to normalize each integral area observed for the individual redox transitions as shown in Table S 10. Note that processes 3 and 4, 5 and 6, 8 and 9 could not be separated as they partially overlap, as shown in Figure S16. Electron transfer numbers were then rounded to the nearest integer number to give the nominal number of electrons transferred. Note that integration of the SWV data is challenging due to the complex nature of the voltammogram, the close spacing and partial overlap of the signals observed.

Table 17: Summary of the integration of the square-wave voltammogram of **1**, and the resulting electron transfer numbers for **1**.

Redox Event	Integral range		Integral Area [A·V]	Estimated number of electrons transferred ^[a]	Nominal number of electrons transferred ^[b]
	E ₁ [V]	E ₂ [V]			
1	0.885	1.090	9.85E-07	0.82	1
2	0.630	0.885	1.54E-06	1.28	1
3+4	0.128	0.630	5.17E-06	2 x 2.15	2 x 2
5+6	-0.289	0.128	3.03E-06	2 x 1.26	2 x 1
7	-0.469	-0.289	8.24E-07	0.69	1
8+9	-0.794	-0.469	1.95E-06	2 x 0.82	2 x 1
10	-1.065	-0.794	1.32E-06	1.10	1
11	-1.281	-1.065	1.29E-06	1.08	1
12	-1.524	-1.281	1.36E-06	1.13	1
13	-1.747	-1.524	1.16E-06	0.97	1
14	-2.000	-1.747	1.11E-06	0.93	1
			Sum	16.47	16

^[a] calculated as Integral Area divided by A_{mean}

^[b] Obtained by rounding the estimated number of electrons transferred to the nearest integer number.

Crystallographic Information

Suitable single crystals were mounted onto a microloop using Fomblin oil. X-ray diffraction intensity data were measured at 150 K on a Bruker D8 QUEST diffractometer ($\lambda(\text{MoK}\alpha) = 0.71073 \text{ \AA}$) equipped with a graphite monochromator. Structure solution was carried out using SHELX-2013^[182] package through OLEX2.^[145,183] Corrections for incident and diffracted beam absorption effects were applied using empirical methods.^[146] Structures were solved by a combination of direct methods and difference Fourier syntheses and refined against F^2 by the full matrix least-squares technique. Most non-hydrogen atoms were refined anisotropically. A two-component twin model was used for refinement. The metal oxo framework was refined fully anisotropically. Restraints (SIMU and DELU) on the counter cations were applied. The CIF files can be obtained free of charge from the CCDC, reference number CCDC 2369209.

Table 18: Crystallographic parameters for the samples

Empirical formula	$C_{126}Cl_2Mg_{0.84}N_8O_{68}V_{27.2}$
CCDC reference no	2369209
Formula weight	4188.27
Temperature/K	150.00
Crystal system	monoclinic
Space group	C2
a/Å	23.189(4)
b/Å	23.197(4)
c/Å	17.660(3)
$\alpha/^\circ$	90
$\beta/^\circ$	90.089(6)
$\gamma/^\circ$	90
Volume/Å ³	9500(3)
Z	4
T / K	150(1)
$\rho_{\text{calc}}/\text{cm}^3$	1.464
μ/mm^{-1}	1.370
F(000)	4668.0
Radiation	MoK α ($\lambda = 0.71073$)
2 Θ range for data collection/ $^\circ$	4.6 to 52.8
Index ranges	$-28 \leq h \leq 28, -29 \leq k \leq 29, -22 \leq l \leq 22$
Reflections collected	94631
Independent reflections	19413 [$R_{\text{int}} = 0.0980, R_{\text{sigma}} = 0.0704$]
Data/restraints/parameters	15471/905/1069
Goodness-of-fit on F^2	1.093
Final R indexes [$I \geq 2\sigma(I)$]	$R_1 = 0.0822, wR_2 = 0.2142$
Final R indexes [all data]	$R_1 = 0.1084, wR_2 = 0.2492$
Largest diff. peak/hole / e Å ⁻³	1.24/-0.85

Electrochemical reference studies

To assess the effects of simple physical mixing of two structurally or chemically related polyoxovanadate clusters, the following studies were performed. 1:1 molar mixtures of the related species $[\text{H}_3\text{V}_{10}\text{O}_{28}]^{3-}$ ^[39] and $\{\text{V}_{10}\}_{\text{red}}$, as well as $\{\text{V}_{12}\}_{\text{bowl}}@\text{MeCN}$ ^[184] and $\{\text{Ca}_2\text{V}_{12}\}$ ^[75] were prepared and analyzed by SWV, see Figure S17. The data show that part of the electrochemical signals is retained, while ⁵¹V-NMR analysis of the reaction solutions indicates that partial degradation and/or conversion of the original clusters is observed, thus the solutions are not fully redox-stable.

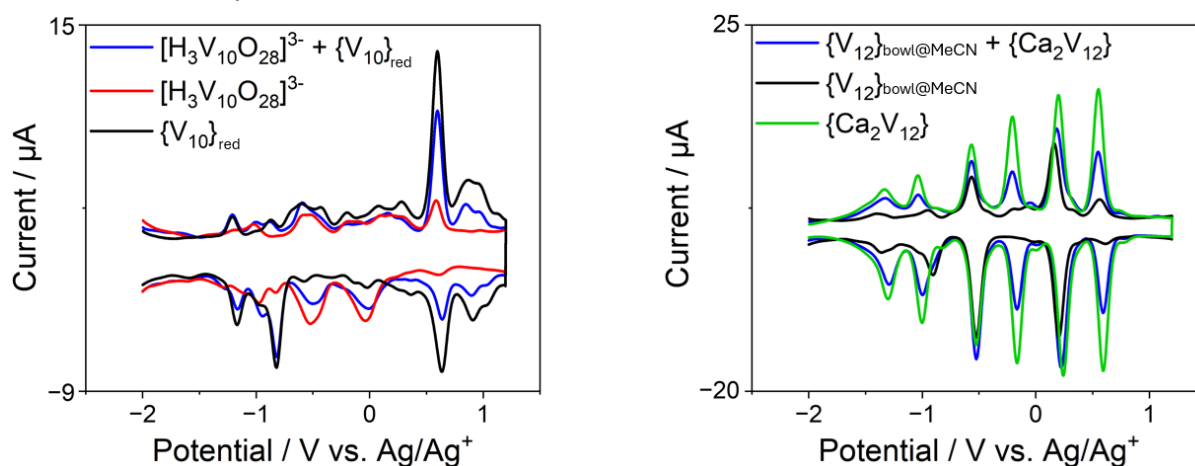
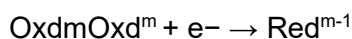


Figure 81: Left: Square-wave voltammograms of $[\text{H}_3\text{V}_{10}\text{O}_{28}]^{3-}$, $\{\text{V}_{10}\}_{\text{red}}$ and their 1:1 molar mixture. Right: Square-wave voltammograms of $\{\text{V}_{12}\}_{\text{bowl}}@\text{MeCN}$, $\{\text{Ca}_2\text{V}_{12}\}$ and their 1:1 molar mixture. Solvent: De-aerated, degassed and dry MeCN containing $(\text{nBu}_4\text{N})\text{PF}_6$ (0.1 M).

Computational Section

Geometry optimizations of the clusters in the gas-phase and solution phase were carried out using density functional theory calculations with the B3LYP^[133] functional combined with the def2-SVP basis set.^[135] Solvation effects were considered using the SMD implicit solvation model (acetonitrile).^[140] All calculations were performed using the Gaussian 16 package.^[142]

Computational redox potentials: One-electron redox process of a redox reaction can be simply defined in terms of a half-cell reaction as follows:



Where Oxd is an oxidized species and Red is a reduced species. The absolute redox potential $E_{\text{ET}}^{\text{abs}}$ of this redox couple is calculated by eq. (7), where $\Delta G^0_{(\text{s})}$ is the free energy change in solution and F is Faraday's constant:

$$E_{\text{ET}}^{\text{abs}} = -\frac{\Delta G^0_{(\text{s})}}{F} \quad (7)$$

The thermodynamic cycle shown below is used to calculate reduction potentials. This is a schematic illustration of gas-phase and solution-phase reactions, as well as the relation between the phases.

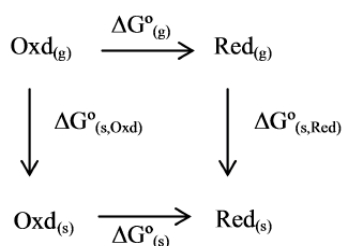


Figure 82: Thermodynamic cycle for the calculation of Gibbs free energies of a one-electron reduction process.

Based on the thermodynamic cycle, $\Delta G^0_{(s)}$ $\Delta G^0_{(s)}$ can be expressed as

$$\Delta G^0_{(s)} = \Delta G^0_{(g)} + \Delta G^0_{(s,\text{Red})} - \Delta G^0_{(s,\text{Oxd})} \quad (8)$$

Where $\Delta G^0_{(s)}$ $\Delta G^0_{(g)}$ is the free energy change in the gas phase, while $\Delta G^0_{(s,\text{Oxd})}$ and $\Delta G^0_{(s,\text{Red})}$ are the solvation free energies of the oxidized and reduced species in acetonitrile, respectively.

Experimentally, the redox potentials are quoted relative to the Fc^+/Fc external standard with a reference potential of $E_{\text{exp,RE}}^{\text{abs}} = 0.40 \text{ V}$ $E_{\text{exp,RE}}^{\text{abs}} = 0.4 \text{ V}$ relative to the standard hydrogen electrode.^[185] The theoretical redox potentials with respect to the experimental reference are calculated using equation (9):

$$E_{\text{ET}}^{\text{calc}} (\text{V vs. Fc/Fc}^+) = E_{\text{ET}}^{\text{abs}} - E_{\text{SHE}}^{\text{abs}} - E_{\text{exp,RE}}^{\text{abs}} \quad (9)$$

Where $E_{\text{SHE}}^{\text{abs}}$ denotes the absolute electrode potential of the standard hydrogen electrode.

The experimental and calculated reduction potential of $\{\text{V}_{14}\}$ and $\{\text{MgV}_{13}\}$ are summarized in table S11.

Table 19: Experimental and calculated reduction potentials for $\{\text{V}_{14}\}$ and $\{\text{MgV}_{13}\}$.

No	Assignment	$E_{\text{exp.}} / \text{V}^{[a]}$	$E_{\text{calcd.}} / \text{V}^{[a]}$
8	$\{\text{MgV}_{13}\}^{4-} + e^- \rightarrow \{\text{MgV}_{13}\}^{5-}$	-0.73	-0.68
9	$\{\text{V}_{14}\}^{4-} + e^- \rightarrow \{\text{V}_{14}\}^{5-}$	-0.83	-0.81

^[a] E_{red} vs. Fc^+/Fc .

Acknowledgements

The authors gratefully acknowledge financial support by the Deutsche Forschungsgemeinschaft DFG (Cluster of Excellence EXC2154, POLiS, project number: 390874152, and project number 389183496). M.A. gratefully acknowledges the State of Baden-Württemberg for a Margarete-von-Wrangell fellowship. C. S. gratefully acknowledges funding by the European Research Council ERC (ERC-CoG “SupraVox”, project number: 101002212), and financial support by Johannes Gutenberg University Mainz, the Rheinland-Pfalz Research Initiative SusInnoScience and the Gutenberg Research College. Open Access funding enabled and organized by Projekt DEAL.

The data that support the findings of this study are openly available in Zenodo.org at 10.5281/zenodo.13002159, reference number 13002159.

Competing Interests

The authors declare no competing interests.

Author Contributions

M. Remmers	Synthesis and characterization, EPR measurements and simulation, UV-Vis measurements, paper writing and revision of the manuscript
B. Mashtakov	Electrochemical measurements paper writing and revision of the manuscript
S. Repp	Synthesis, scXRD measurements, paper writing and discussion of the manuscript
A. S. J. Rein	Synthesis
K. Wang	Computational analysis
M. Anjass	Computational analysis, discussion and revision of the manuscript
Z. Chen	Discussion and revision of the manuscript
L.M. Carrella	EPR results discussion and revision of the manuscript
E. Rentschler	Discussion and revision of the manuscript
C. Streb	Results discussion, writing, discussion and revision of the manuscript

Modifications for the Dissertation

This chapter is based on an article published under the Creative Commons Attribution 4.0 International License (CC BY 4.0). Minor modifications were made for integration into the dissertation. Specifically, the abstract was removed, and the numbering of figures and references was adjusted accordingly. No other changes were made.

3.5. Implementation into Redox-Flow Batteries

Preliminary Note: The following data is part of a manuscript and will be published as: “Mixed-Valent Redox-Equilibrated Polyoxovanadates for Symmetric Non-Aqueous Redox-Flow Batteries” by M. Remmers, B. Mashtakov, Z. Chen, S. Repp, R. Liu, K. Wang, M. Anjass, C. Streb*

3.5.1. Introduction

Electrical energy conversion and storage technologies are crucial to achieve a carbon-neutral energy supply based on renewable energies.^[186–188] Redox-flow batteries (RFBs) are one key technology for the large-scale, stationary and decentralized storage of electrical energy.^[189] Compared with conventional secondary batteries (e.g., lithium-ion batteries), RFBs feature low cost and long service life.^[190] Their unique function allows decoupling of energy storage capacity and power density, making RFBs highly flexible and scalable.^[191]

While the energy content of RFBs can easily be increased by increasing the volume of the electrolyte, reaching higher volumetric energy density is still a major challenge: the volumetric energy density of RFBs is directly proportional to the molar concentration of the active compound in the electrolyte, the number of electrons which can be reversibly exchanged, as well as the potential range in which the system operates, see equation 10:

$$E \text{ [Wh L}^{-1}\text{]} = (c z F U)/3600 \quad (10)$$

Where E = theoretical volumetric energy density, c = molar concentration of active compound, z = number of electrons exchanged, F = Faraday constant, U = operation potential.^[192,193]

Thus, one major thrust in RFBs research is the development of new active materials which combine high solubility, high redox-activity and high stability over a wide potential range.^[194] Moreover, active materials capable of storing and releasing multiple electrons are highly sought-after to increase RFB energy density. In addition, using identical species in both RFB half-cells is advantageous as it results in simple operation, where membrane crossover or electrochemical interference can be avoided.

Historically, aqueous RFBs have been most explored, and a variety of species have been developed, including metal ions,^[195] transition metal complexes^[196] and organic species.^[197] However, aqueous RFBs suffer from several drawback including a small potential window (~1.23 V) due to water oxidation/water reduction,^[198] also, crossover of small-size active species through membrane can lead to self-discharging and loss of capacity.^[199] In addition, many redox-species used in aqueous RFBs offer only one-electron storage, which further limits the theoretical volumetric energy density.^[154,200] Last, most aqueous RFBs utilize highly acidic or basic electrolytes to improve the solubility and stability of the redox-active materials, resulting in high maintenance cost and further diminishing the lifespan of the entire system.^[201]

To overcome these challenges, non-aqueous RFBs (NRFBs) have garnered significant attention.^[202] NRFBs utilize polar organic solvents to achieve wide potential operation windows. As an example, the prototype NRFB solvent acetonitrile has a stable potential window of up to 5 V, which enables redox-events which are not accessible in aqueous systems.^[203] The use of organic solvents also offers greater flexibility in the molecular design of active species and enables the use of redox-active compounds that are insoluble in water, thereby broadening the scope of RFBs.^[204] Notably, the higher voltage of NRFBs compensates for solubility limitation of the active species to deliver competitive or higher energy densities than aqueous RFBs. However, their widespread adoption is currently limited by several technical and economic challenges. Chief among these is the stability of redox-active species in non-aqueous solvents, which affects both the efficiency and longevity of the system. Additionally, the high cost of active species and specialized supporting electrolytes poses economic barriers to scalability. Long-term cycling performance also remains a concern, as capacity fading and side reactions over extended operation can compromise battery lifespan and reliability.^[203] Addressing these issues, particularly improving the stability, solubility, and cost-effectiveness of redox-active species, is critical for advancing NRFB technology toward commercial viability.

Molecular metal oxides, or polyoxometalates (POMs) have received significant interest as potential multi-electron storage molecules for NRFBs.^[205] The promises of POMs clusters lie in their superior structural configuration and excellent redox properties, which facilitate the reversible storage and release of multiple electrons without structure decomposition.^[206] Notably, the solubility and redox properties of POMs clusters can be rationally tailored by introduction different counter cations and various

atoms or ligands. Beyond electrochemistry, nano-sized POMs clusters offer significant advantages over smaller ionic/molecular charge carriers, as their size and charge limits membrane crossing and prevents self-discharge.^[152]

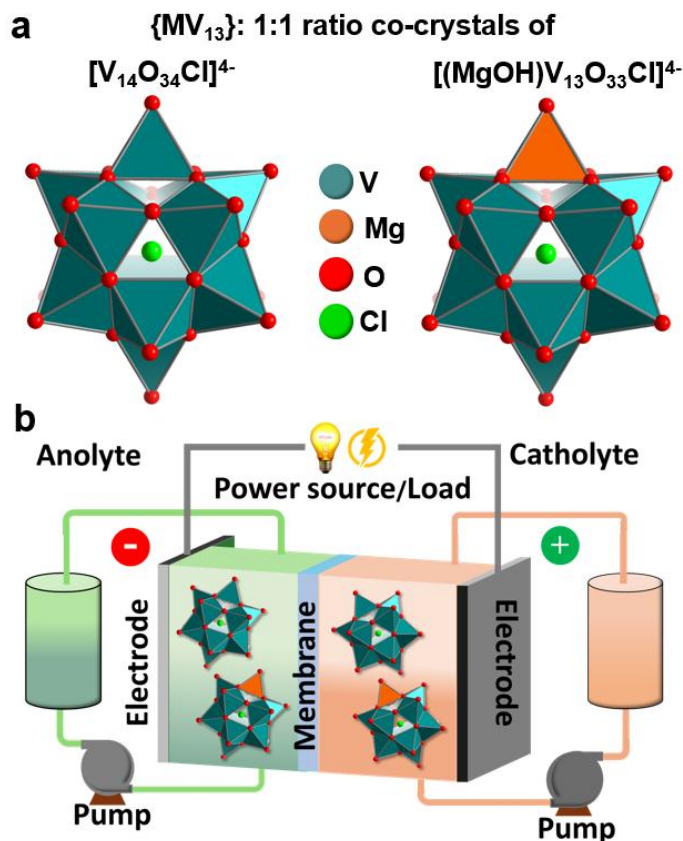


Figure 83: (a) Polyhedral representation of the two vanadate cluster species present as 1:1 molar mixture in the $\{MV_{13}\}$. (b) Schematic illustration of the symmetric $\{MV_{13}\}$ -based nonaqueous redox flow battery setup reported.

The earliest research on RFBs based on POMs was conducted by Sun and colleagues in 1997, who reported an asymmetric aqueous RFB using Keggin POM $H_3[PMo_{12}O_{40}]$ as the anolyte active species and Fe^{3+}/Fe^{2+} as the catholyte active species.^[207] Subsequently, Xiang and coworkers reported an aqueous RFB based on $H_6[CoW_{12}O_{40}]$, which demonstrated reversible transfer of three electrons and enabled symmetric RFB operation.^[208] In recent years, Matson and co-workers have reported seminal studies in the field of NRFBs based on Lindqvist POMs $[V_6O_7(OR)_{12}]$ ($R=CH_3, C_2H_5$). The group also showed how structural modifications (e.g., functionalization with heterometals or different alkoxide ligands) affects NRFB performance.^[29, 88,209,210] Notably, polyoxovanadates (POVs) have attracted widespread attention as RFB active species due to their significantly lower mass ($M(V) = 52 \text{ g mol}^{-1}$) compared to more traditional molybdenum ($M(Mo) = 95 \text{ g mol}^{-1}$) and tungsten ($M(W) = 180 \text{ g mol}^{-1}$) POMs,

implying that POV clusters could offer higher energy density per unit mass than heavier metal oxide clusters.^[1]

To-date, most POM (N)RFBs, only allow the transfer of up to four electrons across different oxidation states, necessitating an asymmetric configuration to handle charge imbalances. Thus, it remains challenging to develop POM-based RFBs that enable multi-electron storage and release in a symmetric system with high operation voltage.^[211]

Recently, some of us reported the synthesis of mixed-valent polyoxovanadate co-crystals $\{MV_{13}\} (nBu_4N)_4[MV_{13}O_{33}Cl]$ ($M = VO^{2+}$ or $MgOH^+$) which demonstrated excellent redox properties: briefly, the $\{MV_{13}\}$ co-crystals contain 1:1 molar mixtures of the five-electron reduced species $[V^{IV}_5V^V_9O_{34}Cl]^{4-}$ ($= \{V_{14}\}$) and the three-electron reduced species $[(MgOH)V^{IV}_3V^V_{11}O_{33}Cl]^{4-}$ ($= \{MgV_{13}\}$). Thus, $\{MV_{13}\}$ can be given as $(nBu_4N)_8[(MgOH)V_{13}O_{33}Cl][V_{14}O_{34}Cl] = (nBu_4N)_8\{MgV_{13}\}\{V_{14}\}$, see Figure 83a. $\{MV_{13}\}$ is soluble in coordinating organic solvents, e.g., acetonitrile (estimated solubility 15 mM), facilitating the design of multi-electron storage systems. In detail, $\{MV_{13}\}$ can reversibly store and release up to 16 electrons in the potential range of -2.2 V – 1.4 V vs Fc^+/Fc as we described in this paper.^[212] This is in line with previous studies on related vanadates, where increased redox-activity depending on the exact metal substitution was observed.^[9, 28, 75] Also, as the two cluster species in $\{MV_{13}\}$ form in the same reaction solution, there are no chemical incompatibilities between these components.

Herein, we demonstrate that acetonitrile solution of $\{MV_{13}\}$ can be used as electrolyte for symmetric NRFB (as shown in Figure 83b).

3.5.2. Results and Discussion

$\{MV_{13}\}$ was synthesized based on the synthetic method reported recently by some of us (for synthesis and characterization, also see Supporting Information).^[212] Here, we first explored the fundamental electrochemical performance of $\{MV_{13}\}$ in acetonitrile under the targeted NRFB conditions. To this end, we utilized a three-electrode cell equipped with a glassy carbon (GC) working electrode, a platinum counter electrode, and a non-aqueous $Ag/AgNO_3$ reference electrode. For experimental details see SI. An acetonitrile solution containing $\{MV_{13}\}$ (0.5 mM) as active species and $(nBu_4N)_4PF_6$ (0.1 M) as supporting electrolyte was used.

The square-wave voltammetry shows the characteristic $\{MV_{13}\}$ redox processes within the potential range between -2.0 V and 1.2 V vs. $Ag/AgNO_3$, which are in line with the

literature.^[212] To gain initial mechanistic insights into the fundamental electrochemical performance of $\{MV_{13}\}$ relevant for NRFB operation, we used variable frequency square-wave voltammetry and linear-sweep voltammetry at a rotating disc electrode at different rotation rates to determine the diffusion coefficient. (For details see SI) The linear slope here scales linear with the number of transferred electrons and perfectly matches the expected numbers reported previously.^[212] Note that due to difficulties because of overlapping signals a Randles–Ševčík analysis was impossible and the determination of diffusion coefficients by the Koutecký-Levich method was limited to the two almost exactly overlapping two electron oxidation processes and only used as reference for comparison (Figure 84).

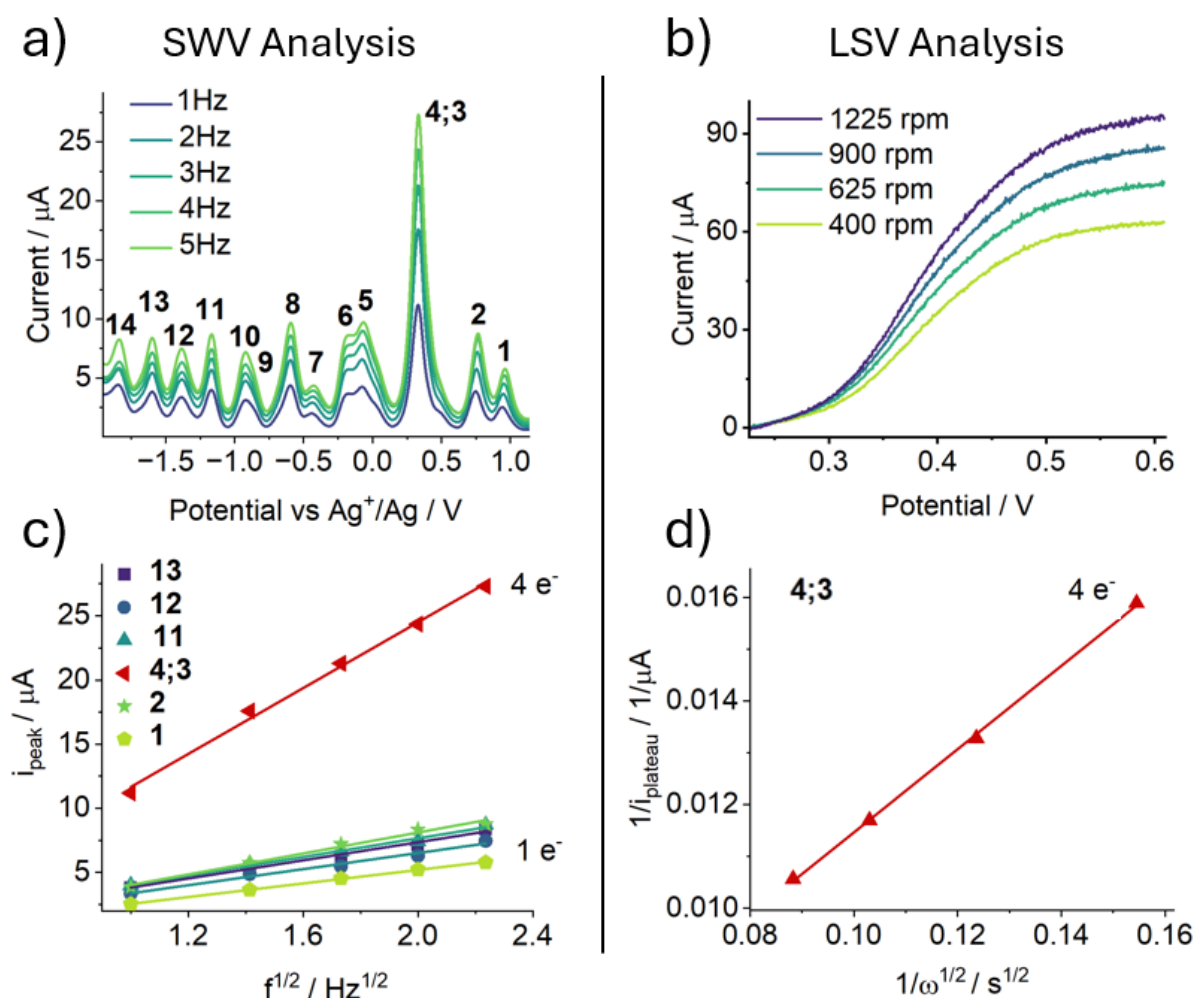


Figure 84: a) SWV of $\{MV_{13}\}$ at different frequencies 1 Hz - 5 Hz. b) LSV of peak 4;3 at different rotation rates. c) linear plot of i_{peak} vs. $f^{1/2}$ and d) the linear plot of $1/i_{plateau}$ vs. $\omega^{-1/2}$. The measurements were conducted at concentration of 0.5 mM in acetonitrile containing 0.1M (nBu₄N)PF₆ as supporting electrolyte.

Table 20: Parameters for the calculation of the diffusion coefficient of {MV₁₃}

Redox process ^a	Number of transferred electrons	Slope	Diffusion coefficient
SWV analysis	n	m [A/Hz^{1/2}]	D₀ [cm² s⁻¹]
ferrocene	1	1.42 × 10 ⁻⁵	2.4 × 10 ⁻⁵ (literature) ^[213]
13	1	3.53 × 10 ⁻⁶	1.48 × 10 ⁻⁶
12	1	3.14 × 10 ⁻⁶	1.17 × 10 ⁻⁶
11	1	3.64 × 10 ⁻⁶	1.57 × 10 ⁻⁶
4;3	4	1.28 × 10 ⁻⁵	1.22 × 10⁻⁶
2	1	4.09 × 10 ⁻⁶	1.98 × 10 ⁻⁶
1	1	2.65 × 10 ⁻⁶	8.30 × 10 ⁻⁷
LSV analysis		m [(As^{1/2})⁻¹]	D₀ [cm² s⁻¹]
4;3	4	80428.17	3.18 × 10⁻⁶

^a Only well-separated redox processes were used in these analyse

D₀ obtained from the two methods are generally consistent, in the order of 10⁻⁷–10⁻⁶ cm² s⁻¹. Table 20: Parameters for the calculation of the diffusion coefficient of {MV₁₃}. Table 20. The slight overestimation of the diffusion coefficient for the LSV analysis compared to the SWV analysis can be explained by the generally more complicated setup of the rotating disc electrode, which is much more vulnerable to errors in rotation rate or turbulence which makes the diffusion coefficient appear larger. Generally, this data is in line with previous reports on redox-active POMs in organic electrolytes.^[210,214] The data also reveal that, despite their size (diameter ~1 nm), {MgV₁₃} and {V₁₄} show suitable mass transport in acetonitrile. Next to fast electron transfer kinetics this feature is important for optimum NRFB operation.

Next, we investigated the membrane crossover rate of {MV₁₃} through a standard commercial Celgard 2400 membrane. Membrane permeability was analyzed in an electrochemical H-cell consisting of two compartments separated by the membrane. Our analyses gave a diffusional permeability of 3.11 × 10⁻⁷ cm² s⁻¹ which is comparable to the values reported previously in the literature for acetonitrile-based systems. (see SI Table 21) Additionally, the precursor {V₁₀}_{red} with the same charge and comparable size was tested under the same conditions resulting in similar values for the diffusional

permeability. In both cases the characteristic UV-Vis spectrum did not show any changes (see SI Figure 91 and Figure 92) confirming the cluster stability under these conditions. [210]

Given the promising features of $\{MV_{13}\}$, we designed a symmetric NRFB operated using an acetonitrile solution containing 1 mM $\{MV_{13}\}$ and 0.1 M $(nBu_4N)PF_6$. Identical solutions were used as anolyte and catholyte, and the half-cells were separated by a Celgard 2400 membrane, see Figure 83b. All NRFB tests reported in this work were performed at room temperature under N_2 atmosphere to avoid undesirable reactions with oxygen or water and flammability issues.

The as-constructed symmetric NRFB was initially tested under galvanostatic conditions at a current density of 1.75 mA cm^{-2} . To avoid overoxidation of the graphite electrode and possible degradation of the electrolyte components in the fully oxidized state, the cutoff voltages for charging and discharging were set to 1.1 V and 0.2 V. Note that the NRFB was operated in 2-electrode configuration, so voltages given for the NRFB are absolute potential differences between the cathode and anode.

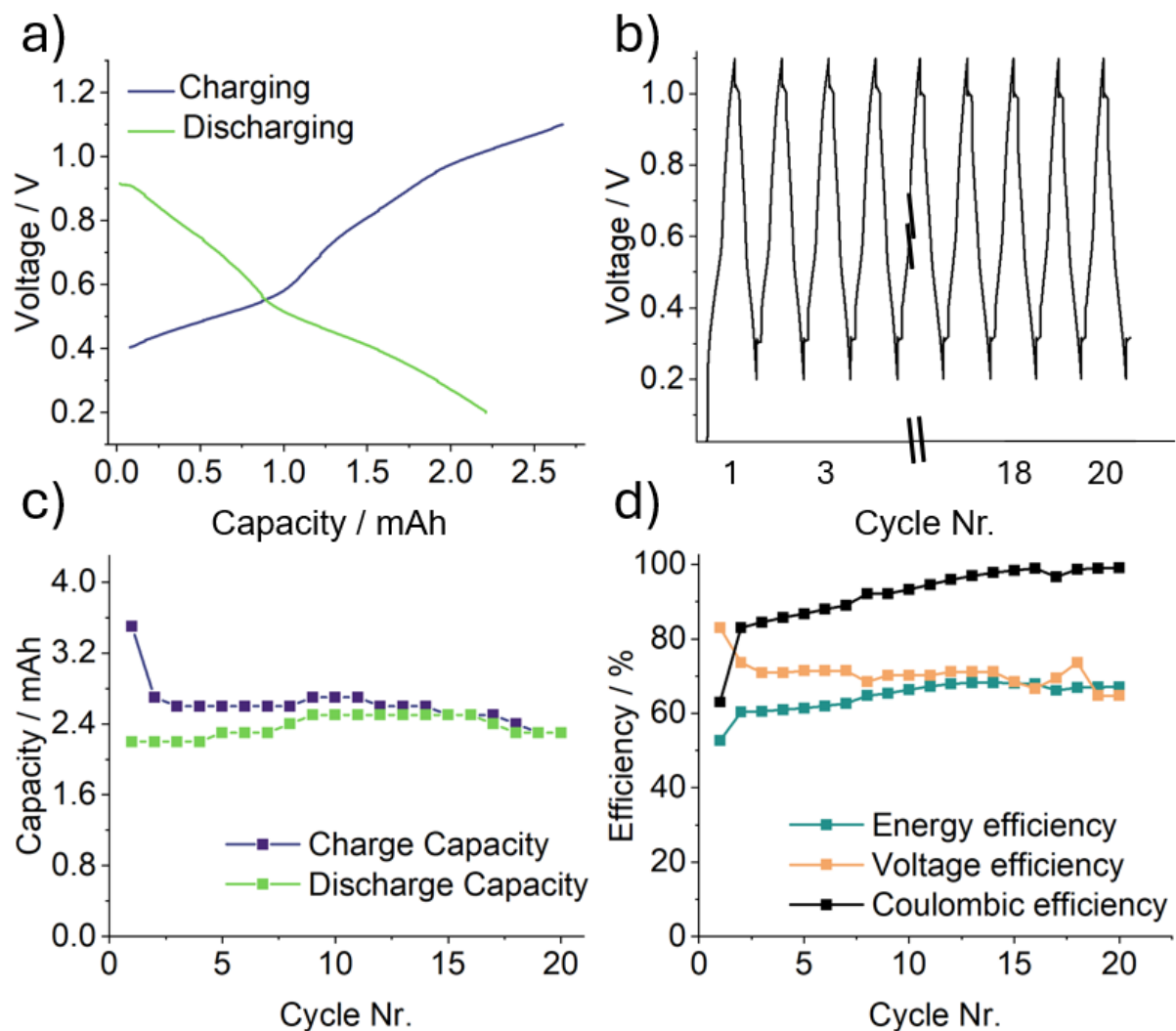


Figure 85: a) Charge and discharge curves of $\{MV_{13}\}$, b) The voltage profile of the NRFBs in cyclability test at current density of 1.75 mA cm^{-2} , (c) the charge discharge capacities of the NRFBs during the 50 cycles cycling test and (d) the coulombic efficiency, voltage efficiency and energy efficiency of the NRFBs during the cycling test.

Under the given conditions, the system features an average charge capacity of 2.6 mAh and an average discharge capacity of 2.4 mAh. (Figure 85a) The coulombic efficiency increased because of activation processes from 83% to 99%. The cycling shows excellent discharge capacity retention with no significant fading after 20 cycles (Figure 85c). The voltage profiles of the NRFB remain nearly identical throughout the 20 cycles test at a constant current density, indicating stable electrode reactions (Figure 85b). Minor differences of capacity and efficiency for the first cycle are most likely due to an electrode/electrolyte activation process.^[179]

As shown in Figure 85a multiple overlapping discharge plateaus were observed between 0.91 V and 0.2 V. The value of the maximum cell voltage closely matches the potential difference of the redox processes **3** to **8** (Figure 84a) in anolyte and catholyte. The average number of stored and released electrons z per $\{MV_{13}\}$ unit during the charge/discharge test was calculated by the average charge capacity using the half-cell volume V of 45 mL at a concentration c of 0.5 mM $\{MV_{13}\}$ and 2.6 mAh charge capacity in equation 11 and indicates that a number of 4.31 electrons during charging and 3.98 electrons during discharging of the theoretical 4 electrons between redox process **3-8** were transferred from anolyte to catholyte. This leads to a discharge capacity of about 99% of the theoretical capacity.

$$\frac{3.6C}{cFV} = z \quad (11)$$

To validate the redox processes involved in the charge and discharge process the OCP was measured during the cycling in the catholyte reservoir. The changes closely match the redox event **4;3** which includes four electrons in total.

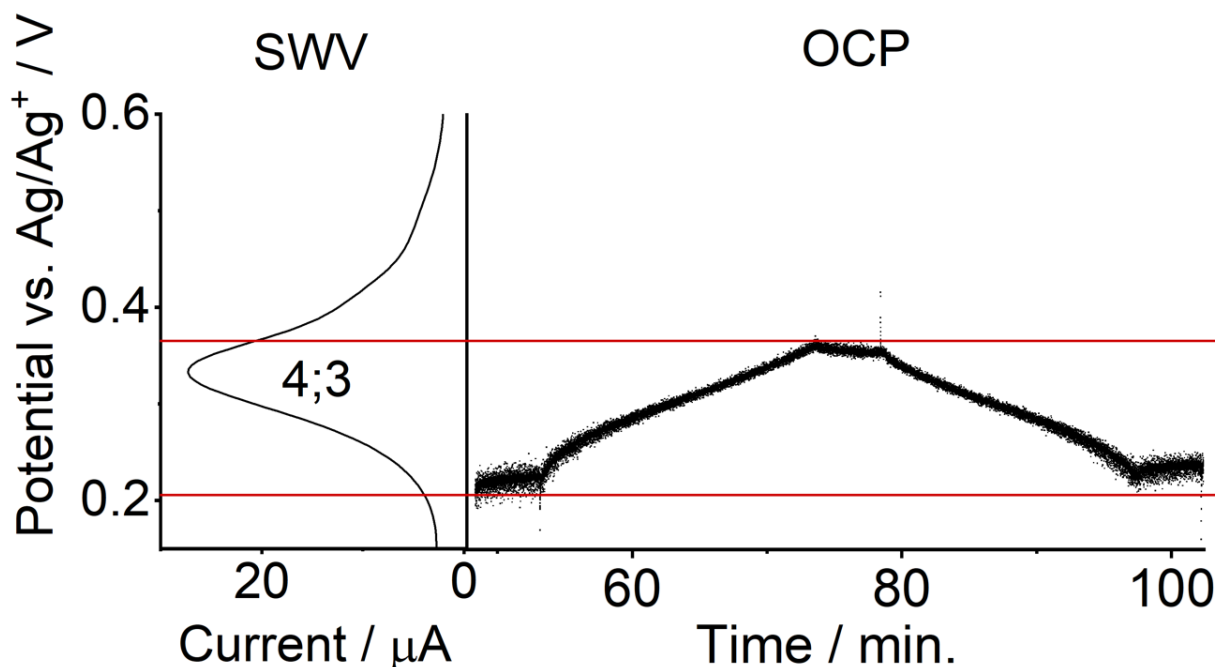


Figure 86: The OCP changes during the charge and discharge process include redox event **4;3** of the SWV data closely matching the expected transfer of four electrons. (shown for cycle 2)

In sum these promising results will be further improved by optimization of the battery setup in terms of the flow rate and charge and discharge parameters. Additionally, in-operando spectroelectro chemistry and OCP shift measurements in both anolyte and catholyte during the charge and discharge process will be included to determine the state of charge depending spectral signature of the compound and its stability during cycling. Further optimization will include pre-charging of the electrolyte towards more negative potentials to benefit from the large theoretical potential difference between the anolyte and catholyte based on the SWV analysis of well above 2 V between process **1** to **14**.

3.5.3. Conclusion

In summary, we demonstrate how a two-component polyoxovanadate compound, $\{MV_{13}\} (nBu_4N)_4[MV_{13}O_{33}Cl]$ ($M = V=O_2^+ \{V_{14}\}$ or $MgOH^+ \{MgV_{13}\}$), can be used as a high-performance active compound for symmetric non-aqueous redox-flow batteries. Our studies show that under NRFB conditions in acetonitrile, $\{MV_{13}\}$ shows multiple reversible electrons transfer. Under standard operating conditions, the system showed a coulombic efficiency of up to 99% at 1.75 mA cm^{-2} and a high stability with a negligible capacity fading rate. Future studies on $\{MV_{13}\}$ NRFBs will be focused on exploring how to improve the stability range as well as solubility in acetonitrile or other suitable NRFB solvents. One promising approach to enhance the solubility is cation metathesis, where introduction of long-chain alkylammonium cations might be a promising route to increase solubility.^[150] Besides, integration of in situ diagnostics or post-mortem analysis to monitor electrode degradation during long-term cycling would provide a more complete perspective on the practical implications of entire NRFBs system regeneration. Using alternative solvents with lower flammability, such as fluorinated solvents or ionic liquids, is a potential solution to improve the safety profile of NRFBs. In sum, this study demonstrates how symmetric NRFBs can be designed based on suitable mixed-valent V(IV/V) polyoxovanadate clusters.

3.6. Supporting Information

3.6.1. Instrumentation

Materials and general information for synthesis: All reagents and solvents were purchased from commercial suppliers and were used without further purification. Solvents for UV-Vis spectroscopy were at least HPLC grade or spectroscopic grade. Solvents for cyclic voltammetry were HPLC grade and water-free, all other solvents were at least high purity grade or HPLC grade.

Attenuated total reflectance-Fourier-transform infrared spectroscopy (ATR-FT-IR) was performed on a Bruker Alpha II equipped with an ATR Platinum Diamond unit. The data were recorded with 24 scans at a resolution of 4 cm^{-1} .

Electrochemical Measurements: The cyclic voltammetry and square-wave voltammetry experiments were carried out inside an argon-filled glovebox (MBraun LABmaster130/M200B eco) in water-free, degassed acetonitrile at room temperature, using $0.1\text{ M nBu}_4\text{NPF}_6$ as supporting electrolyte and were performed on a CH Instruments 760E potentiostat in three-electrode configuration: a glassy carbon with $d = 3.0\text{ mm}$ was used as working electrode, a silver wire in acetonitrile containing $0.1\text{ M nBu}_4\text{NPF}_6$ and 10 mM AgNO_3 was used as reference electrode and a platinum wire was used as counter electrode. All electrodes were cleaned with acetone and acetonitrile each time before use and the working electrode was additionally polished with $0.05\text{ }\mu\text{m Al}_2\text{O}_3$ before each measurement.

For the Koutecký-Levich analysis a glassy carbon rotating disk electrode (RDE with active area of 0.1963 cm^2) was utilized as working electrode, which was polished with $0.05\text{ }\mu\text{m Al}_2\text{O}_3$ prior to use.

Redox flow battery assembly and test: the redox flow battery setup was commercially obtained from Wuhan Zhisheng New Energy Co., Ltd., the structure of the battery was shown in Figure S1. The serpentine flow fields are made from graphite with an effective area of 4 cm². The Celgard 2400 membrane was stored in 0.1 M nBu₄NPF₆ prior to use. The carbon felts were used without any pretreatment. The reservoirs of anolyte and catholyte were both filled with the 45 ml electrolyte of 0.5 mM {MV₁₃} and 0.1 M nBu₄NPF₆. Before the test, the assembled battery was purged with nitrogen (washed through acetonitrile) for 30 min and kept under a slight positive N₂ pressure during the measurement. During the test, the electrolytes were circulated by the peristaltic pump with a flow rate of 15 ml min⁻¹. All the galvanostatic measurements of the battery were performed with a Neware battery tester CT-4008T5V6A-S1 at room temperature.

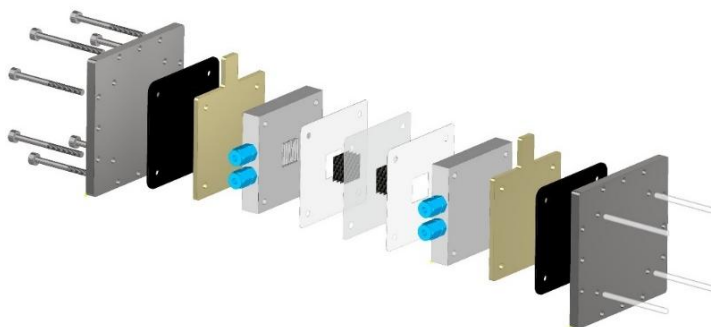


Figure 87: Structure of the RFB setup (Source from <https://redox-flow.com/shop/redox-flow-battery-test-cell/>).

3.6.2. Experimental data

The synthesis of {MV₁₃} is first described in reference^[212] and is given here for completeness.

Synthesis of (nBu₄N)₄[V₁₀O₂₆]: vanadium (V) oxide (3.62 g, 0.02 mol) was dispersed into 20 mL H₂O with vigorous stirring at 60 °C, then 7 mL (50.2 mmol) triethylamine was added and stirred for 20 min. Subsequently, 100 mL acetone containing (nBu₄N)Br (18.9 g, 59 mmol) and 5 ml H₂O containing VOSO₄ (2.17 g, 0.0133 mol) were added into the above solution. The mixture was stirred for 2 h at room temperature, then the precipitate was collected by filtration and washed twice with water, ethanol and diethyl ether, respectively. The product was dried at room temperature overnight. Yield: 93 % (based on V).

Synthesis of $\{MV_{13}\} nBu_4N)_4[MV_{13}O_{33}Cl]$ ($M = V=O^{2+} \{V_{14}\}$ or $MgOH^+ \{MgV_{13}\}$): the obtained precursor $(nBu_4N)_4[V_{10}O_{26}]$ (1.00 g 0.47 mmol) and $MgCl_2$ (0.10 g, 1.06 mmol) were dissolved in 25 ml acetonitrile, the mixture was stirred for 4 h at 75 °C. After cooling, the precipitate was removed by filtration, and the filtrate was setup for diffusion crystallization with diethyl ether as diffusion solvent. After 3 to 4 days, black cubic crystals were collected and washed with water, ethyl acetate and diethyl ether, respectively. The final product $\{MV_{13}\}$ was dried at room temperature. Yield: 65 % based on V.

Characteristic IR bands (in cm^{-1}): 2965, 2936, 2875, 1478, 1456, 1376, 1341, 1273, 1146, 1105, 1056, 985, 890, 817, 743, 667.

ATR-FT-IR spectrum of $\{MV_{13}\}$.

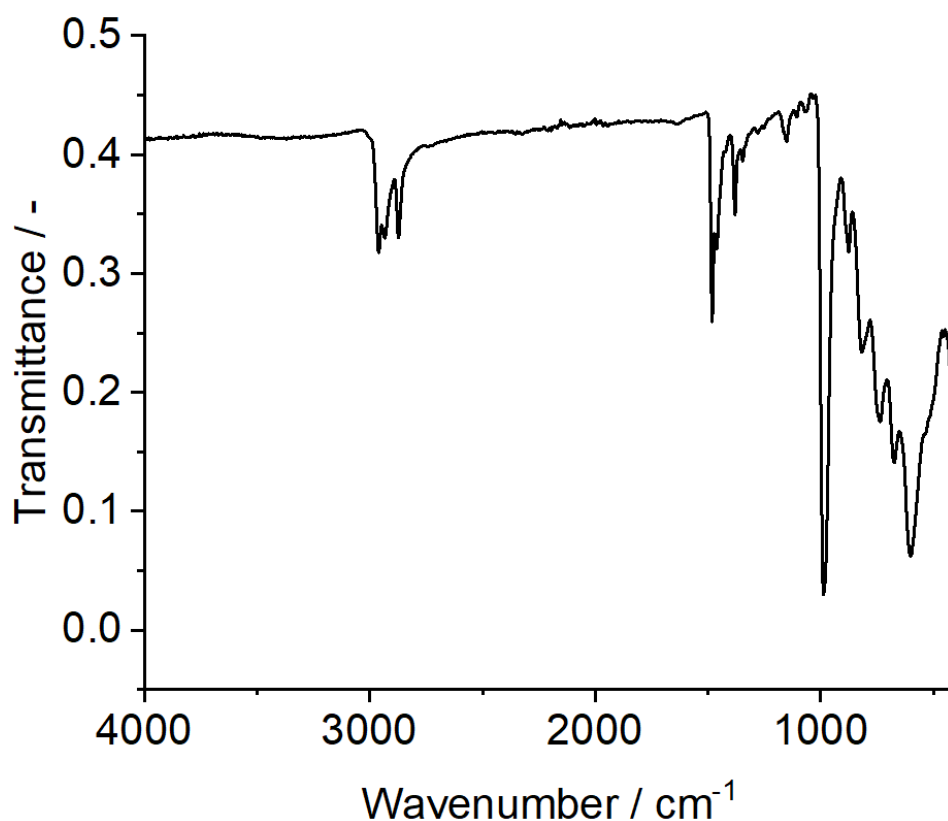


Figure 88: ATR-FT-IR of $\{MV_{13}\}$.

Diffusion coefficient determination by Square-Wave Voltammetry

For reversible redox events the peak current i_p of the square-wave voltammogram depends on the Faraday constant F , the electrochemically active surface area $A = 0.0707 \text{ cm}^2$, the concentration c (0.5 mM) and a constant ψ_p which are kept constant between each measurement, additional to the number of electrons n , the square root of the diffusion coefficient D and the square root of the frequency f . This can be written as equation 12. The slope of the linear fit of i_p vs. $f^{1/2}$ leads to equation 13.^[213]

$$i_p = \frac{FA2^{1/2}c\psi_p}{\pi^{1/2}} \times n \times D^{1/2} \times f^{1/2} \quad (12)$$

$$m = \text{const.} \times n \times D^{1/2} \quad (13)$$

To eliminate the dependence of the unknown constant (const.) ferrocene (fc) is measured at the identical conditions as {MV₁₃} (1). The ratio of the slopes of the linear fits of i_p vs. $f^{1/2}$ can then be expressed by equation 14, which can be used to calculate the diffusion coefficient of {MV₁₃} by equation 15^[213]:

$$\frac{m_1}{m_{fc}} = \frac{n_1}{n_{fc}} \times \frac{D_1^{1/2}}{D_{fc}^{1/2}} \quad (14)$$

$$D_1 = \left(\frac{m_1}{m_{fc}} \frac{n_{fc}}{n_1}\right)^2 \times D_{fc} \quad (15)$$

To ensure as little influence as possible of the electron transfer kinetics due to the quasi-reversible behavior the frequency was kept at small values between 1 and 5 Hz. The number of electrons was assigned based on previous literature.^[212]

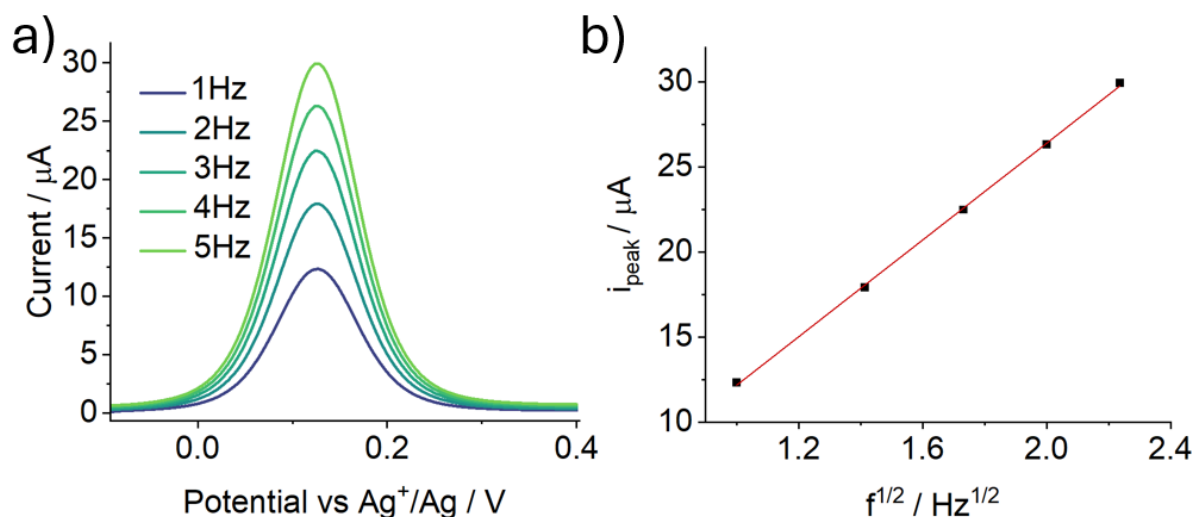


Figure 89: a) SWV of the ferrocene reference sample at different frequencies 1 Hz - 5 Hz at 0.5 mM at the same experimental conditions compared to {MV₁₃}. b) Linear plot of i_p vs. $f^{1/2}$ of ferrocene. The slope m is used to calculate the diffusion coefficients.

Validation by the Koutecký-Levich method

Using the Koutecký-Levich equation (16), the diffusion coefficient D_0 of different redox processes for {MV₁₃} cluster can be determined by a linear fit of the inverse measured plateau current $i_{plateau}^{-1}$ vs. the inverse square root of the rotation rate $\omega^{-1/2}$. The Levich equation (17) shows a relationship between the number of transferred electrons n , Faraday's constant $F = 96485$ C/mol, electrode area $A = 0,1963$ cm², concentration $c = 0.5$ mM for {MV₁₃}, the kinematic viscosity $\nu = 0.465$ mm²/s (= dynamic viscosity η / density ρ ; based on pure acetonitrile at 298.15 K as an approximation)^[215], and D_0 represents the diffusion coefficient included in the Levich constant B_L .^[213]

$$1/i_{plateau} = 1/(B_L\omega^{1/2}) \quad (16)$$

$$B_L = 0.620 n F A c D_0^{2/3} \nu^{-1/6} \quad (17)$$

Permeability studies

The permeability of the {MV₁₃} cluster across the separator was measured by an H-type device with two counterpart reservoirs, which was separated by a commercial Celgard 2400 membrane. One reservoir was filled with a solution of 1 mM for {MV₁₃} or 2 mM {V₁₀}_{red} in acetonitrile, and the second reservoir was filled with acetonitrile containing 1 mM (nBu₄N)PF₆ to prevent significant osmotic pressure. The first reservoir volume V_A was 30 mL. The volume of the second reservoir V_B was adjusted to the same height and includes the volume of the tubing in the UV-Vis flow setup (39 mL total). The absorbance of the first reservoir at 965 nm was measured at the beginning (A₀) and the absorbance of the second reservoir was measured over time using a flow cuvette (path length 10 mm).

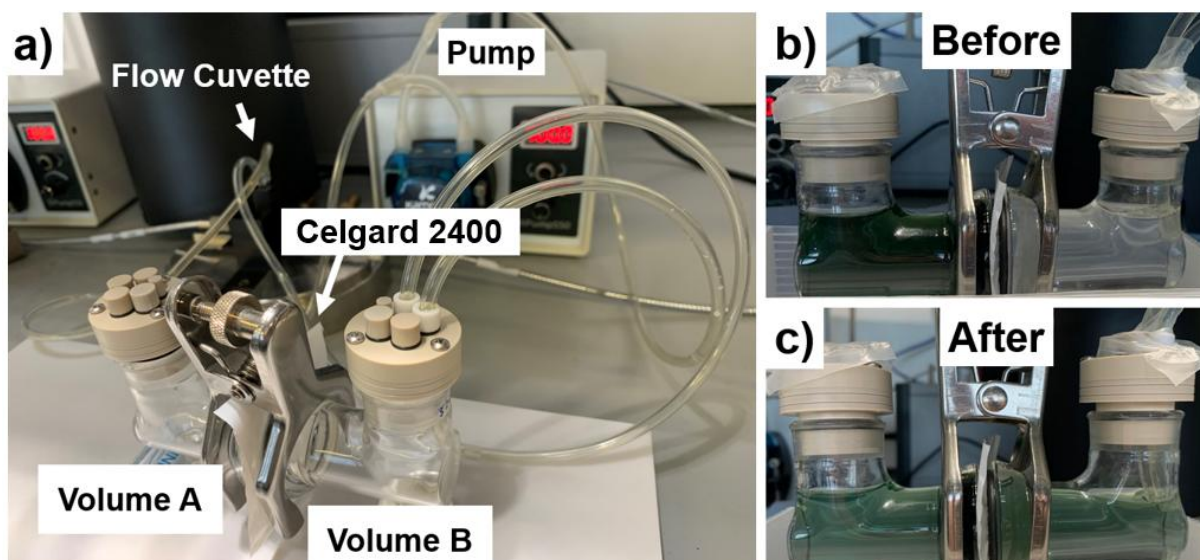


Figure 90: a) Experimental setup for the permeability tests. Volume A is filled with POM solution, and the absorbance of volume B is measured at a constant time interval in a flow cuvette. The total volume including the A and B as well as the tubing was measured b) before and c) after the measurement time and was constant.

The permeability P is defined as the k/L where k is the diffusional permeability and L is the diffusion length and given as the membrane thickness. The permeability can be determined according to Fick's first law assuming a one-dimensional steady state by using equation 18.^[216] A linear fit of $-\ln\left(1 - \frac{A(t)}{A_{eq}}\right)\left(\frac{V_A V_B}{S(V_A + V_B)}\right)$ vs. t where $A(t)$ is the increasing absorbance at time t in compartment B and $A_{eq} (= A_0 \frac{V_A}{V_A + V_B})$ the equilibrium absorbance

of the $\{MV_{13}\}$ after dilution to the total volume of 69 mL, V is the volume of the solution in compartment A and B and S is the effective area of the membrane exposed to solution (4.91cm^2):

$$-\ln\left(1 - \frac{A(t)}{A_{eq}}\right)\left(\frac{V_A V_B}{S(V_A + V_B)}\right) = Pt \quad (18)$$

The diffusional permeability k is often reported in literature and can be calculated using the thickness of the membrane ($25\ \mu\text{m}$).

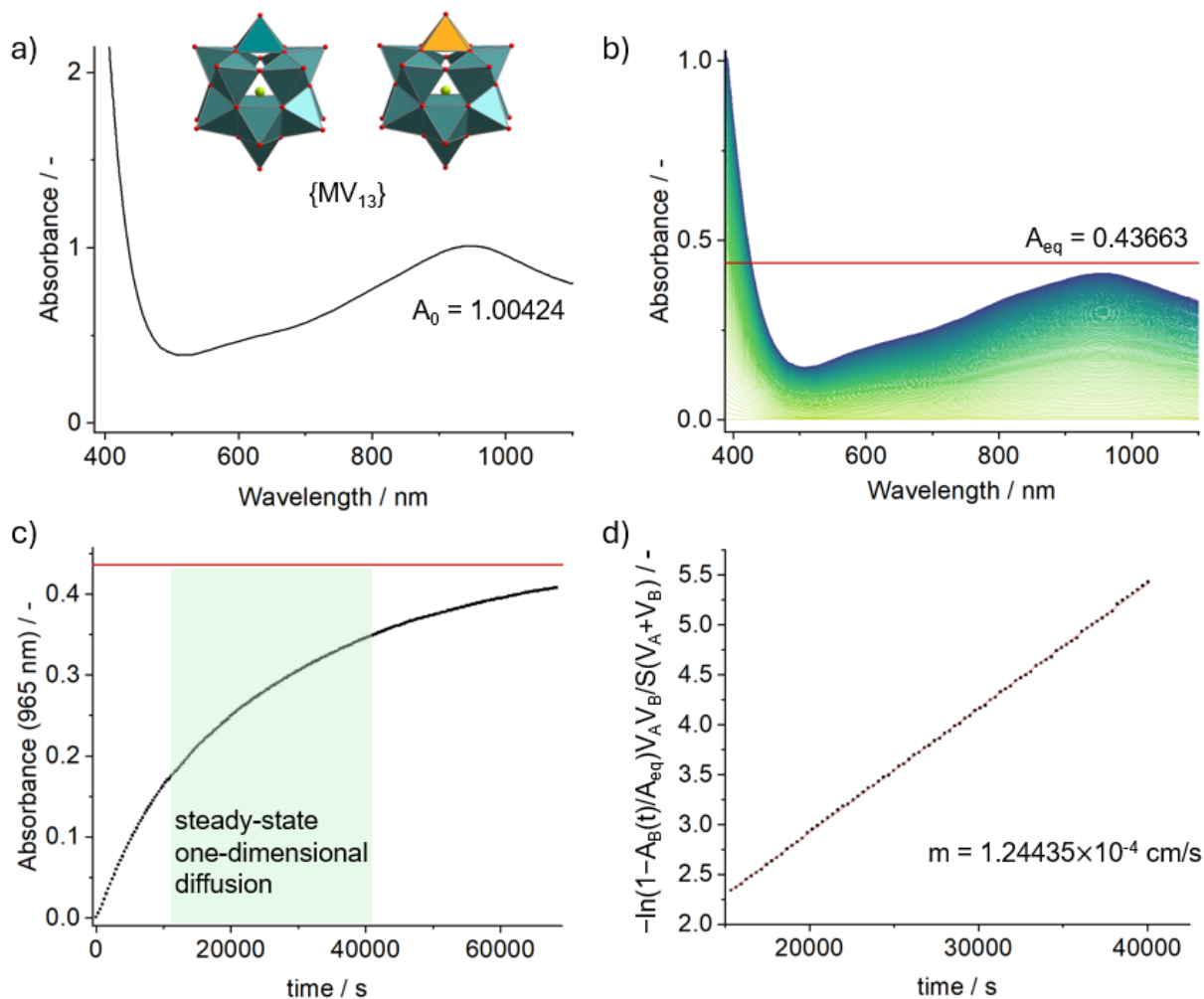


Figure 91: Permeability test to analyze the migration of $\{MV_{13}\}$ across a Celgard 2400 membrane. a) the initial absorbance in reservoir A, b) the increasing absorbance in reservoir B measured every 5 minutes, c) the development of the absorbance in reservoir B at 965 nm over time (The permeability was determined from 15000s to 40000s where steady-state one-dimensional diffusion can be assumed.), and d) the linear fit used to determine the permeability.

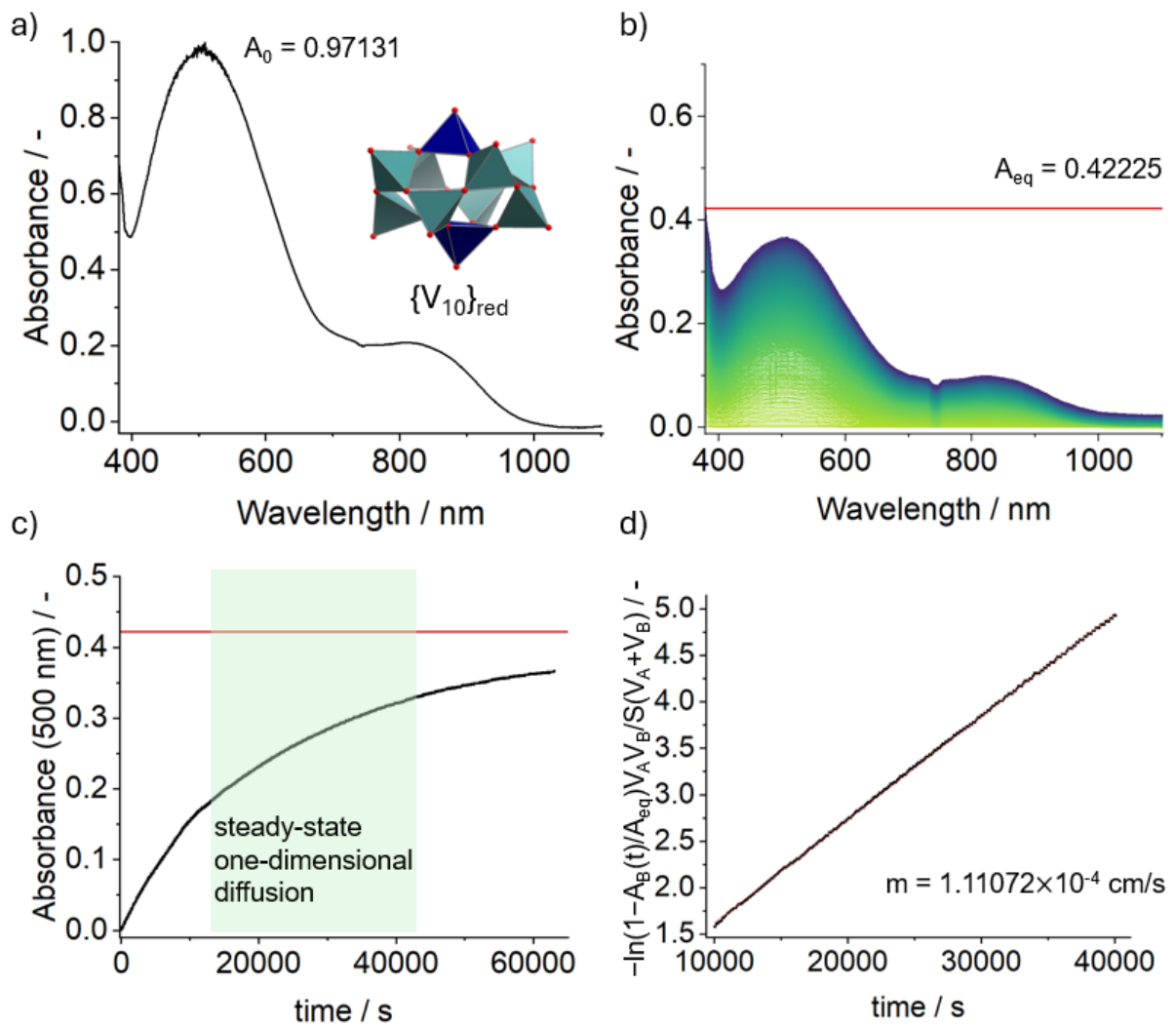


Figure 92: Permeability test to analyze the migration of $\{V_{10}\}_{red}$ across a Celgard 2400 membrane. a) the initial absorbance in reservoir A, b) the increasing absorbance in reservoir B measured every 5 minutes, c) the development of the absorbance in reservoir B at 965 nm over time (The permeability was determined from 15000s to 40000s where steady-state one-dimensional diffusion can be assumed.), and d) the linear fit used to determine the permeability.

Table 21: Diffusional permeability comparison of previously reported active species in electrolyte for RFBs.

Active species	Solvent	Membrane	Diffusional Permeability (cm² s⁻¹)	Ref
{MV ₁₃ }	Acetonitrile	Celgard 2400	3.11×10^{-7}	This work
{V ₁₀ } _{red}	Acetonitrile	Celgard 2400	2.78×10^{-7}	This work
[S ₂ W ₁₈ O ₆₂] ⁴⁻	Acetonitrile	AMI-7001	1.31×10^{-7}	[217]
MV	H ₂ O	Selemion DSV AEM	3.4×10^{-9}	[218]
BTMAP-Vi	H ₂ O	Selemion DSV AEM	6.7×10^{-10}	[218]
(PPBPy)Br ₂	H ₂ O	E620K	1.17×10^{-12}	[219]
PSS-TEMPO	H ₂ O	E620K	5.36×10^{-12}	[219]
(SPr) ₂ V	H ₂ O	N212CEM	8.0×10^{-9}	[220]
BPP-Vi	H ₂ O	N212 CEM	7.0×10^{-11}	[220]

Acknowledgements

The authors gratefully acknowledge financial support by the Deutsche Forschungsgemeinschaft DFG (Cluster of Excellence EXC2154, POLiS, project number: 390874152, and project number 389183496). M.A. gratefully acknowledges the State of Baden-Württemberg for a Margarete-von-Wrangell fellowship. C. S. gratefully acknowledges funding by the European Research Council ERC (ERC-CoG “SupraVox”, project number: 101002212), and financial support by Johannes Gutenberg University Mainz, the Rheinland-Pfalz Research Initiative SusInnoScience and the Gutenberg Research College. Z. C. acknowledges the China Scholarship Council CSC for financial support (no. 202106370057). Open Access funding enabled and organized by Projekt DEAL.

The authors declare no competing interests.

Author Contributions

M. Remmers	Synthesis and electrochemical characterization, paper writing and revision of the manuscript
B. Mashtakov	Electrochemical measurements paper writing and revision of the manuscript
Z. Chen	Initial tests of the battery setup and manuscript writing
S. Repp	Manuscript writing
K. Wang	Manuscript writing
R. Liu	Results discussion
M. Anjass	Discussion and revision of the manuscript
C. Streb	Conceived the idea, results discussion and writing of the manuscript

3.7. The Influence of Mixed Solvent Systems

Preliminary Note: The following data is part of a manuscripts and will be published as: “Oxidation State Guides Solvent Structure Around a Manganese Vanadium Cubane Water Oxidation Catalyst” by S. Tippner, M. Remmers, B. Mashtakov, M. Mondeshki, C. Streb,* L. González* These authors contributed equally: Simon Tippner and Moritz Remmers

3.7.1. Introduction

Catalytic reactivity is often governed by the solvent, as solvent-reagent catalyst interactions affect all steps of a catalytic process.^[221–223] Far from being mere spectators, solvents are increasingly recognized as active reaction participants capable of affecting reagent and catalyst properties, modulating reaction kinetics and influencing reaction pathways.^[224–226] Despite their key role, the influence of solvents on structure and reactivity remains notoriously difficult to characterize, as subtle structural reorganizations and dynamic interactions often elude direct observation. As a result, solvent effects are frequently inferred indirectly, e.g. as differences in reaction rates or solvent-dependent variations in product selectivity, rather than being observed directly at the molecular level. One area where solvent effects are particularly important is catalytic water splitting, a key sustainable energy technology.^[227] Here, water not only serves as solvent but also as reagent to be split into H₂ and O₂. The oxidation of water to molecular oxygen is particularly challenging, as it requires catalysts capable of accessing multiple oxidation states, mediating transfer of four electrons and four protons while maintaining stability under harsh oxidative conditions.^[228,229] Nature has achieved this feat by using the oxygen evolving complex (OEC) - a Mn₄CaO₅ cluster in Photosystem II - for light-induced oxidation of water to oxygen.^[230,231] Thus, it is not surprising that understanding the structural principles underlying this photosynthetic reaction has inspired widespread research into molecular water oxidation catalysts (WOCs).^[228,232] In the field of molecular metal oxides, or polyoxometalates (POMs), this has led to the development of a variety of transition metal functionalized WOC models including Ru, Co and Mn containing systems.^[115, 151,233,234] Among them, the mixed valence manganese-vanadium oxide POM (nBu₄N)₃[Mn^{III}₂Mn^{IV}₂V₄O₁₇(OAc)₃] (hereafter referred to as {MnV}ⁿ⁻, where n denotes the overall anionic charge) serves

as a structural and functional mimic of the natural OEC.^[235] The cluster features a central $[\text{Mn}_4\text{O}_4]^{6+}$ cubane core, capped by a $[\text{V}_4\text{O}_{13}]^{6-}$ vanadate unit, as well as three bridging acetate ligands (Figure 93).

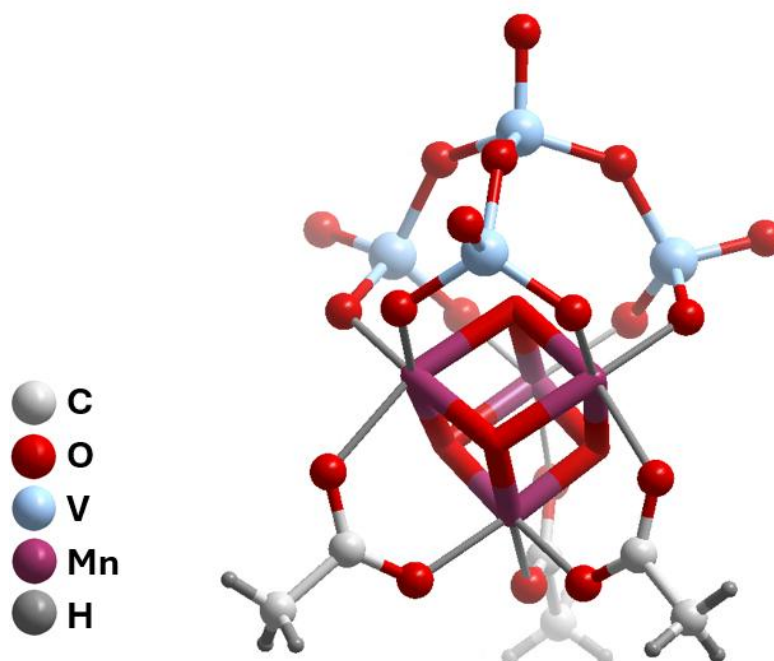


Figure 93: Structure of the $[\text{Mn}^{\text{III}}_2\text{Mn}^{\text{IV}}_2\text{V}_4\text{O}_{17}(\text{OAc})_3]^{3-}$.

The cluster shows promising WOC activity under photochemical and electrochemical conditions with a maximum turnover frequency of up to 3.6 s^{-1} , and maximum turnover numbers as high as 12,000 when operated in acetonitrile/water mixtures. However, the compound is unstable in pure water, undergoing degradation into Mn-V-oxide colloids.^[236] Earlier theoretical and experimental efforts ^[237–241] revealed, that the two experimentally accessible key species are the native cluster $\{\text{MnV}\}^{3-}$ (Mn oxidation states $\text{Mn}^{\text{III}}_2 \text{Mn}^{\text{IV}}_2$), and the one electron oxidized species $\{\text{MnV}\}^{2-}$ (Mn oxidation states $\text{Mn}^{\text{III}}\text{Mn}^{\text{IV}}_3$), while the two electron oxidized species $\{\text{MnV}\}^{1-}$ (Mn oxidation states Mn^{IV}_4), is difficult to stabilize or isolate experimentally. Prior experimental and theoretical studies on $\{\text{MnV}\}^{n-}$ have focused studying reactivity at the individual cluster level, thus neglecting the impact of the solvent environment.^[235,237] However, initial experimental data had shown that major differences in reactivity are observed depending on the acetonitrile : water ratio of the reaction solution. Note that previous works have highlighted significant effects of the solvent environment on a range of molecular WOCs: Meyer and co-workers reported, that the rate of water oxidation of a Ru WOC complex is significantly increased when the compound is operated in non-aqueous

solvents containing water as the reagent, and even observed the emergence of new reaction pathways.^[242,243] Building on this work, Meyer, Yang and co-workers demonstrated that the WOC activity mechanism of a Ru WOC complex is highly dependent on the proton content (i.e., pH value) of the aqueous solution.^[244] In a related work, Bernasconi, Baerends and colleagues suggested that the water shell around an iron WOC complex plays a key role in proton management during the water oxidation cycle.^[245] Similarly, Yang and co-workers demonstrated that intramolecular hydrogen bonding is a key factor in the reactivity of Co complex WOCs.^[246] For heterogeneous electrochemical WOC at IrO₂ nanoparticles operated in acidified acetonitrile water mixtures, Girault and colleagues identified a “tipping point”, at which low water concentrations lead to a decrease of the WOC onset potential. This unusual behavior was linked to the disruption of the hydrogen bond network between water molecules, resulting in the formation of isolated water clusters which are more easily oxidized compared to bulk water.^[247] In the field of POM water oxidation catalysis, there is a major knowledge gap regarding the impact of the solvent environment on POM-WOC activity. This is despite the fact that the chemistry and reactivity of POM anions is often modulated or even controlled by their counter-cations, while the interactions between these ionic species is in turn intrinsically linked to the solvent environment.^[150] In one pioneering study, Nazmutdinov and co-workers used density functional theory (DFT) and molecular dynamics (MD) to theoretically explore the stability and reactivity of the prototype POM WOC Na₁₀[Co₄(H₂O)₂(PW₉O₃₄)₂]. In purely aqueous systems, the authors observed Na⁺/POM ion pairing which also led to Na⁺ mediated formation of a water shell near the POM cluster.^[248] Similarly, Lopez and coworkers showed that the charge of a {V₁₈} cluster, as well as the type of counter-cation controls the cation-induced aggregation behavior in water and acetonitrile, thereby laying the foundation for our study.^[249] Here, we show how the solvent environment governs the redox chemistry, reactivity and stability of the {MnV} POM when operated in acetonitrile-water mixtures. To explore these phenomena, we combine molecular dynamics simulations with spectroscopic and electrochemical experiments to investigate the behavior of acetonitrile and water molecules around the catalyst in different oxidation states. By explicitly resolving solvent-catalyst interactions, we reveal how solvation shells form, how different redox states influence local solvent structure, and how these factors ultimately control the stability and reactivity of POM-based WOCs.

3.7.2. Results and Discussion

As an initial step, we performed a benchmark study of the solvent mixture force field by comparing various force fields and the densities obtained from MD simulations with experimental values. For acetonitrile/water mixtures, the six-site model combined with the SPC/Fw and q-SPC/Fw water model consistently demonstrate excellent agreement with the experimental values (Figure 94). Based on this, we used the six-site ACN with SPC/Fw for all subsequent POM simulations. Further details of the MD simulation setup are provided in the SI.

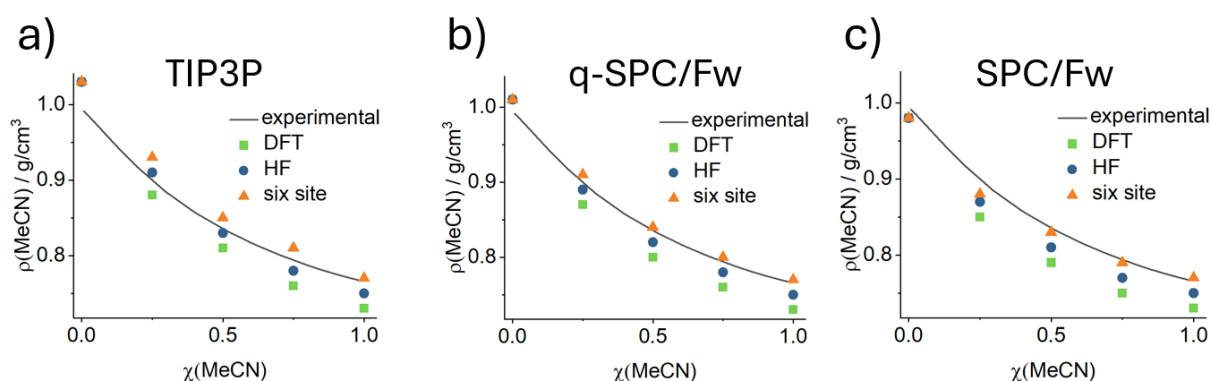


Figure 94: Comparison of the densities of acetonitrile/water mixtures obtained from different MD simulations compared to experimental values from literature.^[250]

POM in Acetonitrile/Water Mixtures

Next, we analyzed the solvation of $\{\text{MnV}\}^{3-}$, $\{\text{MnV}\}^{2-}$ and $\{\text{MnV}\}^{1-}$ in acetonitrile/water mixtures using RDFs. Figure 95a and c show the RDFs between the center of mass (CoM) of the POM and the hydrogen atoms of the solvents (water and acetonitrile) for all three charge states across different volumetric percentages of water. Here, we observe that increasing anionic charge ($\{\text{MnV}\}^{1-} \rightarrow \{\text{MnV}\}^{3-}$) results in increasing RDF intensity for H_2O -CoM. However, the non-linear trend is noteworthy: both $\{\text{MnV}\}^{1-}$ and $\{\text{MnV}\}^{2-}$ show weak solvent fine structuring, while $\{\text{MnV}\}^{3-}$ exhibits a strong interaction with water. This becomes increasingly evident at low water content e.g. at 0.5 vol% H_2O , where the first peak appears at 4.55 Å, with a $g(r)$ value of 8.01 for $\{\text{MnV}\}^{3-}$ which is much more pronounced compared to the value of 0.54 for $\{\text{MnV}\}^{2-}$, and 0.53 for $\{\text{MnV}\}^{1-}$. The accumulation of water molecules around the cluster leading to increased $g(r)$ indicates the formation of a water solvation shell around $\{\text{MnV}\}^{3-}$.

To quantify how strongly each charge state perturbs its surrounding solvent structure, we evaluated $n(r)$ at $r = 10 \text{ \AA}$ and calculated the fraction $q = n(r)/N_{\text{solvent}}$, with N_{solvent} being the total number of solvent molecules located in 10 \AA range to the cluster (Figure 95b and d). Notably, at increasing water content up to 10 vol% the changes in $q(r)$ of $\{\text{MnV}\}^{3-}$ become less pronounced, indicating that the hydration shell might have reached saturation. In contrast, $\{\text{MnV}\}^{2-}$ and $\{\text{MnV}\}^{1-}$ show overall little change in $q(r)$ with increasing water content, indicating that their solvation behavior is nearly independent on water concentration within the cluster stability range. In contrast to water, $q(r)$ of acetonitrile remains identical when adding water and is consistent across all oxidation states, showing that the interaction with acetonitrile is independent of both water content and oxidation state of the catalyst. This behavior shows that the solvent composition is dominated by water in these mixtures.

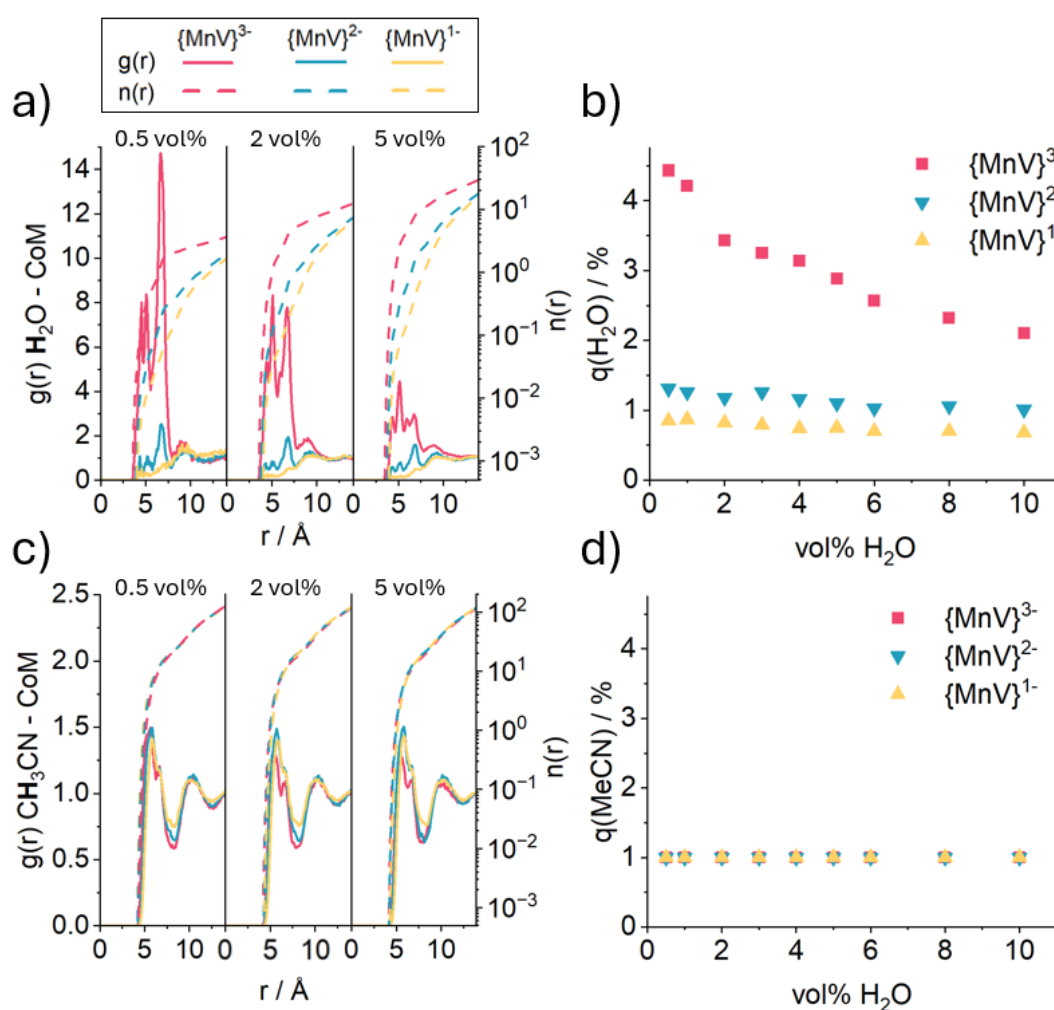


Figure 95: a) Radial distribution functions, $g(r)$, between the center of mass (CoM) of and the hydrogen atoms of water. Dashed lines indicate the corresponding integrated solvation numbers $n(r)$. b) Fraction of water molecules $q(\text{H}_2\text{O})$ residing within 10 \AA range of the cluster. c) Radial distribution functions, $g(r)$, between the center of mass (CoM) of and the hydrogen atoms of acetonitrile. Dashed lines indicate the corresponding integrated solvation numbers $n(r)$. d) Fraction of acetonitrile molecules $q(\text{MeCN})$ residing within 10 \AA range of the cluster.

In sum, the catalyst charge has a pronounced influence on the water microsolvation of $\{\text{MnV}\}^{3-}$ leading to a well-structured hydration shell which was not observed for $\{\text{MnV}\}^{2-}$ and $\{\text{MnV}\}^{1-}$.

Water Titration Study

In earlier work, we showed that the characteristic manganese d-d optical transitions can be used as a sensitive probe to gain insights into local structure changes at or around $\{\text{MnV}\}$.^[251] Here, we performed an experimental titration study to probe cluster solvent interactions in acetonitrile containing 0 - 5 vol% water, which was previously shown to be the stability range for $\{\text{MnV}\}^{3-}$ and $\{\text{MnV}\}^{2-}$.^[237] The $\{\text{MnV}\}^{2-}$ was quantitatively prepared from $\{\text{MnV}\}^{3-}$ by bulk electrolysis,^[235] and both species were fully characterized, see SI, Section 3.8.2. Since $\{\text{MnV}\}^{1-}$ cannot be prepared and stabilized under the given experimental conditions, it was excluded from the study. Upon addition of water to the cluster solution, a color change from light orange to a more intense brown color was observed (see Figure 96a-b). UV-Vis measurements (Figure 96c-d) confirmed an overall increase in absorption while the positions of the absorption maxima remained essentially unchanged. Notably, these characteristic spectral changes are distinct from previously reported changes which were due to cluster protonation or cluster oxidation state changes.^[235,251] The absorption bands can be assigned to the manganese centered d-d transitions of Mn^{4+} at 350 nm, and Mn^{3+} at 600 nm. Figure 96e shows the difference spectra (relative absorbance) of samples containing 5 vol% water compared to the water-free samples. The increase at approximately 350 nm is more pronounced for $\{\text{MnV}\}^{2-}$ due to the higher number of Mn^{4+} centers. At the same time $\{\text{MnV}\}^{3-}$ shows a more pronounced increase at higher wavelengths which are attributed to low intensity, Laporte-forbidden Mn^{3+} d-d transitions.^[251]

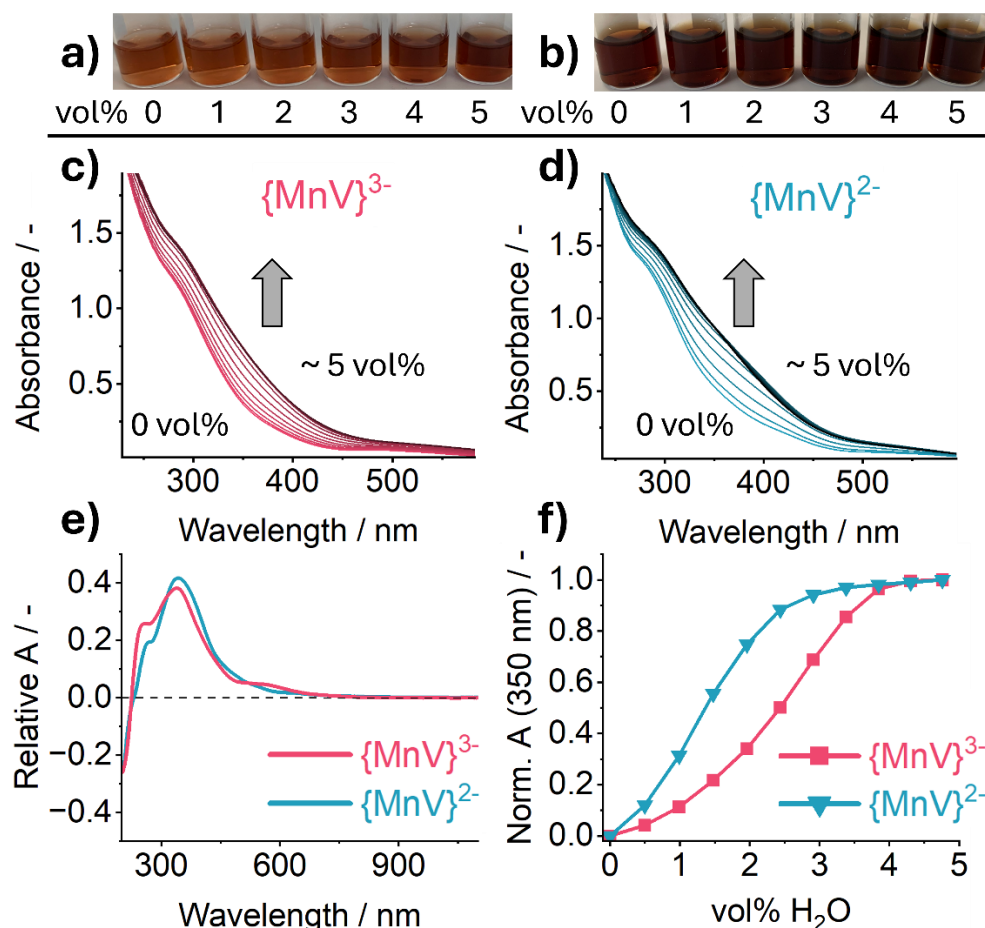


Figure 96: a,b) The increasing absorbance with addition of water is visible by the darker color of samples prepared at 1 mM concentration of the cluster and gradually increasing vol% water. c) UV-Vis spectra of $\{\text{MnV}\}^{3-}$ and d) of $\{\text{MnV}\}^{2-}$ at a cluster concentration of about 50 μM . Water was added in 20 μL steps to 2 mL of water free sample and the spectra were corrected by the dilution factor. e) The relative absorbance of the UV-Vis spectrum at 5 vol% of water after subtraction of the spectrum at 0 vol% of water for $\{\text{MnV}\}^{3-}$ and $\{\text{MnV}\}^{2-}$ and f) the changes of the normalized absorbance at 350 nm with increasing vol% water of $\{\text{MnV}\}^{3-}$ and $\{\text{MnV}\}^{2-}$.

These distinct changes are explained by hydrogen bonding of unsymmetrically distributed water molecules in the solvation shell of the cluster. Breaking the octahedral symmetry through asymmetric vibrations in the presence of hydrogen bonded water molecules can lead to a relaxation of the LaPorte rule, thereby increasing the observed absorbance. Notably, these changes occur earlier for $\{\text{MnV}\}^{2-}$ at water contents up to 3 vol% while $\{\text{MnV}\}^{3-}$ requires about 5 vol% water for this effect to reach completion (see Figure 96f). This is in line with the MD simulations, which show that the saturation of the solvation shell of $\{\text{MnV}\}^{3-}$ requires larger amounts of water compared to $\{\text{MnV}\}^{2-}$, due to the stronger anion-dipole interactions between the more negatively charged POM and the solvent. Note that typically, d-d-based transitions are only weakly affected by bulk solvent effects (e.g., polarity changes upon addition of water), while changes of the first manganese coordination sphere, e.g., by acetate ligand exchange also need to be considered.^[252] Calculations regarding the detailed reaction mechanism are

presented in our previous work and reveal a lower acetate ligand exchange activation barrier for $\{\text{MnV}\}^{2-}$ compared to $\{\text{MnV}\}^{3-}$. (see Figure 96f)^[237] Here, this is verified by liquid FTIR results, which indicate that for $\{\text{MnV}\}^{3-}$ and $\{\text{MnV}\}^{2-}$, approximately one acetate ligand per cluster is exchanged for water ligands on the timescale of the titration experiments (approximately 60 minutes; SI, Section 3.8.2). Further evidence for this ligand exchange is provided by high-resolution electrospray ionization mass spectrometry (HR-ESI-MS), where increasing amounts of free acetate ligands are observed for $\{\text{MnV}\}^{3-}$ with increasing water content (see SI). To confirm the initial formation of a hydrogen-bonded water network around the cluster, we performed a titration study to study the characteristic V=O bands at 930-1000 cm^{-1} using liquid-phase FT-IR spectroscopy. Note that under water-free conditions, we observe the characteristic vibrations at higher wavenumbers for $\{\text{MnV}\}^{2-}$ compared to $\{\text{MnV}\}^{3-}$ (see Figure 97a,b). This is in line with our previous calculations^[251] and arises from changes in electron density at the terminal V=O bonds associated with different charge states. FT-IR analysis shows that increasing water concentrations lead to a weakening and broadening of the vibrational modes, a feature which is more pronounced for $\{\text{MnV}\}^{3-}$. Here the two bands virtually merge while for $\{\text{MnV}\}^{2-}$, the characteristic two-peak pattern is still observed at water contents of 5 vol%. These changes in peak shape and position can be directly attributed to hydrogen bonding between water molecules of the solvation shell and the V=O groups, which lowers the electron density at the terminal oxo ligands and induces fluctuations in the local electronic structure.

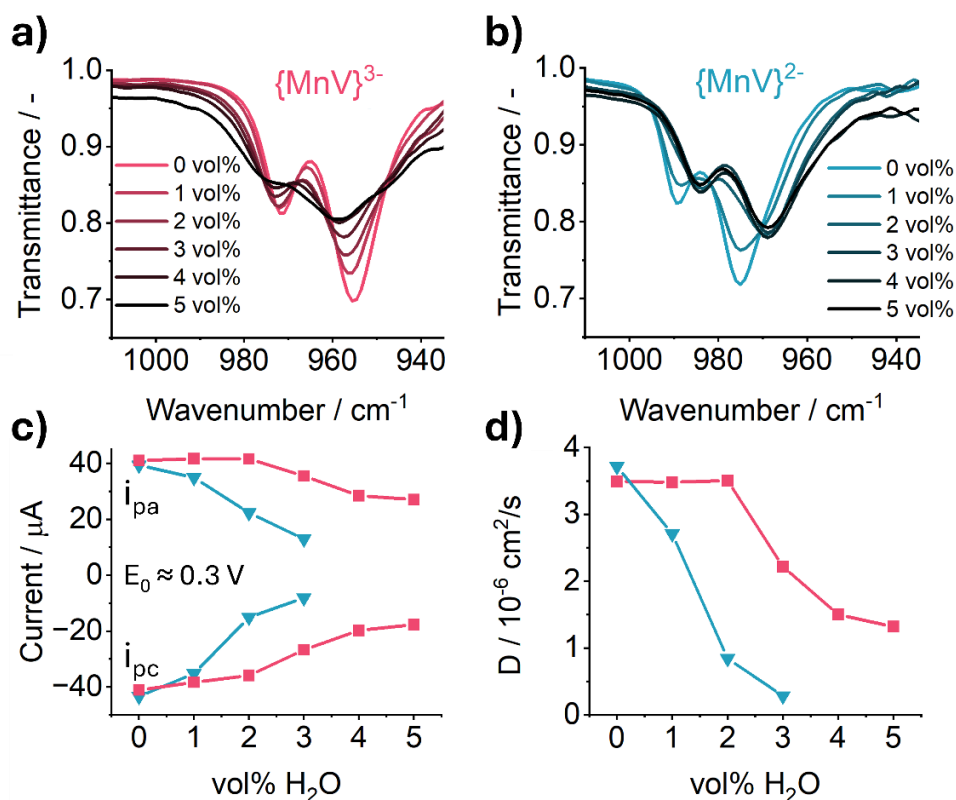


Figure 97: Liquid FTIR spectra of $\{\text{MnV}\}^{3-}$ (a) and $\{\text{MnV}\}^{2-}$ (b), showing changes of the characteristic vibrations with variation of the water content. Conditions: concentration 10 mM, pathlength 0.05 mm c) Electrochemical analysis of the anodic (i_{pa}) and cathodic (i_{pc}) peak current changes with varying water contents for $\{\text{MnV}\}^{3-}$ (red) and $\{\text{MnV}\}^{2-}$ (blue). Conditions concentration 1 mM d) Electrochemical analysis of the diffusion coefficients (determined by RS analysis) for $\{\text{MnV}\}^{3-}$ (red) and $\{\text{MnV}\}^{2-}$ (blue). Conditions: concentration 1 mM

The formation of a solvation shell is further indicated by $^1\text{H-NMR}$ spectroscopy, where a characteristic decrease in T_1 relaxation time of the water protons indicates reduced tumbling rate due to the formation of a hydrogen bonding network with the cluster (see SI). Also, for $\{\text{MnV}\}^{2-}$ we observe the formation of a new species at water contents above 3 vol%. Based on comparison between the solid-state and liquid FT-IR spectra, we propose that this effect is due to (cation- and solvent-mediated) aggregation of several clusters.^[249] Similar behavior has been reported previously for related polyoxovanadates.^[181] Water induced cluster aggregation is further supported by electrochemical analysis which shows less pronounced redox-events and decreasing diffusion coefficients with increasing water content (Figure 97c,d). In fact, aggregation could also contribute to the disappearance of characteristic cluster-based ^1H , $^{51}\text{V-NMR}$ and ESI-MS signals as well as the decreasing T_1 relaxation times observed (for details see SI). The study reveals that the complex behavior of the cluster in solvent mixtures requires the consideration of several solvent induced effects at the same time, thus additional simulations targeting e.g. aggregation are still required to gain deeper understanding of the experimental observations.

3.7.3. Conclusion

In this combined computational and experimental study, we examined the solvation environment of the {MnV} polyoxometalate (POM) catalyst in various oxidation states ($\{\text{MnV}\}^{3-}$, $\{\text{MnV}\}^{2-}$, and $\{\text{MnV}\}^{1-}$) immersed in different acetonitrile-water mixtures. Our results highlighted distinct differences in solvation structures influenced by the oxidation state and charge of the POM. While $\{\text{MnV}\}^{3-}$ forms a strongly pronounced solvation shell this effect cannot be observed for $\{\text{MnV}\}^{2-}$, and $\{\text{MnV}\}^{1-}$. This was confirmed by liquid FTIR and UV-Vis as well as electrochemical measurements which revealed a much more complex interplay between solvation, ligand exchange and aggregation of multiple clusters. Nevertheless, our observation that acetonitrile molecules assist in driving water closer to the catalyst provides a possible explanation for the experimentally observed improved catalytic efficiency in solvent mixtures. With this study, we aim to highlight how the oxidation state of polyoxometalates significantly impacts their local solvent environment. To complete the study a three-dimensional RDF analysis and further MD simulations including multiple clusters will provide valuable information on the hydrogen bonding of the solvent molecules and on a possible aggregation. We hope that this insight will motivate researchers to consider such effects when designing and optimizing new catalysts.

3.8. Supporting Information:

3.8.1. Instrumentation

Attenuated total reflectance Fourier transformed infrared spectroscopy (ATR FT IR) were performed using a Bruker Alpha II equipped with an ATR Platinum Diamond unit. The data were recorded with 24 scans at a resolution of 4 cm^{-1} . All spectra were background corrected within the Bruker OPUS 8.1 program suite.

Liquid Fourier transformed infrared spectroscopy (liquid FT IR) measurements were performed using a Bruker Alpha II equipped with Alpha II T sampling module. The data were recorded with 16 scans at a resolution of 2 cm^{-1} in an Omnis liquid cell with CaF_2 windows at a path length of 0.2 mm. All spectra were background corrected within the Bruker OPUS 8.1 program suite using the solvent as reference.

High resolution electrospray ionization mass spectrometry (ESI-MS) was carried out on an Agilent 6545 QTOF HRAM MS system in negative ion mode at a drying gas temperature of $T = 180\text{ }^\circ\text{C}$.

Nuclear magnetic resonance (NMR) spectroscopy

Bruker Avance Neo NMR spectrometer (Bruker Biospin GmbH, Rheinstetten, Germany) equipped with a 5 mm BBF/F/H TBO iProbe head and Sample Case Plus autosampler was used to record all ^1H -NMR spectra at ^1H frequency of 400.3 MHz. The ^1H spectra were recorded applying a 30° pulse averaging 16 scans with 2 s recycle delay. The ^1H T_1 relaxation was measured using the inversion recovery pulse sequence averaging 16 scans with 5 s recycle delay and variable delays of 0.000005 s, 0.000005 s, 0.00001 s, 0.0001 s, 0.0005 s, 0.001 s, 0.005 s, 0.01 s, 0.1 s, 0.25 s, 0.5 s and 1 s. The NMR spectra were analyzed using the program MestReNova (version 14.3.2 32681 / 23.03.2023, Mestrelab Research S. L.). The oxygen free samples were prepared by three freeze pump thaw cycles and sealed in the glovebox with Leica Cryptoseal (Leica Microsystems Vertrieb GmbH, Wetzlar, Germany). The ^1H -NMR spectra were referenced using the solvent lock (^2H) signal in accordance with the IUPAC recommended secondary referencing methods.^[253] ^{51}V -NMR spectra were referenced to external $\text{VOCl}_3 + 5\% \text{C}_6\text{D}_6$ at 0 ppm.

UV-Vis/NIR spectroscopy was performed on a Cary 3500 UV-Vis/NIR spectrophotometer equipped with a Xenon flash lamp (250 Hz). Measurements were performed in quartz glass cuvettes (d = 10.0 mm).

Electrochemical investigations

All experiments were carried out under ambient conditions in water free acetonitrile at room temperature, using 0.1 M n-Bu₄NPF₆ as supporting electrolyte. **Cyclic voltammetry** and **square-wave voltammetry** were performed on a CH Instruments 760E potentiostat in three electrode configuration: a glassy carbon with d = 3.0 mm was used as working electrode, a silver wire in acetonitrile containing 0.1 M n-Bu₄NPF₆ and 10 mM AgNO₃ was used as reference electrode and a platinum wire was used as counter electrode. All electrodes were cleaned with acetone and acetonitrile each time before use and the working electrode was additionally polished with 0.05 μm Al₂O₃ before each measurement. **Chronoamperometry** was performed on a CH Instruments 760E potentiostat in three electrode configuration: platinum wires were used as working and counter electrode, a silver wire in acetonitrile containing 0.1 M n-Bu₄NPF₆ and 10 mM AgNO₃ was used as a reference electrode. All electrodes were cleaned with acetone and acetonitrile before each experiment. During the experiment the working electrode was kept at the defined potential while the solution was stirred vigorously. The electrolysis was stopped after 2000 s.

Chemicals: All chemical reagents were obtained commercially and used as received unless stated otherwise. (n-Bu₄N)₃[Mn₄V₄O₁₇(OAc)₃] x 3H₂O (= (n-Bu₄N)₃{MnV}) was prepared according to the literature.^[235]

3.8.2. Experimental data

The identity and purity of the brown cubic block shaped single crystals of $(n\text{-Bu}_4\text{N})_3\{\text{MnV}\}$ was confirmed by FT IR, ESI-MS and NMR spectroscopy as well as cyclic voltammetry.

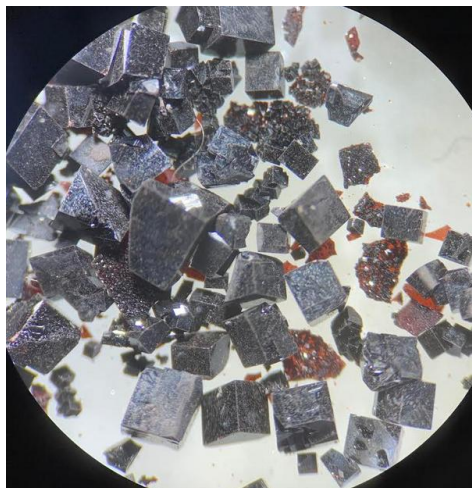


Figure 98: Brown cubic block shaped crystals of $(n\text{-Bu}_4\text{N})_3\{\text{MnV}\}$ were used for all measurements.

FTIR Spectroscopy

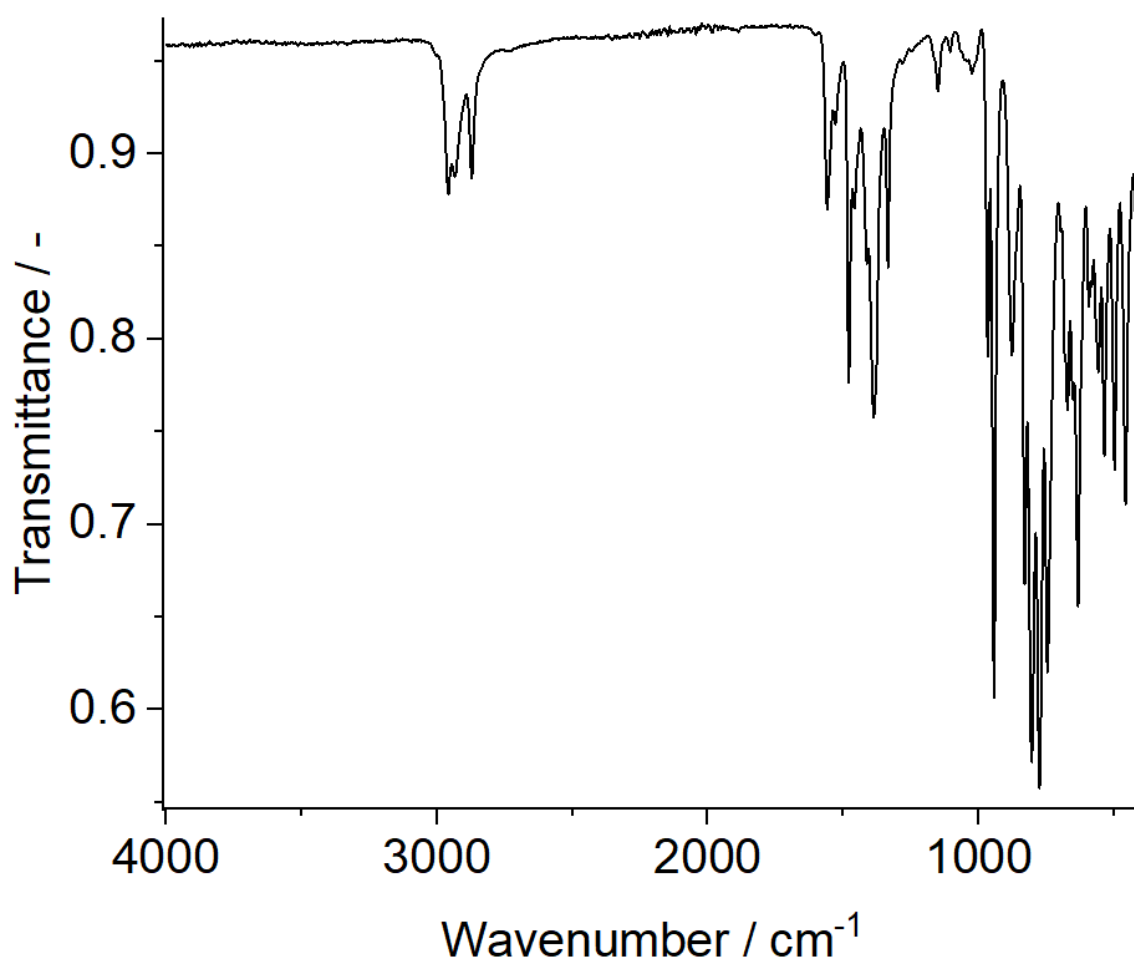


Figure 99: FTIR spectrum of (n-Bu₄N)₃{MnV}.

Electrochemistry: Electrochemical Generation of $\{\text{MnV}\}^{2-}$

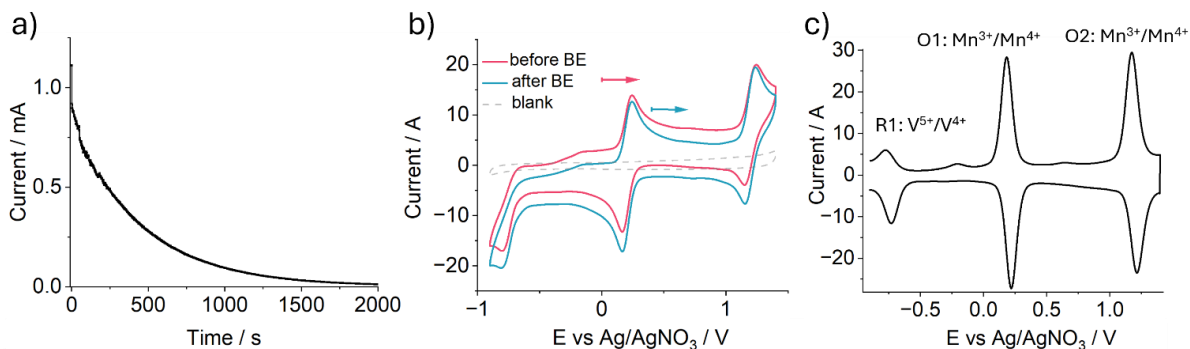


Figure 100: a) Chronoamperogram of bulk electrolysis (BE) at $E = 0.65$ V of 1 mM solution of $(n\text{-Bu}_4\text{N})_3\{\text{MnV}\}$ in water free acetonitrile containing 0.1 M $n\text{-Bu}_4\text{NPF}_6$ as supporting electrolyte. b) A cyclic voltammogram before and after bulk electrolysis was recorded at a glassy carbon electrode (3 mm diam.) scan rate: 100 mV/s vs. Ag/AgNO_3 . The open circuit potentials and scan directions are indicated by arrows. Note that no compound degradation is observed during the one electron oxidation. c) The redox transitions were assigned using square-wave voltammetry according to the literature.^[235]

Electrochemistry: Titration of H_2O

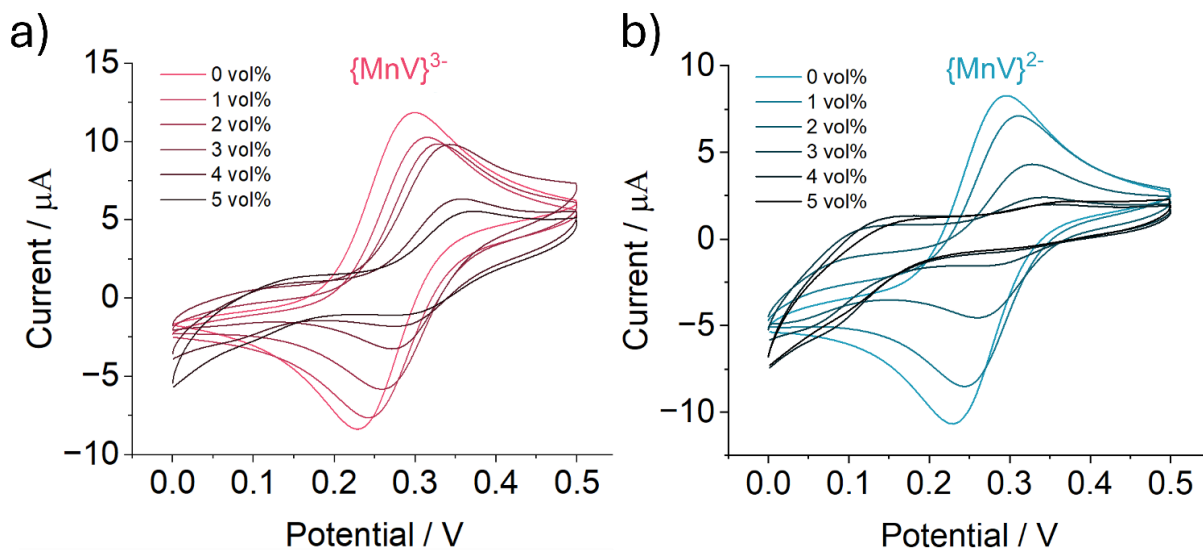


Figure 101: Cyclic voltammogram at increasing vol% water of a) $\{\text{MnV}\}^{3-}$ and b) $\{\text{MnV}\}^{2-}$ at a scan rate of 50 mV/s.

Randles–Ševčík Analysis: Titration of H₂O

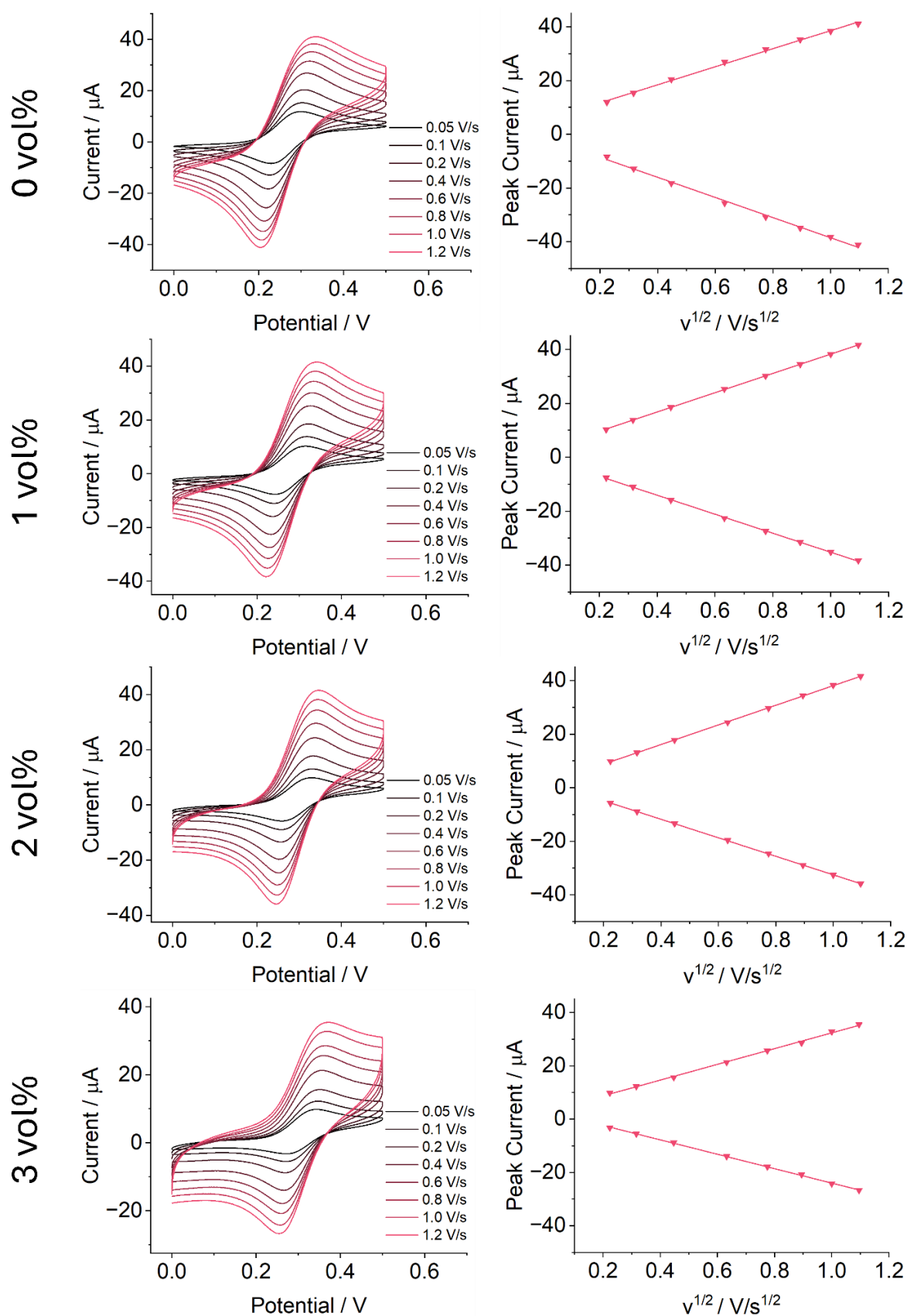


Figure 102: Randles–Ševčík analysis of 1 mM solution of $\{MnV\}^{3-}$ at different vol% of water.

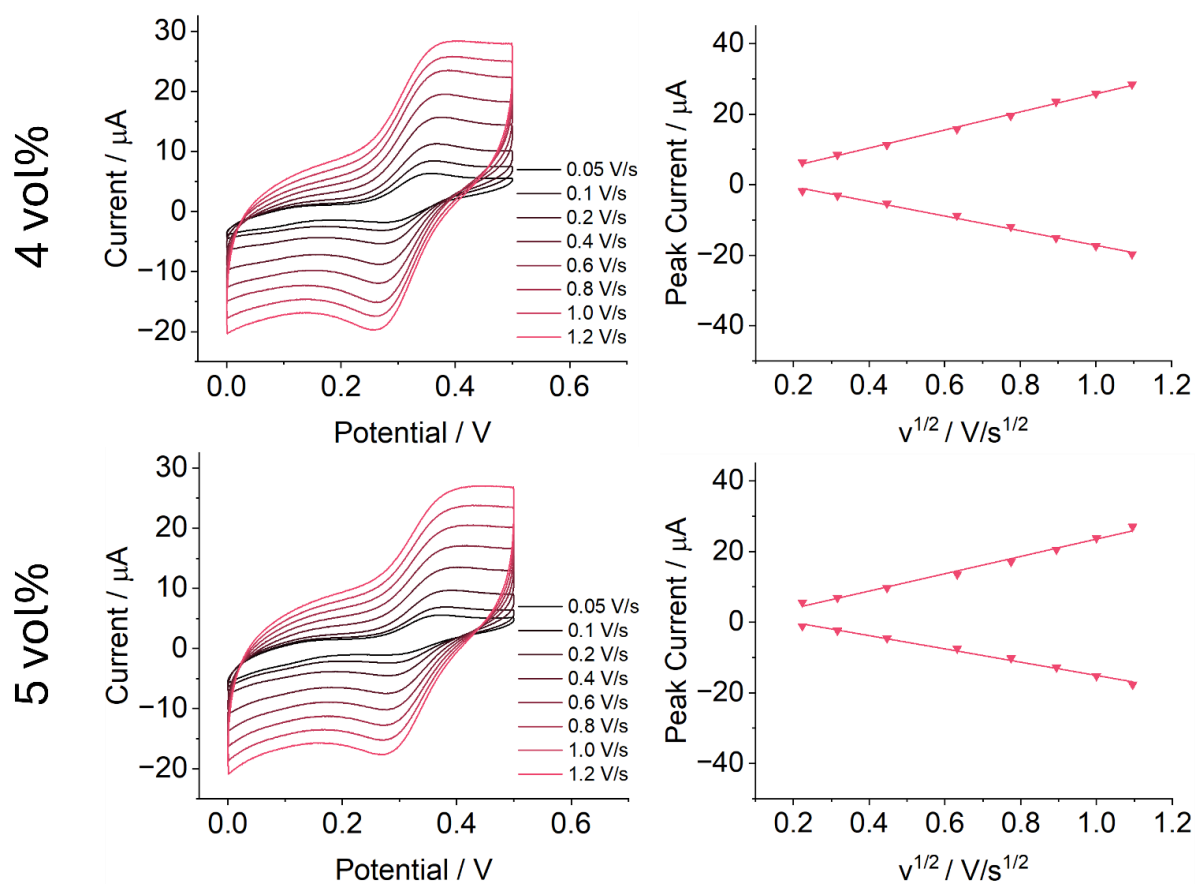


Figure 103: Randles–Ševčík analysis of 1 mM solution of $\{MnV\}^{3-}$ at different vol% of water.

Table 22: Slopes of the linear regression of anodic and cathodic peak currents i_{pa} and i_{pc} and average diffusion coefficients of $\{MnV\}^{3-}$ determined by the Randles–Ševčík equation.

vol% H ₂ O	Slope i_{pa} [A s ^{1/2} V ^{1/2}]	Slope i_{pc} [A s ^{1/2} V ^{1/2}]	Avg. Diffusion Coefficient [cm ² /s]
0	3.36×10^5	3.74×10^5	3.49×10^6
1	3.57×10^5	3.52×10^5	3.48×10^6
2	3.66×10^5	3.46×10^5	3.51×10^6
3	2.95×10^5	2.71×10^5	2.22×10^6
4	2.55×10^5	2.08×10^5	1.50×10^6
5	2.45×10^5	1.88×10^5	1.32×10^6

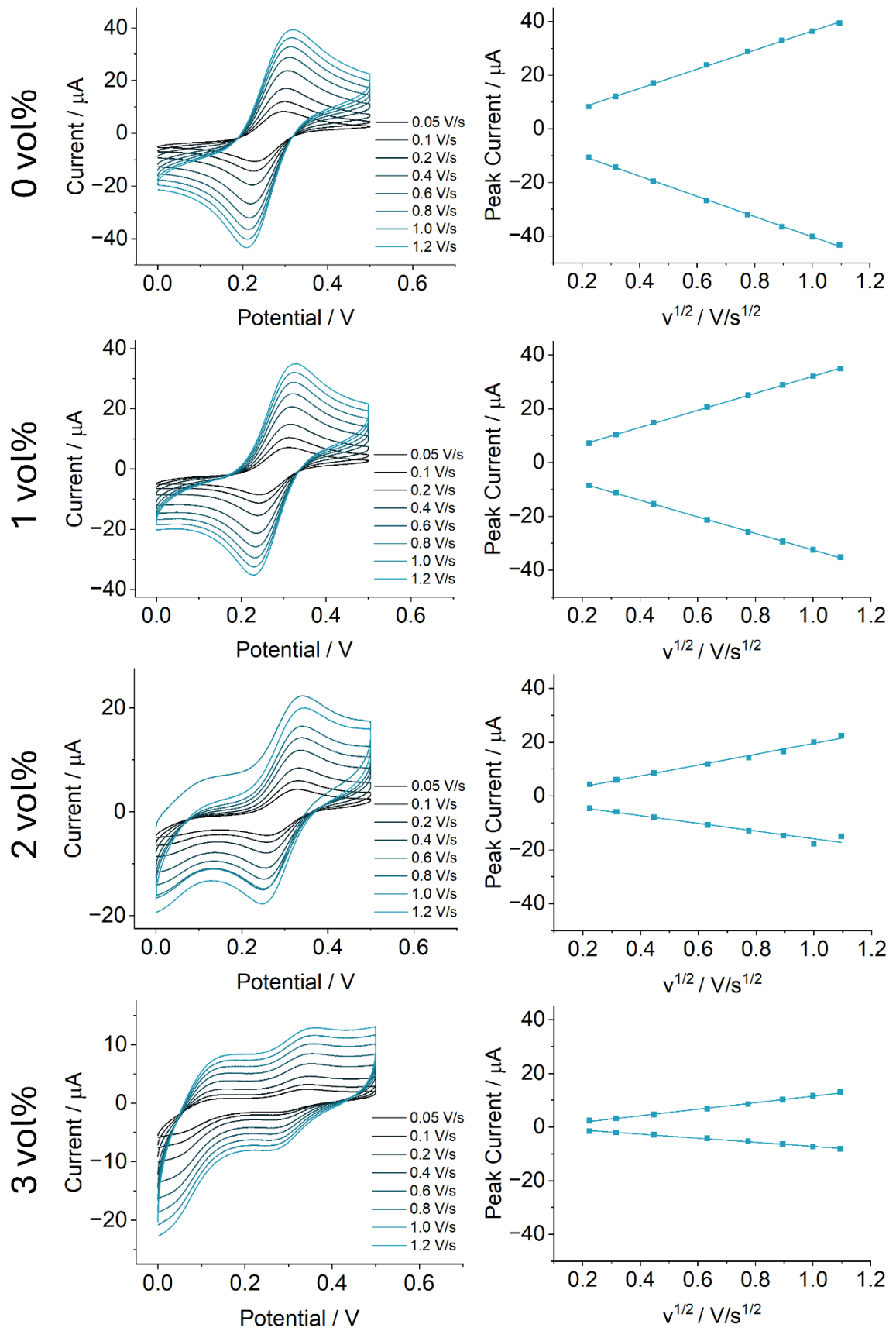


Figure 104: Randles-Ševčík analysis of 1 mM solution of $\{MnV\}^{2-}$ at different vol% of water.

Table 23: Slopes of the linear regression of anodic and cathodic peak currents i_{pa} and i_{pc} and average diffusion coefficients of $\{MnV\}^{2-}$ determined by the Randles–Ševčík equation.

vol% H₂O	Slope i_{pa} $As^{1/2}V^{1/2}$	Slope i_{pc} $As^{1/2}V^{1/2}$	Avg. Diffusion coefficient cm^2/s
0	3.56×10^{-5}	3.77×10^{-5}	3.76×10^{-6}
1	3.17×10^{-5}	3.09×10^{-5}	2.71×10^{-6}
2	2.01×10^{-5}	1.43×10^{-5}	0.84×10^{-6}
3	1.22×10^{-5}	0.76×10^{-5}	0.29×10^{-6}

ESI Mass Spectroscopy: $\{\text{MnV}\}^{3-}$ and $\{\text{MnV}\}^{2-}$

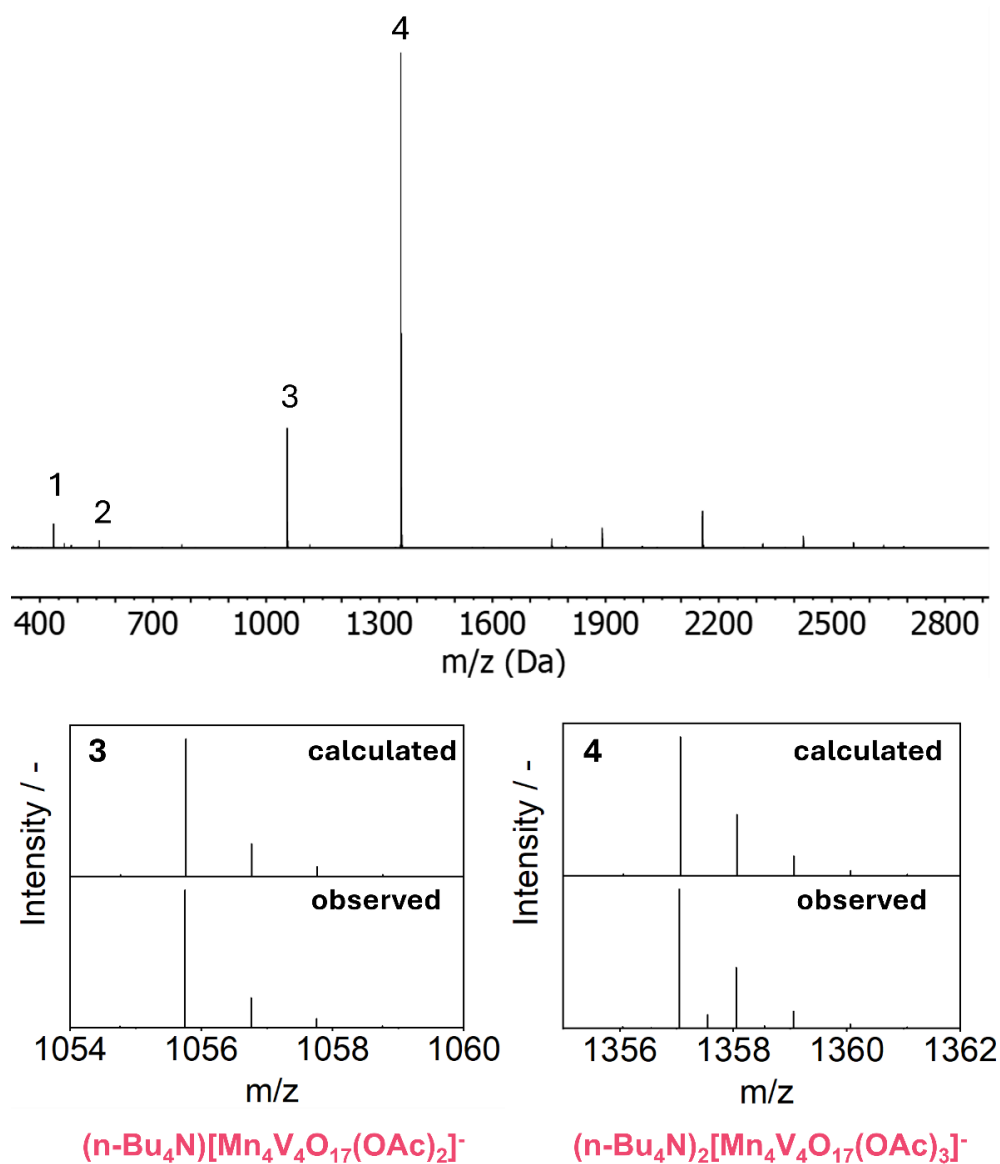


Figure 105: High resolution negative ion mode ESI mass spectrum of $\{\text{MnV}\}^{3-}$ (0.05 mM) in acetonitrile. The isotopic distribution was calculated for the two main signals 3 and 4.

Table 24: Detailed peak assignment of the high resolution negative ion mode ESI mass spectrum of $\{\text{MnV}\}^{3-}$.

Nr.	Fragment	observed / m/z	calculated / m/z
1	$[\text{Mn}_4\text{V}_4\text{O}_{17}(\text{OAc})_3]^{2-}$	436.24	436,25
2	$(n\text{ Bu}_4\text{N})[\text{Mn}_4\text{V}_4\text{O}_{17}(\text{OAc})_3]^{2-}$	557.38	557.39
3	$(n\text{ Bu}_4\text{N})[\text{Mn}_4\text{V}_4\text{O}_{17}(\text{OAc})_2]^-$	1055.75	1055,77
4	$(n\text{ Bu}_4\text{N})_2[\text{Mn}_4\text{V}_4\text{O}_{17}(\text{OAc})_3]^-$	1357.05	1357.06

Note that similar signals have been observed in previous literature.^[235]

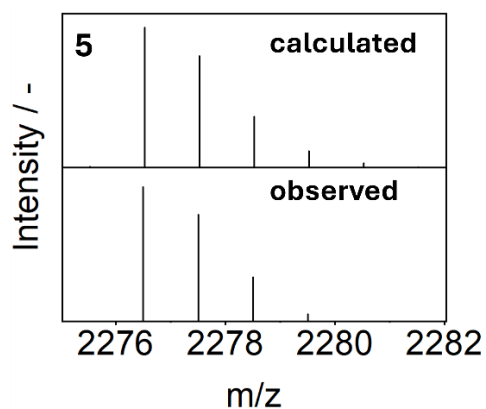
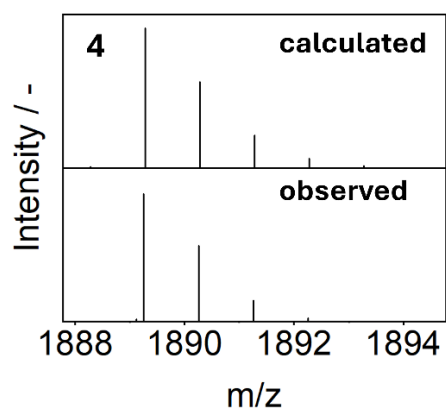
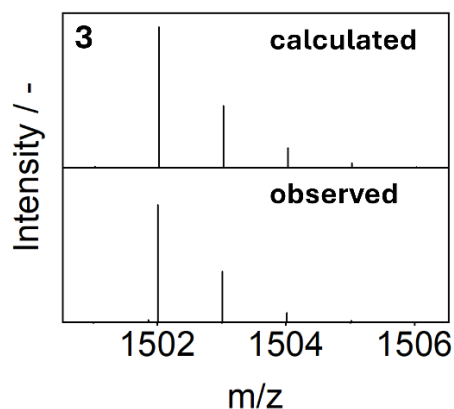
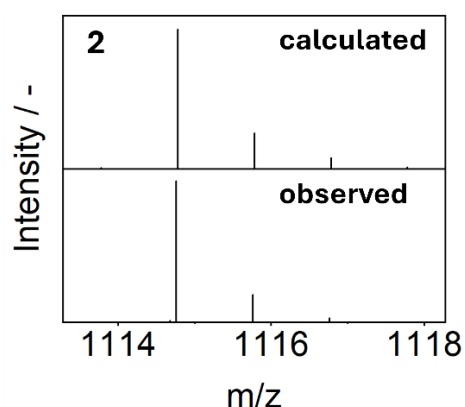
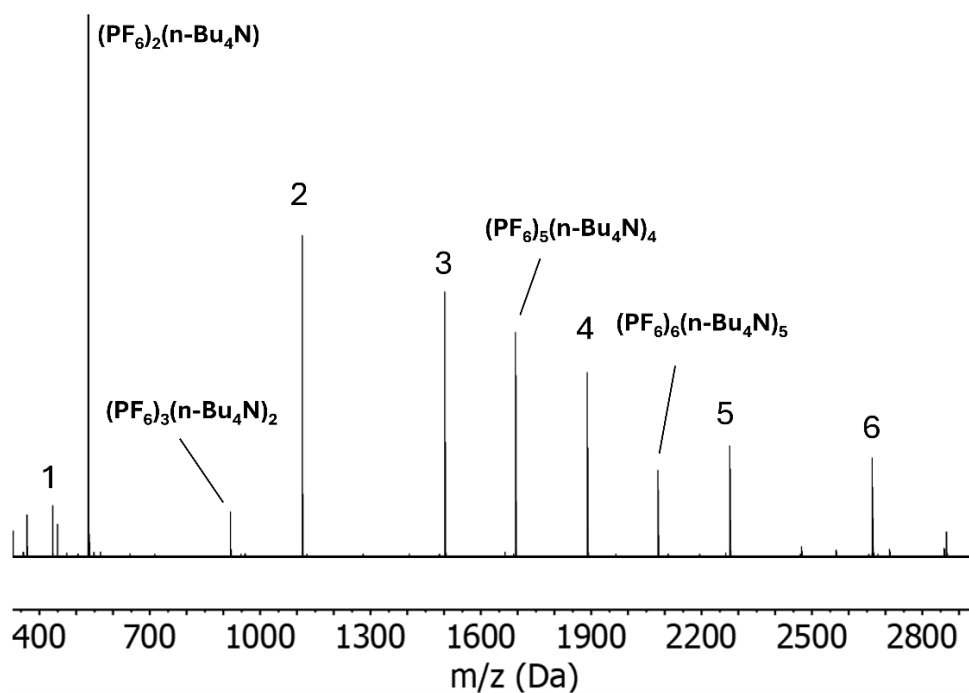


Figure 106: High resolution negative ion mode ESI mass spectrum of $\{\text{MnV}\}^{2-}$ (0.05 mM) in acetonitrile containing residual $(n\text{-Bu}_4\text{N})\text{PF}_6$ from the bulk electrolysis (5 mM).

Table 25: Peak assignments of the high-resolution negative ion mode ESI mass spectrum of $\{\text{MnV}\}^{2-}$.

Nr.	Fragment	observed / m/z	calculated / m/z
1	$[\text{Mn}_4\text{V}_4\text{O}_{17}(\text{OAc})_3]^2$	436.24	436,25
2	$(n \text{ Bu}_4\text{N})[\text{Mn}_4\text{V}_4\text{O}_{17}(\text{OAc})_3]$	1114.76	1114.78
3	$(\text{PF}_6)(n \text{ Bu}_4\text{N})_2[\text{Mn}_4\text{V}_4\text{O}_{17}(\text{OAc})_3]$	1502.01	1502.03
4	$(\text{PF}_6)_2(n \text{ Bu}_4\text{N})_3[\text{Mn}_4\text{V}_4\text{O}_{17}(\text{OAc})_3]$	1889.26	1889.28
5	$(\text{PF}_6)_3(n \text{ Bu}_4\text{N})_4[\text{Mn}_4\text{V}_4\text{O}_{17}(\text{OAc})_3]$	2276.50	2276.53
6	$(\text{PF}_6)_4(n \text{ Bu}_4\text{N})_5[\text{Mn}_4\text{V}_4\text{O}_{17}(\text{OAc})_3]$	2663.74	2663.77

ESI Mass Spectroscopy: Titration of H_2O

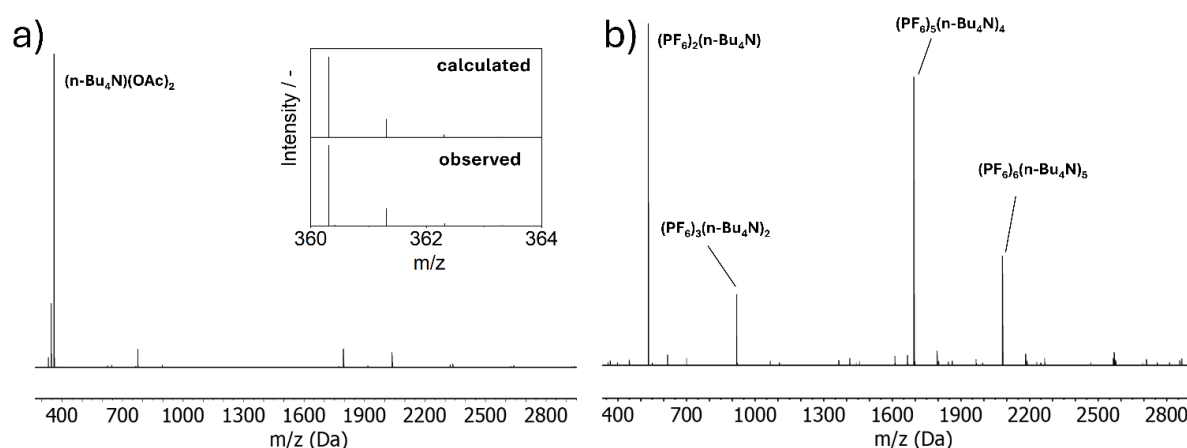


Figure 107: High resolution negative ion mode ESI mass spectrum of a) $\{\text{MnV}\}^{3-}$ including the assignment of $(n\text{-Bu}_4\text{N})(\text{OAc})_2$ and b) $\{\text{MnV}\}^{2-}$ (0.05 mM) in acetonitrile containing 5 vol% water. In both spectra no cluster signals were detected likely due to ion pairing and aggregation.

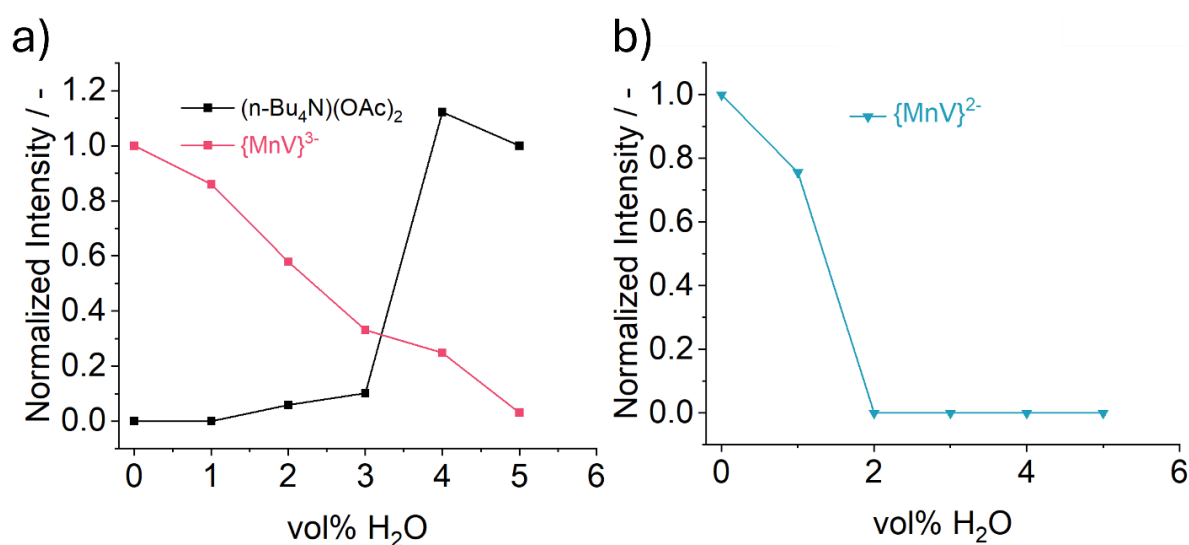


Figure 108: a) Normalized signal intensity of $(n\text{-Bu}_4\text{N})(\text{OAc})_2$ at increasing water content. The cluster signals of $\{\text{MnV}\}^{3-}$ decrease to a water content of 5 vol%. b) The cluster signals of $\{\text{MnV}\}^{2-}$ are not observable at a water content above 2 vol% likely due to aggregation. No acetate related signals were detected in the presence of electrolyte.

UV-Vis Spectroscopy

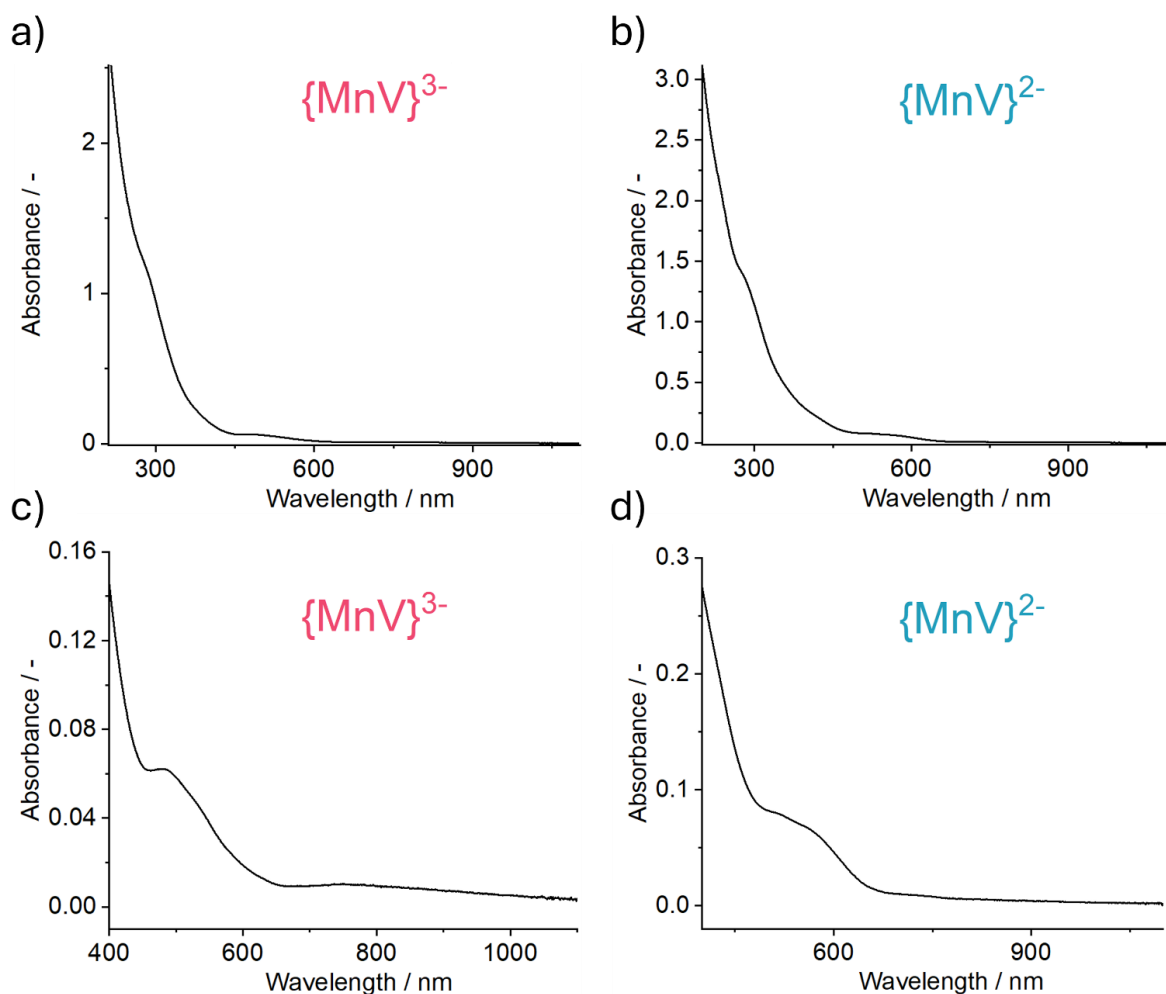


Figure 109: a, b) A UV-Vis spectrum of $\{MnV\}^{3-}$ and $\{MnV\}^{2-}$ was measured at ambient conditions at a concentration of 50 μM . The range of 400 nm to 1100 nm is shown in c) and d).

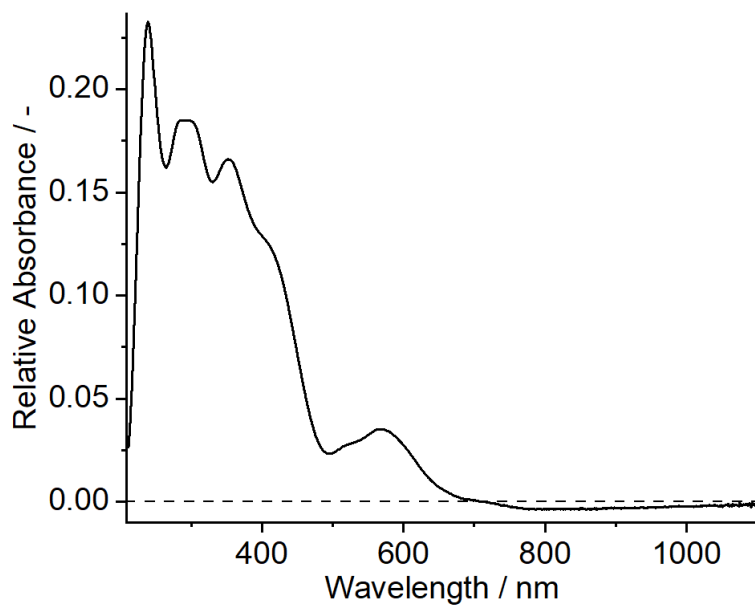


Figure 110: Relative absorbance of $\{MnV\}^{2-}$ compared to $\{MnV\}^{3-}$. The spectrum of $\{MnV\}^{3-}$ was subtracted as reference and agrees with the literature.^[251]

Liquid IR Spectroscopy: Acetic Acid

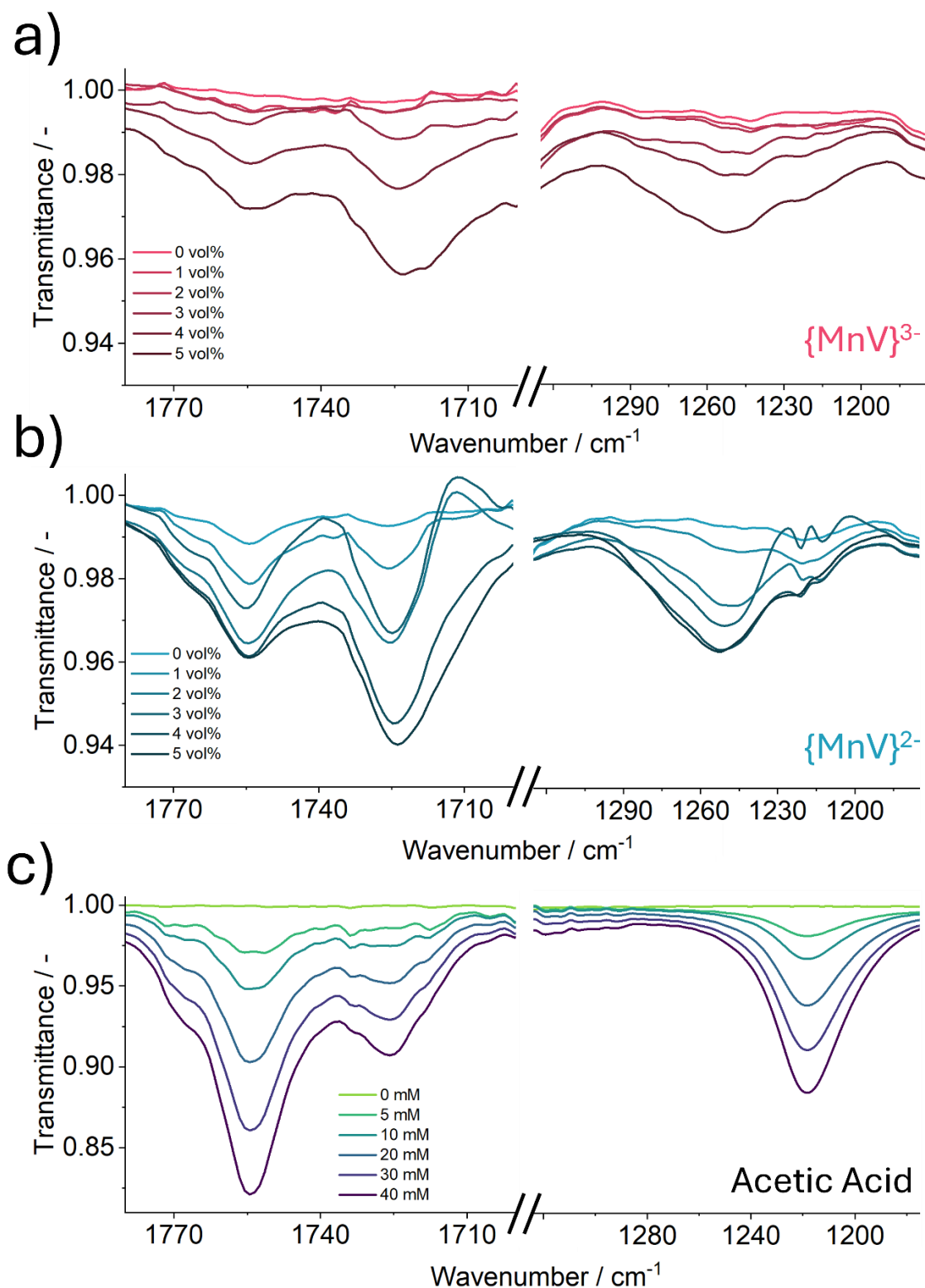


Figure 111: Liquid FTIR signals of acetic acid in solutions of a) 10 mM {MnV}³⁻ and b) {MnV}²⁻ with increasing vol% of water at a pathlength of 0.05 mm. Acetic acid was measured at different concentrations in acetonitrile at a pathlength of 0.05 mm for quantification. The signal at 1218 cm⁻¹ was used for linear regression.

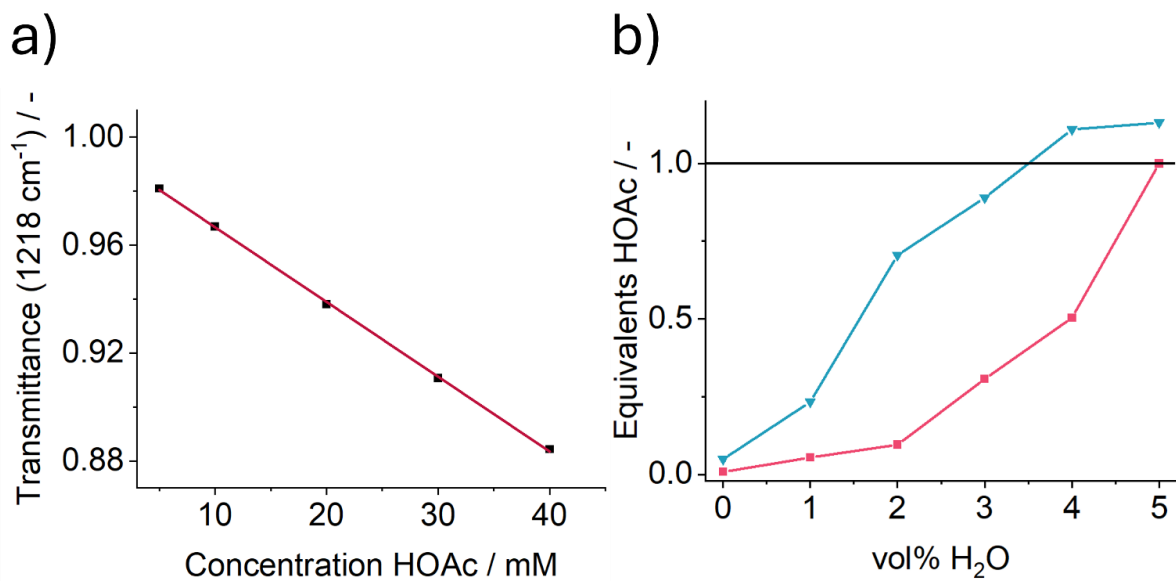


Figure 112: a) Linear regression of the signal intensity at 1218 cm⁻¹ of acetic acid in acetonitrile and b) equivalents of free acetic acid depending on the water content. The signal of acetic acid increases faster for the samples of {MnV}²⁻ compared to {MnV}³⁻. The complex reaction mixture only allows for an estimation of the amount of free acetic acid, which reaches about 1 equivalent compared to the cluster concentration with increasing water content in agreement with the reaction pathway of ligand exchange presented in the literature.^[237]

NMR Spectroscopy of $\{\text{MnV}\}^{3-}$: Peak Assignment

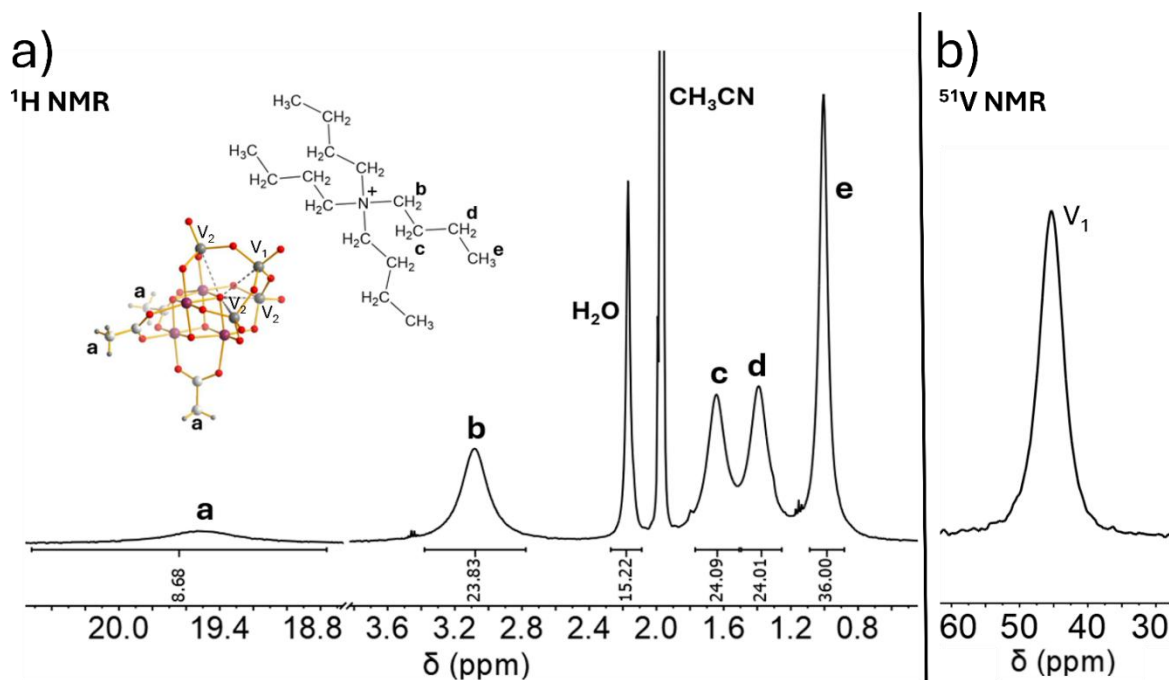


Figure 113: a) ^1H -NMR spectrum of 5 mM $\{\text{MnV}\}^{3-}$ solution in d_3 CH_3CN with the resonances assigned. The sample was prepared under an inert atmosphere in the glove box. The integral of the water signal is slightly higher due to residual water present in the acetonitrile. The signal of the acetate ligand **a** is paramagnetically shifted to 19.5 ppm due to the proximity to the manganese centers. **b)** ^{51}V -NMR spectrum of 1 mM $\{\text{MnV}\}^{3-}$ solution in d_3 CH_3CN . The ^{51}V V_1 resonance is paramagnetically shifted to +45 ppm. The V_2 signals are broadened beyond detection due to the close distance to the paramagnetic cubane core.

NMR Spectroscopy: Titration with H₂O

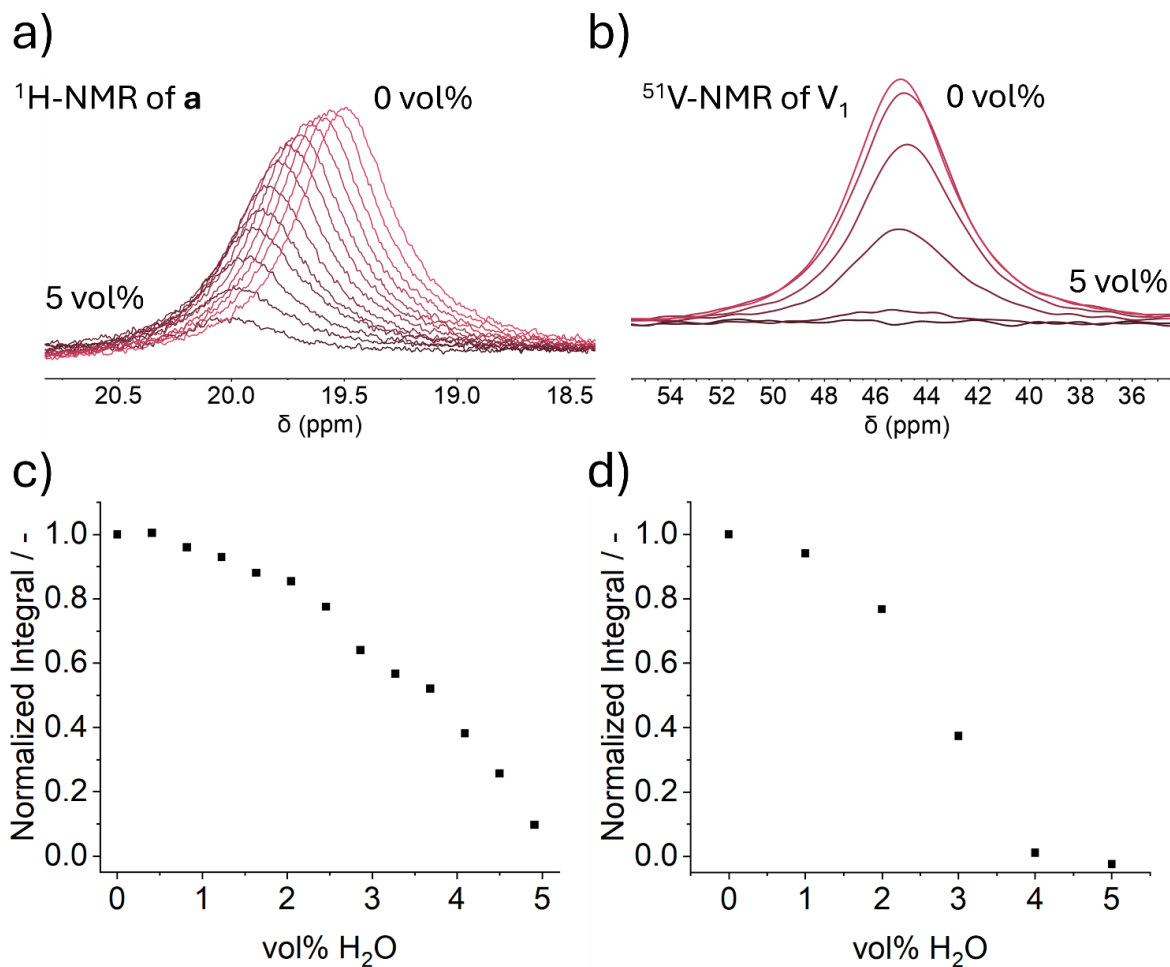


Figure 114: a) Overlaid 1H -NMR spectra of the $\{MnV\}^{3-}$ cluster in d_3 CH_3CN increasing the water content with the spectral region between 18.0 ppm and 21.0 ppm magnified. The samples were prepared by adding 50 M solution of water in acetonitrile in 2.5 μ L steps to a 0.5 mL of a 5 mM solution of $\{MnV\}^{3-}$ in d_3 CH_3CN . Each sample was filled with d_3 CH_3CN to a total volume of 0.55 mL. **b)** ^{51}V -NMR spectrum of $\{MnV\}^{3-}$ at a concentration of 1 mM in deuterated acetonitrile with increasing water content. **c)** Normalized 1H integral of the signal **a** as a function of the water content and **d)** The ^{51}V V_1 resonance becomes too broad to be detected probably due to aggregation or geometry changes by ligand exchange by higher water contents.

^1H -NMR Spectroscopy: T1 Measurements

The ^1H T1 relaxation time constants of the H_2O resonance of samples containing 5 mM $\{\text{MnV}\}^{3-}$ cluster in d_3 CH_3CN increasing the amount of water were measured at ambient temperature using the inversion recovery sequence. To investigate the effect of the dissolved oxygen on the T1 relaxation two separate rows of T1 experiments (with dissolved oxygen and oxygen free) have been measured. The oxygen was removed by three freeze pump thaw cycles. Subsequently, the samples were sealed with Leica Cruptoseal in the glovebox. As the main contribution to the T1 relaxation of all ^1H species in the solutions is the interaction with the paramagnetic cluster hardly any effect of the dissolved oxygen on the T1 relaxation time constants was detected.

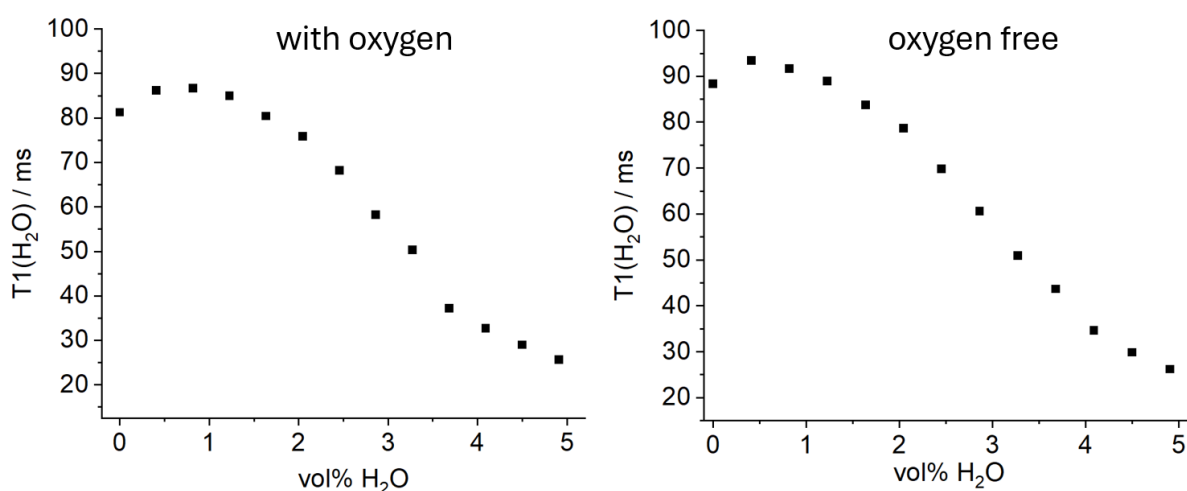


Figure 115: ^1H T1 relaxation time constants of the H_2O resonance of samples containing 5 mM $\{\text{MnV}\}^{3-}$ cluster in d_3 CH_3CN increasing the water content measured with dissolved oxygen (left) and under oxygen free conditions (right) at ambient temperature. The influence of molecular paramagnetic oxygen on the T1 relaxation time constants is obscured by the stronger paramagnetic effect of the cluster.

3.8.3. Molecular Dynamics Simulations

We performed two sets of MD simulations: (i) pure solvent and (ii) solvent containing a single POM. All boxes were constructed with PACKMOL^[254] using a box size of (70 Å)³ containing the appropriate number of water, acetonitrile, POMs and counterions (Table 26 and Table 27). Partial atomic charges for acetonitrile were obtained based on the restrained electrostatic potential method RESP^[255] using antechamber^[256,257], derived from quantum mechanical (QM) calculations from geometry optimizations at B3LYP/ def2-SVP and HF/def2-SVP level of theory.^[134,135,258,259] Dispersion was treated with Grimme's D3(BJ) correction.^[260,261] QM calculations were carried out using Gaussian 16.^[142] For acetonitrile, in addition to the RESP charges derived from quantum mechanical calculations, we also employed the six-site model developed by Nikitin et al.^[262] Water was modeled with TIP3P,^[263] SPC/Fw,^[264] and q-SPC/Fw.^[265] The POM in its oxidation states ($\{\text{MnV}\}^{3-}$, $\{\text{MnV}\}^{2-}$, $\{\text{MnV}\}^{1-}$) was described by the force field of Mai et al.^[239] All simulations were performed with AMBER 22^[266] and accelerated by using its GPU (CUDA) version pmemd.cuda.^[267,268] A cutoff of 10 Å was applied for non-bonded interaction terms. For TIP3P water, we used a 2 fs time step with SHAKE^[269] on water bonds/angles. For flexible water models (SPC/Fw, q-SPC/Fw), SHAKE was disabled and a 0.1 fs time step was used. Each system was minimized for 10,000 steps (5,000 steepest descent + 5,000 conjugate gradient), heated to 100 K over 26.25 ps, then to 300 K over 25 ps under periodic NVT with a Langevin thermostat. Subsequently, NPT (isotropic pressure coupling) equilibration was run for 1 ns, followed by production runs of 10 ns for pure solvent benchmarks and 100 ns for POM-containing systems. Radial distribution functions (RDFs) were computed with CPPTRAJ (AmberTools).

Table 26: Number of molecules used for MD simulations of pristine solvent boxes with varying molar fractions of acetonitrile.

Box Size	x(CH ₃ CN)	# CH ₃ CN	# H ₂ O	Counterion	Catalyst
70 ³ Å ³	0.0	0	11466	-	-
	0.25	2056	6168	-	-
	0.5	3123	3123	-	-
	0.75	3685	1228	-	-
	1.0	3955	0	-	-

Table 27: Number of molecules used for MD simulations of boxes including one POM molecule.

Box Size	vol% (H ₂ O)	# CH ₃ CN	# H ₂ O	Counterion	Catalyst
70 ³ Å ³	0.0	4978	0	3 × n-Bu ₄ N ⁺	{MnV} ³⁻
	0.5	3906	57		
	1.0	3896	114		
	2.0	3870	229		
	3.0	3852	345		
	4.0	3828	461		
	5.0	3802	578		
	6.0	3779	695		
	7.0	3719	957		
	8.0	3659	1175		
100.0	0	11343			
70 ³ Å ³	0.0	3922	0	2 × n-Bu ₄ N ⁺	{MnV} ²⁻
	0.5	3912	57		
	1.0	3906	114		
	2.0	3881	229		
	3.0	3858	345		
	4.0	3834	461		
	5.0	3808	578		
	6.0	3781	698		
	8.0	3664	1177		
	100.0	0	11356		
70 ³ Å ³	0.0	3928	0	1 × n-Bu ₄ N ⁺	{MnV} ¹⁻
	0.5	3918	57		
	1.0	3906	114		
	2.0	3896	229		
	3.0	3868	345		
	4.0	3837	461		
	5.0	3811	578		
	6.0	3781	698		
	8.0	3669	1178		
	100.0	0	11370		

Acknowledgements

his research was funded in whole or in part by the Austrian Science Fund (FWF) [grant DOI 10.55776/I6116] and the Deutsche Forschungsgemeinschaft (DFG) [TRR234 “Cata-Light,” Project No. 364549901, subproject C3]. For open access purposes, the authors have applied a CC-BY public copyright license to any author accepted manuscript version arising from this submission. The authors acknowledge the Vienna Scientific Cluster for the generous allocation of computational resources, the University of Vienna and the Johannes Gutenberg University Mainz for continuous support. We acknowledge access to Leonardo at CINECA, Italy, via an AURELEO (Austrian Users at LEONARDO supercomputer) project.

Author contributions

S. Tippner	Theoretical calculations, evaluation and manuscript writing
M. Remmers	Synthesis, characterization and spectroscopic analysis and manuscript writing
B. Mashtakov	Electrochemical measurements discussion
M. Mondeshki	NMR results discussion and writing of the manuscript
L. González	Discussion and writing of the manuscript
C. Streb	Discussion and writing of the manuscript

4. Summary and Perspective

In this work synthetic approaches towards electrochemically interesting polyoxovanadates are presented including the improvement of the number of electrons stored per cluster and increasing its solubility as well as a novel functionalization strategy using light, which has been a powerful tool to fine tune the redox and catalytic behavior of the clusters. Additionally, the influence of mixed solvent systems was investigated, which can potentially increase the solubility and enhance the catalytic and electrochemical behavior of the clusters.

Controlled Functionalization of Polyoxovanadates

The functionalization of polyoxovanadates with heterometals is known to change their electrochemical and catalytic behavior. To further extend the toolbox of controlled heterometal functionalization we investigated the use of visible light for photochemical reduction of $\{V_{12}\}_{\text{tube}}$ to introduce magnesium to the two binding sites. The placeholder strategy developed by Streb et al. was successfully applied and it was shown that the metal center undergoes a competitive binding equilibrium with the placeholder molecule DMA. Based on the principle of Le Chatelier we were able to shift the equilibrium and by the addition of excess DMA no product was formed. Furthermore, the reduction was not possible in the presence of oxygen e.g. by triplet quenching. The presence of the 1:1 adduct of Magnesium and $\{V_{12}\}_{\text{tube}}$ was shown by ^{51}V -NMR titration and ^1H DOSY. The change of the signal from two to four signals was due to the reduced symmetry of the mono functionalized species. This was further supported by ESI-MS and ^{51}V - ^{51}V TOCSY-NMR revealing that all four signals belong to one molecule. It was possible to follow the reduction by the increase of the IVCT band due to the mixed valent cluster. The single-crystal X-ray diffraction shows the successful synthesis of the di functionalized cluster. The ^{51}V -NMR further supports this by the presence of only two signals due to the symmetric functionalization at both binding positions. Additionally, we were able to transfer the method to calcium functionalization, which indicates that the light induced reduction can be applied to other metal

functionalization as well providing an eco-friendly alternative to the toxic N_2H_4 as a reducing agent used in previous work.

Further research will focus on expanding the functionalization by two different metal centers to investigate the synergistic effects on catalysis and the electrochemical profile. First experiments by our group indicate that water can replace DMA as a placeholder by introducing a more labile charge neutral stabilizing group at the lacunary position in asymmetric functionalized $\{V_{12}\}_{tube}$. Preliminary results show that a second metal could bind to the cluster without forming mixtures of different functionality. It is important to note that the charge of the heterometal was the most crucial for the functionalization and was much easier to achieve when the overall cluster charge remained more negative. Additionally initial experiments indicate that the selection of the counter anion can also affect the binding of the heterometals.

The introduction of anionic organic ligands will be used in the future to bridge monomeric clusters to form oligomeric species designed for supramolecular catalysis and dissipative systems (Figure 116). First examples of dimers and polymers were found pathing the way for further development in this direction.

Development of Electrochemically Active Clusters for Redox Flow Batteries

To maximize the number of electrons stored on a defined potential range, we demonstrated how a one pot self-assembly strategy can lead to a redox self-equilibrated cluster system. The mixed valent $(nBu_4N)_4\{V_{10}\}_{red}$ was chosen as a precursor which was fragmented in the presence of magnesium chloride as a Lewis acid. The measurement of the temperature dependent UV-Vis thereby allowed for the determination of the activation energy by the Arrhenius equation. This will provide a starting point for comparable Lewis acid-induced fragmentation processes and their mechanisms. The amount of magnesium chloride was determined from the changes in the IVCT band of the mixed valent system and a theoretical amount of 1.12 eq. was found to fully convert the precursor. We were able to fully characterize the material by ESI-MS, ICP-OES, Elemental analysis, TGA, FTIR, NMR and single-crystal X-ray diffraction. To determine the number of electrons on both clusters of the co crystallized

structure by bulk electrolysis and EPR was used. This led to the conclusion of a 1:1 composition of three electron reduced $\{MgV_{13}\}$ and five electrons reduced $\{V_{14}\}$. The material showed 14 electron transfer processes and a number of up to 16 electrons in the potential range of acetonitrile. Notably, the transitions were perfectly aligned against each other unlike the otherwise often observed 0.5 V gap between two redox processes.

In summary a highly redox active material was synthesized, which perfectly suits the application in a redox flow battery setup. The assignment of the transitions to the respective cluster was not possible so far, thus further studies will focus on the separation of both. Preliminary investigations based on a magnesium free synthesis strategy irreversibly reducing the $\{V_{12}\}_{\text{protonated}}$ led to a protonated $\{V_{13}\}$ species, which is likely structurally similar to $\{V_{14}\}$. The introduction of magnesium or other metal cations followed by deprotonation can potentially lead to the controllable formation of $\{MV_{13}\}$ or $\{V_{14}\}$ respectively. The protonation replacing a vanadium position in the cluster shell is specifically interesting since the redox events are shifted to higher potential. In combination with the functionalization with heterometals, this enables a greater range for the tuning of the redox events as well as the design of stimuli responsive systems (Figure 116).

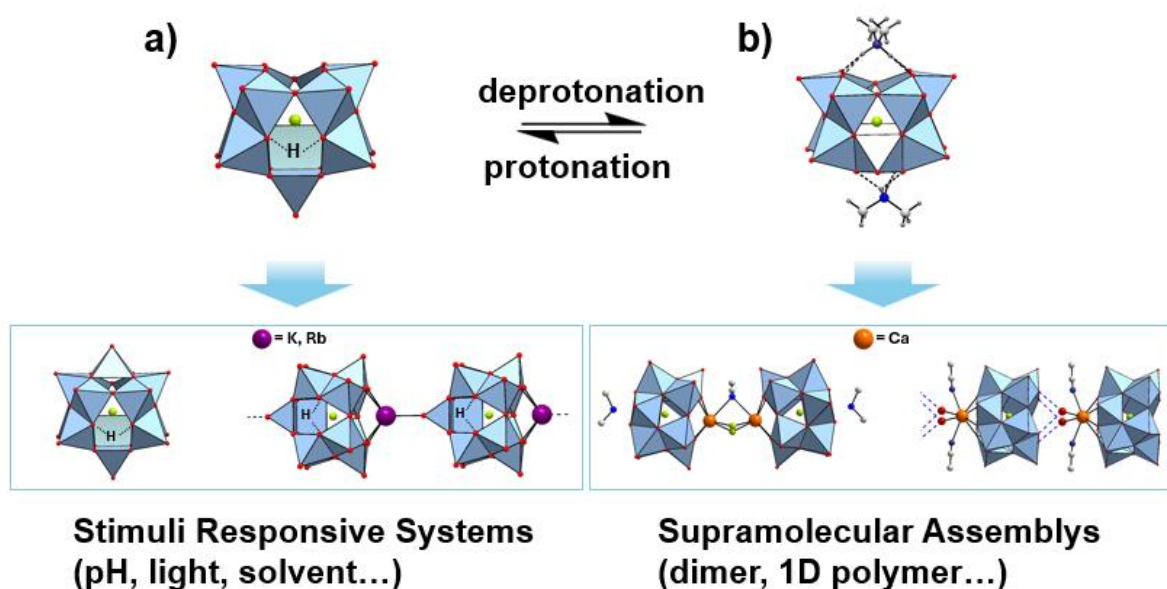


Figure 116: Preliminary results on the development of novel highly redox active and stimuli responsive clusters. This will include $\{V_{12}\}_{\text{protonated}}$ shown in a) and further development of the placeholder strategy and $\{V_{12}\}_{\text{tube}}$ in b). Specifically, the supramolecular aggregation to polymeric structures will be the focus in future investigations.

Implementation in Redox Flow Battery Setups

We were able to introduce the $\{MV_{13}\}$ ($= (nBu_4N)_4[MV_{13}O_{33}Cl]$ ($M= V^{IV}=O^{2+}$ or $MgOH^+$)) co-crystallized material in a nonaqueous redox-flow battery setup. Initial electrochemical LSV and SWV analysis revealed diffusion coefficients in the range of $10^{-7\sim-6}$ cm^2 offering suitable mass transport. The permeability of Celgard 2400 was tested and a diffusional permeability of 3.11×10^{-7} $cm^2 s^{-1}$ was determined, which is comparable to the literature values of similar materials in acetonitrile. It was demonstrated how the mixed-valent $V^{IV/V}$ oxidation state enabled a symmetric configuration, while the organo solubility of $\{MV_{13}\}$ allowed deployment in acetonitrile. Initial test demonstrated excellent cycling stability with negligible capacity fading over 20 cycles at a current density of 1.75 $mA cm^{-2}$ and a coulombic efficiency of up to 99% combined with good voltage efficiency and energy efficiency of about 67%. The theoretical calculation shows that 54% of the maximum capacity is reached and further optimization of the parameters is required.

Mechanistic insights into the charge and discharge behavior and the stability of the compound will be gained by in-operando liquid FTIR and UV-Vis measurements as well as tracking of the OCP in the anolyte and catholyte reservoir. Specifically, the assignment of the redox events to the isolated cluster species and the different oxidation states will be a future challenge.

In summary we successfully applied $\{MV_{13}\}$ in a nonaqueous symmetrical redox flow battery providing a blueprint for the design and integration of mixed-valent metal oxide clusters in such systems.

To further enhance the battery capacity future challenges include maximizing the solubility of the cluster. Initial results indicate that counter ions with longer alkyl chains like tetrahexyl, tetraoctyl or tetradecyl ammonium can be used to synthesize {MV₁₃} ionic liquids by a cation exchange route (Figure 117). Additionally, the use of mixed solvent systems and more optimized conditions could finally lead to enhanced battery performance.

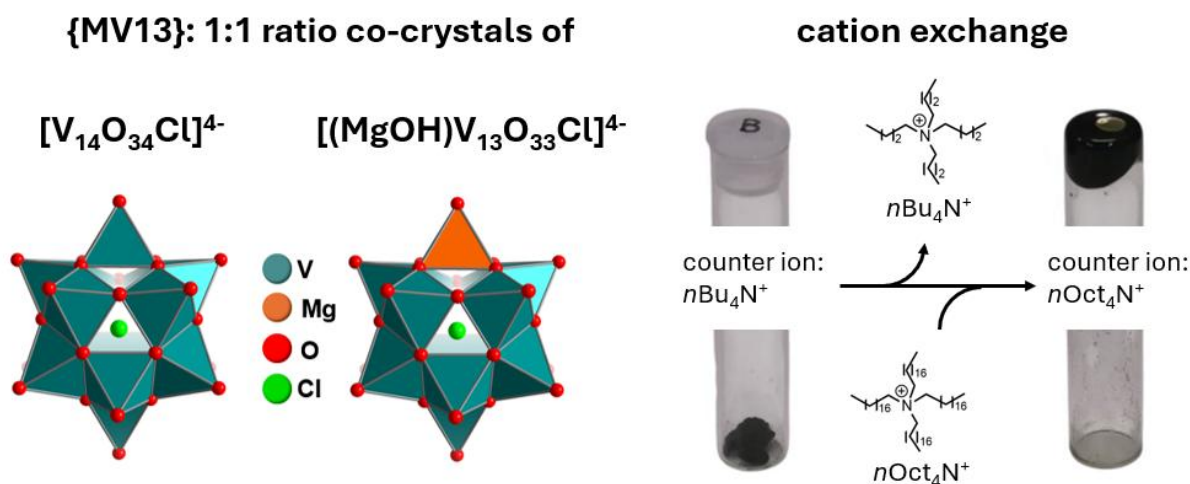


Figure 117: Cation exchange strategy to enhance the solubility of {MV₁₃} shown for tetraoctyl ammonium.

The influence of mixed solvent systems on molecular polyoxovanadates

In a combined computational and experimental study, the solvent environment of the {MnV} polyoxometalate (POM) catalyst in various oxidation states ({MnV}³⁻, {MnV}²⁻, and {MnV}¹⁻) was investigated in different acetonitrile water mixture. It was revealed that the solvation strongly depends on the oxidation state and charge of the cluster. For {MnV}³⁻ a strongly pronounced solvation shell is formed while this cannot be observed for {MnV}²⁻, and {MnV}¹⁻. The results were confirmed by various analytical techniques and confirmed the computational result. In addition, ligand exchange and aggregation were observed as a consequence of the increasing water content. This indicates that, while computational results can focus on isolated properties, the experimental conditions are considerably more complex, and multiple mechanisms can contribute to the observations. Regardless, this study provides valuable insights into the solution behavior of polyoxovanadates thereby supporting the rational design and application of these clusters for catalysis and energy storage.

References

- [1] M. Anjass, G. A. Lowe, C. Streb, *Angewandte Chemie International Edition* **2021**, *60*, 7522–7532.
- [2] F. Qureshi, M. Tahir, *Int J Hydrogen Energy* **2024**, *69*, 760–776.
- [3] A. Rana, J. M. Andino, *Catalysts* **2025**, *15*, 273.
- [4] F. Kurul, B. Doruk, S. N. Topkaya, *Discover Chemistry* **2025**, *2*, 68.
- [5] V. Talanquer, *J Chem Educ* **2018**, *95*, 1905–1911.
- [6] D.-L. Long, E. Burkholder, L. Cronin, *Chem. Soc. Rev.* **2007**, *36*, 105–121.
- [7] J. Forster, B. Rösner, M. M. Khusniyarov, C. Streb, *Chemical Communications* **2011**, *47*, 3114.
- [8] K. Kastner, J. T. Margraf, T. Clark, C. Streb, *Chemistry – A European Journal* **2014**, *20*, 12269–12273.
- [9] S. Repp, M. Remmers, A. S. J. Rein, D. Sorsche, D. Gao, M. Anjass, M. Mondeshki, L. M. Carrella, E. Rentschler, C. Streb, *Nat Commun* **2023**, *14*, 5563.
- [10] C. Streb, in *Structure and Bonding in Molecular Vanadium Oxides: From Templates via Host–Guest Chemistry to Applications*, in: *Polyoxometalate-Based Assemblies and Functional Materials* (Ed.: YF. Song), Springer, Cham, **2017**, pp. 31–47.
- [11] J. J. Berzelius, *Ann Phys* **1826**, *82*, 369–392.
- [12] J. F. Keggin, *Proceedings of the Royal Society of London. Series A, Containing Papers of a Mathematical and Physical Character* **1934**, *144*, 75–100.
- [13] J. F. KEGGIN, *Nature* **1933**, *131*, 908–909.
- [14] L.-L. Liu, L. Wang, X.-Y. Xiao, P. Yang, J. Zhao, U. Kortz, *Coord Chem Rev* **2024**, *506*, 215687.
- [15] L. C. W. Baker, J. S. Figgis, *J Am Chem Soc* **1970**, *92*, 3794–3797.
- [16] N. I. Gumerova, A. Rompel, *Nat Rev Chem* **2018**, *2*, 0112.
- [17] I. A. Weinstock, J. J. Cowan, E. M. G. Barbuzzi, H. Zeng, C. L. Hill, *J Am Chem Soc* **1999**, *121*, 4608–4617.
- [18] X. López, J. J. Carbó, C. Bo, J. M. Poblet, *Chem Soc Rev* **2012**, *41*, 7537.
- [19] A. Müller, E. Beckmann, H. Bögge, M. Schmidtman, A. Dress, *Angewandte Chemie International Edition* **2002**, *41*, 1162–1167.
- [20] J.-C. Liu, J.-W. Zhao, C. Streb, Y.-F. Song, *Coord Chem Rev* **2022**, *471*, 214734.
- [21] H. Wang, B. Li, *Molecules* **2024**, *29*, 3216.

- [22] M. Grabau, J. Forster, K. Heussner, C. Streb, *Eur J Inorg Chem* **2011**, 2011, 1719–1724.
- [23] L. Pettersson, I. Andersson, O. W. Howarth, *Inorg Chem* **1992**, 31, 4032–4033.
- [24] W. Guan, L. Yan, Z. Su, E. Wang, X. Wang, *Int J Quantum Chem* **2006**, 106, 1860–1864.
- [25] M. I. S. Veríssimo, D. V. Evtuguin, M. T. S. R. Gomes, *Front Chem* **2022**, 10, DOI 10.3389/fchem.2022.840657.
- [26] Y. Hayashi, *Coord Chem Rev* **2011**, 255, 2270–2280.
- [27] I. Werner, J. Griebel, A. Masip-Sánchez, X. López, K. Załęski, P. Kozłowski, A. Kahnt, M. Boerner, Z. Warneke, J. Warneke, K. Yu. Monakhov, *Inorg Chem* **2023**, 62, 3761–3775.
- [28] K. Kastner, J. Forster, H. Ida, G. N. Newton, H. Oshio, C. Streb, *Chemistry – A European Journal* **2015**, 21, 7686–7689.
- [29] L. E. VanGelder, W. W. Brennessel, E. M. Matson, *Dalton Transactions* **2018**, 47, 3698–3704.
- [30] S. Greiner, B. Schwarz, C. Streb, M. Anjass, *Chemistry – A European Journal* **2021**, 27, 13435–13441.
- [31] J. Kim, J. H. Kang, W. H. Kwon, I. Lee, S. J. Park, C.-H. Kim, W. Jeong, J. S. Choi, K. Kim, *Biomater Res* **2023**, 27, DOI 10.1186/s40824-023-00466-8.
- [32] D. Flores, C. M. Granadeiro, in *Applied Polyoxometalate-based Electrocatalysis*, Wiley, **2025**, pp. 1–25.
- [33] D. C. Crans, C. D. Rithner, L. A. Theisen, *J Am Chem Soc* **1990**, 112, 2901–2908.
- [34] M. Aureliano, C. A. Ohlin, M. O. Vieira, M. P. M. Marques, W. H. Casey, L. A. E. Batista de Carvalho, *Dalton Transactions* **2016**, 45, 7391–7399.
- [35] Y. Hayashi, T. Shinguchi, T. Kurata, K. Isobe, in *Vanadium: The Versatile Metal*, Am. Chem. Soc., Vol. 974, Ch. 29, **2007**, pp. 408–423.
- [36] H. Iwai, T. Kasamatsu, S. Kuwajima, Y. Kikukawa, Y. Hayashi, *Polyhedron* **2022**, 224, 115985.
- [37] J. Fuchs, S. Mahjour, J. Pickardt, *Angewandte Chemie International Edition in English* **1976**, 15, 374–375.
- [38] P. Roman, A. San Jose, A. Luque, J. M. Gutierrez-Zorrilla, *Inorg Chem* **1993**, 32, 775–776.

- [39] V. W. Day, W. G. Klemperer, D. J. Maltbie, *J Am Chem Soc* **1987**, *109*, 2991–3002.
- [40] S. Kuwajima, Y. Kikukawa, Y. Hayashi, *Chem Asian J* **2017**, *12*, 1909–1914.
- [41] S. Nakamura, T. Ozeki, *Journal of the Chemical Society, Dalton Transactions* **2001**, 472–480.
- [42] J. Forster, B. Rösner, R. H. Fink, L. C. Nye, I. Ivanovic-Burmazovic, K. Kastner, J. Tucher, C. Streb, *Chem. Sci.* **2013**, *4*, 418–424.
- [43] D. Long, R. Tsunashima, L. Cronin, *Angewandte Chemie International Edition* **2010**, *49*, 1736–1758.
- [44] A. Müller, *Nature* **1991**, *352*, 115.
- [45] Y. Kikukawa, *J Incl Phenom Macrocycl Chem* **2025**, *105*, 579–592.
- [46] W. G. Klemperer, T. A. Marquart, O. M. Yaghi, *Mater Chem Phys* **1991**, *29*, 97–104.
- [47] Y. Kikukawa, H. Kitajima, Y. Hayashi, *Dalton Transactions* **2019**, *48*, 7138–7143.
- [48] Y. Kikukawa, K. Seto, S. Uchida, S. Kuwajima, Y. Hayashi, *Angewandte Chemie International Edition* **2018**, *57*, 16051–16055.
- [49] Y. Kikukawa, K. Seto, D. Watanabe, H. Kitajima, M. Katayama, S. Yamashita, Y. Inada, Y. Hayashi, *Angewandte Chemie International Edition* **2020**, *59*, 14399–14403.
- [50] Y. Kikukawa, M. Taga, Y. Horikawa, R. Mitsuhashi, Y. Hayashi, *Inorg Chem* **2025**, *64*, 344–350.
- [51] A. Müller, H. Reuter, S. Dillinger, *Angewandte Chemie* **1995**, *107*, 2505–2539.
- [52] J. Tucher, K. Peuntinger, J. T. Margraf, T. Clark, D. M. Guldi, C. Streb, *Chemistry – A European Journal* **2015**, *21*, 8716–8719.
- [53] A. Müller, E. Krickemeyer, M. Penk, R. Rohlfing, A. Armatage, H. Bögge, *Angewandte Chemie International Edition in English* **1991**, *30*, 1674–1677.
- [54] A. Müller, R. Sessoli, E. Krickemeyer, H. Bögge, J. Meyer, D. Gatteschi, L. Pardi, J. Westphal, K. Hovemeier, R. Rohlfing, J. Döring, F. Hellweg, C. Beugholt, M. Schmidtman, *Inorg Chem* **1997**, *36*, 5239–5250.
- [55] S. Repp, K. L. Junginger, D. Sorsche, T. Zorn, A.-C. Pöppler, Y. Kikukawa, Y. Hayashi, C. Streb, *Dalton Transactions* **2023**, *52*, 4002–4007.
- [56] S. Repp, M. Steiner, M. Anjass, D. Sorsche, C. Streb, *Chemical Communications* **2022**, *58*, 13397–13400.

- [57] Y. Inoue, Y. Kikukawa, S. Kuwajima, Y. Hayashi, *Dalton Transactions* **2016**, *45*, 7563–7569.
- [58] S. Kuwajima, Y. Arai, H. Kitajima, Y. Kikukawa, Y. Hayashi, *Acta Crystallogr C Struct Chem* **2018**, *74*, 1295–1299.
- [59] C. Liu, G. Kalandia, J. N. H. Reek, T. N. Parac-Vogt, *Chemistry – A European Journal* **2025**, *31*, DOI 10.1002/chem.202403856.
- [60] D. Fujita, Y. Ueda, S. Sato, H. Yokoyama, N. Mizuno, T. Kumasaka, M. Fujita, *Chem* **2016**, *1*, 91–101.
- [61] N. Judge, L. Wang, Y. Y. L. Ho, Y. Wang, *Macromol Res* **2018**, *26*, 1074–1084.
- [62] W. He, Y. Yu, K. Iizuka, H. Takezawa, M. Fujita, *Nat Chem* **2025**, *17*, 653–662.
- [63] C. Liu, M. A. Moussawi, G. Kalandia, D. E. Salazar Marcano, W. E. Shepard, T. N. Parac-Vogt, *Angewandte Chemie International Edition* **2024**, *63*, DOI 10.1002/anie.202401940.
- [64] T. Kurata, A. Uehara, Y. Hayashi, K. Isobe, *Inorg Chem* **2005**, *44*, 2524–2530.
- [65] K. Kastner, M. Lechner, S. Weber, C. Streb, *ChemistrySelect* **2017**, *2*, 5542–5544.
- [66] L. E. VanGelder, P. L. Forrestel, W. W. Brennessel, E. M. Matson, *Chemical Communications* **2018**, *54*, 6839–6842.
- [67] S. Chakraborty, B. E. Petel, E. Schreiber, E. M. Matson, *Nanoscale Adv* **2021**, *3*, 1293–1318.
- [68] Y. Kikukawa, K. Ogihara, Y. Hayashi, *Inorganics (Basel)* **2015**, *3*, 295–308.
- [69] S. Kuwajima, Y. Ikinobu, D. Watanabe, Y. Kikukawa, Y. Hayashi, A. Yagasaki, *ACS Omega* **2017**, *2*, 268–275.
- [70] G. B. Karet, W. E. Streib, J. C. Bollinger, G. Christou, Z. Sun, D. N. Hendrickson, *Chemical Communications* **1999**, 2249–2250.
- [71] Y. Hayashi, N. Miyakoshi, T. Shinguchi, A. Uehara, *Chem Lett* **2001**, *30*, 170–171.
- [72] N. Kato, Y. Hayashi, *Dalton Transactions* **2013**, *42*, 11804.
- [73] M. H. Anjass, K. Kastner, F. Nägele, M. Ringenberg, J. F. Boas, J. Zhang, A. M. Bond, T. Jacob, C. Streb, *Angewandte Chemie International Edition* **2017**, *56*, 14749–14752.
- [74] B. Schwarz, M. Dürr, K. Kastner, N. Heber, I. Ivanović-Burmazović, C. Streb, *Inorg Chem* **2019**, *58*, 11684–11688.

- [75] S. Greiner, B. Schwarz, M. Ringenberg, M. Dürr, I. Ivanovic-Burmazovic, M. Fichtner, M. Anjass, C. Streb, *Chem Sci* **2020**, *11*, 4450–4455.
- [76] A. Seliverstov, C. Streb, *Chemistry – A European Journal* **2014**, *20*, 9733–9738.
- [77] Q. Fang, J. Fu, F. Wang, Z. Qin, W. Ma, J. Zhang, G. Li, *New Journal of Chemistry* **2019**, *43*, 28–36.
- [78] D. Li, J. Song, P. Yin, S. Simotwo, A. J. Bassler, Y. Aung, J. E. Roberts, K. I. Hardcastle, C. L. Hill, T. Liu, *J Am Chem Soc* **2011**, *133*, 14010–14016.
- [79] C. P. Pradeep, D. Long, G. N. Newton, Y. Song, L. Cronin, *Angewandte Chemie International Edition* **2008**, *47*, 4388–4391.
- [80] D. E. Salazar Marcano, M. A. Moussawi, A. V. Anyushin, S. Lentink, L. Van Meervelt, I. Ivanović-Burmazović, T. N. Parac-Vogt, *Chem Sci* **2022**, *13*, 2891–2899.
- [81] D. E. Salazar Marcano, G. Kalandia, M. A. Moussawi, K. Van Hecke, T. N. Parac-Vogt, *Chem Sci* **2023**, *14*, 5405–5414.
- [82] G. Kalandia, C. Liu, D. E. Salazar Marcano, M. A. Moussawi, S. Bleus, B. Van Meerbeek, W. Dehaen, T. N. Parac-Vogt, *Angewandte Chemie International Edition* **2025**, *64*, DOI 10.1002/anie.202420773.
- [83] S. Zhang, F. Ou, S. Ning, P. Cheng, *Inorg Chem Front* **2021**, *8*, 1865–1899.
- [84] H.-R. Tian, Y.-W. Liu, Z. Zhang, S.-M. Liu, T.-Y. Dang, X.-H. Li, X.-W. Sun, Y. Lu, S.-X. Liu, *Green Chemistry* **2020**, *22*, 248–255.
- [85] M. Han, W. Sun, W. Hu, Y. Liu, J. Chen, C. Zhang, J. Li, *Energy Storage Mater* **2024**, *71*, 103576.
- [86] S. T. Revankar, in *Storage and Hybridization of Nuclear Energy*, Elsevier, **2019**, pp. 177–227.
- [87] R. M. Darling, K. G. Gallagher, J. A. Kowalski, S. Ha, F. R. Brushett, *Energy Environ. Sci.* **2014**, *7*, 3459–3477.
- [88] L. E. VanGelder, A. M. Kosswattaarachchi, P. L. Forrestel, T. R. Cook, E. M. Matson, *Chem Sci* **2018**, *9*, 1692–1699.
- [89] M. Dagar, D. M. M. M. Dissanyake, D. N. Kesler, M. Corr, J. D. McPherson, W. W. Brennessel, J. R. McKone, E. M. Matson, *Dalton Transactions* **2024**, *53*, 93–104.
- [90] L. E. VanGelder, E. Schreiber, E. M. Matson, *J Mater Chem A Mater* **2019**, *7*, 4893–4902.

- [91] M. Ghosh, D. Sorsche, R. Binte Ahmed, M. Anjass, *ChemSusChem* **2023**, *16*, DOI 10.1002/cssc.202300631.
- [92] R. C. McNulty, K. Penston, S. S. Amin, S. Stal, J. Y. Lee, M. Samperi, L. Pérez-García, J. M. Cameron, L. R. Johnson, D. B. Amabilino, G. N. Newton, *Angewandte Chemie International Edition* **2023**, *62*, DOI 10.1002/anie.202216066.
- [93] S. Herrmann, A. Seliverstov, C. Streb, *J Mol Eng Mater* **2014**, *02*, 1440001.
- [94] A. Misra, C. Zambrzycki, G. Kloker, A. Kotyrba, M. H. Anjass, I. Franco Castillo, S. G. Mitchell, R. Güttel, C. Streb, *Angewandte Chemie International Edition* **2020**, *59*, 1601–1605.
- [95] A. Misra, I. Franco Castillo, D. P. Müller, C. González, S. Eyssautier-Chuine, A. Ziegler, J. M. de la Fuente, S. G. Mitchell, C. Streb, *Angewandte Chemie International Edition* **2018**, *57*, 14926–14931.
- [96] S. Herrmann, M. Kostrzewa, A. Wierschem, C. Streb, *Angewandte Chemie International Edition* **2014**, *53*, 13596–13599.
- [97] H. Cruz, A. L. Pinto, J. C. Lima, L. C. Branco, S. Gago, *Materials Letters: X* **2020**, *6*, 100033.
- [98] J. Meng, M. Lei, C. Lai, Q. Wu, Y. Liu, C. Li, *Angewandte Chemie International Edition* **2021**, *60*, 23256–23266.
- [99] L. Cronin, A. Müller, *Chem Soc Rev* **2012**, *41*, 7333.
- [100] Y. Gao, M. Choudhari, G. K. Such, C. Ritchie, *Chem Sci* **2022**, *13*, 2510–2527.
- [101] B. E. Petel, W. W. Brennessel, E. M. Matson, *J Am Chem Soc* **2018**, *140*, 8424–8428.
- [102] E. Schreiber, A. A. Fertig, W. W. Brennessel, E. M. Matson, *J Am Chem Soc* **2022**, *144*, 5029–5041.
- [103] B. E. Petel, R. L. Meyer, M. L. Maiola, W. W. Brennessel, A. M. Müller, E. M. Matson, *J Am Chem Soc* **2020**, *142*, 1049–1056.
- [104] T. Zhang, A. Solé-Daura, S. Hostachy, S. Blanchard, C. Paris, Y. Li, J. J. Carbó, J. M. Poblet, A. Proust, G. Guillemot, *J Am Chem Soc* **2018**, *140*, 14903–14914.
- [105] Y. Ji, L. Huang, J. Hu, C. Streb, Y.-F. Song, *Energy Environ Sci* **2015**, *8*, 776–789.
- [106] C. Ritchie, A. Ferguson, H. Nojiri, H. N. Miras, Y. Song, D. Long, E. Burkholder, M. Murrie, P. Kögerler, E. K. Brechin, L. Cronin, *Angewandte Chemie International Edition* **2008**, *47*, 5609–5612.

- [107] E. Coronado, *Nat Rev Mater* **2019**, *5*, 87–104.
- [108] I. A. Weinstock, R. E. Schreiber, R. Neumann, *Chem Rev* **2018**, *118*, 2680–2717.
- [109] M. Bonchio, Z. Syrgiannis, M. Burian, N. Marino, E. Pizzolato, K. Dirian, F. Rigodanza, G. A. Volpato, G. La Ganga, N. Demitri, S. Berardi, H. Amenitsch, D. M. Guldi, S. Caramori, C. A. Bignozzi, A. Sartorel, M. Prato, *Nat Chem* **2019**, *11*, 146–153.
- [110] A. Kondinski, T. N. Parac-Vogt, *Front Chem* **2018**, *6*, DOI 10.3389/fchem.2018.00346.
- [111] J. M. Clemente-Juan, E. Coronado, A. Gaita-Ariño, *Chem Soc Rev* **2012**, *41*, 7464.
- [112] A. Sartorel, M. Carraro, F. M. Toma, M. Prato, M. Bonchio, *Energy Environ Sci* **2012**, *5*, 5592.
- [113] S.-S. Wang, G.-Y. Yang, *Chem Rev* **2015**, *115*, 4893–4962.
- [114] C. Li, K. Yamaguchi, K. Suzuki, *Angewandte Chemie International Edition* **2021**, *60*, 6960–6964.
- [115] D. Gao, I. Trentin, L. Schwiedrzik, L. González, C. Streb, *Molecules* **2019**, *25*, 157.
- [116] J. Lehmann, A. Gaita-Ariño, E. Coronado, D. Loss, *Nat Nanotechnol* **2007**, *2*, 312–317.
- [117] M. Shiddiq, D. Komijani, Y. Duan, A. Gaita-Ariño, E. Coronado, S. Hill, *Nature* **2016**, *531*, 348–351.
- [118] A. Bijelic, M. Aureliano, A. Rompel, *Angewandte Chemie International Edition* **2019**, *58*, 2980–2999.
- [119] F. de Azambuja, J. Moons, T. N. Parac-Vogt, *Acc Chem Res* **2021**, *54*, 1673–1684.
- [120] R. Pütt, X. Qiu, P. Kozłowski, H. Gildenast, O. Linnenberg, S. Zahn, R. C. Chiechi, K. Yu. Monakhov, *Chemical Communications* **2019**, *55*, 13554–13557.
- [121] F. Li, L. E. VanGelder, W. W. Brennessel, E. M. Matson, *Inorg Chem* **2016**, *55*, 7332–7334.
- [122] S. Greiner, M. Anjass, C. Streb, *CrystEngComm* **2021**, *23*, 3946–3950.
- [123] C. Li, A. Jimbo, K. Yamaguchi, K. Suzuki, *Chem Sci* **2021**, *12*, 1240–1244.
- [124] C. Streb, *Dalton Trans.* **2012**, *41*, 1651–1659.
- [125] T. Yamase, *Chem Rev* **1998**, *98*, 307–326.
- [126] T. Yamase, *Catalysis Surveys from Asia* **2003**, *7*, 203–217.

- [127] E. Papaconstantinou, A. Hiskia, in *Polyoxometalate Molecular Science*, Springer Netherlands, Dordrecht, **2003**, pp. 381–416.
- [128] T. Yamase, *Polyhedron* **1986**, *5*, 79–86.
- [129] T. Yamase, M. Suzuki, K. Ohtaka, *Journal of the Chemical Society, Dalton Transactions* **1997**, 2463–2472.
- [130] M. Zhao, Y. Wang, N. Wu, J. Zhang, B. Liu, *Dalton Transactions* **2020**, *49*, 9662–9667.
- [131] J. Lee, S. Dey, S. E. Dutton, C. P. Grey, *Angewandte Chemie International Edition* **2022**, *61*, DOI 10.1002/anie.202112688.
- [132] M. Klueker, M. Mondeshki, M. Nawaz Tahir, W. Tremel, *Langmuir* **2018**, *34*, 1700–1710.
- [133] A. D. Becke, *J Chem Phys* **1993**, *98*, 5648–5652.
- [134] C. Lee, W. Yang, R. G. Parr, *Phys Rev B* **1988**, *37*, 785–789.
- [135] F. Weigend, R. Ahlrichs, *Physical Chemistry Chemical Physics* **2005**, *7*, 3297.
- [136] C. Tanielian, C. Schweitzer, R. Seghrouchni, M. Esch, R. Mechin, *Photochemical & Photobiological Sciences* **2003**, *2*, 297–305.
- [137] K. Suzuki, N. Mizuno, K. Yamaguchi, *ACS Catal* **2018**, *8*, 10809–10825.
- [138] K. Momma, F. Izumi, *J Appl Crystallogr* **2011**, *44*, 1272–1276.
- [139] I. D. Brown, D. Altermatt, *Acta Crystallogr B* **1985**, *41*, 244–247.
- [140] A. V. Marenich, C. J. Cramer, D. G. Truhlar, *J Phys Chem B* **2009**, *113*, 6378–6396.
- [141] V. Barone, M. Cossi, *J Phys Chem A* **1998**, *102*, 1995–2001.
- [142] M. J. Frisch, G. W. Trucks, H. B. Schlegel, *Gaussian 16, Revision A.03*, Gaussian, Inc., Wallingford CT, **2016**.
- [143] E. F. Wilson, H. Abbas, B. J. Duncombe, C. Streb, D.-L. Long, L. Cronin, *J Am Chem Soc* **2008**, *130*, 13876–13884.
- [144] G. M. Sheldrick, *Acta Crystallogr C Struct Chem* **2015**, *71*, 3–8.
- [145] O. V. Dolomanov, L. J. Bourhis, R. J. Gildea, J. A. K. Howard, H. Puschmann, *J Appl Crystallogr* **2009**, *42*, 339–341.
- [146] R. H. Blessing, *Acta Crystallogr A* **1995**, *51*, 33–38.
- [147] L. S. Van Rompuy, T. N. Parac-Vogt, *Curr Opin Biotechnol* **2019**, *58*, 92–99.
- [148] M. Moors, J. Warneke, X. López, C. de Graaf, B. Abel, K. Yu. Monakhov, *Acc Chem Res* **2021**, *54*, 3377–3389.
- [149] M. Stuckart, K. Yu. Monakhov, *Chem Sci* **2019**, *10*, 4364–4376.

- [150] A. Misra, K. Kozma, C. Streb, M. Nyman, *Angewandte Chemie International Edition* **2020**, *59*, 596–612.
- [151] A. Sartorel, M. Bonchio, S. Campagna, F. Scandola, *Chem. Soc. Rev.* **2013**, *42*, 2262–2280.
- [152] T. Ueda, *ChemElectroChem* **2018**, *5*, 823–838.
- [153] D. G. Nocera, *J Am Chem Soc* **2022**, *144*, 1069–1081.
- [154] Z. Li, Y. Lu, *Advanced Materials* **2020**, *32*, DOI 10.1002/adma.202002132.
- [155] Y. Nishimoto, D. Yokogawa, H. Yoshikawa, K. Awaga, S. Irle, *J Am Chem Soc* **2014**, *136*, 9042–9052.
- [156] H. Wang, S. Hamanaka, Y. Nishimoto, S. Irle, T. Yokoyama, H. Yoshikawa, K. Awaga, *J Am Chem Soc* **2012**, *134*, 4918–4924.
- [157] J.-J. Chen, M. D. Symes, L. Cronin, *Nat Chem* **2018**, *10*, 1042–1047.
- [158] J.-J. Chen, L. Vilà-Nadal, A. Solé-Daura, G. Chisholm, T. Minato, C. Busche, T. Zhao, B. Kandasamy, A. Y. Ganin, R. M. Smith, I. Colliard, J. J. Carbó, J. M. Poblet, M. Nyman, L. Cronin, *J Am Chem Soc* **2022**, *144*, 8951–8960.
- [159] K. Y. Monakhov, M. Moors, P. Kögerler, in *Adv Inorg Chem* (Eds.: R. van Eldik, L. Cronin), Academic Press, Vol. 69, **2017**, pp. 251–286.
- [160] K. Yu. Monakhov, W. Bensch, P. Kögerler, *Chem Soc Rev* **2015**, *44*, 8443–8483.
- [161] D. Gatteschi, L. Pardi, A. L. Barra, A. Müller, *Molecular Engineering* **1993**, *3*, 157–169.
- [162] K. R. Proe, E. Schreiber, E. M. Matson, *Acc Chem Res* **2023**, *56*, 1602–1612.
- [163] L. E. VanGelder, T. R. Cook, E. M. Matson, *Comments on Inorganic Chemistry* **2019**, *39*, 51–89.
- [164] L. E. VanGelder, E. M. Matson, *J Mater Chem A Mater* **2018**, *6*, 13874–13882.
- [165] N. Arya, T. Philipp, S. Greiner, M. Steiner, C. Kranz, M. Anjass, *Angewandte Chemie International Edition* **2023**, *62*, DOI 10.1002/anie.202306170.
- [166] A. Bino, S. Cohen, C. Heitner-Wirguin, *Inorg Chem* **1982**, *21*, 429–431.
- [167] K. Okaya, T. Kobayashi, Y. Koyama, Y. Hayashi, K. Isobe, *Eur J Inorg Chem* **2009**, *2009*, 5156–5163.
- [168] A. Kondo, R. Kurosawa, J. Ryu, M. Matsuoka, M. Takeuchi, *The Journal of Physical Chemistry C* **2021**, *125*, 10937–10947.
- [169] P. Kögerler, B. Tsukerblat, A. Müller, *Dalton Trans.* **2010**, *39*, 21–36.
- [170] A. Müller, P. Kögerler, A. W. M. Dress, *Coord Chem Rev* **2001**, *222*, 193–218.

- [171] J. Wang, C. Näther, P. Kögerler, W. Bensch, *Inorganica Chim Acta* **2010**, *363*, 4399–4404.
- [172] O. Linnenberg, P. Kozłowski, C. Besson, J. van Leusen, U. Englert, K. Yu. Monakhov, *Cryst Growth Des* **2017**, *17*, 2342–2350.
- [173] T. Kobayashi, S. Kuwajima, T. Kurata, Y. Hayashi, *Inorganica Chim Acta* **2014**, *420*, 69–74.
- [174] S. Stoll, A. Schweiger, *Journal of Magnetic Resonance* **2006**, *178*, 42–55.
- [175] R. L. Belford, N. D. Chasteen, H. So, R. E. Tapscott, *J Am Chem Soc* **1969**, *91*, 4675–4680.
- [176] Q. Chen, D. P. Goshorn, C. P. Scholes, X. L. Tan, J. Zubieta, *J Am Chem Soc* **1992**, *114*, 4667–4681.
- [177] K. J. Laidler, *J Chem Educ* **1984**, *61*, 494.
- [178] T. Ueda, K. Kodani, H. Ota, M. Shiro, S.-X. Guo, J. F. Boas, A. M. Bond, *Inorg Chem* **2017**, *56*, 3990–4001.
- [179] Y. Cao, J.-J. J. Chen, M. A. Barteau, *Journal of Energy Chemistry* **2020**, *50*, 115–124.
- [180] N. Fay, A. M. Bond, C. Baffert, J. F. Boas, J. R. Pilbrow, D.-L. Long, L. Cronin, *Inorg Chem* **2007**, *46*, 3502–3510.
- [181] O. Linnenberg, M. Moors, A. Solé-Daura, X. López, C. Bäumer, E. Kentzinger, W. Pyckhout-Hintzen, K. Yu. Monakhov, *The Journal of Physical Chemistry C* **2017**, *121*, 10419–10429.
- [182] G. M. Sheldrick, *Acta Crystallogr A* **2008**, *64*, 112–122.
- [183] L. J. Bourhis, O. V. Dolomanov, R. J. Gildea, J. A. K. Howard, H. Puschmann, *Acta Crystallogr A Found Adv* **2015**, *71*, 59–75.
- [184] V. W. Day, W. G. Klemperer, O. M. Yaghi, *J Am Chem Soc* **1989**, *111*, 5959–5961.
- [185] R. M. Olson, A. V. Marenich, C. J. Cramer, D. G. Truhlar, *J Chem Theory Comput* **2007**, *3*, 2046–2054.
- [186] S. Chu, A. Majumdar, *Nature* **2012**, *488*, 294–303.
- [187] B. Dunn, H. Kamath, J.-M. Tarascon, *Science (1979)* **2011**, *334*, 928–935.
- [188] Z. Yang, J. Zhang, M. C. W. Kintner-Meyer, X. Lu, D. Choi, J. P. Lemmon, J. Liu, *Chem Rev* **2011**, *111*, 3577–3613.
- [189] G. L. Soloveichik, *Chem Rev* **2015**, *115*, 11533–11558.
- [190] R. Yan, Q. Wang, *Advanced Materials* **2018**, *30*, DOI 10.1002/adma.201802406.

- [191] W. Wang, Q. Luo, B. Li, X. Wei, L. Li, Z. Yang, *Adv Funct Mater* **2013**, *23*, 970–986.
- [192] M. Kapoor, R. K. Gautam, V. K. Ramani, A. Verma, *Chemical Engineering Journal* **2020**, *379*, 122300.
- [193] M. Dagar, E. M. Matson, *Dalton Transactions* **2025**, *54*, 10164–10177.
- [194] M. Park, J. Ryu, W. Wang, J. Cho, *Nat Rev Mater* **2016**, *2*, 16080.
- [195] C. Sun, H. Zhang, *ChemSusChem* **2022**, *15*, DOI 10.1002/cssc.202101798.
- [196] B. Liu, Y. Li, G. Jia, T. Zhao, *Electrochemical Energy Reviews* **2024**, *7*, 7.
- [197] F. Zhong, M. Yang, M. Ding, C. Jia, *Front Chem* **2020**, *8*, DOI 10.3389/fchem.2020.00451.
- [198] M. L. Perry, K. E. Rodby, F. R. Brushett, *ACS Energy Lett* **2022**, *7*, 659–667.
- [199] P. Leung, X. Li, C. Ponce de León, L. Berlouis, C. T. J. Low, F. C. Walsh, *RSC Adv* **2012**, *2*, 10125.
- [200] F. Zhu, W. Guo, Y. Fu, *Chem Soc Rev* **2023**, *52*, 8410–8446.
- [201] L. Yang, Y. Hao, J. Lin, K. Li, S. Luo, J. Lei, Y. Han, R. Yuan, G. Liu, B. Ren, J. Chen, *Advanced Materials* **2022**, *34*, DOI 10.1002/adma.202107425.
- [202] Z. Rhodes, J. R. Cabrera-Pardo, M. Li, S. D. Minteer, *Isr J Chem* **2021**, *61*, 101–112.
- [203] K. Gong, Q. Fang, S. Gu, S. F. Y. Li, Y. Yan, *Energy Environ Sci* **2015**, *8*, 3515–3530.
- [204] S.-H. Shin, S.-H. Yun, S.-H. Moon, *RSC Adv* **2013**, *3*, 9095.
- [205] L. Yang, J. Lei, J. Fan, R. Yuan, M. Zheng, J. Chen, Q. Dong, *Advanced Materials* **2021**, *33*, DOI 10.1002/adma.202005019.
- [206] Q. Li, L. Zhang, J. Dai, H. Tang, Q. Li, H. Xue, H. Pang, *Chemical Engineering Journal* **2018**, *351*, 441–461.
- [207] P. G. Y. Sun, W. You, Z. Tan, *Journal of Electrochemistry* **1997**, *3*, DOI 10.61558/2993-074X.2650.
- [208] Y. Liu, S. Lu, H. Wang, C. Yang, X. Su, Y. Xiang, *Adv Energy Mater* **2017**, *7*, DOI 10.1002/aenm.201601224.
- [209] L. E. VanGelder, H. D. Pratt, T. M. Anderson, E. M. Matson, *Chemical Communications* **2019**, *55*, 12247–12250.
- [210] E. Schreiber, R. E. Garwick, M. J. Baran, M. A. Baird, B. A. Helms, E. M. Matson, *ACS Appl Mater Interfaces* **2022**, *14*, 22965–22972.
- [211] L. Zhang, R. Feng, W. Wang, G. Yu, *Nat Rev Chem* **2022**, *6*, 524–543.

- [212] M. Remmers, B. Mashtakov, S. Repp, A. S. J. Rein, K. Wang, M. Anjass, Z. Chen, L. M. Carrella, E. Rentschler, C. Streb, *Angewandte Chemie International Edition* **2025**, *64*, DOI 10.1002/anie.202418864.
- [213] A. J. Bard, L. R. Faulkner, H. S. White, *Electrochemical Methods: Fundamentals and Applications*, John Wiley & Sons, Ltd., **2022**.
- [214] C. L. Peake, A. J. Kibler, G. N. Newton, D. A. Walsh, *ACS Appl Energy Mater* **2021**, *4*, 8765–8773.
- [215] T. M. Aminabhavi, B. Gopalakrishna, *J Chem Eng Data* **1995**, *40*, 856–861.
- [216] L. Cao, A. Kronander, A. Tang, D.-W. Wang, M. Skyllas-Kazacos, *Energies (Basel)* **2016**, *9*, 1058.
- [217] Z.-F. Chen, Y.-L. Yang, C. Zhang, S.-Q. Liu, J. Yan, *J Energy Storage* **2021**, *35*, 102281.
- [218] E. S. Beh, D. De Porcellinis, R. L. Gracia, K. T. Xia, R. G. Gordon, M. J. Aziz, *ACS Energy Lett* **2017**, *2*, 639–644.
- [219] M. Gao, M. Salla, Y. Song, Q. Wang, *Angewandte Chemie International Edition* **2022**, *61*, DOI 10.1002/anie.202208223.
- [220] S. Jin, E. M. Fell, L. Vina-Lopez, Y. Jing, P. W. Michalak, R. G. Gordon, M. J. Aziz, *Adv Energy Mater* **2020**, *10*, DOI 10.1002/aenm.202000100.
- [221] P. J. Dyson, P. G. Jessop, *Catal Sci Technol* **2016**, *6*, 3302–3316.
- [222] D. S. Potts, D. T. Bregante, J. S. Adams, C. Torres, D. W. Flaherty, *Chem Soc Rev* **2021**, *50*, 12308–12337.
- [223] A. J. Orr-Ewing, *Chem Soc Rev* **2017**, *46*, 7597–7614.
- [224] T. Kitanosono, K. Masuda, P. Xu, S. Kobayashi, *Chem Rev* **2018**, *118*, 679–746.
- [225] A. K. Chew, T. W. Walker, Z. Shen, B. Demir, L. Witteman, J. Euclide, G. W. Huber, J. A. Dumesic, R. C. Van Lehn, *ACS Catal* **2020**, *10*, 1679–1691.
- [226] J. J. Varghese, S. H. Mushrif, *React Chem Eng* **2019**, *4*, 165–206.
- [227] S. Nishioka, F. E. Osterloh, X. Wang, T. E. Mallouk, K. Maeda, *Nature Reviews Methods Primers* **2023**, *3*, 42.
- [228] R. Matheu, P. Garrido-Barros, M. Gil-Sepulcre, M. Z. Ertem, X. Sala, C. Gimbert-Suriñach, A. Llobet, *Nat Rev Chem* **2019**, *3*, 331–341.
- [229] M. D. Kärkäs, B. Åkermark, *Dalton Transactions* **2016**, *45*, 14421–14461.
- [230] Y. Umena, K. Kawakami, J.-R. Shen, N. Kamiya, *Nature* **2011**, *473*, 55–60.
- [231] H. Li, Y. Nakajima, E. Nango, S. Owada, D. Yamada, K. Hashimoto, F. Luo, R. Tanaka, F. Akita, K. Kato, J. Kang, Y. Saitoh, S. Kishi, H. Yu, N. Matsubara, H.

- Fujii, M. Sugahara, M. Suzuki, T. Masuda, T. Kimura, T. N. Thao, S. Yonekura, L.-J. Yu, T. Tosha, K. Tono, Y. Joti, T. Hatsui, M. Yabashi, M. Kubo, S. Iwata, H. Isobe, K. Yamaguchi, M. Suga, J.-R. Shen, *Nature* **2024**, *626*, 670–677.
- [232] S. Paul, F. Neese, D. A. Pantazis, *Green Chemistry* **2017**, *19*, 2309–2325.
- [233] H. Lv, Y. V. Geletii, C. Zhao, J. W. Vickers, G. Zhu, Z. Luo, J. Song, T. Lian, D. G. Musaev, C. L. Hill, *Chem Soc Rev* **2012**, *41*, 7572.
- [234] J. Li, C. A. Triana, W. Wan, D. P. Adiyeri Saseendran, Y. Zhao, S. E. Balaghi, S. Heidari, G. R. Patzke, *Chem Soc Rev* **2021**, *50*, 2444–2485.
- [235] B. Schwarz, J. Forster, M. K. Goetz, D. Yücel, C. Berger, T. Jacob, C. Streb, *Angewandte Chemie International Edition* **2016**, *55*, 6329–6333.
- [236] B. Schwarz, J. Forster, M. H. Anjass, S. Daboss, C. Kranz, C. Streb, *Chem. Commun.* **2017**, *53*, 11576–11579.
- [237] G. Cárdenas, I. Trentin, L. Schwiedrzik, D. Hernández-Castillo, G. A. Lowe, J. Kund, C. Kranz, S. Klingler, R. Stach, B. Mizaikoff, P. Marquetand, J. J. Nogueira, C. Streb, L. González, *Chem Sci* **2021**, *12*, 12918–12927.
- [238] L. Schwiedrzik, V. Brieskorn, L. González, *ACS Catal* **2021**, *11*, 13320–13329.
- [239] G. Cárdenas, P. Marquetand, S. Mai, L. González, *Catalysts* **2021**, *11*, 493.
- [240] S. Tippner, P. Lechner, L. González, S. Mai, *J Chem Phys* **2024**, *160*, DOI 10.1063/5.0189673.
- [241] S. Mai, M. Holzer, A. Andreeva, L. González, *Chemistry – A European Journal* **2021**, *27*, 17066–17077.
- [242] C. J. Gagliardi, A. K. Vannucci, J. J. Concepcion, Z. Chen, T. J. Meyer, *Energy Environ Sci* **2012**, *5*, 7704.
- [243] Z. Chen, J. J. Concepcion, J. W. Jurss, T. J. Meyer, *J Am Chem Soc* **2009**, *131*, 15580–15581.
- [244] X. Lin, X. Hu, J. J. Concepcion, Z. Chen, S. Liu, T. J. Meyer, W. Yang, *Proceedings of the National Academy of Sciences* **2012**, *109*, 15669–15672.
- [245] L. Bernasconi, A. Kazaryan, P. Belanzoni, E. J. Baerends, *ACS Catal* **2017**, *7*, 4018–4025.
- [246] J. F. Khosrowabadi Kotyk, C. M. Hanna, R. L. Combs, J. W. Ziller, J. Y. Yang, *Chem Sci* **2018**, *9*, 2750–2755.
- [247] J. C. Hidalgo-Acosta, M. D. Scanlon, M. A. Méndez, P. Peljo, M. Opallo, H. H. Girault, *ChemElectroChem* **2016**, *3*, 2003–2007.

- [248] D. A. Tuzov, E. M. Zueva, T. T. Zinkicheva, R. R. Nazmutdinov, *Electrochim Acta* **2024**, *508*, 145182.
- [249] A. Solé-Daura, A. Notario-Estévez, J. J. Carbó, J. M. Poblet, C. de Graaf, K. Yu. Monakhov, X. López, *Inorg Chem* **2019**, *58*, 3881–3894.
- [250] H. T. French, *J Chem Thermodyn* **1987**, *19*, 1155–1161.
- [251] S. Mai, S. Klingler, I. Trentin, J. Kund, M. Holzer, A. Andreeva, R. Stach, C. Kranz, C. Streb, B. Mizaikoff, L. González, *Chemistry – A European Journal* **2021**, *27*, 17078–17086.
- [252] N. S. Hush, J. R. Reimers, *Chem Rev* **2000**, *100*, 775–786.
- [253] R. K. Harris, E. D. Becker, S. M. Cabral de Menezes, R. Goodfellow, P. Granger, *Pure and Applied Chemistry* **2001**, *73*, 1795–1818.
- [254] L. Martínez, R. Andrade, E. G. Birgin, J. M. Martínez, *J Comput Chem* **2009**, *30*, 2157–2164.
- [255] C. I. Bayly, P. Cieplak, W. Cornell, P. A. Kollman, *J Phys Chem* **1993**, *97*, 10269–10280.
- [256] J. Wang, W. Wang, P. A. Kollman, D. A. Case, *J Mol Graph Model* **2006**, *25*, 247–260.
- [257] J. Wang, R. M. Wolf, J. W. Caldwell, P. A. Kollman, D. A. Case, *J Comput Chem* **2004**, *25*, 1157–1174.
- [258] J. P. Perdew, *Phys Rev B* **1986**, *33*, 8822–8824.
- [259] F. Weigend, *Physical Chemistry Chemical Physics* **2006**, *8*, 1057.
- [260] S. Grimme, S. Ehrlich, L. Goerigk, *J Comput Chem* **2011**, *32*, 1456–1465.
- [261] S. Grimme, J. Antony, S. Ehrlich, H. Krieg, *J Chem Phys* **2010**, *132*, DOI 10.1063/1.3382344.
- [262] A. M. Nikitin, A. P. Lyubartsev, *J Comput Chem* **2007**, *28*, 2020–2026.
- [263] W. L. Jorgensen, J. Chandrasekhar, J. D. Madura, R. W. Impey, M. L. Klein, *J Chem Phys* **1983**, *79*, 926–935.
- [264] Y. Wu, H. L. Tepper, G. A. Voth, *J Chem Phys* **2006**, *124*, DOI 10.1063/1.2136877.
- [265] F. Paesani, W. Zhang, D. A. Case, T. E. Cheatham, G. A. Voth, *J Chem Phys* **2006**, *125*, DOI 10.1063/1.2386157.
- [266] D. A. Case, R. E. Duke, R. C. Walker, N. R. Skrynnikov, T. E. Cheatham III, O. Mikhailovskii, C. Simmerling, Y. Xue, A. Roitberg, S. A. Izmailov, K. M. Merz, K. Kasavajhala, R. Luo, K. Belfon, P. Li, J. Shen, T. Darden, R. Harris, C. Sagui, A.

Onufriev, F. Pan, S. Izadi, J. Wang, Y. Xiong, D. R. Roe, W. Xiongwu, S. LeGrand, H. Gohlke, J. Swails, S. Schott-Verdugo, A. W. Götz, R. Qi, J. Smith, H. Wei, D. Cerutti, S. Zhao, T. Lee, E. King, J. BERRYMAN, A. ET, *AMBER 22 Reference Manual*, University Of California, **2022**.

[267] R. Salomon-Ferrer, A. W. Götz, D. Poole, S. Le Grand, R. C. Walker, *J Chem Theory Comput* **2013**, *9*, 3878–3888.

[268] A. W. Götz, M. J. Williamson, D. Xu, D. Poole, S. Le Grand, R. C. Walker, *J Chem Theory Comput* **2012**, *8*, 1542–1555.

[269] J.-P. Ryckaert, G. Ciccotti, H. J. C. Berendsen, *J Comput Phys* **1977**, *23*, 327–341.

5. Figures

Figure 1: Difference between α - and β - isomer of the Keggin structure. The β -isomer is obtained by the 60° rotation of one $[M_3O_{13}]$ triad highlighted by a darker color.^[16,17]3

Figure 2: Examples for iso- and heteropolyoxometalates are given. Isopolyoxometalates include decavanadate a) and the hexaniobate Lindqvist structure b) and heteropolyoxometalates include the Wells-Dawson tungstate c), the Andersson-Evans molybdate d) or the mono-functionalized α -Keggin tungstate e). The given general color code for the coordination polyhedra is used in this work to distinguish the different addenda atoms. Heteroatom color scheme: P = olive; metal site (M) = orange.

.....5

Figure 3: a) Condensation reaction of the initial reaction steps during the self-assembly of polyoxometalates. The connection of two octahedral coordinated addenda atoms can be b) corner sharing, c) edge sharing or rarely d) face sharing.^[10,32].....6

Figure 4: pH dependent vanadate species in aqueous medium. Lowering the pH from 13 leads to a changing V:O ratio and the condensation to $\{V_2\}$, $\{V_4\}$, $\{V_5\}$ and $\{V_{10}\}_{ox}$ species followed by hydrolysis to $[VO_2(H_2O)_2]^+$ at low pH values.^[26].....7

Figure 5: General formula of a salt metathesis reaction with the example of the conversion of sodium decavanadate to the insoluble tetrabutylammonium decavanadate in water.8

Figure 6: DMSO stabilizes small vanadyl fragments as building blocks for more complex structures.^[42]9

Figure 7: Schematic influences of internal and external templates as well as heterometals on the formation of polyoxometalate clusters.^[44].....10

Figure 8: $\{V_{12}\}_{bowl}$ stabilized by a) acetonitrile, b) benzonitrile and c) nitromethane as internal neutral templates and d) the top view of the cluster without template and a flipped V=O unit highlighted in dark blue.11

Figure 9: $\{V_{24}\}$ encapsulates the neutral internal template molecules a) acetonitrile and b) nitromethane and c) without template and a flipped V=O unit highlighted in dark blue.13

Figure 10: The size of the template defines the cluster shape, demonstrated by the example of a) perchlorate, b) azide and c) iodide as internal weak interacting anionic template.....	14
Figure 11: External templates stabilize polyoxovanadate structures by hydrogen bonding. Examples include a) cyclen at the top of $\{V_{12}\}_{\text{bowl}}$, b) ammonium at the top of tube-type tetradecavanadate and c) dimethylammonium (DMA) at the top of $\{V_{12}\}_{\text{tube}}$. Possible hydrogen bonds are marked in blue. The internal template was omitted for clarity.....	16
Figure 12: Heterometals stabilize different ring sizes of polyoxovanadates. Examples are a) $\{V_{10}\}_{\text{red}}$, b) $[PdV_6O_{18}]^{4-}$, c) $[Cu_2V_8O_{24}]^{4-}$ and d) $[Ni_4V_{10}O_{30}(OH)_2(H_2O)_6]^{4-}$. Color scheme of the heterometals: Pd = dark yellow; Cu = green; Ni = purple. The vanadium positions of oxidation state +4 are marked in dark blue.....	17
Figure 13: Methoxylated hexavanadate Lindqvist structure functionalized by a) one and b) two titanium centers with the very specific conditions for the respective hydrothermal reaction.....	18
Figure 14: Synthesis of $\{V_{12}\}_{\text{tube}}$ by complete fragmentation of $\{V_4\}$ in presence of indium chloride and dimethylamine hydrochloride.....	19
Figure 15: Chemoselective reaction of decavanadate to $\{V_{12}\}_{\text{bowl}}@MeCN$	20
Figure 16: Exchange of the nitromethane template by halides at $\{V_{12}\}_{\text{bowl}}$	20
Figure 17: Conversion reactions between $\{V_{12}\}_{\text{bowl}}@Cl$, $\{V_{12}\}_{\text{protonated}}$ and $\{V_{12}\}_{\text{tube}}$	21
Figure 18: Controlled functionalization of a α -Keggin polyoxotungstate by controlled basic hydrolysis to form a lacunary structure followed by the introduction of a heterometal M and increasing the pH to obtain the mono-functionalized structure... ..	23
Figure 19: Different related lacunary and closed shell vanadate clusters containing a chloride template. The definition of the arche type structure is difficult due to the structural flexibility of the vanadates.....	24
Figure 20: Replacement of a first placeholder cation DMA by a reactive metal center at the fully oxidized state in an equilibrium.....	25
Figure 21: Replacement of the second placeholder cation DMA by a reactive metal center. Due to a lower overall cluster charge after the binding of the first metal center	

a reduction of one V^V to V^{IV} is often required to stabilize the di-functionalized structure.	25
Figure 22: Schematic of a possible Tris-NH ₃ functionalization of vanadium functionalized Wells-Dawson tungstate a), hexavanadate Lindqvist b) and Andersson-Evans structure c) (heterometal Cu = brown).....	26
Figure 23: POM-POM hybrid material covalently connected via triol linkers. (heterometal Cr = orange).....	26
Figure 24: Vanadium Lindqvist structure functionalized by triol linkers. The pillar[5]arene derivate was introduced by a post-functionalization strategy.	27
Figure 25: Calcium di-functionalized $\{V_{12}\}_{tube}$. Three DMF molecules bridge the gap between two heterometal positions to form one-dimensional polymeric structures. Color scheme: Ca = dark orange; C = light grey; N = blue	28
Figure 26: Two-dimensional metal organic framework of 1,1'-(1,4-butanediyl)bis(imidazole) and copper coordinating the mixed valent decavanadate $\{V_{10}\}_{red}$. Color scheme: Cu = orange; C = light grey; N = blue	28
Figure 27: Schematic setup of a redox flow battery.....	29
Figure 28: The salt metathesis of decavanadate leads to ordered nanostructures for gem and to amorphous packing for nBu ₄ N ⁺ as counter ion after precipitation. ^[92]	32
Figure 29: Possible counter ions forming ionic liquids in combination with the α -Keggin tungstate. ^[98]	33
Figure 30: Structural and spectroscopic information on the formation of $\{Mg_2V_{12}\}$: (a) side view of $\{Mg_2V_{12}\}$; (b) top view of the Mg binding site in $\{Mg_2V_{12}\}$; (c) time-lapse UV-Vis/NIR spectroscopy of the $\{Mg_2V_{12}\}$ reaction mixture containing $\{V_{12}\}$ and MgCl ₂ in acetonitrile. (d) time-dependent reduction of $\{V_{12}\}$ in the presence (green squares) and absence (orange squares) of Mg ²⁺ . Conditions: irradiation with a broadband high-power LED light source ($P_{optical} \sim 5$ W), $[\{V_{12}\}] = 0.05$ mM, $[Mg^{2+}] = 0.21$ mM.	40
Figure 31: Experimental verification for the in-situ formation of the photoactive $\{MgV_{12}\}$ intermediate under reaction conditions. (a) UV-Vis/NIR spectral changes observed upon reaction of $\{V_{12}\}$ (0.05 mM) with Mg ²⁺ (0.21 mM) in acetonitrile, resulting in the formation of the visible-light photoactive $\{MgV_{12}\}$. (b) ⁵¹ V NMR spectroscopic observation of the characteristic four-line pattern of mono-functionalized $\{MgV_{12}\}$	

formed by reaction of $\{V_{12}\}$ (10 mM) with Mg^{2+} (42 mM) in acetonitrile. ^{51}V NMR spectra of $\{V_{12}\}$ (in acetonitrile) and $\{Mg_2V_{12}\}$ (in dimethyl sulfoxide) are shown for comparison. (c) ^{51}V TOCSY NMR spectrum indicating that all four signals belong to one ^{51}V spin system i.e., one $\{MgV_{12}\}$ cluster. Non-diagonal signals are marked with red circles. Conditions: $[\{V_{12}\}] = 5.0$ mM, $[Mg^{2+}] = 21.1$ mM, solvent: acetonitrile. (d) Negative ion-mode high-resolution ESI mass spectrum showing the observed and simulated isotopic pattern for $[HMgV_{12}O_{32}Cl]^{2-}$ ($= H\{MgV_{12}\}$), $[\{V_{12}\}] = 0.05$ mM, $[Mg^{2+}] = 0.21$ mM, solvent: acetonitrile. 42

Figure 32: In-situ ^{51}V NMR spectroscopic titration to assess the $\{MgV_{12}\}$ formation. Top: stacked ^{51}V NMR spectra of acetonitrile solutions containing $\{V_{12}\}$ and varying Mg^{2+} molar equivalents (between 0 eq. to 4 eq. relative to $\{V_{12}\}$). Bottom: the area integrals of the three characteristic $\{MgV_{12}\}$ signals marked a), b), c) are shown. In each instance, integral changes are only observed up to 1.0 Mg^{2+} equivalents, indicating that a 1:1 species, i.e., $\{MgV_{12}\}$ is formed. Conditions: $[\{V_{12}\}] = 5.0$ mM, $[Mg^{2+}] = 0 - 21.1$ mM, solvent = acetonitrile. 44

Figure 33: Proposed coupled solution-phase equilibria during $\{Mg_2V_{12}\}$ formation: (a) the light-independent pre-equilibrium forming the photoactive intermediate $\{MgV_{12}\}$ and (b) light-driven formation of the di-Mg-functionalized $\{Mg_2V_{12}\}$ 46

Figure 34: Normalized emission spectrum of the 20 W LED light source, and comparison with the absorbance of the standard $\{V_{12}\} / MgCl_2 / MeCN$ reaction solution. 51

Figure 35: UV-Vis/NIR spectrum of a DMF solution of 1 (56 μ M): ϵ_{338} : 11,875 $M^{-1} cm^{-1}$; ϵ_{991} : 1,400 $M^{-1} cm^{-1}$. Inset: magnified view of the region between 750 nm and 1100 nm, showing the characteristic IVCT transition indicative of the presence of a mixed-valent VIV/V species. 54

Figure 36: Black: Solid state CW-EPR spectrum of 1 between 225 mT to 450 mT with a modulation of 1mT, a microwave power of 25 mW and a sweep time of 120 s. Red: simulation with $S = \frac{1}{2}$, $g_1 = 1.904(1)$, $g_2 = 1.979(1)$, $g_3 = 2.049(1)$ and isotropic line width = 0.696(5) GHz. 54

Figure 37: 1H NMR spectrum of 1. Conditions: solvent: DMSO- d_6 , 400 MHz, 64 scans. Signal assignments: δ (ppm) = 3.44 (s, H_2O); 3.18 (m, 2 H, nBu_4N^+); 2.45 (impurity);

2.07 (s, acetonitrile); 1.56 (m, 2 H, nBu ₄ N ⁺); 1.30 (s, 2 H, nBu ₄ N ⁺); 0.92 (t, 3 H, nBu ₄ N ⁺)	55
Figure 38: ⁵¹ V NMR spectrum of 1. Conditions: [1] ca. 7.5 mM in DMSO-d ₆ , 10,000 scans; 105 MHz, δ (ppm) = - 557.0 (s, 4V); - 578.3 (s, 8V).	55
Figure 39: ⁵¹ V NMR spectrum of 1, {Mg ₂ V ₁₂ } in MeCN, indicating that upon dissolving {Mg ₂ V ₁₂ } in MeCN, one Mg ²⁺ is released and {MgV ₁₂ } is re-formed. Conditions: [1] ca. 5.0 mM in MeCN.	56
Figure 40: ATR-FT-IR spectrum of compound 1. Characteristic IR bands (in cm ⁻¹): 3336; 2961 (C-H stretching, alkane); 2934 (C-H stretching, alkane); 2874 (C-H stretching, alkane); 1659; 1641; 1613; 1482; 1461; 1381; 1422; 1345; 1278; 1251; 1163; 1151; 1107; 1067; 995 (symmetric V=O, terminal Oxygen); 890; 875 (anti-symmetric stretching V-O); 817; 752 (V-O-V, symmetric); 661 (V ₃ -Oμ ₃ , asymmetric); 593; 412.	56
Figure 41: Thermogravimetric analysis (under air) of compound 1. A weight loss of 5.01 wt.-% between 30 °C and 116 °C is shown, which corresponds to the loss of three acetonitrile (calc.: 5.21 wt.-%). A further weight loss of 41.97 wt.-% between 116 °C and 434 °C, corresponds to the loss of four tetra-n-butylammonium cations (calc.: 41.04 wt.-%). The loss of 4.47 wt.-% above 436 °C can be assigned to the loss of the three chlorides (calc.: 4.50 %).	57
Figure 42: High-resolution negative-ion mode ESI mass spectra of (a) the reference sample, {V ₁₂ } (0.05 mM) dissolved in MeCN; (b) the reaction solution containing {V ₁₂ } (0.05 mM) and MgCl ₂ (0.21 mM) dissolved in MeCN. Detailed peak assignment, see below.	57
Figure 43: ORTEP illustration of the single-crystal XRD structure of {Mg ₂ V ₁₂ }. Probability ellipsoids drawn at 50 % probability.	60
Figure 44: ⁵¹ V NMR spectra of {V ₁₂ } in acetonitrile upon addition of MgCl ₂ before and after irradiation for 24 h, in comparison with ⁵¹ V NMR spectra of the {V ₁₂ } (in acetonitrile) and {Mg ₂ V ₁₂ } (in DMSO) reference compounds. Conditions: [Mg ²⁺] ca. 42 mM, [{V ₁₂ }] ca. 10 mM.	62
Figure 45: ¹ H NMR spectra ((a) 6 - 8 ppm region, (b) 1 – 3.5 ppm region) of pure {V ₁₂ } (red) as well as a mixture of {V ₁₂ } (10 mM) and MgCl ₂ (42 mM) in CD ₃ CN immediately after preparation (green), and after 24 h irradiation using a 20 W broadband LED light	

source (blue). The characteristic low-field shift of the DMA N-H protons upon MgCl_2 addition shown in (a) indicate the release of one DMA upon formation of $\{\text{MgV}_{12}\}$ and release of another DMA cation upon light-induced formation of $\{\text{Mg}_2\text{V}_{12}\}$, see main manuscript, Fig. 4 for a schematic illustration of the processes..... 62

Figure 46: Stacked ^1H NMR spectra ((a) 5.6 – 7.5 ppm region, (b) 0.9 – 3.3 ppm region) of acetonitrile solutions containing $\{\text{V}_{12}\}$ and varying Mg^{2+} molar equivalents (between 0 eq. to 4 eq. relative to $\{\text{V}_{12}\}$). Upon Mg^{2+} addition, characteristic low-field shifts of the N-H protons of the DMA cations are observed ($\delta \sim 6.3$ ppm to $\delta \sim 7.0$ ppm), indicating a dynamic equilibrium between cluster-bound and “free” DMA. Conditions: $[\{\text{V}_{12}\}] = 5.0$ mM, $[\text{Mg}^{2+}] = 0 - 21.1$ mM, solvent = acetonitrile..... 63

Figure 47: ^1H NMR spectra of $\{\text{V}_{12}\}$ (red), the $\{\text{V}_{12}\}/\text{Mg}^{2+}$ reaction mixture (green) and pure DMA (black) in CD_3CN . The ammonium resonance for the $\{\text{V}_{12}\}/\text{Mg}^{2+}$ mixture is located between the resonances of the “free” and the cluster-bound DMA, suggesting a Mg^{2+} -concentration-dependent dynamic equilibrium in solution. The DMA ^1H methyl resonance is virtually unaffected in all measurements shown, as the chemical environment for the methyl groups does not significantly change, independent on whether the species is cluster-bound or “free” in solution. Bottom: ^1H DOSY NMR spectra of $\{\text{V}_{12}\}$ (red), the $\{\text{V}_{12}\}/\text{Mg}^{2+}$ reaction mixture (green) and pure DMA (black) overlaid. The data show that the diffusion coefficients decrease in the order “free” DMA $< \{\text{MgV}_{12}\} < \{\text{V}_{12}\}$. This is expected, as the $\{\text{MgV}_{12}\}$ reaction solution contains a mixture of cluster-bound and “free” DMA (released during Mg^{2+} binding), so that an averaged signal of the two DMA species is observed. Conditions: solvent: CD_3CN , $[\text{Mg}^{2+}] = 21$ mM, $[\{\text{V}_{12}\}] = 5.0$ mM, $[\text{DMA}] = 10$ mM. 64

Figure 48: ^{51}V NMR spectrum of $\{\text{V}_{12}\}$ upon addition of MgCl_2 at HR-ESI-MS concentrations. Conditions: solvent: CH_3CN , $[\text{Mg}^{2+}] = 0.21$ mM, $[\{\text{V}_{12}\}] = 0.05$ mM. 64

Figure 49: Time-lapse UV-Vis spectra of $\{\text{V}_{12}\}$ when irradiated with a broadband high-power LED light source ($P_{\text{nominal}} = 20$ W). Conditions: solvent: acetonitrile, $[\{\text{V}_{12}\}] = 50$ μM , Ar atmosphere. Note that no reduction (indicated by the characteristic IVCT transitions between 600 nm – 1100 nm) of $\{\text{V}_{12}\}$ is observed..... 65

Figure 50: UV-Vis/NIR spectra of $\{\text{V}_{12}\}$ in the absence (black) and presence (red) of Mg^{2+} . (a) showing the reaction mixture before irradiation, indicating the in-situ formation of $\{\text{MgV}_{12}\}$ (characteristic changes between 300 nm to 500 nm). (b) after 6 h irradiation, showing the formation of the 1-electron-reduced $\{\text{Mg}_2\text{V}_{12}\}$ (by the characteristic IVCT

transitions between 700 nm – 1100 nm). Conditions: solvent: acetonitrile, $[\{V_{12}\}] = 50 \mu\text{M}$, $[\text{MgCl}_2] = 211 \mu\text{M}$, Ar atmosphere.....65

Figure 51: UV-Vis spectroscopic analysis of changes of the IVCT absorption band (detected at $\lambda = 955 \text{ nm}$) when the $\text{Mg}^{2+} / \{V_{12}\}$ reaction mixture or the $\{V_{12}\}$ reference is irradiated with monochromatic LEDs (405 nm or 470 nm). Conditions: solvent: acetonitrile, $[\{V_{12}\}] = 0.05 \text{ mM}$, $[\text{Mg}] = 0.21 \text{ mM}$66

Figure 52: UV-Vis/NIR spectra of the $\{V_{12}\} + \text{MgCl}_2$ reaction mixture in the presence and absence of DMAcI. (a) before irradiation; (b) after 6 h irradiation with a broadband high-power LED light source ($P_{\text{nominal}} = 20 \text{ W}$). In the presence of DMAcI, no reduced vanadate species are formed (indicated by the absence of the characteristic IVCT band). We propose that this indicates the presence of an excess of DMA cations affects the $\{V_{12}\} / \{\text{MgV}_{12}\}$ equilibrium, prevents the formation of the photoactive $\{\text{MgV}_{12}\}$ and can therefore be used as a supramolecular control parameter to trigger or prevent vanadate photoreduction. Conditions: solvent: acetonitrile, $[\{V_{12}\}] = 50 \mu\text{M}$, $[\text{MgCl}_2] = 211 \mu\text{M}$, Ar atmosphere.66

Figure 53: UV-Vis spectrum comparison of $\{V_{12}\} + \text{MgCl}_2$ when irradiated with a broadband high-power LED light source ($P_{\text{nominal}} = 20 \text{ W}$) after 6 hours. Conditions: solvent: acetonitrile, $[\{V_{12}\}] = 50 \mu\text{M}$, $[\text{MgCl}_2] = 211 \mu\text{M}$67

Figure 54: Cyclic voltammetry analysis. (a): CV analysis of the electrolyte when purged with Ar or O_2 . (b) CV analysis of DMAcI (Ar atmosphere). (c) CV analysis of $(\text{DMA})_2\{V_{12}\}$ (Ar atmosphere). Conditions: solvent: anhydrous MeCN containing 0.1 M nBu_4NPF_6 ; $[\text{DMAcI}] = 2 \text{ mM}$, $[(\text{DMA})_2\{V_{12}\}] = 1 \text{ mM}$; samples referenced against Fc^+/Fc as internal standard. Scan rate: 100 mV/s.67

Figure 55: ^{51}V NMR spectra of $\{V_{12}\}$ upon addition of MgCl_2 and upon addition of $\text{CaCl}_2 \times 2 \text{ H}_2\text{O}$ under otherwise identical reaction conditions. In both cases, the characteristic four-line signal indicating the formation of the mono-metal-functionalized species (i.e., $\{\text{MgV}_{12}\}$ or $\{\text{CaV}_{12}\}$) is observed. Conditions: $[\text{Mg}^{2+}]$ ca. 21 mM, $[\text{Ca}^{2+}]$ ca. 21 mM, $[\{V_{12}\}]$ ca. 5.0 mM, solvent: CH_3CN68

Figure 56: UV-Vis/NIR spectra showing the formation of the characteristic IVCT band indicative of formation of a reduced vanadate cluster upon irradiation of a DMF solution containing Ca^{2+} and $\{V_{12}\}$. Conditions: $[\text{Ca}^{2+}]$ ca. 0.21 mM, $[\{V_{12}\}]$ ca. 0.05 mM, solvent: DMF.....68

Figure 57: Left: Calculated HOMO-LUMO levels of {MgV ₁₂ } and {Mg ₂ V ₁₂ }. Right: Calculated UV-Vis/NIR spectra for {MgV ₁₂ } and {Mg ₂ V ₁₂ }.	69
Figure 58: Top: orbital illustrations for the calculated high oscillator-strength LMCT transitions in {MgV ₁₂ } and {Mg ₂ V ₁₂ }. Bottom: orbital illustrations for the calculated high oscillator-strength IVCT transitions in {Mg ₂ V ₁₂ }.	69
Figure 59: Formal assembly Scheme and structure comparison of the mixed-cluster cocrystal 1 , compared with structurally related literature-known single-cluster species (nBu ₄) ₄ [V ₁₆ O ₃₈ Cl] and (nBu ₄) ₄ [V ₁₅ O ₃₆ Cl]. ^[71,72] Note that synthetically, 1 is obtained using [V ₁₀ O ₂₆] ⁴⁻ as vanadate precursor.	74
Figure 60: Characterization of 1 . a) ATR-IR spectroscopy showing the presence of O-H vibrations; b) UV-Vis/NIR spectroscopy showing characteristic V(IV/V) intervalence charge-transfer (IVCT) transitions; c), d) simulated and observed isotopic patterns from high resolution ESI-MS analyses, indicating the presence of {MgV ₁₃ } and {V ₁₄ }.	76
Figure 61: Simulated and experimental EPR spectra (T=40 °C) of: a) the reference compound (nBu ₄ N) ₄ [V ^{IV} ₂ V ^V ₈ O ₂₄] ^[166] (3 mM in MeCN); b) compound 1 (3 mM in MeCN). Comparison of the spin counts gave a value of 1.87 unpaired electrons for 1	77
Figure 62: a) Time-lapse UV-Vis/NIR spectroscopy of the conversion of {V ₁₀ } _{red} to 1 at time intervals of 1 min. Three isosbestic points at λ ₁ =665 nm, λ ₂ =446 nm and λ ₃ =340 nm indicate a direct conversion process. Conditions: T=35 °C, cuvette path length 10.0 mm, [{V ₁₀ } _{red}] : [MgCl ₂ (anhydrous)]=1 : 1.2, [{V ₁₀ } _{red}]=230 μM). b) Decrease of {V ₁₀ } _{red} concentration as a function of [Mg ²⁺] concentration, monitored by following the characteristic {V ₁₀ } _{red} absorbance at λ=500 nm; samples were equilibrated for 1 h before measurement; c) Increase of the concentration of 1 as a function of Mg ²⁺ concentration, monitored by following the characteristic absorbance of 1 at λ=1000 nm; samples were equilibrated for 1 h before measurement. d) Kinetic traces and mono-exponential fits of the {V ₁₀ } _{red} -to- 1 conversion (monitored by following the decrease of {V ₁₀ } _{red} concentration at λ=500 nm) at temperatures between 25 °C to 65 °C. Conditions: ΔT=10 °C, cuvette path length 2.0 mm, [{V ₁₀ } _{red}] : [MgCl ₂ (anhydrous)]=1 : 2.2, [{V ₁₀ } _{red}]=500 μM. d) Arrhenius plot based on the kinetic traces shown in e).	78
Figure 63: a) Square-wave voltammogram and b) cyclovoltammogram of 1 , showing 14 pseudo-reversible redox transitions in the scan range between -2.15 V to +1.35 V	

vs Fc+/Fc, open circuit potential and scan direction are indicated by the red arrow. Conditions: anhydrous, deoxygenated acetonitrile containing nBu ₄ NPF ₆ (0.1 M) as supporting electrolyte. Scan rate 50 mV s ⁻¹ , [1]: 0.5 mM, Ar atmosphere.	80
Figure 64: ¹ H-NMR of compound 1 in deuterated acetonitrile.	86
Figure 65: Structure of the {V ₁₀ } _{red} cluster indicating an axial symmetry of the system. ^[167]	87
Figure 66: TGA measurement of compound 1. The observed weight loss of 45 % between 200 °C and 600 °C indicates the presence of 8 nBu ₄ N ⁺ cations in 1 (calcd.: 43 %).	88
Figure 67: High-resolution negative-ion mode ESI mass spectrum of 1 (0.05mM) in MeCN.	90
Figure 68: UV-Vis/NIR spectra of 1 in MeCN. left: [1] = 15.625 μmol/L; right: [1] = 125 μmol/L.	91
Figure 69: UV-Vis/NIR spectra of {V ₁₀ } _{red} in MeCN. left: [{V ₁₀ } _{red}] = 31.25 μmol/L; right: [{V ₁₀ } _{red}] = 250 μmol/L.....	91
Figure 70: Temperature dependent UV-Vis/NIR Spectra were measured with a time increment of 60 s, cuvette path length of 2.0 mm, [{V ₁₀ } _{red}] : [MgCl ₂ (anhydrous)] = 1 : 2.2 and [{V ₁₀ } _{red}] = 500 μM.	92
Figure 71: Linear change of ln(Abs (λ = 500 nm)) vs time confirms the first order kinetics.	93
Figure 72: UV-Vis/NIR of {V ₁₀ } _{red} was measured during the equilibration time of 1h with a time interval of 1 min at [{V ₁₀ } _{red}] = 230 μM, a temperature of 35 °C and a cuvette pathlength of 10 mm pathlength.	95
Figure 73: ATR-FT-IR spectrum of compound 1.	96
Figure 74: ATR-FT-IR spectrum of {V ₁₀ } _{red}	96
Figure 75: Cyclic voltammogram (left) and square-wave voltammogram (right) of 1. Conditions: anhydrous, deoxygenated acetonitrile containing nBu ₄ NPF ₆ (0.1 M) as supporting electrolyte (scan rate 0.05 V s ⁻¹), [1]: 0.5 mM.	97
Figure 76: Left: Comparison of CVs of 1 before (dark blue) and after (turquoise) bulk reduction (BR) (E = - 1.45 V). Open circuit potentials and scan directions are indicated	

by arrows. Right: UV-Vis/NIR absorption spectra of 1 before (dark blue) and after (turquoise) bulk reduction.	98
Figure 77: Left: Square wave voltammogram of 1 before (dark blue) and after (turquoise) bulk reduction (E = - 1.45 V). Right: Chronoamperogram of bulk electrolysis (E = -1.45 V).	98
Figure 78: Left: Comparison of CVs of 1 before (dark blue) and after (green) bulk oxidation (BOx) (E = + 1.22 V) and after re-reduction (Re-Red) (blue) (E = + 0.09 V). Open circuit potentials and scan directions are indicated by arrows. Right: UV-Vis/NIR absorption spectra of 1 before (dark blue) and after (green) bulk oxidation.....	99
Figure 79: Left: Square-wave voltammogram of 1 before (dark blue) and after (green) bulk electrolysis (E = + 1.22 V) and after re-reduction (Re-Red) (blue) (E = + 0.09 V). Right: Chronoamperogram of bulk electrolysis (E = + 1.22 V).	99
Figure 80: Upper segment of square-wave voltammogram of 1 showing the integration limits indicated by differently colored regions. The integrals were used to estimate the numbers of electrons transferred for each process, see below.	100
Figure 81: Left: Square-wave voltammograms of $[H_3V_{10}O_{28}]^{3-}$, $\{V_{10}\}_{red}$ and their 1:1 molar mixture. Right: Square-wave voltammograms of $\{V_{12}\}_{bowl}@MeCN$, $\{Ca_2V_{12}\}$ and their 1:1 molar mixture. Solvent: De-aerated, degassed and dry MeCN containing $(nBu_4N)PF_6$ (0.1 M).	104
Figure 82: Thermodynamic cycle for the calculation of Gibbs free energies of a one-electron reduction process.	105
Figure 83: (a) Polyhedral representation of the two vanadate cluster species present as 1:1 molar mixture in the $\{MV_{13}\}$. (b) Schematic illustration of the symmetric $\{MV_{13}\}$ -based nonaqueous redox flow battery setup reported.	110
Figure 84: a) SWV of $\{MV_{13}\}$ at different frequencies 1 Hz - 5 Hz. b) LSV of peak 4;3 at different rotation rates. c) linear plot of i_{peak} vs. $f^{1/2}$ and d) the linear plot of $i_{plateau}$ vs. $\omega - 1/2$. The measurements were conducted at concentration of 0.5 mM in acetonitrile containing 0.1M $(nBu_4N)PF_6$ as supporting electrolyte.	112
Figure 85: a) Charge and discharge curves of $\{MV_{13}\}$, b) The voltage profile of the NRFBs in cyclability test at current density of 1.75 mA cm^{-2} , (c) the charge discharge capacities of the NRFBs during the 50 cycles cycling test and (d) the coulombic	

efficiency, voltage efficiency and energy efficiency of the NRFBs during the cycling test.	115
Figure 86: The OCP changes during the charge and discharge process include redox event 4;3 of the SWV data closely matching the expected transfer of four electrons. (shown for cycle 2)	116
Figure 87: Structure of the RFB setup (Source from https://redox-flow.com/shop/redox-flow-battery-test-cell/).	119
Figure 88: ATR-FT-IR of {MV ₁₃ }.	120
Figure 89: a) SWV of the ferrocene reference sample at different frequencies 1 Hz - 5 Hz at 0.5 mM at the same experimental conditions compared to {MV ₁₃ }. b) Linear plot of i_p vs. $f^{1/2}$ of ferrocene. The slope m is used to calculate the diffusion coefficients.	122
Figure 90: a) Experimental setup for the permeability tests. Volume A is filled with POM solution, and the absorbance of volume B is measured at a constant time interval in a flow cuvette. The total volume including the A and B as well as the tubing was measured b) before and c) after the measurement time and was constant.....	123
Figure 91: Permeability test to analyze the migration of {MV ₁₃ } across a Celgard 2400 membrane. a) the initial absorbance in reservoir A, b) the increasing absorbance in reservoir B measured every 5 minutes, c) the development of the absorbance in reservoir B at 965 nm over time (The permeability was determined from 15000s to 40000s where steady-state one-dimensional diffusion can be assumed.), and d) the linear fit used to determine the permeability.	124
Figure 92: Permeability test to analyze the migration of {V ₁₀ } _{red} across a Celgard 2400 membrane. a) the initial absorbance in reservoir A, b) the increasing absorbance in reservoir B measured every 5 minutes, c) the development of the absorbance in reservoir B at 965 nm over time (The permeability was determined from 15000s to 40000s where steady-state one-dimensional diffusion can be assumed.), and d) the linear fit used to determine the permeability.	125
Figure 93: Structure of the [Mn ^{III} ₂ Mn ^{IV} ₂ V ₄ O ₁₇ (OAc) ₃] ³⁻	129
Figure 94: Comparison of the densities of acetonitrile/water mixtures obtained from different MD simulations compared to experimental values from literature. ^[250]	131

Figure 95: a) Radial distribution functions, $g(r)$, between the center of mass (CoM) of and the hydrogen atoms of water. Dashed lines indicate the corresponding integrated solvation numbers $n(r)$. b) Fraction of water molecules $q(\text{H}_2\text{O})$ residing within 10 Å range of the cluster. c) Radial distribution functions, $g(r)$, between the center of mass (CoM) of and the hydrogen atoms of acetonitrile. Dashed lines indicate the corresponding integrated solvation numbers $n(r)$. d) Fraction of acetonitrile molecules $q(\text{MeCN})$ residing within 10 Å range of the cluster. 132

Figure 96: a,b) The increasing absorbance with addition of water is visible by the darker color of samples prepared at 1 mM concentration of the cluster and gradually increasing vol% water. c) UV-Vis spectra of $\{\text{MnV}\}^{3-}$ and d) of $\{\text{MnV}\}^{2-}$ at a cluster concentration of about 50 μM . Water was added in 20 μL steps to 2 mL of water free sample and the spectra were corrected by the dilution factor. e) The relative absorbance of the UV-Vis spectrum at 5 vol% of water after subtraction of the spectrum at 0 vol% of water for $\{\text{MnV}\}^{3-}$ and $\{\text{MnV}\}^{2-}$ and f) the changes of the normalized absorbance at 350 nm with increasing vol% water of $\{\text{MnV}\}^{3-}$ and $\{\text{MnV}\}^{2-}$ 134

Figure 97: Liquid FTIR spectra of $\{\text{MnV}\}^{3-}$ (a) and $\{\text{MnV}\}^{2-}$ (b), showing changes of the characteristic vibrations with variation of the water content. Conditions: concentration 10 mM, pathlength 0.05 mm c) Electrochemical analysis of the anodic (i_{pa}) and cathodic (i_{pc}) peak current changes with varying water contents for $\{\text{MnV}\}^{3-}$ (red) and $\{\text{MnV}\}^{2-}$ (blue). Conditions concentration 1 mM d) Electrochemical analysis of the diffusion coefficients (determined by RS analysis) for $\{\text{MnV}\}^{3-}$ (red) and $\{\text{MnV}\}^{2-}$ (blue). Conditions: concentration 1 mM 136

Figure 98: Brown cubic block shaped crystals of $(n\text{-Bu}_4\text{N})_3\{\text{MnV}\}$ were used for all measurements. 140

Figure 99: FTIR spectrum of $(n\text{-Bu}_4\text{N})_3\{\text{MnV}\}$ 141

Figure 100: a) Chronoamperogram of bulk electrolysis (BE) at $E = 0.65\text{ V}$ of 1 mM solution of $(n\text{-Bu}_4\text{N})_3\{\text{MnV}\}$ in water free acetonitrile containing 0.1 M $n\text{-Bu}_4\text{NPF}_6$ as supporting electrolyte. b) A cyclovoltammogram before and after bulk electrolysis was recorded at a glassy carbon electrode (3 mm diam.) scan rate: 100 mV/s vs. Ag/AgNO_3 . The open circuit potentials and scan directions are indicated by arrows. Note that no compound degradation is observed during the one electron oxidation. c) The redox transitions were assigned using square-wave voltammetry according to the literature.^[235] 142

Figure 101: Cyclic voltammogram at increasing vol% water of a) $\{\text{MnV}\}^{3-}$ and b) $\{\text{MnV}\}^{2-}$ at a scan rate of 50 mV/s.	142
Figure 102: Randles–Ševčík analysis of 1 mM solution of $\{\text{MnV}\}^{3-}$ at different vol% of water.....	143
Figure 103: Randles–Ševčík analysis of 1 mM solution of $\{\text{MnV}\}^{3-}$ at different vol% of water.....	144
Figure 104: Randles–Ševčík analysis of 1 mM solution of $\{\text{MnV}\}^{2-}$ at different vol% of water.....	145
Figure 105: High resolution negative ion mode ESI mass spectrum of $\{\text{MnV}\}^{3-}$ (0.05 mM) in acetonitrile. The isotopic distribution was calculated for the two main signals 3 and 4.	147
Figure 106: High resolution negative ion mode ESI mass spectrum of $\{\text{MnV}\}^{2-}$ (0.05 mM) in acetonitrile containing residual (n-Bu ₄ N)PF ₆ from the bulk electrolysis (5 mM).	148
Figure 107: High resolution negative ion mode ESI mass spectrum of a) $\{\text{MnV}\}^{3-}$ including the assignment of (n-Bu ₄ N)(OAc) ₂ and b) $\{\text{MnV}\}^{2-}$ (0.05 mM) in acetonitrile containing 5 vol% water. In both spectra no cluster signals were detected likely due to ion pairing and aggregation.	149
Figure 108: a) Normalized signal intensity of (n-Bu ₄ N)(OAc) ₂ at increasing water content. The cluster signals of $\{\text{MnV}\}^{3-}$ decrease to a water content of 5 vol%. b) The cluster signals of $\{\text{MnV}\}^{2-}$ are not observable at a water content above 2 vol% likely due to aggregation. No acetate related signals were detected in the presence of electrolyte.....	149
Figure 109: a, b) A UV-Vis spectrum of $\{\text{MnV}\}^{3-}$ and $\{\text{MnV}\}^{2-}$ was measured at ambient conditions at a concentration of 50 μM. The range of 400 nm to 1100 nm is shown in c) and d).	150
Figure 110: Relative absorbance of $\{\text{MnV}\}^{2-}$ compared to $\{\text{MnV}\}^{3-}$. The spectrum of $\{\text{MnV}\}^{3-}$ was subtracted as reference and agrees with the literature. ^[251]	150
Figure 111: Liquid FTIR signals of acetic acid in solutions of a) 10 mM $\{\text{MnV}\}^{3-}$ and b) $\{\text{MnV}\}^{2-}$ with increasing vol% of water at a pathlength of 0.05 mm. Acetic acid was	

measured at different concentrations in acetonitrile at a pathlength of 0.05 mm for quantification. The signal at 1218 cm⁻¹ was used for linear regression. 151

Figure 112: a) Linear regression of the signal intensity at 1218 cm⁻¹ of acetic acid in acetonitrile and b) equivalents of free acetic acid depending on the water content. The signal of acetic acid increases faster for the samples of {MnV}²⁻ compared to {MnV}³⁻. The complex reaction mixture only allows for an estimation of the amount of free acetic acid, which reaches about 1 equivalent compared to the cluster concentration with increasing water content in agreement with the reaction pathway of ligand exchange presented in the literature.^[237] 152

Figure 113: a): ¹H-NMR spectrum of 5 mM {MnV}³⁻ solution in d₃ CH₃CN with the resonances assigned. The sample was prepared under an inert atmosphere in the glove box. The integral of the water signal is slightly higher due to residual water present in the acetonitrile. The signal of the acetate ligand **a** is paramagnetically shifted to 19.5 ppm due to the proximity to the manganese centers. **b)** ⁵¹V-NMR spectrum of 1 mM {MnV}³⁻ solution in d₃ CH₃CN. The ⁵¹V V₁ resonance is paramagnetically shifted to +45 ppm. The V₂ signals are broadened beyond detection due to the close distance to the paramagnetic cubane core. 153

Figure 114: a): Overlaid ¹H-NMR spectra of the {MnV}³⁻ cluster in d₃ CH₃CN increasing the water content with the spectral region between 18.0 ppm and 21.0 ppm magnified. The samples were prepared by adding 50 M solution of water in acetonitrile in 2.5 μL steps to a 0.5 mL of a 5 mM solution of {MnV}³⁻ in d₃ CH₃CN. Each sample was filled with d₃ CH₃CN to a total volume of 0.55 mL. **b)** ⁵¹V-NMR spectrum of {MnV}³⁻ at a concentration of 1 mM in deuterated acetonitrile with increasing water content. **c)** Normalized ¹H integral of the signal **a** as a function of the water content and **d)** The ⁵¹V V₁ resonance becomes too broad to be detected probably due to aggregation or geometry changes by ligand exchange by higher water contents. 154

Figure 115: ¹H T₁ relaxation time constants of the H₂O resonance of samples containing 5 mM {MnV}³⁻ cluster in d₃ CH₃CN increasing the water content measured with dissolved oxygen (left) and under oxygen free conditions (right) at ambient temperature. The influence of molecular paramagnetic oxygen on the T₁ relaxation time constants is obscured by the stronger paramagnetic effect of the cluster. 155

Figure 116: Preliminary results on the development of novel highly redox active and stimuli responsive clusters. This will include {V₁₂}_{protonated} shown in a) and further

development of the placeholder strategy and $\{V_{12}\}_{\text{tube}}$ in b). Specifically, the supramolecular aggregation to polymeric structures will be the focus in future investigations.....161

Figure 117: Cation exchange strategy to enhance the solubility of $\{MV_{13}\}$ shown for tetraoctyl ammonium.163

6. Tables

Table 1: List of abbreviations.	ix
Table 2: List of compounds.	x
Table 3: Reaction conditions for the synthesis of methoxylated hexavanadate Lindqvist structures a) with one and b) with two titanium centers. ^[66]	18
Table 4: ESI MS peak assignments for $\{V_{12}\}$ and the reaction mixture, $\{V_{12}\}+MgCl_2$	58
Table 5: Crystallographic Parameters for 1	59
Table 6: Bond Valence Sum calculation summary for the vanadium atoms of 1.	61
Table 7: Summary of the observed 1H and ^{51}V NMR signals.	63
Table 8: EPR simulation parameters for $\{V_{10}\}_{red}$	87
Table 9: EPR simulation parameters for compound 1.	88
Table 10: Possible distributions of electrons on $\{V_{14}\}$	89
Table 11: Possible distributions of electrons on $\{MgV_{13}\}$	89
Table 12: Detailed peak assignment of the high-resolution negative-ion mode ESI mass spectrum of 1	90
Table 13: The fit parameters of the mono-exponential fit Figure 62d were used for the Arrhenius Plot Figure 62c.	94
Table 14: The fit parameters of the Arrhenius Plot were used to calculate the activation energy.	94
Table 15: Summary of electrochemical intervals between individual redox events in selected classical single-cluster polyoxometalates.	97
Table 16: Summary of bulk electrolyses with calculated average number of transferred electrons per cluster.	100
Table 17: Summary of the integration of the square-wave voltammogram of 1 , and the resulting electron transfer numbers for 1	101
Table 18: Crystallographic parameters for the samples	103
Table 19: Experimental and calculated reduction potentials for $\{V_{14}\}$ and $\{MgV_{13}\}$	105
Table 20: Parameters for the calculation of the diffusion coefficient of $\{MV_{13}\}$	113

Table 21: Diffusional permeability comparison of previously reported active species in electrolyte for RFBs.....	126
Table 22: Slopes of the linear regression of anodic and cathodic peak currents i_{pa} and i_{pc} and average diffusion coefficients of $\{MnV\}^{3-}$ determined by the Randles–Ševčík equation.	144
Table 23: Slopes of the linear regression of anodic and cathodic peak currents i_{pa} and i_{pc} and average diffusion coefficients of $\{MnV\}^{2-}$ determined by the Randles–Ševčík equation.	146
Table 24: Detailed peak assignment of the high resolution negative ion mode ESI mass spectrum of.....	147
Table 25: Peak assignments of the high-resolution negative ion mode ESI mass spectrum of $\{MnV\}^{2-}$	149
Table 26: Number of molecules used for MD simulations of pristine solvent boxes with varying molar fractions of acetonitrile.	157
Table 27: Number of molecules used for MD simulations of boxes including one POM molecule.....	157
Table 28: Use of AI Tools	200

Scientific Contributions

Publications in Peer Reviewed Journals:

1. **(MR1)** S. Repp, M. Remmers, A.S.J. Rein et al. Coupled reaction equilibria enable the light driven formation of metal functionalized molecular vanadium oxides. *Nat Commun* **14**, 5563 (2023). <https://doi.org/10.1038/s41467-023-41257-y>
2. **(MR2)** M. Remmers, B. Mashtakov, S. Repp, A. S. J. Rein, K. Wang, M. Anjass, Z. Chen, L. M. Carrella, E. Rentschler, C. Streb, *Angew. Chem. Int. Ed.* 2025, **64**, e202418864. <https://doi.org/10.1002/anie.202418864>

Conferences:

Date	Conference	Contribution
20.10.23 - 22.10.23	POM Symposium Paris, France	Oral presentation, poster
13.12.23 - 14.12.23	EPSRC JSPS Core to Core Collaboration Hiroshima, Japan	poster
28.07.24 - 03.08.24	45th International Conference on Coordination Chemistry Fort Collins, USA	poster
16.09.24 - 20.09.24	12. Sommerschule „Grundlagen der Einkristallstrukturanalyse“ Warendorf, Germany	participation
03.06.25 - 05.06.25	Gutenberg Workshop: Lab Automation Mainz, Germany	participation
21.07.25 - 25.07.25	FMOCS VIII: Frontiers in Metal Oxide Cluster Science Mainz, Germany	Oral presentation, poster

Curriculum Vitae

Personal Profile

Name: Moritz Remmers
Date of Birth: September 14th 1997
Place of Birth: Aschaffenburg
Nationality: German

Education

10/2022– today Ph.D. studies at Johannes Gutenberg-University Mainz
(Mainz Germany)
04/2020 – 08/2022 Master of Science, Johannes Gutenberg-University Mainz
(Mainz Germany)
10/2019 – 03/2020 Semester abroad, CIC nanoGUNE
(San Sebastian Spain)
10/2016 – 09/2019 Bachelor of Science, Johannes Gutenberg-University Mainz
(Mainz Germany)
2008 – 2016 Abitur, Hermann-Staudinger-Gymnasium
(Erlenbach Germany)

Eigenständigkeitserklärung

Hiermit erkläre ich Moritz Remmers, dass ich die vorliegende Arbeit mit dem Titel:

“Synthesis and Functionalization of Molecular Vanadium Oxides”

selbstständig verfasst und keine anderen als die angegebenen Quellen und Hilfsmittel (dazu zählen auch KI basierte Anwendungen oder Werkzeuge*) benutzt habe. Sämtliche wörtlichen oder sinngemäßen Übernahmen und Zitate sind kenntlich gemacht und nachgewiesen (dies gilt auch für Texte, die durch generative KI, wie Chat GPT erzeugt wurden). Ich versichere, dass ich keine Hilfsmittel verwendet habe, deren Nutzung die Prüferin oder der Prüfer explizit ausgeschlossen hat. Im Anhang „Nutzung KI-Tools“ habe ich die verwendeten KI-Tools dokumentiert. Mit Abgabe der vorliegenden Leistung übernehme ich die Verantwortung für das eingereichte Gesamtprodukt. Ich verantworte damit auch jegliche KI generierten Inhalte, die ich in meine Arbeit übernommen habe. Die Richtigkeit übernommener (KI-generierter) Aussagen und Inhalte habe ich nach bestem Wissen und Gewissen geprüft.

Mir ist bekannt, dass ein Verstoß gegen die genannten Punkte prüfungsrechtliche Konsequenzen hat und insbesondere dazu führen kann, dass die Promotionsleistung als mit „nicht bestanden“ bewertet wird. Die Einschreibung kann für bis zu zwei Jahre widerrufen werden, wenn Studierende zweimal oder häufiger bei Prüfungsleistungen täuschen (§ 69 Abs. 4 und 5 HochSchG).

Ort, Datum und Unterschrift

Table 28: Use of AI Tools

ChatGPT	Rephrasing	Rephrasing complex content to achieve clearer formulations	throughout the entire thesis
---------	------------	--	------------------------------